MODELLING OF CARBIDE AND LAVES PHASE PRECIPITATION IN 9–12 WT% CHROMIUM STEELS

By

Joseph Douglas Robson

Clare College

Cambridge

A dissertation submitted for the degree of

Doctor of Philosophy,

at the University of Cambridge,

October 1996

PREFACE

This dissertation is submitted for the degree of Doctor of Philosophy at the University of Cambridge. The research described in this dissertation was conducted under the supervision of Dr. H.K.D.H. Bhadeshia in the Department of Materials Science and Metallurgy, Cambridge, between October 1993 and September 1996. This work is to the best of my knowledge original, except where acknowledgment and reference is made to previous work. Neither this, nor any substantially similar dissertation has been or is being submitted for any degree, diploma or other qualification at this, or any other, university. This dissertation contains less than 60,000 words.

Joseph Robson

September 1996

ACKNOWLEDGEMENTS

I would like to thank Professors A.H. Windle and C.J. Humphreys for the provision of laboratory facilities in the Department of Materials Science and Metallurgy at the University of Cambridge. I am indebted to my supervisor, Dr Harry Bhadeshia who has provide inspiration and encouragement throughout the course of this work.

Thanks are due to National Power and in particular to Dr D. Gooch for providing financial support. I would also like to acknowledge and thank David Gooch, Andrew Strang, Rod Vanstone and Rachel Thomson for their helpful suggestions and assistance during a number of valuable discussions. The assistance provided by Mr H. Davies of the National Physical Laboratory with MTDATA computations is also appreciated, as is the help of the department technical staff with specimen preparation and electron microscopy.

It is with pleasure that I acknowledge and thank all the members of the PT-Group who have both helped me and provided an enjoyable working environment for the past three years. In particular thanks go to Rachel Thomson, Howard Read, Phil Shipway, Steve Jones, Tracey Cool and Mike Lord. Thanks also to my other friends in Cambridge who have made my time here so pleasant.

Finally, I would like to thank Angela for her patience and support and my family for their unfailing encouragement and advice.

ABSTRACT

The ability of steels to resist creep deformation depends on the presence in the microstructure of carbide and intermetallic compounds which precipitate during tempering or elevated temperature service. The precipitation occurs in a sequence which leads to thermodynamic equilibrium. A knowledge of which phases form is important since it is well established that some enhance creep resistance more than others. Calculations based on thermodynamics give information about the relative stability of the possible precipitates, however but those observed in practice will also depend on the kinetics.

The work presented in this thesis deals primarily with the prediction of the rate at which a complex series of precipitation reactions occur in multicomponent steels of the kind used in power plant. Following a survey of the literature, it is demonstrated that the well–established Johnson–Mehl–Avrami theory cannot be applied effectively to reactions involving the precipitation of more than one phase. The theory has therefore been developed so that the "extended volume" argument can deal with many reactions occurring simultaneously. The resulting equations have to be integrated numerically in all but the simplest cases, however, this is seen as an advantage because it permits an incorporation of changing boundary conditions. It has been possible therefore, to model the precipitation of M_3C, M_2X, $M_{23}C_6$, MX and Laves phase in power plant steels of widely varying chemical composition using a single set of interfacial energies and number densities. Furthermore, the values of these fitting parameters are found to be quite sensible. There are some remarkable predictions. For example, M_2C in $2\frac{1}{4}$Cr1Mo steel has been predicted to be unstable in some circumstances if cementite were to form with it equilibrium composition.

The theoretical work has been compared extensively against published and new experimental data. It is now possible to construct time–temperature–transformation diagrams for precipitation reactions in power plant steels.

NOMENCLATURE AND ABBREVIATIONS

A	Constant in Norton's Law
C	Constant
c	Speed of light in a vacuum
C_1	Constant
C_2	Constant
$c^{\alpha\beta}$	Concentration of solute in α in equilibrium with β
$c_r^{\alpha\beta}$	The composition of α in equilibrium with a curved β interface
$\bar{c}$	Mean solute concentration
D	Diffusion coefficient
d	Thickness of cementite plate
D_0	Intrinsic diffusion coefficient
d_{hkl}	Plane spacing of hkl planes
$\bar{d}$	Mean distance between particles
e	Charge on an electron
f	Fraction of phase
f_M	Maximum fraction of phase
G^*	Free energy barrier to nucleation
G^β	Free energy of β
G_r^β	Free energy of β with a curved interface of radius r
ΔG	Free energy change
ΔG_0	Overall free energy change for transformation
ΔG_n	Driving force for nucelation per mole
ΔG_v	Chemical driving force for nucleation per volume of nucleus
h	Planck constant
hkl	Lattice plane indicies
I	Nucleation rate, per unit volume
I_A	Nucleation rate due to nuclei formed at 'A' sites
K	Constant relating the volume fractions of two phases precipitating simultaneously
k	Boltzmann constant
$\bar{l}$	Mean needle length
L	Camera length
L	Larson–Miller parameter
m	Constant in Zener–Hillert equation

m_e	Electron rest mass
n	Exponent in Avrami equation
N^*	Concentration of critical nuclei
N_0	Number of sites for nucleation per unit volume
N_A	Number of 'A' nucleation sites per unit volume
Q	Activation energy (diffusion or nucleation)
R	Molar gas constant
r	Radius
r^*	Critical radius for a viable nucleus
r^f	Final radius of precipitating particles
r^I	Instantaneous radius
r_0	Average grain size of cementite before Ostwald ripening
r_c	Critical radius of curvature
$\bar{r}$	Mean particle radius
R_{hkl}	Measured distance between transmitted and diffracted spots on micrograph
T	Temperature
t	Time
t_f	Rupture lifetime
T_M	Melting temperature
T_{eq}	Thermodynamic transformation temperature
T_{max}	Temperature at whick kinetics are most rapid
V	Total volume of the assembly
v	Growth rate
v^β	Volume per atom of β
V_e^β	Extended volume of β
V_m	Molar volume
V_β^{eq}	Equilibrium fraction of β
V_{accel}	Accelerating voltage
w_τ	Volume of an individual particle nucleated at time τ
x	Position coordinate
x^I	Instantaneous position (*e.g.* of interface)
y^D	Effective diffusion distance
z	Cube root of ζ
α	Ferrite

α_3	Dimensionless 3–dimensional parabolic growth constant
χ	3–dimensional parabolic growth constant (incorporating diffusion coefficient)
δ	δ–ferrite
$\dot{\epsilon}$	Creep rate
Γ	Capillarity coefficient
γ	Austenite
λ	Electron wavelength
∇	Laplace operator
ν	Rate at which post critical nuclei can form
Ω	Dimensionless supersaturation
Φ	Extent of reaction parameter
ϕ	M_2X needle aspect rato
σ	Interfacial energy
σ_a	Applied stress
σ_g	Internal stress due to grain boundary hardening
σ_l	Internal stress due to solution hardening
σ_u	Internal stress due to precipitation hardening
τ	Incubation time
ζ	Normalised volume fraction
$\frac{dO}{dn}$	Rate of increase of surface energy on adding an atom
b.c.c.	Body centred cubic
COST	A collaborative European research programme
CTE	Coefficient of thermal expansion
EDX	Energy dispersive X–ray analysis
f.c.c.	Face centred cubic
HP	High pressure
IP	Intermediate pressure
LHS	Left–hand side
LP	Low pressure
MAP	Materials algorithms project
MTDATA	Metallurgical and Thermochemical Databank
RHS	Right–hand side
SADP	Selected area diffraction pattern
TTT	Time–temperature–transformation

CHAPTER ONE

Introduction to 9–12 wt% Chromium Steels

This chapter gives an introduction to the work presented in this thesis. Included is a summary of power plant operation, a description of power plant steels currently in use and a review of the development of 9–12 wt% Cr steels.

1.1 Overview

There is a strong motivation from both an economic and environmental perspective to improve the efficiency of fossil fuel fired power plant. Over the last forty years there has been a continuous increase in the performance of such plant so that in 1990 the mean fuel mass required to generate one kilowatt–hour of electricity was approximately half that required in 1950 [Wachter and Ennis, 1995]. Since the early 1980s increased concern over rising fuel costs coupled with a drive to reduce emissions of gases such as CO_2 and SO_2 which are thought to contribute to global warming has emphasised the importance of this work.

Process control measures such as reducing the amount of excess air are able to contribute to increased thermodynamic efficiency but the most significant increases may only be obtained by increasing the live steam temperature. For example, an increase in steam conditions from 538°C at a pressure of 30 MPa to 650°C at a pressure of 40 MPa is expected to produce an increase in turbine efficiency of approximately 8% [Takeda and Masuyama, 1991].

As well as an improvement in efficiency there are other factors to be considered in the design and manufacture of new power plant. Not least of these is the requirement for a reliable service life, which may be in excess of 28 years in the case of steam turbines [Berger *et al.* 1993]. Also the plant must be resistant to the effects of cycles in temperature which arise when components are shut down and started up due to a change in demand for electricity or for servicing.

Critical in the realisation of such power plant is the development, study and understanding of new materials which are able to be made into components which can withstand the exacting design criteria. Predictive models, based on established metallurgical principle may provide an invaluable tool in suggesting new approaches and interpreting observations.

1.2 Power Plant Operation

The essential function of a power station is to convert energy from the fuel (nuclear or fossil) into electrical energy. In steam power plant this conversion involves consuming the fuel to produce heat which is then used to produce steam to drive a turbine. The mechanical energy of the turbine is then converted to electrical energy by an alternator. The steam temperature on entrance to the turbine in fossil fuel fired plant is considerably greater than that in nuclear plant [Weisman and Eckart, 1985]. The high strength 9-12wt% Cr steels[1] are therefore being

[1] In this work the term "9–12 wt% Cr steels" refers to a class of chromium rich, ferritic steels which may also contain significant quantities of other alloying elements such as Mo and V. Further details are given later in this chapter.

developed primarily for fossil fuel fired power stations.

1.2.1 The Steam Cycle

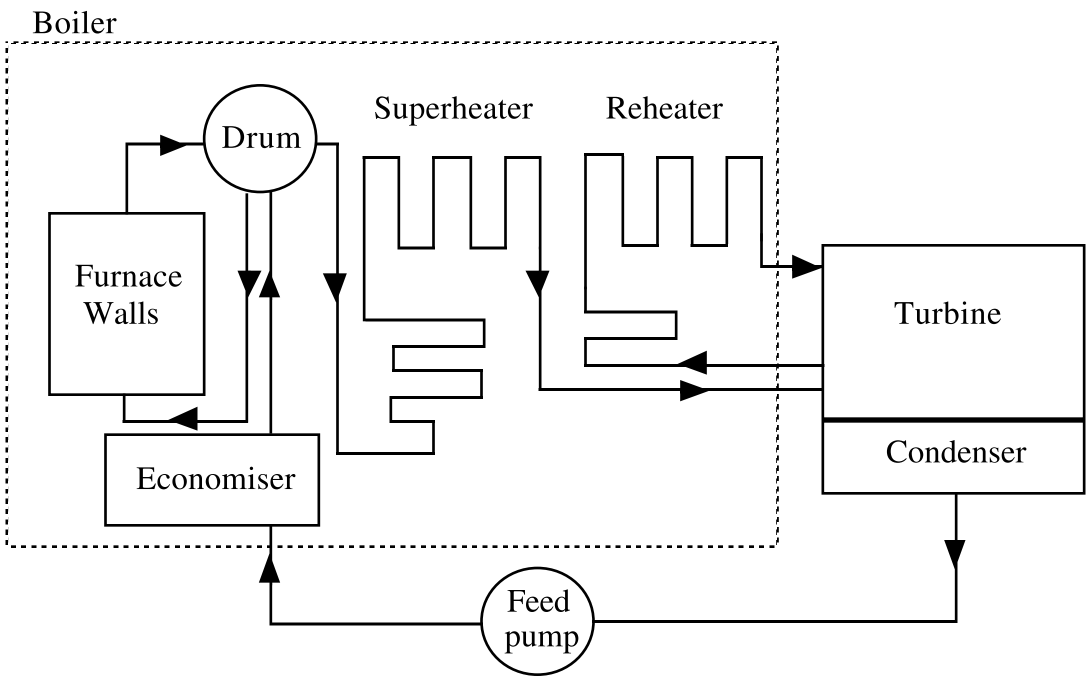

Figure 1.1 Water and steam circulation in power plant [Davison and Yeldham, 1975]

The route for steam and water circulation in fossil fuel fired power plant is shown schematically in Figure 1.1. Water is supplied to the boiler by feed pumps. The feedwater first passes through the economiser, which is situated next to the tubes carrying steam exiting the furnace walls. This preheats the feedwater which then passes into the steam drum. The water is then drawn from the steam drum into the tubes lining the furnace walls and is returned to the drum as a mixture of water and steam. Water and steam are separated within the steam drum, the water being returned to the furnace walls by boiler recirculating pumps. Hot gases from the combustion chamber flow across the boiler horizontally to heat the superheaters, reheaters and economiser elements, before flowing to the gas airheater which heats the incoming air to the combustion chamber. Steam from the drum passes through the superheater to the high pressure (HP) cylinder from where it is directed through nozzles onto the turbine blades to rotate the turbine. Exhaust steam from the HP cylinder returns to the boiler to pass through the reheater which restores its temperature. The reheated steam is then passed to the intermediate pressure (IP) turbine from where the exhaust steam is passed directly to the low pressure (LP) turbines. The HP, IP and LP cylinders are coupled together to drive the rotor of the generator.

1.2.2 Methods of Increasing Plant Efficiency

The overall efficiency of the conventional steam cycle as described above is approximately 40%. There are a number of process control measures which can be used to improve this efficiency. The efficiency improvements for changes in operating conditions which may be realistically achieved are shown in Table 1.1. Also shown are the improvements in efficiency due to changing the steam conditions. The declared (arbitrary) target efficiency level is 45% [Takeda and Masuyama, 1991]. It is apparent that while the process controls may provide a significant improvement in performance, a change in steam conditions is necessary if the target efficiency is to be achieved.

Control Measure	Increase in Efficiency/%
Reducing excess air by 10%	0.25
10°C decrease in flue gas temperature	0.25
Use of double reheat	1
Reduction of condenser pressure by 50%	1.5
60°C increase in steam temperature	1.4
20% increase in steam pressure	0.3

Table 1.1: Anticipated efficiency improvements for changes in power plant operating conditions [Wachter and Ennis, 1995]

1.2.3 Critical Components

The maximum steam temperature and pressure is limited by the performance of certain components. The main components which are critical are steam headers, superheater and reheater tubing in boilers, turbine valve chests, rotors and casings, main steam and reheat pipework, generator rotors and bolts used for high temperature applications. The life of boiler components is limited by corrosion and creep. Pipework also suffers creep as well as weld cracking and thermal fatigue. Turbine components are subject to creep and fatigue (both thermal and mechanical). High temperature bolting may also be subject to stress erosion.

1.3 Creep Deformation

Creep may be defined as the time dependent and permanent deformation of a material when exposed to a constant stress. Creep deformation is a thermally activated process and the rate of deformation (creep rate) is extremely temperature sensitive. In metals, creep deformation becomes important at temperatures greater than about $0.4T_M$, where T_M is the absolute melting temperature.[Reed-Hill and Abbaschian, 1992]. In the case of 9-12% Cr steels this temperature is approximately 450°C. Clearly power plant materials operate in the temperature regime where creep processes are significant. The creep properties of the materials used limits the operating temperature of many power plant components, such as the turbines. Development of materials with an increased creep resistance is central to the use of power plant with higher steam temperatures.

1.3.1 Creep Mechanisms

Creep deformation can occur by a variety of different mechanisms. The mechanism that dominates depends on the stress and temperature conditions as well as the microstructure of the material.

In the case of power plant steels the stress levels are relatively high and the temperatures (compared to the melting point) are relatively low. In this case creep deformation is controlled primarily by dislocation movement and the thermal energy available for dislocations to overcome obstacles. A deformation mechanism map gives information about which mechanism will dominate for a particular set of conditions. Such a diagram for a 1CrMoV steel is shown in Figure 1.2. For the exposure conditions for this material power law creep is expected to dominate.

Power law creep involves the movement of dislocations and the creep rate is a result of the balance between work hardening and recovery. Work hardening results in an increased dislocation density, whilst recovery leads to a reduction in dislocation density. If the dislocation density remains constant then the creep rate is given by Norton's Law [Norton, 1929].

$$\dot{\epsilon} = A(\sigma_a - \sigma_l - \sigma_u - \sigma_g)^4 \tag{1.1}$$

In this equation σ_a is the applied stress. σ_l, σ_u and σ_g are the internal stresses due to solution, precipitation and grain boundary hardening respectively. For high temperature strength, particle hardening is the most important [Bjärbo, 1994]. The most effective method for reducing the creep rate is therefore to form a suitable distribution of particles which are able to act as barriers to dislocation motion.

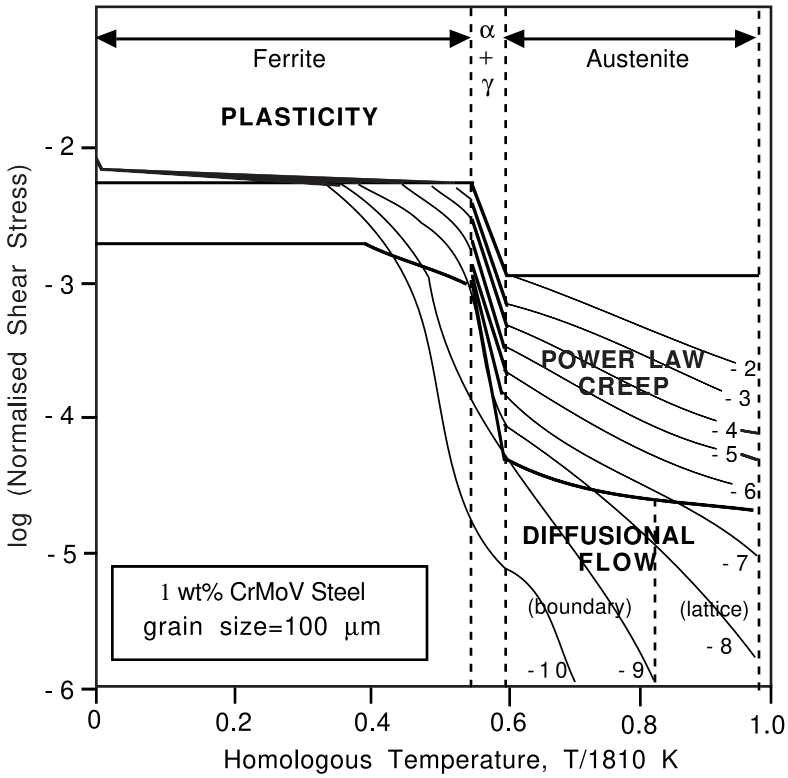

Figure 1.2: A deformation mechanism map for a 1CrMoV steel [Frost and Ashby, 1982]. The x axis is the homologous temperature ($\frac{T}{T_M}$ where T_M is the melting temperature) and the y axis the logarithm of normalised shear stress (shear stress/shear modulus). Also marked are contour lines corresponding to constant strain rates (with the logarithm of the strain rate marked). Using this diagram it is possible to determine the deformation mechanism given any two of these three variables.

To determine what the optimum particle size and distribution is, it is necessary to consider how dislocations overcome barriers to their motion. The barriers presented by the particles may be overcome in three ways.

(i) Orowan Bowing – Dislocation segments bend and pass between adjacent particles. An expanding dislocation loop forms around the particles which meets up and cancels enabling the dislocation to continue its motion. A dislocation ring is left around the particle generating a stress field which adds resistance to the motion of the next dislocation. The ease at which dislocations can pass particles by this mechanism increases as the particle spacing increases.

(ii) Particle Cutting – When particles are coherent dislocations can cut directly through them.

(iii) Dislocation Climb – Dislocations can bypass obstacles by a process termed climb.

This involves the diffusion of vacancies and is therefore easier at higher temperatures.

1.3.2 Methods of Increasing Creep Resistance

A study of the possible creep mechanisms suggests microstructures which would be expected to have good creep resistance under the conditions used in power plant. In general, creep resistant alloys are based on a matrix which is a solid solution. The presence of misfitting solute atoms in solid solution makes the passage of dislocations through the matrix more difficult. However, the majority of the creep resistance, at least in the early stages of service is derived from precipitate particles. Ideally these particles should be small, and they should be widely distributed in large numbers throughout the matrix. The particles need to be stable at the temperatures for which the alloy is designed and they should be resistant to coarsening as this will reduce their effectiveness as strengtheners. In general, excessive work hardening and a very fine grain size which provide strengthening at ambient temperatures are considered detrimental in high temperature alloys. This is because both of these provide easy diffusion paths and therefore lead to an increased creep rate.

In power plant steels the formation of carbides (and possibly nitrides) provides the precipitate hardening. Other alloying elements are also present in the matrix and these provide solution hardening. This is discussed further in section 2.4.

1.3.3 Creep Tests

The creep behaviour of a material may be characterised by a number of different parameters which can be measured by performing the appropriate creep test. For metallic materials most creep tests are conducted in uniaxial tension with a dumbell shaped specimen similar to that used for tensile testing. The tests are carried out at a constant temperature and under either a constant load or stress. Applying a constant stress is more useful if the test is being employed to provide information about the creep mechanism. A typical creep curve for a metal is shown in Figure 1.3. The curve may be divided into three regions, primary, secondary and tertiary creep. Primary creep is characterised by a continuously decreasing creep rate. This increase in creep resistance is due to strain hardening. Secondary or steady state creep is often the stage of longest duration. The creep rate is constant as a result of the balance between work hardening and recovery processes (Section 1.3.1). Finally for tertiary creep there is an acceleration in the creep rate followed by failure. This failure is termed creep rupture and may be due to microstructural and/or metallurgical changes; for example grain boundary separation, and the formation of internal cracks, cavities and voids.

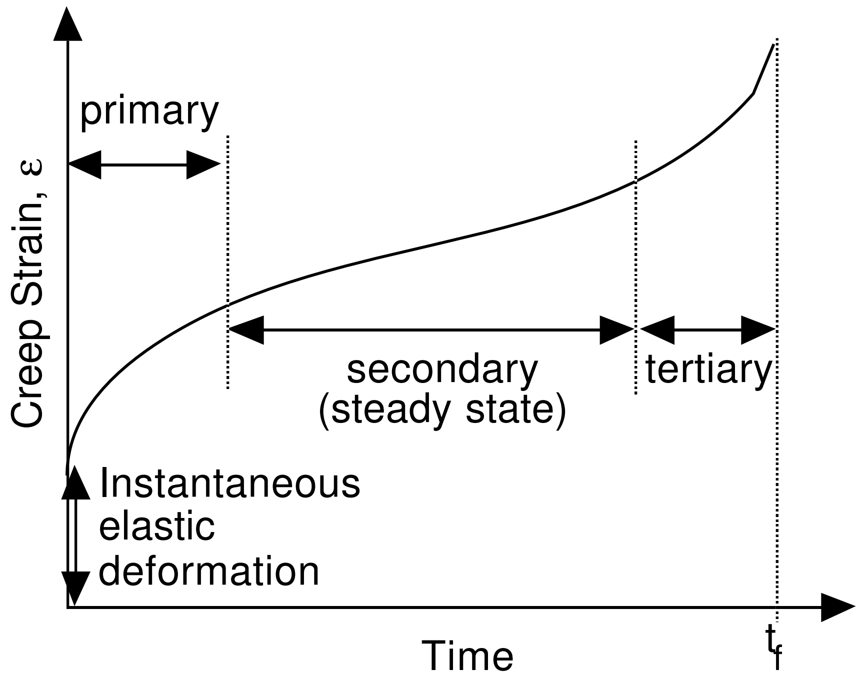

Figure 1.3 A typical creep curve of strain *vs.* time at constant stress and elevated temperature. t_f is the rupture lifetime [Callister, 1991]

For alloy steels such as those used in power plant the real creep curves may be more complex than that shown in Figure 1.3. This is because in these steels there are microstructural changes which occur throughout the creep test. These changes may include the precipitation of secondary phases which enhance creep resistance (this is known as secondary hardening). There may also be depletion of solute in the matrix by precipitation of coarse phases. This will lead to softening and the creep rate will increase. In this case tertiary creep (where the creep rate increases with time) may have the longest duration [Williams and Wilshire, 1977]. These changes are discussed in more detail in section 2.5.

The creep parameter that is considered in component design depends on the application. For example in long–life applications the steady state creep rate is an important parameter. The time to failure is also an often used design parameter. It is determined by carrying out a creep test at constant load and temperature to the failure point of the material, this is known as a “creep rupture test” and the time to failure is termed the “rupture lifetime”. Often a number of different creep rupture tests are carried out at different stresses and temperatures. These data are then often plotted in the form of a stress *vs.* Larson–Miller parameter plot. The Larson–Miller parameter is a commonly used in extrapolation of high temperature, short time creep data to lower temperatures. It combines temperature and time to give a single quantity, which is chosen to be constant at any stress level. The form of this parameter is

$$L = T(C + \log t_f) \tag{1.2}$$

where C is a constant (typically 20) for T in Kelvin and the rupture lifetime t_f in hours. Care must be taken when using this parameter since it does not account for the temperature dependence of the precipitation and dissolution reactions typical of power plant steels.

1.4 Power Plant Materials

The majority of fossil fired power plant currently used throughout the world are constructed using low alloy steels containing Cr, Mo and V as the major alloying elements. Such steels include $\frac{1}{2}$Cr$\frac{1}{2}$Mo$\frac{1}{2}$V which is probably the most widely used and 2$\frac{1}{4}$Cr1Mo steel which is used for superheater tubing and as a filler material for joining $\frac{1}{2}$Cr$\frac{1}{2}$Mo$\frac{1}{2}$V steel pipes (all compositions are given in wt%). The use of these materials places limitations on the operating temperature and pressure which may be employed in operation of the plant. For example, in the U.K. the maximum steam conditions are a temperature of 565°C and a pressure of $\simeq$ 30 MPa [Gooch, 1993]. To operate at temperatures and pressures in excess of those currently used requires the use of materials which have a higher creep strength combined with a greater corrosion resistance. Figure 1.4 is a plot of 100 000 hour creep rupture strength plotted against temperature for a number of steels. It is apparent that the temperature corresponding to a certain creep rupture strength increases significantly in going from a low–alloy ferritic steel to high–alloy ferritic steels and austenitic stainless steel.

1.4.1 Austenitic Stainless Steels

Examination of Figure 1.4 suggests that austenitic stainless steels are the best candidates for use in high temperature power plant. Austenitic materials have already been employed in a small number of pilot plants manufactured in America and Europe. These have been operated at temperatures up to $\simeq$ 650°C. There are, however, a number of serious problems associated with the use of austenitic steels in this application. These problems include the high cost of austenitic steels, the high coefficient of thermal expansion (CTE), low thermal conductivity and susceptibility to stress corrosion cracking [Berger *et al.* 1993]. The low thermal conductivity and high CTE of austenitic steels makes them highly susceptible to thermal fatigue and this severely restricts the cyclic capabilities of the power plant. To construct a plant capable of cyclic operation alternative materials are required. Ferritic stainless steels offer an attractive alternative as they exhibit a lower CTE and higher thermal conductivity (see Table 1.2). The use of these steels is then limited by their high temperature properties. Current work worldwide

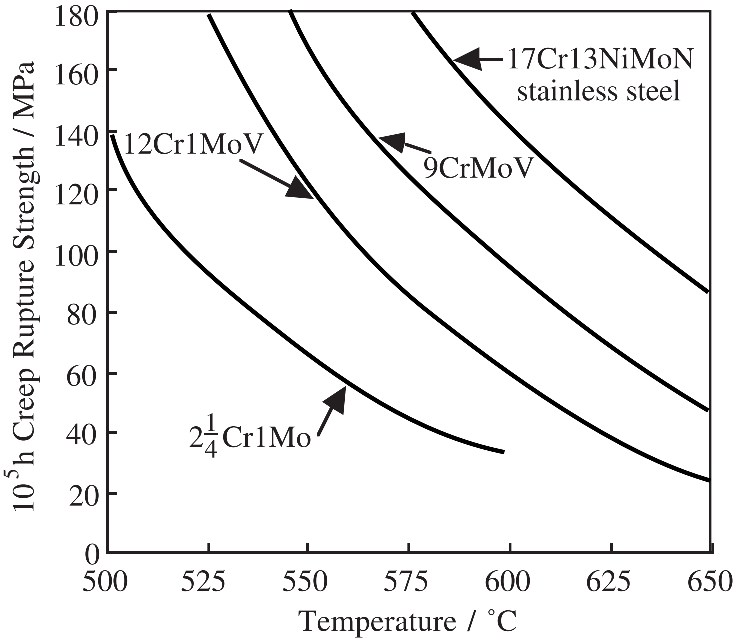

Figure 1.4 Creep rupture strength of various steels as a function of temperature [Blum *et al.* 1993]

is focussed on modifying the composition and heat treatment of these steels to optimise long term high temperature performance.

Steel	CTE/$Wm^{-1}K^{-1}$	Thermal conductivity/μK^{-1}
12Cr ferritic	9.9	24.9
20Cr1Ni austenitic	15.3	13.5

Table 1.2: Comparison of CTE and thermal conductivity for an austenitic and a ferritic stainless steel [Harvey, 1982]

1.4.2 9-12wt% Cr ferritic steels

The development of 9-12wt% Cr ferritic steels started in 1912 [Brigg and Parker, 1965] when Krupp and Mannesmann made a 12Cr steel with 2 - 5 Mo, principally for corrosion resistance. This type of steel was used for steam turbine blades. In the 1940s and 50s the requirements of the jet engine led to the development of 12Cr steels with greater high temperature strength. This was achieved by alloying with strong carbide formers. Today the main application for these steels is steam power plant. New steels have been designed largely on an empirical basis with new compositions being derived from established steels using experience and skill

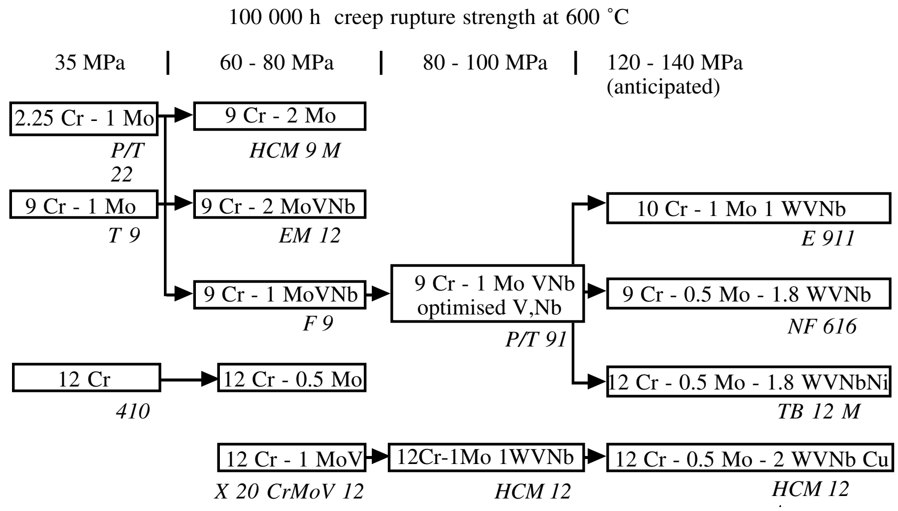

Figure 1.5 Flowchart showing the development of 9-12 wt% Cr steels (Adapted from Wachter and Ennis, 1995)

to produce alloys with improved properties for specific applications. Figure 1.5 is a summary of this development.

The steels on the right hand side of the chart may be subdivided into two main groups. The top three (E 911 to TB 12M) are designed to have a low (<5%) δ–ferrite content. The final steel, HCM12, has a high δ–ferrite content (20 - 30%). It can be seen that there is a general trend towards more complex compositions with alloying additions being made for a variety of reasons. The effects of the commonly used alloying elements are summarised in section 2.5.

Further development of these steels is in progress in an attempt to improve their performance. In the European COST programme a number of new steels have been developed on the basis of a review of currently existing steel grades. These steels are based on 9CrMoV to 12CrMoV with varying additions of other alloying elements. The compositions of these steels are summarised in Table 1.3.

The objective of the programme is to develop ferritic materials for operation at 600°C. In the case of rotor forgings the following minimum performance targets have been defined [Nickel *et al.* 1995; Gooch, 1993].

- 100 000 hour creep rupture strength at 600°C of 100 MPa together with long term creep rupture ductility at least as good as 1CrMoV (preferably > 10%) and no notch sensitivity.
- Charpy impact energy at least as good as 1CrMoV, i.e. > 40 J at room temperature.

	A(+N)	B(+B)	D(+W)	E(+W/Mo)	F(+Mo)
C	0.05-0.08	0.15-0.18	0.10-0.16	0.10-0.18	0.10-0.18
Si	0.1-0.3	0.1	0.1	0.1	0.1
Mn	0.2-0.7	0.1	0.5	0.5	0.45
P	–	<.01	<.01	<.01	<.01
S	<.005	<.005	<.005	<.005	<.005
Al	–	<.02	<.01	<.01	<.01
Cr	9-12.5	9-10.5	10-12	10-12	9.5-12
Mo	1-2	1.5	<.5	1	1-2
Ni	0.5-1.0	0.1	0.5-1.0	0.5-1.0	0.5-1.0
V	0.2	0.3	0.2	0.2	0.2
W	–	–	2	1	–
Nb	0.06	0.06	0.06	0.06	0.06
B	–	.005-0.01	–	–	–
N	0.09–0.22	–	<.07	<.07	<.07

Table 1.3: Composition of trial melts used in COST 501/II programme [Berger *et al.* 1993]. All values given in weight percent.

- Room temperature tensile proof stress > 600 MPa

The steels produced are being subjected to a rigorous testing programme to identify the most promising alloys. In addition to this testing there is a concerted effort to study the relationship between the composition, microstructure and properties of these steels. Attempts are also being made to produce models, both physical and empirical, to describe these relationships with the ultimate aim being to be able to predict properties for any given composition and heat treatment.

1.5 Summary

The need for more efficient power plant has lead to a drive to develop new materials capable of operation at higher temperatures than those currently used. 9-12 wt% Cr ferritic steels have been shown to be the most promising in providing the required creep and corrosion resistance.

CHAPTER TWO

The Physical Metallurgy of Power Plant Steels

This chapter reviews the physical metallurgy of power plant steels, with an emphasis on those containing 9–12 wt% Cr. The phases which are observed in these steels are discussed. Microstructural changes which occur during the service lives of these materials are also summarised.

2.1 The Fe–Cr–C System

The Fe–Cr–C phase system is complex with the possibility of many different equilibrium phases depending on composition and temperature. This complexity arises from the transition from ferrite stabilising (Fe–Cr) to austenite stabilising (Fe–C) phase regions. Iron may be present either as ferrite (α or δ), austenite (γ), or a mixture of both. There is also the possibility of the formation of a number of different chromium based carbides, some of which have a high solubility for iron. A vertical section through the phase diagram at 0.10wt% C is shown in Figure 2.1. It can be seen that for compositions in the range Fe–9Cr–0.1C to Fe–12Cr–0.2C the equilibrium state at 600°C is α + carbides.

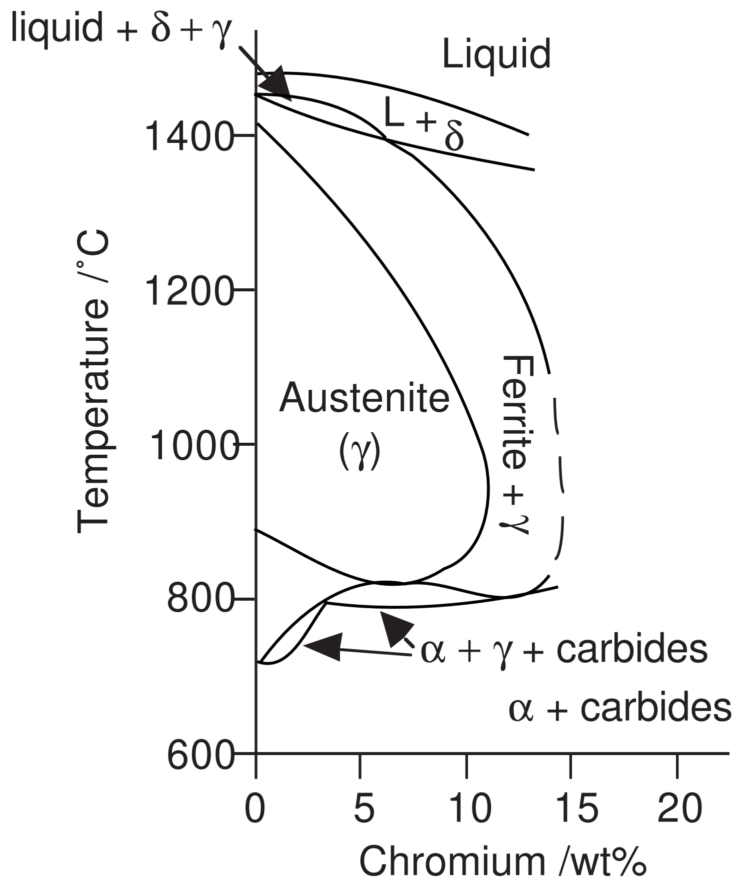

Figure 2.1 Phase diagram for Fe–xCr–0.1C [Sanderson, 1977]

Adding other alloying elements to the Fe–Cr–C system increases the complexity of the phase diagram still further. Alloying elements are added for a variety of different reasons. The majority of alloying additions form carbides (and nitrides if nitrogen is added) to provide precipitation strengthening. Often these additions are ferrite stabilisers. It may be necessary to balance these additions with austenite stabilising elements such as Ni to prevent excessive δ–ferrite formation. The phases which may be present and the effect of the various alloying additions are discussed in more detail in the following sections.

2.2 Transformations from Austenite

There exists for all the 9-12 wt% Cr steels a temperature range where the only stable phase is austenite. On cooling there are a variety of transformations which can occur depending on the alloy composition, cooling rate and the availability of lower energy sites for nucleation.

2.2.1 The Distribution of Alloying Elements

When the transformation from austenite to ferrite occurs on slow cooling the way in which the alloying elements distribute may be split into three categories. Alloying elements such as P and Si are normally found in the ferrite phase, their solubility in cementite and alloy carbides being quite low. Some elements can either form stable carbides or remain in solid solution in the ferrite. Elements which exhibit this type of behaviour include Mn, Mo, Cr, V, W, Ti and Nb. Often there is insufficient carbon in the steel to take up the available quantity of each element, in this case the remainder goes into solid solution. Finally there are elements which primarily enter the carbide phase. Nitrogen is the main example of an element which exhibits this behaviour, forming carbo–nitrides with many alloying elements. Nitrogen is also capable of forming alloy nitride phases particularly in the presence of Ti or Al.

Relatively large atoms such as Cr, Mo, Mn *etc.* form a solid solution with iron by substituting iron atoms on lattice sites. Small atoms such as C and N occupy interstitial sites between lattice atoms. These are therefore referred to as substitutional and interstitial atoms respectively.

2.2.2 The Effect of Cooling Rate

9-12 wt% Cr alloys will only form the equilibrium microstructure with partitioning of elements as described above if they are cooled from the austenite phase field at a very slow rate in the furnace. If cooling is at a faster rate (*e.g.* air or water quench) then there is insufficient time for the redistribution of substitutional alloying elements and so the equilibrium microstructure does not form. Instead of forming the equilibrium phases, quenching gives rise to metastable martensite. This phase has the same composition as the original austenite. The reason martensite forms is because its transformation mechanism does not require diffusion. Martensite has a body–centred cubic structure (b.c.c.) in common with ferrite unless the carbon is ordered in which case it has a body centred tetragonal structure. Unlike ferrite however, martensite is highly supersaturated in carbon which is trapped in the b.c.c. lattice as the martensite forms.

Martensite is a very hard but brittle phase and therefore almost all technological steels have to be tempered to increase their toughness. When martensite is heated sufficiently the trapped carbon is rejected from the b.c.c. lattice and forms carbides, either with iron or with the other alloying elements. The final microstructure consists of a dispersion of carbides within a ferrite matrix which often bears no resemblance to the as–quenched martensite. It is also possible that the martensite reaction does not go to completion on quenching in which case the microstructure will also contain some retained austenite. In 9-12 wt% Cr steels δ–ferrite is also often observed. This phase forms during austenitising for certain compositions which lie to the right of the $\gamma/\gamma+\delta$ phase boundary (Figure 2.1).

Both δ–ferrite and retained austenite are considered detrimental to mechanical properties. The presence of δ–ferrite accelerates the formation of α–ferrite/carbide direct from the austenite by raising the concentration of ferrite forming elements at the ferrite/austenite interface. The weaker α–ferrite formed during the accelerated transformation serves as a favoured fracture path resulting in a degradation of the creep resistance [Gooch, 1982]. Retained austenite is detrimental because at elevated temperatures it may decompose into α–ferrite/carbide with a resultant negative effect on creep resistance. However if it is stable then some retained austenite may be desirable as it is able to act as a good crack stopper [Pickering, 1995].

2.2.3 Commercial Heat Treatment

A typical commercial heat treatment for a power plant alloy involves austenitisation followed by a quench to martensite and subsequent temper. The temperature and duration of each of these steps can have an influence on the microstructure of the alloy. During austenitisation the aim is to dissolve all precipitates into the austenite phase without precipitating δ–ferrite. Precipitates which are not redissolved may coarsen rapidly at the austenitising temperature. In 9-12 wt% Cr steels the target temperature band is often quite narrow. For example, in studies on a 9Cr-1Mo alloy Pickering and Vassiliou [1980] have shown that $M_{23}C_6$ carbide does not completely dissolve until 1020°C whilst above 1200°C an increasing quantity of δ–ferrite is formed. Some precipitates such as Nb(C,N) are not dissolved during austenitisation [Nickel *et al.* 1995]. Fortunately these particles do not coarsen rapidly and so remain as a fine dispersion in the matrix.

Quenching follows austenitisation. In general the 9–12 wt% Cr steels are fully air hardenable. This means that a fully martensitic structure is formed on air cooling from the austenitising temperature. The cooling rates achieved in practice will depend on the component geometry. For example, the cooling rate at the centre of a large rotor forging will be considerably less than at the surface, and may be as low as 2°C s^{-1}. At these very low cooling rates it is possible that there will be sufficient time for the undesirable formation of α–ferrite and carbides directly from the austenite.

Following quenching tempering is carried out to increase the toughness of the martensite. The maximum tempering temperature must be less than the temperature at which the martensite reverts to austenite but needs to be relatively high to produce a thermally stable microstructure.

2.3 Tempering of Martensite

The tempering of martensite is usually carried out in the range 150–700°C. For steels destined for high temperature applications tempering is carried out towards the top of this range. Sometimes two or more stage tempering treatments will be used depending on the required properties. The combination of heat treatments are chosen to produce a suitable dispersion of precipitate particles, which are then stabilised by a high temperature treatment. For example in the COST project tempering was carried out in two stages, the first at 570°C and the second between 685°C and 730°C [Berger, 1992].

Extensive studies have been carried out on the tempering behaviour of power plant steels. Most of this work to date has focused on the most widely used steels, 1CrMoV and $2\frac{1}{4}$Cr1Mo. The 9–12 wt% Cr steels undergo similar microstructural changes to these steels although the transformation kinetics are considerably faster. The tempering of $2\frac{1}{4}$Cr1Mo steel has been divided into four stages [Balluffi *et al.* 1951; Baker and Nutting, 1959]

1. Precipitation of ϵ carbide. This has a hexagonal crystal structure and a composition $Fe_{2.4}C$ and forms as narrow plates with a well–defined orientation relationship.
2. Retained austenite decomposes, possibly to bainite and cementite.
3. Cementite precipitates, and as it grows ϵ carbide will disappear.
4. Complex alloy carbides precipitate and there is complimentary dissolution of cementite. These alloy carbides may themselves dissolve at later times as different carbides start to precipitate.

The first three stages require only the diffusion of the interstitial atoms whereas the final stage also requires diffusion of substitutional species. These stages are therefore very rapid compared to the final stage. For example Baker and Nutting found that stages 1–3 were complete after 5 hours at 500°C whereas stage 4 was still in progress at the longest times investigated (1000 hours). It is the behaviour during stage 4 which is of greatest importance with reference to the creep properties.

During stage 4 of tempering there is a sequence of ever more stable but kinetically less favoured precipitates. The initial metastable precipitates are those for which nucleation is easiest. At longer times other phases may form. Although nucleation of these phases is more difficult, their formation leads to a reduction in the free energy of the system and is therefore thermodynamically favourable. The formation of more stable precipitates is often accompanied by the dissolution of the previous precipitates. However, it is also possible for small quantities of thermodynamically stable phases to form early in the tempering sequence (or be present after austenitisation *e.g.* Nb(C,N)). Such phases do not dissolve during subsequent tempering.

Many studies have been carried out to identify and characterise the phases observed during the tempering of martensite (*e.g.* Kuo, 1953; Shaw and Quarrel, 1957; Baker and Nutting, 1959; Woodhead and Quarrel, 1965; Yakel, 1985). This work is summarised for each of the phases commonly observed in power plant steels. Typically many alloying elements are soluble in each of these phases to some extent. The chemical formula are therefore often written wih M representing the total metal content and X representing the total C and N content. Data for carbide phases commonly observed in steels are summarised in Table 2.1.

2.3.1 M_3C

In iron carbon alloys cementite forms with the composition Fe_3C. This phase is an approximately close packed hexagonal structure of iron atoms with localised distortions to accommodate the interstitial carbon atoms. In alloy steels the partitioning of several alloying elements into the cementite changes the composition significantly. Woodhead and Quarrel (1965) have reported significant quantities of manganese and chromium in M_3C. Thomson (1992) has measured chromium levels in excess of 30 wt% in a $2\frac{1}{4}$Cr1Mo steel at 565°C. Tungsten and vanadium also have limited solubilities in cementite.

Studies of cementite precipitation have shown that it probably forms by a paraequilibrium transformation mechanism which involves partitioning of interstitial but not substitutional species (section 3.7) [Hultgren, 1947; Bhadeshia and Christian, 1990]. On tempering, the cementite will enrich and approach its equilibrium composition. The rate of enrichment will be fastest when the cementite particles are small and the ferrite is highly supersaturated in carbide forming solute atoms [Bhadeshia, 1992]. In low chromium power plant steels the cementite enriches slowly and does not reach its equilibrium composition within the component lifetime. In these steels the level of enrichment can be used to give an estimate of the combined time and temperature exposure of the alloy. In high chromium alloys cementite enriches more rapidly and then dissolves as alloy carbides precipitate so it is not possible to use this technique [Thomson, 1992].

2.3.2 M_2X

In many cases M_2X is the next phase to precipitate after cementite. It has a hexagonal structure and commonly precipitates as fine needles parallel to the $< 100 >_\alpha$. The orientation relationship is that of Pitsch–Schrader (1958):-

$$(0001)_{M_2X} \parallel (011)_\alpha \text{and } [11\bar{2}0])_{M_2X} \parallel [100]_\alpha$$

M_2X is generally considered to nucleate on matrix dislocations and martensite lath boundaries. Studies of an Fe–Mo–C alloy have shown that Mo_2C can also nucleate on ferrite/cementite boundary followed by in–situ transformation of cementite [Raynor *et al.* 1966]. This transformation mechanism has not been reported in the chromium containing alloys.

The composition can vary widely with with molybdenum, chromium and vanadium soluble in significant quantities. In steels with molybdenum, no nitrogen and a low chromium content M_2X is often close to the ideal Mo_2C composition [Baker and Nutting, 1959]. However, in 9-12 wt% Cr steels containing nitrogen the M_2X composition is found to be closer to Cr_2N [Sanderson, 1977]. Precipitation is often accompanied by an increase in alloy strength (secondary hardening). In low alloy ferritic steels it is said to be the precipitation of M_2X which is the major factor in conferring creep resistance on the steel. It has also been shown that the 0.2% proof stress of 12 wt% Cr steels may be increased by stabilisation of the M_2X phase [Irvine and Pickering, 1964]. However, other factors, such as avoiding δ–ferrite limits the amount of stabilising elements which may be added. Generally in 9-12 wt% Cr alloys M_2X dissolves after long term exposure at elevated temperature and so does not enhance the long term creep resistance [Vanstone, 1994] though its precipitation may have a profound influence on the carbides that form subsequently.

2.3.3 M_7C_3

M_7C_3 is a chromium rich carbide with a trigonal crystal structure. Iron and manganese are also soluble in this phase. If observed, it occurs after M_2X formation [Baker and Nutting, 1959], or after cementite formation without any intermediate M_2X being observed [Janovec *et al.* 1994]. Woodhead and Quarrell (1965) state that M_7C_3 will only be observed if the chromium content is sufficiently high compared to other alloying elements. If molybdenum is present it is possible that $M_{23}C_6$ will form after M_2X rather than M_7C_3. Nucleation can occur either on fresh sites or in–situ at the ferrite/cementite interface [Darbyshire and Barford, 1966]. Sakuma *et al.* (1981) observe that M_7C_3 particles coarsen rapidly. These particles are not considered to contribute greatly to the creep resistance.

When looking for M_7C_3 it is useful to note that its diffraction patterns show characteristic streaks, making it easier to distinguish from other carbides. The streaks have been attributed to faults lying on {10.0} planes (Beech and Warrington, 1966).

2.3.4 $M_{23}C_6$

$M_{23}C_6$ is also a chromium rich carbide which may also contain tungsten, molybdenum, vanadium and nickel [Woodhead and Quarrell, 1965]. It has a complex face centred cubic (f.c.c.) crystal structure. It forms after either M_7C_3 or M_2X. In 9-12 wt% Cr steels it is often the equilibrium carbide, and is predominant after typical tempering treatments. Nucleation occurs almost exclusively on prior austenite grain boundaries and martensite lath boundaries [Senior, 1988]. $M_{23}C_6$ forms as large particles and does not directly contribute to the creep strength, although it has been suggested that it may stabilise the lath boundaries [Bjärbo, 1994].

2.3.5 M_6C

In steels containing molybdenum and relatively low levels of chromium M_6C is the equilibrium carbide. It has an f.c.c. crystal structure and is molybdenum rich but may also contain chromium and vanadium. Nucleation can occur on the M_2X or $M_{23}C_6$ interphase boundary [Kurzydlowski and Zielinski, 1984]. Fresh site nucleation is also possible on prior austenite grain and lath boundaries. As for $M_{23}C_6$, particles tend to be large and do not enhance creep resistance.

2.3.6 MX

In complex 9-12 wt% Cr alloys MX carbonitrides may be observed. These have an f.c.c. crystal structure and show two different morphologies. Small spheroidal MX precipitates, which may contain titanium, vanadium and niobium are observed in as–quenched material and are thought to remain undissolved during austenitisation [Janovec *et al.* 1994]. After tempering, plate like MX forms containing chromium and vanadium. This nucleates on the spheroidal MX particles forming a characteristic “V–wing” morphology [Nickel *et al.* 1995].

MX particles form a fine dispersion within the martensite laths, and it is therefore thought that they are important in enhancing the creep resistance of steels where they are present.

2.3.7 Laves Phase

Laves phase has the general composition Fe_2M and a hexagonal crystal structure. “M” can be tungsten, molybdenum or some combination of both. It is often observed in 9-12 wt% Cr steels containing tungsten or molybdenum after long term exposure to elevated temperatures (around 600°C) where it is an equilibrium phase. The formation of Fe_2Mo is thought to require an atomic ratio Mo/C greater than 5, and the formation of Fe_2W a W/C ratio greater than 3.3 [Briggs and Parker, 1965]. Other elements may act as catalysts for Laves phase, causing it to form at lower atomic ratios. V, Ti and Co may all exhibit this catylitic effect. Silicon also appears to have a marked effect in controlling Laves phase formation. For example Hosoi *et al.* found considerable quantities of Laves phase in a 9Cr–2 wt% Mo alloy which contained 0.67 wt% Si. When the silicon content was reduced to 0.008 wt% only small amounts of Laves phase were observed. Senior (1989) concludes that the solubility of Laves phase is dependent on the silicon content of the alloy. Nickel appears to have a role in controlling the kinetics of formation. Iseda *et al.* (1992) examined two samples after creep tests, one which contained 0.3 wt% Ni which had been creep tested for 3627 hours and one which contained 1.2 wt% Ni which had been creep tested for 2053 hours. In both cases they found the same amount of Laves phase and concluded that nickel additions accelerated its formation. This conclusion is not necessarily correct however, since it is possible that the equilibrium volume fraction of Laves phase forms at a shorter time than that at which observations were made in which case the conclusion would be that nickel additions do not alter the equilibrium volume fraction. Manganese additions are thought to have the opposite effect, retarding the kinetics of Laves phase precipitation. Hosoi *et al.* (1986) compared to similar samples of 9Cr–2 wt% Mo steel with different manganese concentrations. They found that the onset of Laves phase formation was delayed in a sample containing 1.17 wt% Mn compared to one containing 0.58 wt% Mn.

Studies of the preferred sites for Laves phase formation show that it forms initially on prior austenite grain boundaries followed by precipitation at lath boundaries and finally some precipitation within laths as ageing proceeds [Senior, 1989]. Precipitation frequently occurs in the chromium depleted regions surrounding $M_{23}C_6$ particles. Laves phase is considered to be undesirable for creep properties. It forms as large particles which do not contribute significantly to precipitation strengthening and it reduces the solid solution strengthening by depleting tungsten and molybdenum in the matrix. It is also believed to have an adverse effect on toughness and has been shown to raise the ductile to brittle transformation temperature [Hosoi *et al.* 1986].

2.3.8 Precipitation Sequences

The alloy composition and heat treatment will not only determine which precipitates are observed, but will also govern the order in which they form. Several studies have been undertaken into characterising the precipitation sequences in $2\frac{1}{4}$Cr1Mo steels and the results have been presented in the form of carbide stability diagrams [Baker and Nutting, 1959; Yu, 1989].

Carbide	Structure	Lattice Parameters /Å	Formula Units / Cell	Density g cm^{-3}
M_3C	Orthorhombic	a = 4.5241	4	7.704
		b = 5.0883		
		c = 6.7416		
M_7C_3	Trigonal	a = 13.982	8	6.965
		c = 4.506		
$M_{23}C_6$	Cubic F	a = 10.638	4	6.996
M_6C	Cubic F	a = 11.082	16	6.325
M_2X	Hexagonal	a = 3.002	1	9.188
		c = 4.724		

Table 2.1: Data for common alloy carbides found in steels. Note that the density and lattice parameter values will vary depending on the composition of each carbide [Andrews *et al.* 1967]

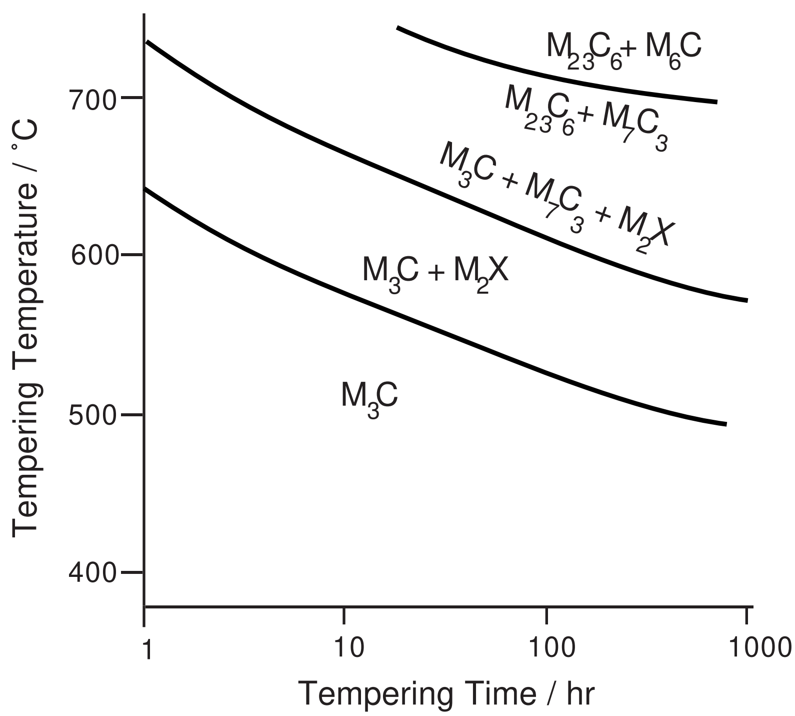

Figure 2.2 Carbide stability diagram for a $2\frac{1}{4}Cr1Mo$ steel with an initially martensitic microstructure (modified from Baker and Nutting, 1959)

The sequence of changes observed by Baker and Nutting may be summarised as follows:

$$
\begin{array}{l}
M_3C \rightarrow M_3C + M_2X \rightarrow M_{23}C_6 \rightarrow M_6C \\
\qquad\qquad\qquad\qquad\qquad\quad \downarrow \\
\qquad\qquad\qquad\qquad\qquad\quad M_7C_3 \rightarrow M_6C
\end{array}
$$

Yu observed the same sequence in a low silicon steel, but showed that increasing the silicon concentration to 0.6 wt% stabalises the M_6C phase. This alters the sequence so that M_6C is observed directly after M_2X formation. Kuo (1953) states that the Mo:C ratio is important in determining the precipitation sequence. For example, if Mo:C is greater than approximately 1.2 then M_6C will form directly from M_2C without any intermediate $M_{23}C_6$.

Precipitation sequences such as these are also observed in 9-12 wt% Cr steels. In these steels M_6C is only observed after tempering at very high temperatures ($\geq$ 760°C) [Briggs and Parker, 1965]. At lower temperatures $M_{23}C_6$ is the characteristic carbide. Also, if the molybdenum or vanadium levels are sufficiently high then M_7C_3 is not observed and precipitation of $M_{23}C_6$ will occur directly after M_2X formation. The kinetics of precipitation are also considerably faster in these steels due to the high concentration of carbide forming elements. For example in a 12Cr1MoV steel $M_{23}C_6$ was observed after only 15 minutes at 700°C [Thomson, 1992].

2.4 Effect of Alloying Elements on Microstructure and Creep Properties

Alloying additions are made for a variety of purposes. Most are used to stabilise phases which provide creep resistance (*e.g.* M_2X, MX). Elements are also added to provide solid solution strengthening, suppress undesirable phases or for other specific purposes. The effects of the commonly used alloying additions on high temperature microstructure and properties has been reviewed by several authors [Briggs and Parker, 1965; Greenwell and Beech, ?]. These effects are summarised below.

2.4.1 Chromium

Chromium is a ferrite stabilising element which is able form a number of different carbides. Increasing chromium content increases susceptibility to δ–ferrite formation. Large chromium additions provide hardenability and resistance to corrosion. Chromium contents above 12.5 wt% are undesirable as they may lead to embrittlement of the steel at elevated temperatures. This is due to the formation of an α'' chromium rich phase by spinodal decomposition.

2.4.2 Molybdenum

Molybdenum is a ferrite stabilising element and is also a carbide former. Additions of molybdenum stabilise the M_2X phase. Fujita (1978) suggests an optimum molybdenum content of

1.5 wt%. A molybdenum content greater than this leads to δ–ferrite formation. Also, if the molybdenum to carbon ratio is greater than five then Laves phase (Fe_2Mo) may form. Some molybdenum also remains in the ferrite where it contributes to solid solution strengthening.

2.4.3 Nickel

Nickel is an austenite stabilising element which does not normally form carbides. It counters the effect of ferrite stabilising additions and therefore suppress δ–ferrite formation. It tends to lead to a reduction in the creep rupture strength in 9-12 wt% steels but rupture ductility is not significantly affected. The decrease in rupture strength has been attributed by Hosoi *et al.* (1986) to accelerated Laves phase precipitation kinetics when nickel is present.

2.4.4 Tungsten

Tungsten is a ferrite stabilising element which is also soluble in a number of carbides. It stabilises M_2X phase, but is less effective than molybdenum since for an equivalent effect almost twice (wt%) as much tungsten is required. Increasing tungsten also increases the amount of Laves phase which forms. Tungsten also contributes to the solid solution strengthening but its contribution diminishes with tempering time and after 100 000 hours is predicted to be negligible.

2.4.5 Vanadium

Vanadium is a ferrite stabilising element and a strong carbide former. Like tungsten and molybdenum, vanadium stabilises the M_2X phase. It may also combine with carbon and nitrogen to form vanadium–rich carbides and carbonitrides. The ratio of vanadium to carbon is important in determining how effective the vanadium will be as a strengthener. The affinity of vanadium for carbon is greater than that of molybdenum. The strengthening effect of vanadium may be enhanced by the removal of the available carbon into vanadium carbides, leaving the molybdenum in the matrix where it contributes to solid solution strengthening [Gooch, 1981].

2.4.6 Niobium

Niobium is a ferrite stabilising element which forms stable MX precipitates with carbon and nitrogen. The effect of niobium depends on the austenitisation temperature as this governs the amount of MX precipitate which is taken into solution.

2.4.7 Titanium

Titanium is a strong nitride former which leads to an increase in creep rupture strength (its potency being between that of vanadium and tungsten). However, titanium additions result in a large reduction in rupture ductility, suggested by Fujita (1978) to be due to titanium based inclusions which prevent deformation at the grain boundaries.

2.4.8 Boron

Boron is considered to be one of the most beneficial elements for high temperature strength. Additions of boron leads to increased precipitation at grain boundaries. Excessive boron additions are detrimental to strength due to the formation of undissolved boride phases [Park and Fujita, 1982].

2.4.9 Carbon

Carbon occupies interstitial sites in both austenite and ferrite with a greater solubility in austenite which it stabilises relative to the ferrite. Increasing carbon naturally encourages carbide precipitation. Although carbon strengthens the steel it can have be detrimental to toughness. In practice a carbon level of approximately 0.15 wt% is the maximum which can be tolerated in power plant steels[Irvine and Pickering, 1969]. High carbon steels are generally not weldable due to cracking in the heat affected martensitic zones.

2.4.10 Silicon

Silicon is a ferrite stabilising element which can influence the kinetics of carbide precipitation [Woodhead and Quarrel, 1965]. Silicon is unusual in that it reduces the lattice parameter of the ferrite, thus increasing the mismatch between the carbides and the matrix leading to enhancement of the secondary hardening. Silicon additions in excess of 1 wt% leads to the formation of excessive δ–ferrite as well as intermetallic complex silicides which are both undesirable [Irvine and Pickering, 1969].

2.4.11 Nitrogen

Nitrogen also occupies interstitial sites and is an austenite stabiliser. Increasing nitrogen stabilise M_2X relative to carbide precipitates. The formation of an increased amount of fine M_2X needles has been suggested as the reason why nitrogen increases the creep rupture strength [Irvine and Pickering, 1964]. Fujita (1968) however has shown that in some circumstances nitrogen additions lead to a reduction in the creep rupture strength. He investigated the effect of varying the nitrogen content from 0.01 to 0.05 wt% in a steel with a base composition 0.2C–11Cr–1Mo–0.2V–0.2Nb-0.03 wt% B. At 550°C the high N steel was marginally stronger than the low N variant for all test durations. At 650°C and test durations greater than 1000 hours the high N steel became progressively weaker than the low N material. Similar behaviour has been observed in a 0.2C–10.5Cr–1.5 wt% Mo steel studied by Tsuchiyama and Fujita (1981).

There is disagreement on the effect of N on creep rupture ductility at 650°C, with nitrogen found to increase the rupture ductility in the first investigation and decrease it in the second.

2.5 Microstructural Changes During Creep Deformation

It has already been stated that many common power plant steels are far from their equilibrium state when they enter into service. The subsequent changes in the microstructure during service ultimately limit the performance of the steel. These changes, which involve a change in the dislocation structure as well as precipitation and dissolution of carbides, nitrides and inter–metallics are strongly dependent on temperature and are influenced by stress.

Often creep behaviour is characterised by accelerated creep tests at a higher temperature than that expected for service. An extrapolation procedure, such as Larson–Miller is then used to estimate the behaviour at the service temperature. However, in the 9-12 wt% chromium steels, because the precipitation of secondary phases is so temperature dependent it is dangerous to extrapolate data from accelerated creep tests, since the microstructural changes may not be the same in both cases. Such extrapolation may be possible, but only within certain composition and heat treatment bounds deduced from experience. These are given by Fujita, 1992 as

- Composition: 9–12 Cr, 0.05–0.2C , <0.06 N, <0.2 C+N, <0.05 B, 0.1–0.3 V, 0.03–0.15 Nb (all wt%). Also if N = 0.02 to 0.03 wt%, then Mo + 0.5W > 1.0 wt%; and if N = 0.05 to 0.06 wt% then Mo + 0.5W > 1.5 wt%.
- Heat treatment: Austenitisation at 1050–1150 °C followed by air or oil quench; temper at 750–800°C, air cool.

To ensure reliable data requires creep tests are often carried out at the anticipated service temperature. Because the anticipated lifetimes of the components are great and some microstructural changes occur extremely slowly these creep tests are carried out to very long times (in excess of 100 000 hours).

For the 9-12 wt% chromium steels most creep data are represented in the form of creep stress against either time to rupture or Larson–Miller parameter. A schematic of a typical curve is shown for a high chromium ferritic power plant steel in Figure 2.3. Also shown are the contributions from the various active mechanisms [Berger, 1995]. The contribution due to precipitation strengthening fluctuates as precipitates dissolve and others begin to form. Precipitation removes solute from the matrix and is accompanied by a reduction in the contribution of solid solution strengthening. In many cases this is compensated for by an increase in the contribution to precipitate strengthening. This is not the case for Laves phase, the contribution it makes to precipitation strengthening is small because of the small number density of particles. The precipitation of Laves phase is therefore accompanied by a reduction in the creep strength (Figure 2.3). It is worth noting that the Larson–Miller extrapolation from higher temperature data may not show the effect of Laves phase if it is not thermodynamically stable at the artificially elevated temperature.

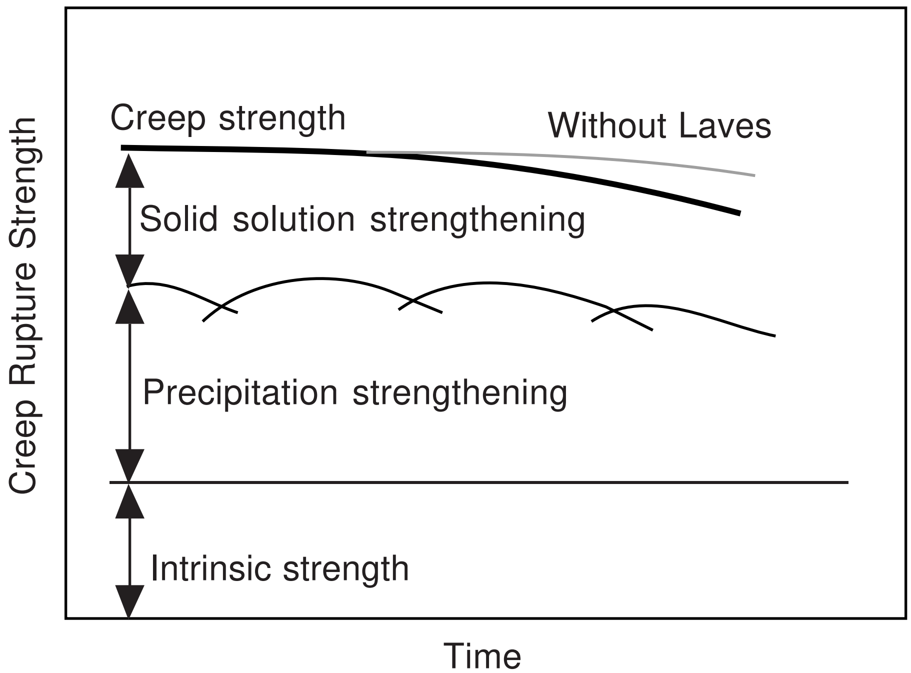

Figure 2.3 A schematic plot of creep strength against time for a high chromium ferritic power plant steel at 600°C, showing the contributions from the various strengthening mechanism [Berger, 1995]

Several studies have been carried out to relate microstructural changes to creep properties in the 9-12 wt% chromium steels *e.g.* [Vanstone, 1994; Straub *et al.* 1993; Spriadek *et al.* 1994]. Some of the important changes which occur during creep are illustrated in Figure 2.4 which shows schematically how the microstructure changes in a 10Cr–2W–0.3Mo–0.2 wt% V steel tested at 600°C. The processes which occur are summarised as follows, assuming that the microstructure prior to creep exposure consists of $M_{23}C_6$ and MX precipitates as shown in Figure 2.4 (a).

2.5.1 Changes in Dislocation Structure

The movement of the dislocations is resisted initially by other dislocations because of the reasonably uniform high dislocation density within the martensite laths. Intra–granular particles of MX and the strain fields associated with elements in solid solution also inhibit the motion of dislocations. As creep progresses the uniform dislocation structure within the laths changes as the dislocations start to form sub–grains. This is accompanied by a reduction in the dislocation density [Nickel, 1995]. On further exposure to elevated temperature the sub–grains will tend to grow. The sub–grain boundaries are stabilised by $M_{23}C_6$ and possibly Laves phase formation. The precipitation of Laves phase is accompanied by a reduction in the solid solution strengthening. As the sub–grains grow the creep rupture strength is reduced, and the creep resistance becomes less dependent on the movement of individual dislocations though the matrix, and more on the resistance to sub–grain growth.

2.5.2 Changes in Particle Distribution

After the typical quench and temper treatment the microstructure of the 10Cr–2W–0.3Mo–0.2 wt% V steel consists of $M_{23}C_6$ particles on the lath and block boundaries, with small MX and M_2X particles within the laths. For all the steels listed in table 3) MX and $M_{23}C_6$ were observed after exposure to creep conditions. M_2X however was found to dissolve relatively rapidly during many of the tests. It was therefore concluded that M_2X, which plays a dominant role in the strengthening of $2\frac{1}{4}$ wt% Cr steels is less important in the mechanical properties of the 9-12 wt% Cr alloys. As the creep progresses small $M_{23}C_6$ particles on the lath boundaries dissolve and larger $M_{23}C_6$ particles on the block boundaries coarsen. Laves phase also starts to precipitate. The time at which Laves phase is first observed depends on the temperature and the chemical composition, for example, the absence of tungsten in a steel appears to delay its formation by several thousand hours [Vanstone, 1994]. The MX precipitates are the most resistant to coarsening[1] and remain as a fine dispersion within the laths.

2.5.3 Optimum Microstructure For Creep Resistance

Interpretation of the results of the experimental studies have been used to suggest desirable properties for a creep resistant microstructure. Some of the key features of such a microstructure are summarised below.

- Dislocation sub–grain boundaries need to be stabilised. This may be achieved by forming a suitable dispersion of particles.
- To reduce the rate of recovery the initial dislocation density should be reduced.
- The precipitation of Laves phase should be suppressed, since this results in a reduction in the solid solution strengthening.

These criteria lead to the complex compositions and heat treatments that are used in practice.

[1] Coarsening involves the growth of large particles at the expense of small ones whilst the volume fraction remains constant (section 3.10)

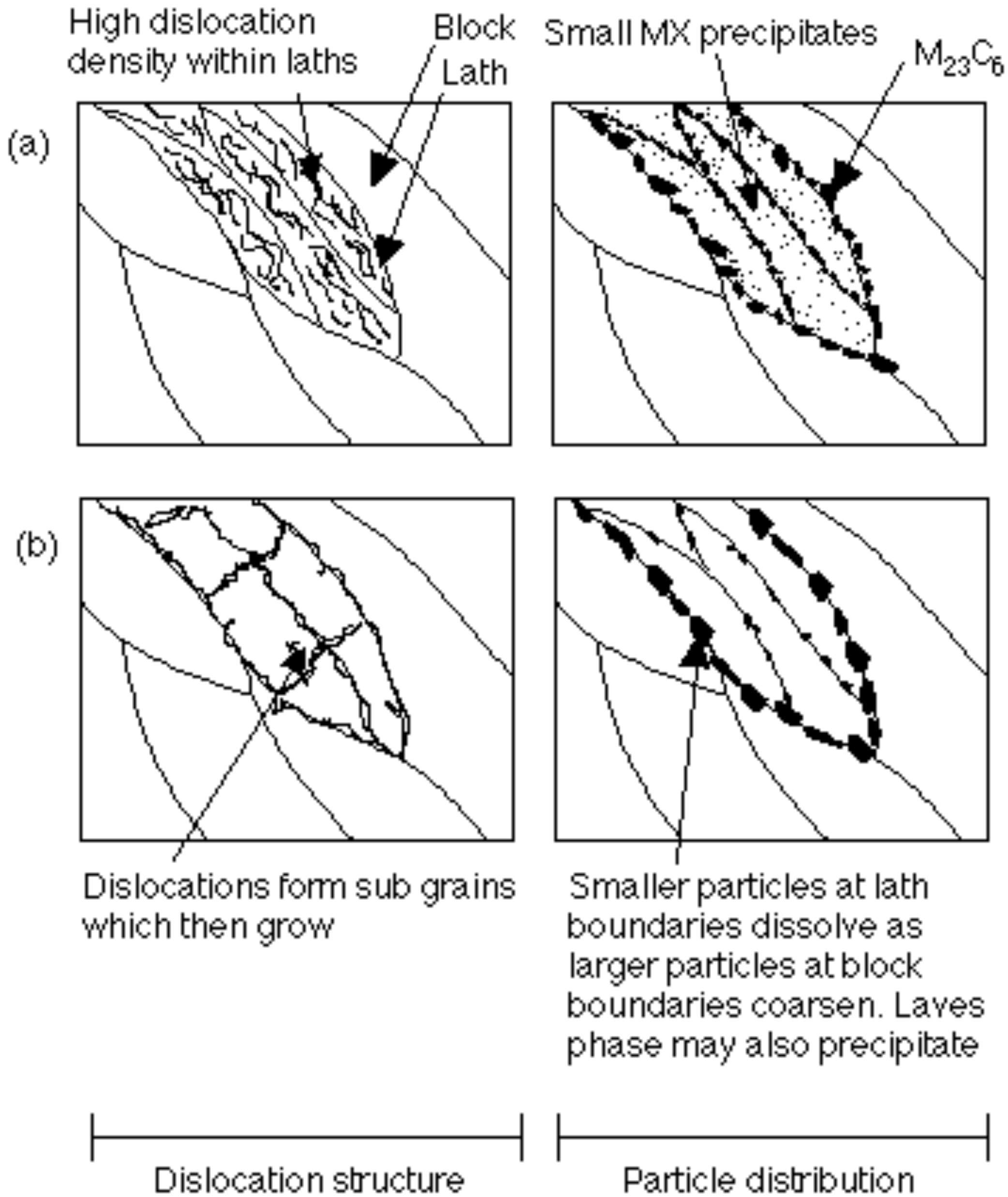

Figure 2.4 An illustration of the changes in microstructure during creep testing of a 10Cr–2W–0.3Mo–0.2 wt% V steel at 600°C(a) shows the dislocation and particle distributions before the creep test (b) shows the structure after 25 000 hours at 150 MPa (adapted from report in COST minutes, Leige, 1994)

2.6 Summary

The metallography of the 9-12 wt% Cr steels is complex due to the large number of alloying additions as well as the inherent complexity of the Fe–Cr–C system. These steels are air hardenable and martensite forms on cooling from austenitisation. On tempering a large number of possible phases may precipitate depending on composition and heat treatment. Many alloying elements are highly soluble in these precipitates. Other elements remain in solid solution where they contribute to the creep strength. Precipitates will also contribute provided there is a high particle density. If the precipitates form as large, widely spaced particles then they will lead to a reduction in creep strength due to the removal of atoms from solid solution. During creep exposure the microstructure changes, with a general trend towards coarsening of the larger particles and dissolution of the smaller ones. The creep rate then becomes less dependent on the movement of individual dislocations and more on the stability of the dislocation sub–grains [Vanstone, 1994]. Experiments have led to the specification of some key features of the microstructure required for good creep resistance.

CHAPTER THREE

Modelling Overall Transformation Kinetics

The theory used when modelling the overall transformation kinetics is presented here, with emphasis on power plant steels. These relevant transformations involve nucleation and growth, and the models used to describe both are discussed. Finally, some established models for precipitation in power plant steels are summarised.

3.1 Introduction

Traditionally new alloys have been designed in a fairly empirical fashion, with new compositions being based on variants of established alloys. The metallurgists involved in the development of a new steel use their skill and experience to estimate what composition changes are required to enhance the properties of interest, whether it be the corrosion resistance, creep strength *etc.* Usually a variety of trial alloys are then produced and tested from which the optimum composition is selected. This can be an expensive and slow process since the creep testing of the trial alloys takes several years. There is, therefore, a desire to model the changes in microstructure so that creep behaviour can be predicted theoretically from alloy composition. Such models would allow alloy designers to investigate the effect of composition variations without resorting to costly experiments, and also on a much shorter time scale. The most promising alloys from such a theoretical investigation could then be produced and tested. Also, it is hoped that models based on physical principles rather than empirical data fitting will give alloy designers a better understanding of the effect of individual elements and may suggest new, previously untried compositions. The way modelling work is intended to combine with experimental work in the development of new alloys is summarised in a flowchart (Figure 3.1)[Cerjak *et al.* 1995]

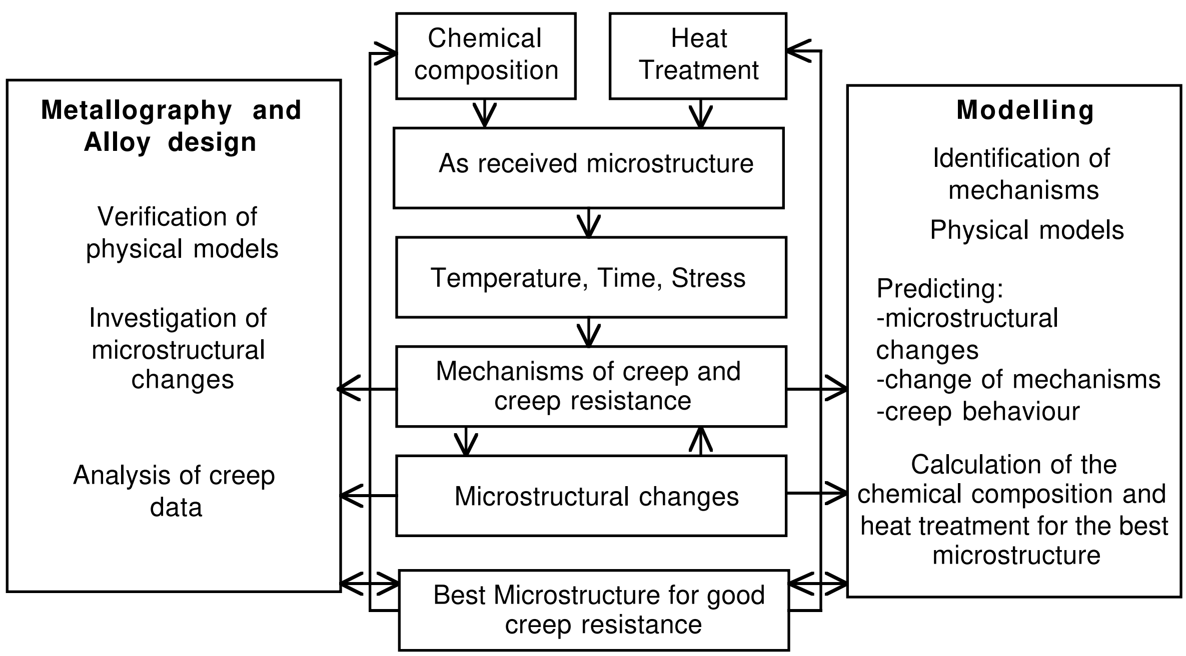

Figure 3.1 A flowchart showing how modelling activities integrate with other work in the design of new alloys with optimum creep resistance

The complexity of the 9-12wt% steels makes the task of modelling their creep behaviour more difficult. The microstructural changes during creep have been discussed in section 2.5, and include precipitation, dissolution and coarsening of a variety of secondary phases as well as alterations to the dislocation structure. The ultimate goal – a complete model will account for all of these phenomena. Useful information may still be obtained however from models which describe individual aspects of the microstructure. The work in this thesis focuses on the development of models for the precipitation of the secondary phases, since it is well established that the volume fraction, nature and distribution of these phases plays a key part in determining creep strength.

3.2 Nucleation and Growth Transformations

The precipitation reactions which occur on tempering may all be classified as nucleation and growth transformations. The rate of transformation in such reactions depends both on the rate at which stable nuclei form and on their subsequent growth rates. In some cases one or other process will be considerably slower and will therefore control the reaction rate. Most often, however, both processes are potentially rate limiting. Although nucleation and growth transformations occur in a diverse number of systems, ranging from the condensation of a liquid from a vapour to precipitation of carbides in steel, they have several common characteristics, summarised as follows [Christian, 1975 p.10].

3.2.1 Dependence on Time

At any temperature the amount of transformation will increase with time until a state of minimum free energy for the assembly is reached (the equilibrium state). The rate at which the transformation occurs can vary greatly, and may be so slow that no transformation is detected in any observable time period. Conversely, the transformation may be so rapid it appears to be almost instantaneous.

3.2.2 Dependence on Temperature

Given sufficient time the transformation will go to completion at all temperatures. The final amount of transformation depends only on how the equilibrium state varies with temperature. The principle influence temperature has is to change the rate of transformation, which typically is extremely temperature sensitive. At all temperatures below the thermodynamic transformation temperature there will be a driving force for transformation. At the thermodynamic transformation temperature the rate of reaction is zero, since at this point the energy required for nucleation is infinite. As the temperature is reduced, the free energy of formation of a critical nucleus decreases rapidly, and the nucleation rate increases. When there is a composition difference between the precipitating and matrix phases the continuation of transformation requires the transfer of atoms across the interphase boundary and inter-diffusion of atoms. Both of these processes become more difficult as the temperature is reduced. The combination of these two contradictory processes leads to a rate which increases below the thermodynamic transformation temperature to some maximum value at a lower temperature, below which the rate decreases. When temperature is plotted against the time taken to reach a certain fraction of transformation, this leads to a characteristic "C–curve", an example of which is shown in Figure 3.2.

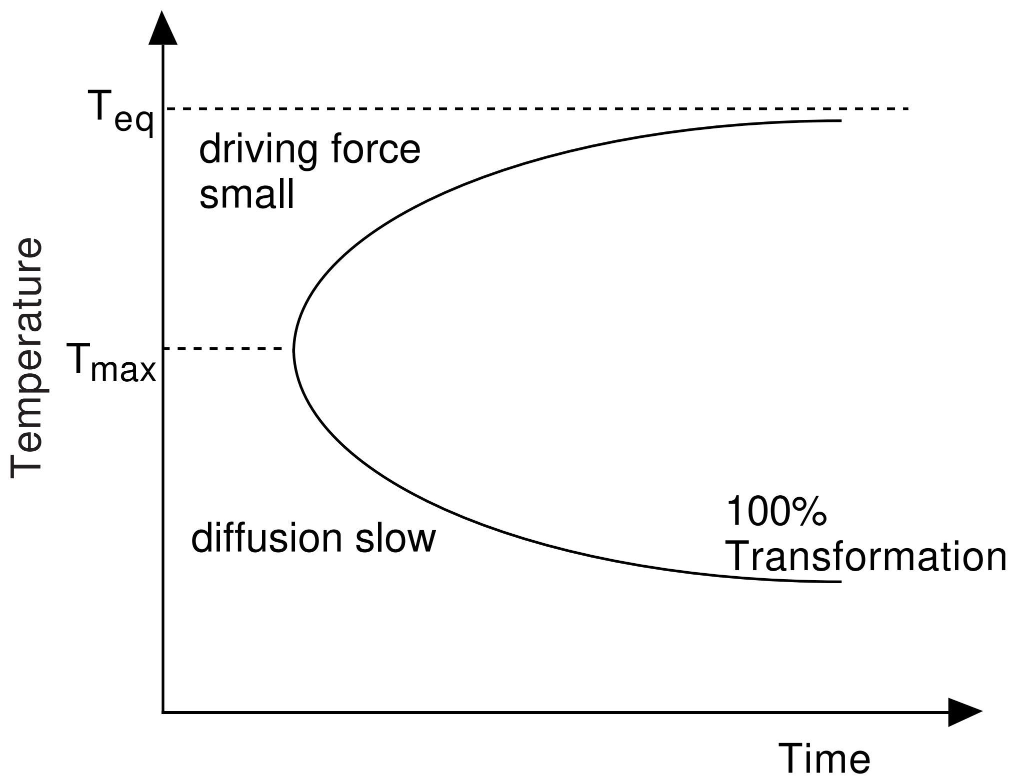

Figure 3.2 A schematic illustration of the C–curve kinetics, typical of nucleation and growth transformations. T_{eq} is the thermodynamic transformation temperature. T_{max} is the temperature at which the growth and nucleation rates are such that the transformation kinetics are most rapid.

3.2.3 Irreversibility of the Transformation

In a reconstructive transformation individual atoms move independently there is no correlation between the initial position of an atom and its final position if the transformation is reversed. This is in contrast to a displacive transformation where there is an ordered movement of atoms with a one-to-one correspondence between positions in the initial and final phases. The transformation is thus irreversible in that once the original structure (*i.e.* grain distribution, sizes and orientations) is lost by forward transformation, it cannot be reproduced by back transformation.

3.2.4 Effect of Plastic Deformation

Nucleation and growth transformations are often accelerated by plastic deformation prior to transformation. There are several possible reasons for this. Nucleation may be easier in deformed regions of lattice, since the effective driving force is increased, and the free energy barrier decreased. Diffusion may be enhanced in regions which are heavily deformed. Deformation will also result in a large temporary increase in the number of vacancies, which will have a minor transient effect on diffusion. However, if the effects of plastic deformation are rapidly removed by recovery and recrystallisation then it will not affect the transformation kinetics.

3.2.5 Composition, Atomic Volume and Shape of the New Phase

The composition and atomic volume of the new phase need not be related to the composition of the parent phase. The shape of the transformed regions resulting from nucleation and growth can vary considerably, and will depend on the relative importance of the surface energy and strain energy associated with the transformed region. For example, if there is no strain energy, and surface energy is isotropic then spherical particles will form (*e.g.* as in a liquid condensing from a vapour). If there is a volume change on transformation which has associated strain energy then the new phase will often form in the shape of plates or needles, oriented with respect to the original lattice so that the best atomic fit is obtained across the interface. This results in a Widmanstätten structure.

3.3 Introduction to Modelling Isothermal Transformations

Nucleation and growth transformations are often modelled using the Johnson–Mehl–Avrami theory for transformation kinetics [Johnson and Mehl, 1939; Avrami, 1939, 1940, 1941]. This theory, which describes how the total volume fraction of a forming phase varies with time is applicable to a wide variety of transformations. The approach used is the same irrespective of the type of growth and nucleation, and so for clarity it will be presented here for the simplest case, where there is a constant nucleation rate (I) and a constant, isotropic growth rate (v).

Consider a product phase β forming from a parent phase α. The size of a particular transformed region will depend on the time at which it nucleated (the incubation period, τ) and the subsequent time available for growth. The volume of such a region will therefore be zero at times shorter than the incubation time (*i.e.* before nucleation) after which it will be a function of the time elapsed since nucleation.

$$w_\tau = (4\pi/3)v^3(t-\tau)^3 \qquad (t > \tau) \tag{3.1}$$

$$w_\tau = 0 \qquad (t < \tau)$$

where t is the time defined to be zero at the instant the sample reaches the isothermal transformation temperature.

In the whole assembly the number of new β regions nucleated in the time interval between $t = \tau$ and $t = \tau + d\tau$ is $IV^\alpha d\tau$. If interactions between neighbouring growing regions are neglected then the increase in the volume of β due to particles nucleated in this time interval is given by

$$dV_e^\beta = IV(4\pi/3)v^3(t-\tau)^3 d\tau \tag{3.2}$$

where V is the total volume of the system.

Clearly in reality, only those parts of the change in volume which lie in untransformed regions of the parent phase can contribute to the change in real volume of β. The increase in volume calculated using this expression ignores this constraint, and is therefore not a real volume increase, but rather an *extended* volume increase. The extended volume may be related to the real volume by considering the geometry of impingement. The probability that any change in extended volume lies in untransformed parent is proportional to the fraction of untransformed material. It follows that the actual change in volume is related to the change in extended volume by

$$dV_\beta = \left(1 - \frac{V_\beta}{V}\right) dV_\beta^e \tag{3.3}$$

$$V_\beta^e = -V \ln\left(1 - \frac{V_\beta}{V}\right) \tag{3.4}$$

so that

$$-\ln\left(1 - \frac{V_\beta}{V}\right) = (4\pi/3)v^3 \int_0^t I(t-\tau)^3 d\tau \tag{3.5}$$

In making this conversion from extended to real volume, all information about individual particles is lost, so that the application of the Avrami model can only yield average quantities such as grain size, volume fraction but not grain size or grain volume distributions.

If the nucleation and growth rates are constant then the integration followed by rearranging leads to an expression for ζ, the volume of β as a fraction of the total volume.

$$\frac{V_\beta}{V} = \zeta = 1 - \exp\left(-\pi v^3 I t^4/3\right) \tag{3.6}$$

This equation is one example of the more general relationship which can be used to describe three-dimensional growth and nucleation processes when the growth and nucleation rates vary. It is written

$$\zeta = 1 - \exp\left(-Ct^n\right) \tag{3.7}$$

Where C and n are constants, whose values will depend on the nucleation and growth conditions. This equation is often used in the interpretation of experimental results since it is found that in many types of phase transformation the volume fraction of the product phase varies with time according to this type of relationship. A plot of $\log(\log{(1-\zeta)}^{-1})$ against $\log t$ will then give a straight line, with gradient n, and intercept $\log C$. The value of n is then often used to make inferences about the nature of the transformation, although this can be dangerous since different combinations of growth and nucleation behaviour can result in the same value for n. The application of the Avrami method to more complex cases, such as diffusion controlled growth is discussed in section 3.9.

3.4 Diffusion in the Solid State

Studies of the precipitation of many of the phases which precipitate in power plant steels show that they form with compositions close to their equilibrium compositions (*e.g.* Thomson, 1994). Since the equilibrium compositions of the precipitates are very different from the composition of the parent material, their formation requires transport of atoms to and from the parent phase. This transport occurs by solid state diffusion, and is driven by concentration gradients established as the precipitating phase starts to grow[1] .

The diffusion of substitutional atoms is typically several orders of magnitude slower than that of interstitial atoms. Transformations which require diffusion of substitutional atoms are termed reconstructive and are generally slow compared with displacive transformations which require either no diffusion, or the diffusion of interstitial species only.

With one exception, the precipitation of carbides, nitrides and Laves phase are all reconstructive transformations, requiring the diffusion of substitutional and interstitial atoms. The exception is the precipitation of cementite, which as it has already been stated, forms by a paraequilibrium transformation mechanism (section 3.7). This requires only interstitial atoms to diffuse and is therefore a displacive transformation which occurs rapidly compared to the reconstructive formation of the other phases. In this case the growth rate is limited by

[1] Strictly speaking, diffusion is driven by chemical potential gradients. In this work the chemical potential and composition gradients are always in the same direction, so it is adequate to work in terms of composition

the diffusion rate of the interstitial atoms. The subsequent enrichment of cementite requires diffusion of substitutional atoms, and is therefore slow compared to its growth.

3.5 Diffusion Controlled Growth

In reconstructive transformations where the interface between the product and parent phases is relatively mobile the volume diffusion rate will ultimately limit the growth velocity. In practice, the situation is complex due to the multi–component nature of the alloys which means that many species will be diffusing simultaneously. The discussion presented here will be confined to transformations where the diffusion of a single species is rate controlling. The way such theory is adapted to handle multi–component diffusion is presented in the next section.

To derive the Avrami equation we have assumed that after nucleation, regions of transformed material grow at a constant rate. In general, this will be the case when the composition profile beyond the advancing interface remains constant throughout transformation. This, however, is often not the situation when an isolated precipitate particle of β grows into a phase α which has a different composition. The concentration gradient must become shallower as transformation proceeds. This is illustrated schematically in Figure 3.3 and results in a reduction in the growth rate. In many cases the particle dimension (*e.g.* radius) of the growing phase varies with $t^{\frac{1}{2}}$, i.e., it varies parabolically with time.

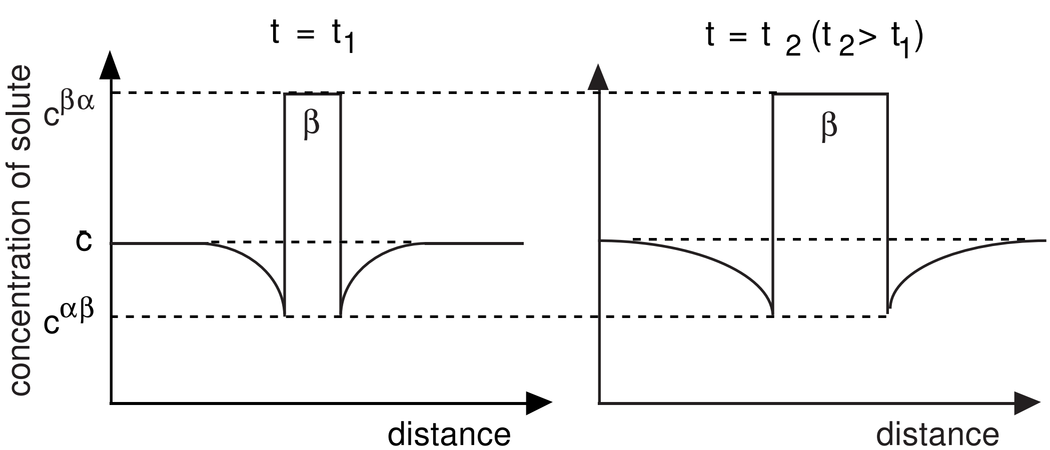

Figure 3.3 An illustration of how the composition gradient ahead of a growing precipitate varies as time increases. As the gradient becomes shallower, the growth rate slows down.

In the discussion that follows, it is assumed that the precipitating β phase grows with local equilibrium. The compositions $c^{\alpha\beta}$ and $c^{\beta\alpha}$ are given by a tie line on the phase diagram (as shown in Figure 3.4). The supersaturation (Ω) is a dimensionless parameter which is a function of the compositions and is found to be important in kinetic theory. It has a value is given by

$$\Omega = \frac{\bar{c} - c^{\alpha\beta}}{c^{\beta\alpha} - c^{\alpha\beta}} \tag{3.8}$$

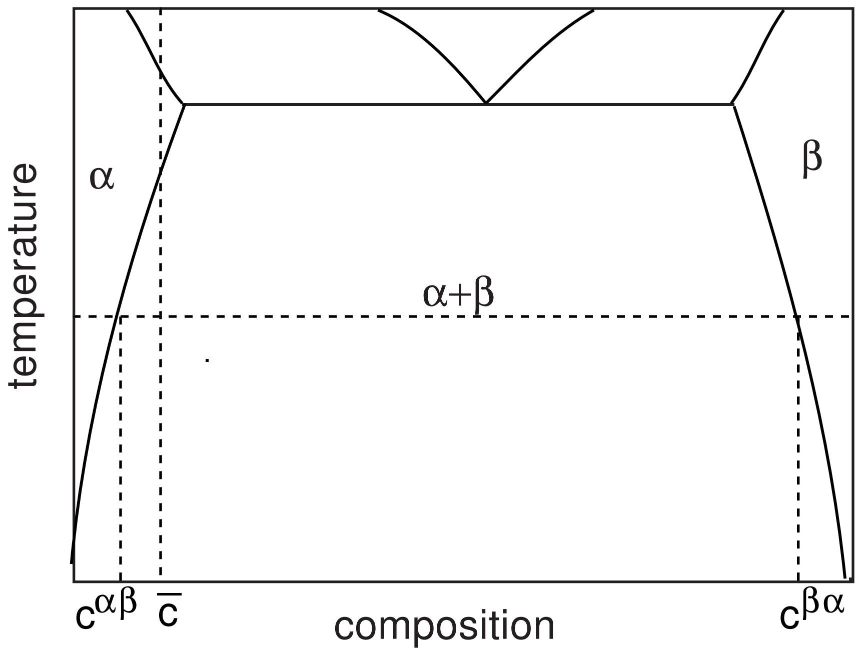

Figure 3.4 A schematic phase diagram showing the equilibrium compositions of the α and β phases ($c^{\alpha\beta}$ and $c^{\beta\alpha}$ respectively). The mean composition $\bar{c}$ lies much closer to the α than the β phase field, which corresponds to a low supersaturation in α.

3.5.1 The Diffusion Equation

In general, for any transformation involving long–range transport, the diffusion equation

$$\frac{\partial c(x,t)}{\partial t} = D\nabla^2 c(x,t) \tag{3.9}$$

must be satisfied at each point in the metastable phase, with the concentration $c(x,t)$ being a function of both position x and time t. Note that here we are considering the diffusion coefficient to be independent of composition. This is a commonly used approximation, although in practice D is usually a function of composition.

To find the distribution of solute it is necessary to solve the diffusion equation for appropriate boundary conditions. If there is no precipitate at time $t = 0$ and the matrix has a homogeneous composition then there is the starting condition

$$c(x,0) = \bar{c} \tag{3.10}$$

Choosing the other boundary conditions is not necessarily straightforward, and will depend on whether growth is assumed to be interface or diffusion controlled. The requirement for conservation of mass determines a relationship between the velocity of the interface and the flux of solute to or from the interface region. The problem is made more complex during the growth of more than one particle. Each growing particle is surrounded by a region in which the composition of the matrix is changed owing to the diffusion to or form the particle (see Figure 3.4). As particles grow the extent of their diffusion fields increase, until at some point they begin to overlap. This is termed soft impingement, to differentiate it from hard impingement which is the physical contact of particles. Soft impingement leads to a change in concentration gradients, the growth rate eventually becoming zero.

3.5.2 The Zener Model for Growth

One of the most common approximate growth models applicable where there is local equilibrium at the interface is due to Zener (1946). His treatment is described here for the one–dimensional growth of a planar interface.

The variation of composition normal to the growing interfaces is assumed to be linear as shown in Figure 3.5 . Let x be the coordinate normal to the interface. When the boundary is in a position $x = x^I$ the diffusion flux of solute atoms across unit area, J, in a time ∂t will be

$$J = D\left(\frac{\partial c}{\partial x}\right)_{x=x^I} \partial t \tag{3.11}$$

If during this time interval the interface advances a distance Δx, the amount of solute which will be required is $(c^{\beta\alpha} - c^{\alpha\beta})\Delta x$. This can only come from diffusion, so equating it with the diffusion flux gives the growth velocity as

$$v = \frac{dx^I}{dt} = \frac{D}{c^{\beta\alpha} - c^{\alpha\beta}}\left(\frac{\partial c}{\partial x}\right)_{x=x^I} \tag{3.12}$$

$(\partial c/\partial x)_{x=x^I}$ may be written as $(\bar{c} - c^{\alpha\beta})/y^D$, where y^D is an effective diffusion distance. This gives the expression for the growth rate as

$$v = \frac{\bar{c} - c^{\alpha\beta}}{c^{\beta\alpha} - c^{\alpha\beta}}\frac{D}{y^D} \tag{3.13}$$

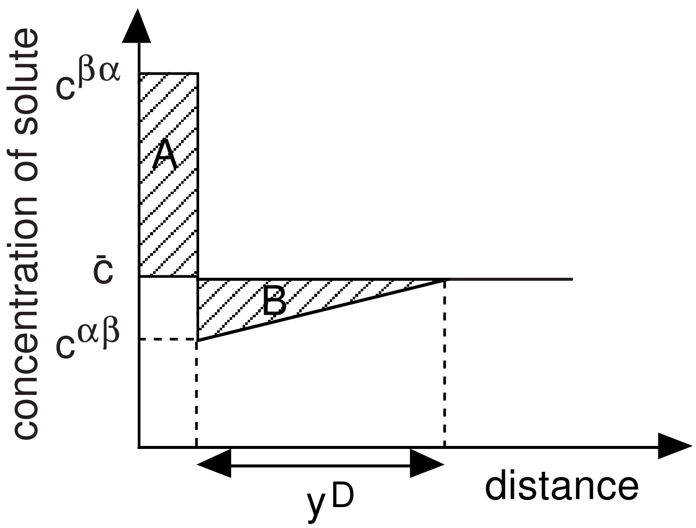

Figure 3.5 The linear composition gradient approximation. For the growth of a planar interface shaded areas "A" and "B" must be equal for mass balance.

The effective diffusion distance y^D can be found by invoking a mass balance argument. For the growth of a planar interface this corresponds to equating the shaded areas A and B shown in Figure 3.5. The growth rate then becomes

$$v = \frac{dx^I}{dt}\frac{D(\bar{c} - c^{\alpha\beta})^2}{2(c^{\beta\alpha} - c^{\alpha\beta})(c^{\beta\alpha} - \bar{c})x^I} \tag{3.14}$$

In many cases this equation may be simplified by assuming $c^{\beta\alpha} - \bar{c} \simeq c^{\beta\alpha} - c^{\alpha\beta}$. Integration of the expression for growth rate then gives

$$x = \Omega\sqrt{Dt} \tag{3.15}$$

and a corresponding expression for the growth rate

$$v = \frac{1}{2}\Omega\sqrt{\frac{D}{t}} \tag{3.16}$$

It is apparent that this corresponds to a parabolic growth law. A similar analysis also gives a parabolic growth law for spherical and cylindrical particles growing radially. The growth of needles and thin plates which do not follow a parabolic law are discussed in the next sub-section.

The growth velocity increases with increased supersaturation and an increasing diffusion coefficient. The supersaturation will increase as the temperature is reduced below the thermodynamic transformation temperature. The diffusion coefficient, however, will decrease as the temperature is reduced. These competing effects lead to a growth rate which is zero at the transformation temperature, increases to a maximum as the temperature is reduced, and then decreases on further cooling.

3.5.3 Growth of Needles and Plates

The lengthening of needles and growth of thin plates along their edges are found experimentally to follow a linear, rather than a parabolic growth law. The reason is that in these cases the needle or plate is continually growing into fresh material of constant composition. The build up or depletion of solute ahead of the interface which leads to parabolic kinetics does not occur since solute may be removed from or dumped to the matrix in a different direction to that in which the needle or plate is growing.

Growth is also complicated because the tip of a needle or edge of a plate has a high surface curvature, and this leads to a modification of the compositions at the interface due to surface energy effects. This change of compositions is known as the Gibbs–Thomson effect and may be summarised as follows.

For a particle of β with a curved interface, new interfacial area must be created as the particle grows. Additional surface energy is therefore needed, and this has the effect of increasing the free energy of β thus modifying the equilibrium conditions at the interface. The effect is illustrated in Figure 3.6.

The curve G^β shows the free energy variation for β without modifications due to surface energy (capillarity) effects. The curve G^β_r shows the effect of capillarity on the free energy of β. The increase in free energy is given by $\sigma\frac{dO}{dn}$ where σ is the interfacial energy per unit area, and $\frac{dO}{dn}$ is the rate at which surface energy increases with the addition of an extra atom to the β phase. As shown in Figure 3.6 one effect of increasing the free energy of β is to alter the composition of the α phase in equilibrium with β, so that it approaches the mean composition of the alloy ($\bar{c}$). The smaller the particle size, the larger $\frac{dO}{dn}$ will be, and the closer $c_r^{\alpha\beta}$ will be to $\bar{c}$. For a critical minimum particle size, $c_r^{\alpha\beta}$ will be equal to $\bar{c}$ and transformation will cease. This minimum size is associated with a critical radius, r_c, below which transformation will not occur. In the case of needles or plates the analogous parameter is the critical radius of curvature of the needle tip or plate edge.

One of the most commonly used treatments for the problem of needle and plate growth is the Zener theory as described previously, but with modifications to the composition terms to allow for capillarity effects. The theory will be presented here for the growth of a needle shaped precipitate; the approach used for plates is very similar. The assumption is made that the tip of a growing needle is hemispherical. This means the curvature is the same at all points on the needle tip, and so the composition of the α phase at the interface, $c_r^{\alpha\beta}$ is constant over

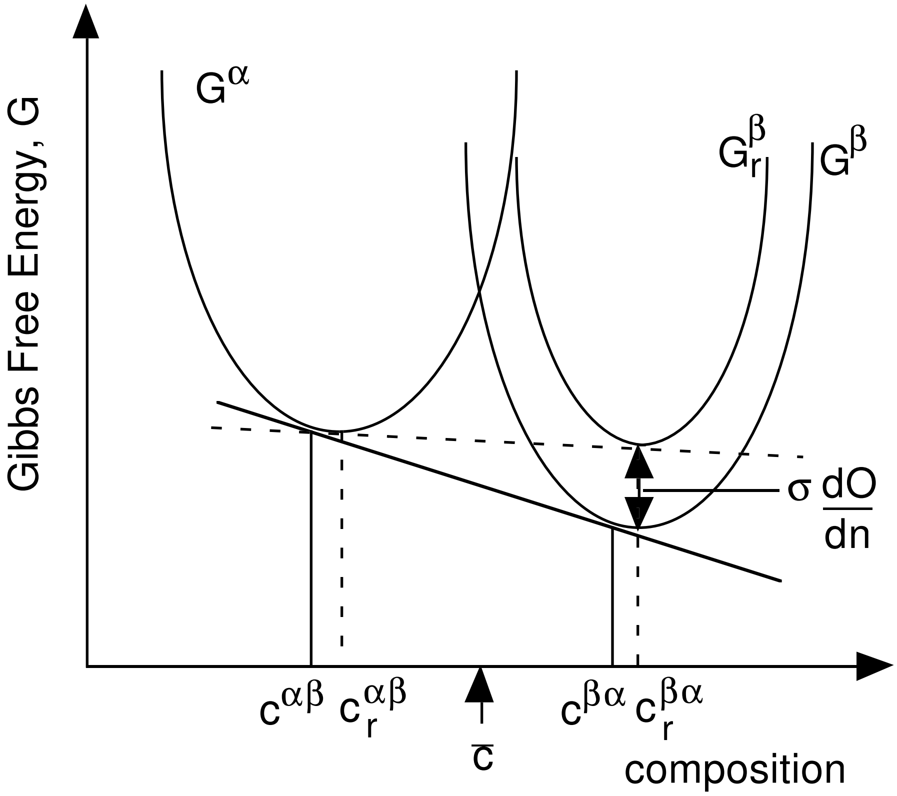

Figure 3.6 Diagram to show the effect of surface curvature on equilibrium compositions (the Gibbs–Thomson effect)

the curved surface. The supersaturation at the interface is therefore given by

$$\Omega_r = \frac{\bar{c} - c_r^{\alpha\beta}}{c_r^{\beta\alpha} - c_r^{\alpha\beta}} \tag{3.17}$$

It is found that $c_r^{\beta\alpha} - c_r^{\alpha\beta}$ may be approximated to $c^{\beta\alpha} - c^{\alpha\beta}$. It is then possible to express the supersaturation at the interface in terms of the the needle tip radius, the critical radius, and the supersaturation without capillarity effects. The relationship is

$$\Omega_r = \left(1 - \frac{r_c}{r}\right)\Omega \tag{3.18}$$

By making the assumption that the diffusion distance y^D is proportional to the tip radius an expression is produced for the growth rate.

$$v = \left(\frac{D\Omega}{C_1 r}\right)\left(1 - \frac{r_c}{r}\right) \tag{3.19}$$

where $y^D = C_1 r$. C_1 is a constant which is approximately equal to 1 [Christian, 75 p. 495]. This equation gives a relationship between the growth velocity and the tip radius, but does not predict either uniquely.

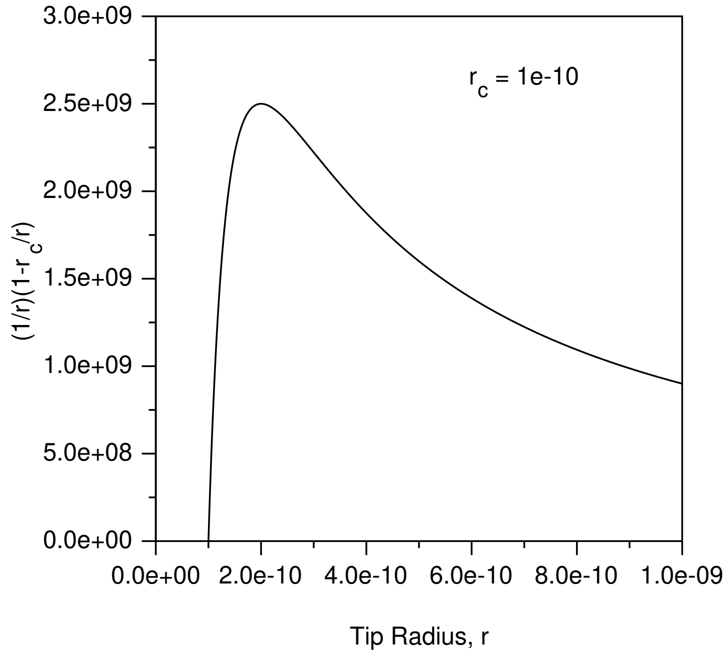

Figure 3.7: A graph showing how the growth rate of a needle shaped precipitate varies as the tip radius changes.

Figure 3.7 is a plot showing how the growth rate is expected to vary with the tip radius. From being zero when $r = r_c$ the growth rate passes through a maximum at $r = r_c$ and then tends towards a steady value as $r \to \infty$. The form of this curve is due to the competing effects of diffusion which favours a fine needle tip for rapid growth, and capillarity which opposes this by reducing the driving force for transformation as the tip radius decreases. Zener assumed that the observed velocity will be this maximum possible velocity. While this assumption has no fundamental basis, experiments have shown that in some cases it is valid (Purdy, 71). This assumption then uniquely defines the tip radius and growth rate as

$$r = 2r_c \tag{3.20}$$

and the growth rate is given by

$$v = \frac{D\Omega}{4C_1 r_c} \tag{3.21}$$

The critical radius r_c is given by [Christian, 75 p. 493]

$$r_c = \frac{2c^{\alpha\beta}\Gamma}{(\bar{c} - c^{\alpha\beta})} \tag{3.22}$$

where Γ, the capillarity coefficient is given by [Christian, 75 p. 181]

$$\Gamma = \left(\frac{\sigma v^{\beta}}{kT}\right)\left(\frac{1 - c^{\alpha\beta}}{c^{\beta\alpha} - c^{\alpha\beta}}\right) \tag{3.23}$$

Several workers have attempted to solve the problem of needle and plate growth in a more rigorous manner [Hillert, 1957; Horvay and Cahn, 1961; Trevedi, 1970]. In each case different assumptions have been made to find a suitable steady-state solution to the diffusion equation. Hillert, for example, has produced a model for plate growth which assumes that the concentration in the plane perpendicular to the plate has the form

$$c - c^{\alpha\beta} = C_2 \exp\left(\frac{-\pi x_2^2}{16m^2}\right) \tag{3.24}$$

where x_2 is the co-ordinate in the perpendicular direction and C_2 and m are arbitrary constants. Using this assumption, the steady state growth rate is given by

$$v = \frac{D\Omega}{2} \frac{(c^{\beta\alpha} - c_r^{\alpha\beta})}{(c^{\beta\alpha} - \bar{c})} \frac{1}{m} \left(1 - \frac{m_c}{m}\right) \quad (m \simeq r) \tag{3.25}$$

This corresponds to Zener's equation with $C_1 = 2(c^{\beta\alpha} - \bar{c})/(c^{\beta\alpha} - c_r^{\alpha\beta})$. For low supersaturations $(c^{\beta\alpha} - \bar{c})/(c^{\beta\alpha} - c_r^{\alpha\beta})$ is approximately equal to 1, and so the Hillert equation becomes identical to the Zener equation, with a value of 2 for C_1. Hillert has used a similar approach to find the growth rate of needle shaped particles which he finds have a maximum value 1.5 times that for a plate.

More recently Trivedi (1970) has given an exact solution for the diffusion problem, assuming that needles may be represented as paraboloids of revolution which, as they grow, preserve their shape. His treatment accounts for the change in curvature along the interface, and the associated change in composition. The method also allows for the free energy dissipated in moving the interface. However, it is still necessary to invoke the maximum growth rate principle to uniquely define the growth rate. In general, growth rates predicted using the Trivedi theory are smaller than those predicted by Zener theory. The Zener theory is still used widely used because of its simplicity.

3.5.4 Growth of Spherical Particles

It has already been stated that the growth of spherical precipitates would be expected to follow a parabolic law. It is therefore expected that the radius of a spherical particle will vary with time as

$$r^I = Ct^{\frac{1}{2}} \tag{3.26}$$

To determine the value of C it is necessary to evaluate equation 3.9. To do this the composition function $c(r,t)$ must be found by solving the general diffusion equation, which for 3–dimensional growth takes the form

$$\frac{\partial c}{\partial t} = D\left(\frac{\partial^2 c}{\partial r^2}\right) + \frac{2D}{r}\left(\frac{\partial c}{\partial r}\right) \tag{3.27}$$

The boundary conditions for the solution of this equation are 3.10 and

$$c(r^I, t) = c_r^{\alpha\beta} \tag{3.28}$$

which corresponds to the composition of the α phase at the interface always being $c_r^{\alpha\beta}$. If capillarity effects are ignored then $c_r^{\alpha\beta}$ can be taken as having a constant value $c^{\alpha\beta}$. The solution to the diffusion equation for these boundary conditions is [Christian, 1975 p. 487]

$$c(r,t) = \bar{c} + (c^{\alpha\beta} - \bar{c})\frac{\phi_3[r/(Dt)^{0.5}]}{\phi_3[r^I/(Dt)^{0.5}]} \tag{3.29}$$

where $\phi_3(x) = \int_x^\infty \eta^{-2}\exp(-\eta^2/4)d\eta$

Since for parabolic growth, $r^I \propto (Dt)^{0.5}$ (which can be verified by dimensional arguments), the quantity $r^I/(Dt)^{0.5}$ is a dimensionless function of the concentrations which determines the growth velocity. This quantity is often referred to as the parabolic rate coefficient and is usually written (for 3-dimensional growth) as α_3. Evaluating equation 3.27 using the composition function shown in equation 3.29 gives

$$\frac{1}{\Omega}\frac{dr^I}{dt} = \frac{\left(\alpha_3^{-2}\right)}{\phi_3[\alpha_3]}\exp\left(\frac{-\alpha_3^2}{4}\right)D^{\frac{1}{2}}t^{\frac{1}{2}} \tag{3.30}$$

and hence

$$\alpha_3^3 = \frac{2\Omega\exp\left(\frac{-\alpha_3^2}{4}\right)}{\phi_3[\alpha_3]} \tag{3.31}$$

This gives an implicit expression for α_3 in terms of Ω, and for any supersaturation the growth law is then given by

$$r^I = \alpha_3(Dt)^{\frac{1}{2}} \tag{3.32}$$

It is possible to produce simpler expressions for α_3 by considering approximate solutions. For example, for low supersaturations it is possible to use a steady state solution for the diffusion equation, in which case the parabolic growth coefficient becomes

$$\alpha_3 \simeq \sqrt{2}\frac{(\bar{c} - c^{\alpha\beta})^{\frac{1}{2}}}{(c^{\beta\alpha} - \bar{c})^{\frac{1}{2}}} \tag{3.33}$$

Often the diffusion coefficient is combined with α_3 to give a single term which is also constant. Here, this is referred to as χ and the growth law then becomes

$$r^I = \chi t^{\frac{1}{2}} \text{ with } \chi = \alpha_3 D^{\frac{1}{2}} \tag{3.34}$$

In all the analyses for spherical growth which have been presented so far the effects of capillarity have been neglected. When the particle radius r_I is much greater than the critical radius r_c

the effects of capillarity are small. When the particle radius is close to the critical radius the interfacial compositions will be significantly different from those expected if capillarity is ignored. In the case of needle growth the tip radius remains constant and may be close to the critical radius throughout growth. In the case of spherical particles the radius is constantly increasing, and so will be in the regime where capillarity is important for only a fraction of the total growing time. Because of this, capillarity effects may often be ignored when considering the growth of spherical particles.

3.6 Growth in Ternary and Higher Order Systems

In our discussion so far we have assumed that we are considering a binary system, in which the compositions of the precipitating and parent phases can be found from a tie line of the phase diagram (see Fig. 3.4). Power plant steels, which may contain around 12 components are clearly considerably more complex than simple binary systems and as a consequence of this it becomes more difficult to determine the compositions at the interface between the parent and product phases.

Clearly, in a system containing many components, the growth rate of the precipitating phase must be the same regardless of which component is considered. For the Zener growth theory this corresponds to simultaneously satisfying the following equations.

$$v(c_1^{\beta\alpha} - c_1^{\alpha\beta}) = \frac{D_1(\bar{c}_1 - c_1^{\alpha\beta})}{y_D} \tag{3.35}$$

$$v(c_2^{\beta\alpha} - c_2^{\alpha\beta}) = \frac{D_2(\bar{c}_2 - c_2^{\alpha\beta})}{y_D} \tag{3.36}$$

$$v(c_k^{\beta\alpha} - c_k^{\alpha\beta}) = \frac{D_k(\bar{c}_k - c_k^{\alpha\beta})}{y_D} \tag{3.37}$$

where D_k is the diffusion coefficient of the kth component. $c_k^{\beta\alpha}$ and $c_k^{\alpha\beta}$ are the concentrations of this component in the β and α phases respectively.

In general, it is impossible to satisfy these conditions simultaneously using a tie line passing through the mean alloy composition, as is the case when considering a binary alloy. By choosing the correct compositions, these equations may be satisfied however. This is possible because as extra components are added, the number of degrees of freedom increases and the compositions of the phases are no longer fixed to unique values by the common tangent as in a binary alloy. This is best visualised with reference to a ternary system.

Figure 3.8 shows the free energy curves for an Fe–C–X system when two phases, α and γ are in equilibrium. As in the case of a binary alloy, the equilibrium compositions of the two phases may be found using the common tangent construction to find the minimum overall Gibbs free energy. In the binary case there is only one tangent line common to both free energy curves, and the compositions are therefore uniquely defined. In the ternary case however, there is a common tangent plane. This plane may be rocked, whilst still in contact with both free energy surfaces, to find a set of tie lines, and a corresponding set of equilibrium compositions. By projecting onto the composition plane as shown in Figure 3.8 the extent of the $\alpha + \gamma$ phase field is defined for any particular temperature.

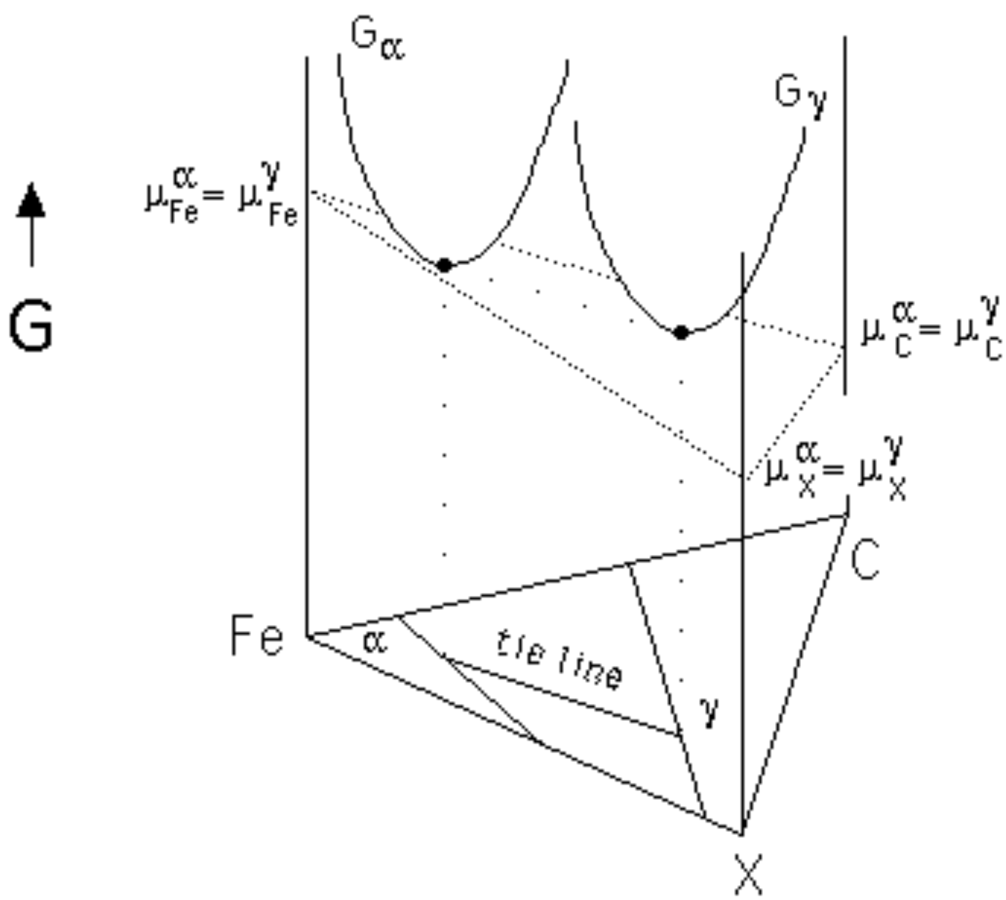

Figure 3.8 An extension of the common tangent construction to a ternary system. Each pair of points defined by the contact of the common tangent plane to both the austenite and ferrite free energy surfaces defines a tie line of an isothermal section of the Fe–C–X phase diagram. The tangent plane can be rocked, whilst maintaining contact with the two free energy surfaces to generate a set of tie lines which define the $\alpha + \gamma$ equilibrium phase field

Equations 3.35–3.37 can now be satisfied by choosing an appropriate tie line. Consider our example system, Fe–C–X. The following condition must be satisfied for the growth of α

$$v(c_X^{\alpha\gamma} - c_X^{\gamma\alpha}) = \frac{D_X(\bar{c}_X - c_X^{\gamma\alpha})}{y_D} \tag{3.38}$$

$$v(c_C^{\alpha\gamma} - c_C^{\gamma\alpha}) = \frac{D_C(\bar{c}_C - c_C^{\gamma\alpha})}{y_D} \tag{3.39}$$

If X is a substitutional element (*e.g.* Mn) then D_C will be much greater than D_X. This condition can therefore only be satisfied if either (a) the concentration gradient of element X is increased, or (b) the concentration gradient of C is decreased.

3.6.1 P–LE Transformation

If a tie line is chosen so that the concentration gradient of the rapidly diffusing species (C in our example) is almost constant across the interface, then the concentration gradient of this species will be considerably reduced and this will counter the high diffusivity. There will, however, be a concentration gradient of the slower diffusing species, implying extensive partitioning between the product and parent phases, and hence a relatively slow growth rate. This is termed *partitioning local equilibrium* or P–LE growth.

3.6.2 NP–LE Transformation

The alternative is to choose a tie line for which the concentration of substitutional solute is approximately the same in both phases. There will be a sharp concentration spike at the interface because less solute is being partitioned across it. This spike leads to a large concentration gradient which compensates for the lower diffusion rate of the substitutional species. The small amount of partitioning necessary means that the growth rate is relatively rapid. This mode of transformation is called *negligible partitioning local equilibrium* or NP–LE.

3.7 Non–Equilibrium Transformations

Apart from the transformation mechanisms described above, where the species partition constrained by the requirement for thermodynamic equilibrium, there are other mechanisms which may operate which do not result in equilibrium growth. Such mechanisms, since they do not lead to a minimisation of the Gibbs free energy of the system require greater driving forces, but less diffusion and can therefore occur more rapidly.

3.7.1 Paraequilibrium Transformation

If the driving force for transformation is sufficiently large, and the transformation is sufficiently rapid then the situation can arise when there is insufficient time for the redistribution of the substitutional species and the concept of local equilibrium becomes invalid. Transformation may then occur by a *paraequilibrium* mechanism. In such a transformation only the rapidly diffusing interstitial species redistribute between the phases to maintain constant chemical potential throughout the system. Substitutional species are trapped and the chemical potential of the substitutional species will not be the same in both phases. It is therefore not possible to use the parallel tangent construction (and therefore the equilibrium phase diagram) to determine what the phase compositions are.

3.7.2 Martensitic Transformation

When the driving force for transformation is very large a martensitic transformation may occur. In this case transformation is by a diffusional shear process in the parent phase lattice which is highly crystallographic in character and requires no diffusion. This type of transformation is therefore extremely rapid.

The composition profiles of substitutional and interstitial solute for the various transformation mechanisms are shown in Figure 3.9.

3.8 The Classical Theory of Nucleation in Solids

The transformations in power plant steels require nucleation before growth. Consider the precipitation of a phase, β from a matrix α, supersaturated in solute X. For the nucleation of β, X atoms within the α matrix must first diffuse together to form a small volume with the β composition, and then, if necessary, the atoms must rearrange themselves into the β structure. This will require the formation of an α/β interface, which requires energy. Also, if there is a volume change associated with the nucleation which cannot be accommodated by plastic flow in the matrix then there will be a strain energy contribution. For simplicity, the case where the strain energy is negligible is considered here.

The free energy change on forming a nucleus will be composed of opposite terms. There is a free energy reduction associated with forming the more stable β phase, but also a free energy increase due to the interfacial energy. Assuming that this interfacial energy is isotropic, the free energy for formation of nucleus of radius r may be written

$$\Delta G = 4\pi r^2 \sigma + \frac{4}{3}\pi r^3 \Delta G_v \tag{3.40}$$

where σ is the interfacial energy of the nucleus and ΔG_v is the chemical driving force for formation of the β phase.

The first term in this equation which is the positive contribution to the free energy depends on r^2, while the second term which is the negative contribution depends on r^3. The

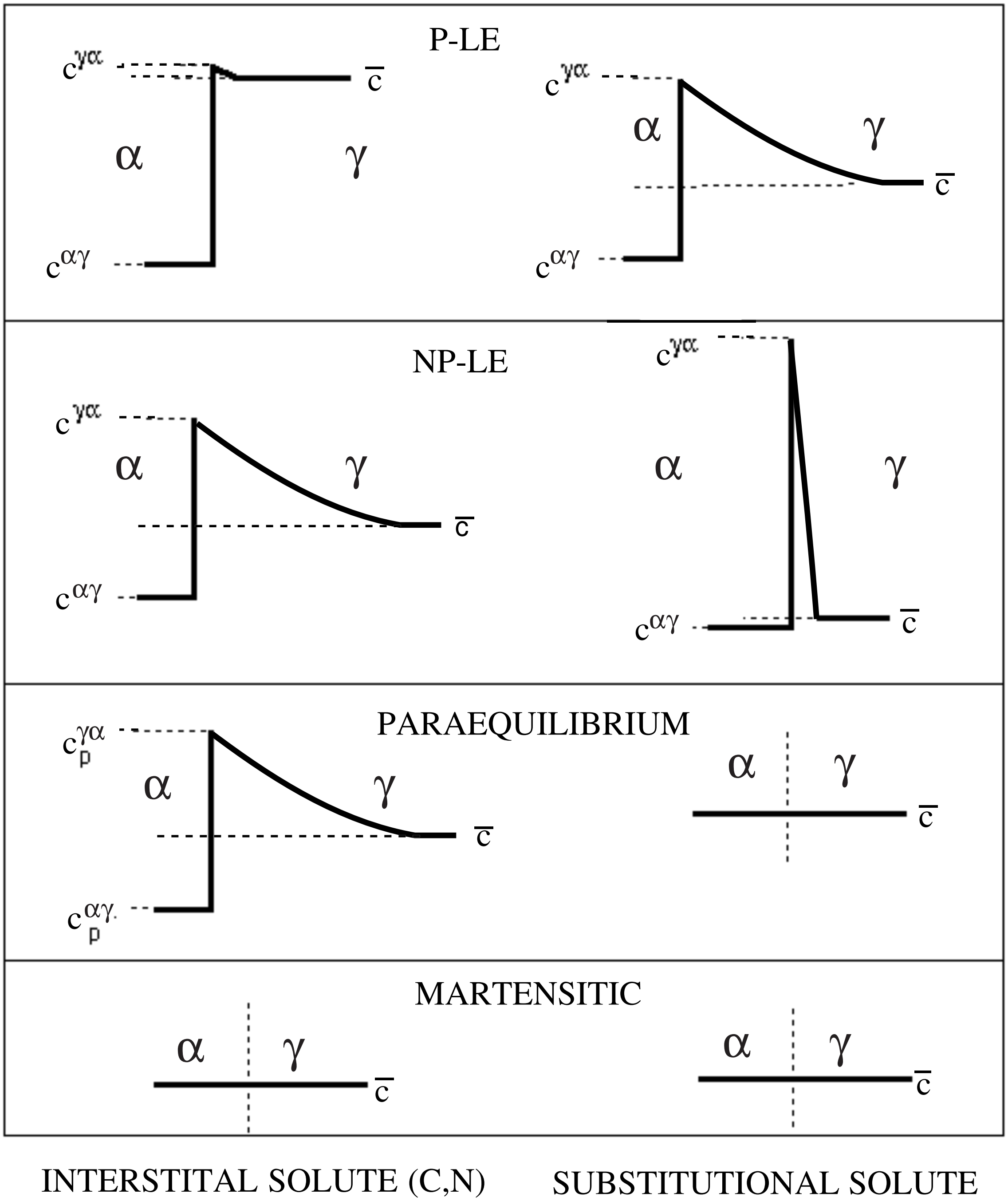

Figure 3.9 Schematic representation of the composition expected in the vicinity of the interface for a variety of growth mechanisms [Bhadeshia, 1992]

superposition of these two terms gives an overall free energy change which varies with the radius of the nucleus as shown in Figure 3.10.

The nucleus will be viable (*i.e.* will tend to grow rather than dissolve) when an increase

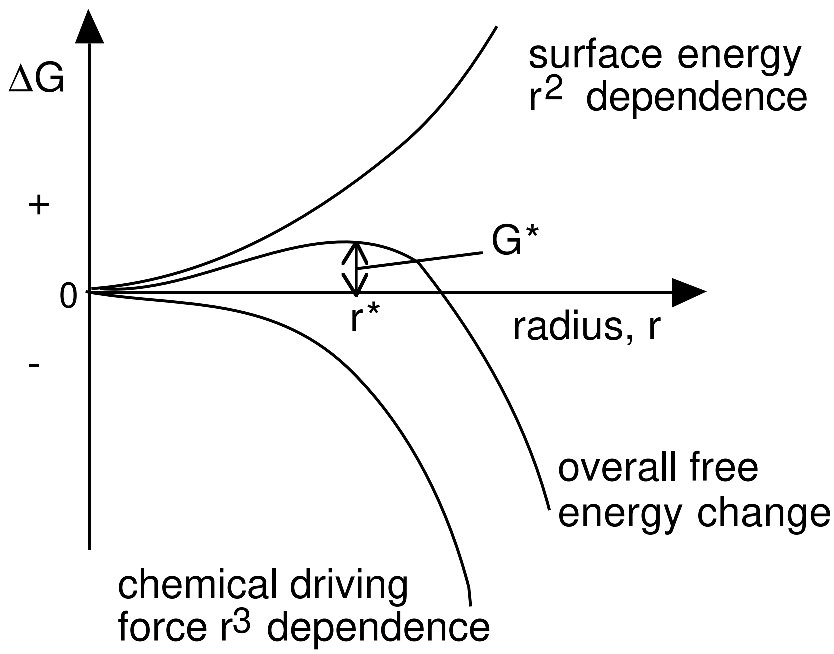

Figure 3.10 The free energy change associated with the formation of a nucleus of radius r forms

in its size leads to a reduction in the free energy (when $\frac{dG}{dr}$ is negative). As can be seen from Figure 3.11 this occurs when the radius of the nucleus exceeds a critical value r^*. Below this size, the nucleus is not viable and will tend to dissolve to reduce the free energy. It can also be seen that to form such a post critical nucleus it is necessary to overcome a free energy barrier of height G^*. Finding the maximum in equation 3.40 gives r^* which can then be used to find G^*

$$G^* = \frac{16\pi\sigma^3}{3\Delta G_v^2} \tag{3.41}$$

The probability of the barrier to nucleation being overcome by a potential nucleus is given by a Boltzman expression, and so the concentration of critical-sized nuclei N^* will be given by

$$N^* = N_0 \exp\left(\frac{-G^*}{kT}\right) \tag{3.42}$$

where N_0 is the number of nucleation sites per unit volume. The nucleation rate will then depend on the rate ν at which post critical nuclei can form. Furthermore we have so far only considered the free energy of the nucleus once it has formed, and have neglected the barrier to the transfer of atoms across the α/β interface. If this barrier is of magnitude Q then the nucleation rate per unit volume is given by

$$I = N_0\nu \exp\left(\frac{G^* + Q}{kT}\right) \tag{3.43}$$

The attempt frequency ν may be written as kT/h from classical thermodynamics, and the final expression for the nucleation rate can then be written as

$$I = N_0 \frac{kT}{h} \exp\left(\frac{G^* + Q}{kT}\right) \tag{3.44}$$

It should be noted that Q is temperature independent, while G^* is strongly temperature dependent. To solve this equation we need to evaluate G^*, and to do this we need to determine the chemical driving force for nucleation ΔG_v which is the temperature dependent parameter.

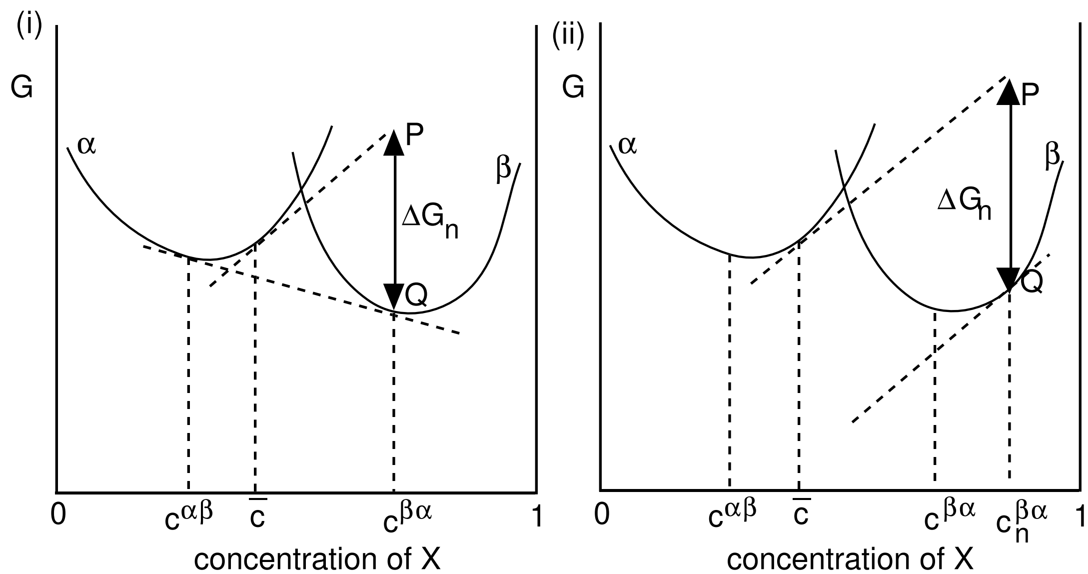

Figure 3.11 The common and parallel tangent constructions for finding the driving force for nucleation (i) The common tangent construction, assuming that β nucleates with its equilibrium composition (ii) The parallel tangent construction which gives the maximum driving force

Figure 3.12(i) shows schematic free energy curves when β precipitates from a supersaturated matrix of α. The overall driving force for the transformation, given by the familiar common tangent construction is ΔG_0. This, however is not the driving force for nucleation of β, since the formation of the first nuclei of this phase does not significantly alter the composition of α. To find the correct driving force the nucleation of β may be considered in the following way

(i) A small amount of material with the nucleus composition is removed from the α phase. This material has a free energy given by the point P in Figure 3.12. By removing this material, the free energy is decreased by this amount.

(ii) The atoms in this material are then rearranged from the α to the β structure.

(iii) The β material is now replaced. This increases the free energy by an amount given by the point Q, so there is a net decrease in free energy P-Q, which is the driving force for nucleation per mole.

The driving force for nucleation per mole ΔG_n may be converted into a driving force per volume of nucleus by dividing by the molar volume of β

$$\Delta G_v = \frac{\Delta G_n}{V_m^\beta} \tag{3.45}$$

In drawing Figure 3.12(i) the composition of the β nucleus was assumed to be equal to the equilibrium composition of the β phase according to the common tangent construction. The free energy reduction on forming a nucleus could be increased however by forming a β nucleus at a composition displaced from the equilibrium composition. The composition of β which leads to the maximum free energy change is given by plotting a tangent to the β free energy curve which is parallel to the tangent to the α curve. This is known as the *parallel tangent construction* and is shown in Figure 3.12(ii). In many cases, however, the compositions and driving forces predicted by both constructions are similar, and in such cases it is simpler to use the common tangent approximation.

3.8.1 Heterogeneous Nucleation

In the theory as described above it has been implicitly assumed that nucleation can occur with equal probability throughout the assembly. This *homogeneous* nucleation is, however, rare in solid to solid transformations. More usually, the presence of defects in the lattice will enable nuclei to form with a much lower activation energy at specific sites in the matrix. This *heterogeneous* nucleation will occur at sites such as grain boundaries, impurity particles and dislocations. This is because, at such sites the creation of a nucleus will either relax lattice strain or destroy a defect, both of which will release free energy, reducing the net free energy required to form a nucleus. Table 3.1 shows an approximate ranking of the free energy released at various sites. Nucleation is easiest at sites low in the table.

Fortunately, the theory for homogeneous nucleation may be adapted for heterogeneous nucleation by using the values for site density and critical free energy appropriate to the site in question. The ratio of the nucleation rates at a site A and a site B is then given by

$$\frac{I_A}{I_B} = \frac{N_A}{N_B} \exp\left(\frac{G_B^* - G_A^*}{kT}\right) \tag{3.46}$$

Whether nucleation at site A will dominate that at site B will therefore depend on (a) the ratio of the number of available sites and (b) the difference between the activation energies for

Rank	Nucleation Site
1	homogeneous sites
2	vacancies
3	dislocations
4	stacking faults
5	grain and interphase boundaries
6	free surfaces

Table 3.1: Nucleation sites ranked according to the activation energy for nucleation. Nucleation is easiest for high ranking sites [Porter and Easterling, 1992]

nucleation. In general, sites for which the activation energy is greatest tend to have the largest number density (for example, each atom in the matrix is potentially a site for homogeneous nucleation) and these two effects will compete to determine the dominant site.

3.9 Overall Transformation Kinetics - Diffusion Controlled Transformations

The kinetics of diffusion controlled transformations are more complicated than the simple example discussed in section 3.3. This is because of the effects of soft impingement as discussed in 3.5.1. First, the effects of soft impingement will be ignored. The validity of this assumption is discussed at the end of the section.

3.9.1 Without Soft Impingement

For a spherical particle nucleated at a time τ, with a growth rate controlled by long range diffusion processes, the volume at a later time t will be

$$v_\tau = \frac{4\pi}{3}\chi^3 D^{\frac{3}{2}}(t-\tau)^{\frac{3}{2}} \quad (t \geq \tau) \tag{3.47}$$

For a linear growth process, the method used previously (section 3.3) gave

$$\zeta = 1 - \exp\left(-\int_0^t v_\tau I d\tau\right) \tag{3.48}$$

In this case ζ was defined as the fraction of the whole assembly which has transformed. In the case of a diffusional controlled transformation, the maximum fraction of the precipitating phase is limited by the equilibrium volume fraction and ζ must be redefined. If V^β is the equilibrium volume fraction of β in the whole assembly of volume V then the lever rule (conservation of solute atoms) requires

$$\frac{V^\beta}{V} = \frac{\bar{c} - c^{\alpha\beta}}{c^{\beta\alpha} - c^{\alpha\beta}} \tag{3.49}$$

If the total volume of β at any instant is V_β then the fraction of transformation is given by

$$\zeta = \frac{V^\beta(t)}{V^\beta} = \left(\frac{V^\beta(t)}{V}\right) \frac{c^{\beta\alpha} - c^{\alpha\beta}}{\bar{c} - c^{\alpha\beta}} \tag{3.50}$$

Using the same method for hard impingement gives

$$\zeta = 1 - \exp\left(-\frac{c^{\beta\alpha} - c^{\alpha\beta}}{\bar{c} - c^{\alpha\beta}} \int_0^t v_\tau I d\tau\right) \tag{3.51}$$

It can be seen that this equation is substantially the same as the Avrami equation derived for the simplest case.

Whether it is valid to ignore soft impingement will depend on the location and volume fraction of the precipitating particles. If the particles nucleate in such a way that they are widely spaced relative to the diffusion distance then during the early stages of precipitation there will be negligible overlap of the diffusion fields, and soft impingement may be safely ignored. Generally, however, soft impingement will have a significant effect on the kinetics and should be accounted for.

3.9.2 Accounting for Soft Impingement

To account for soft impingement in a rigorous way is often not practical. This is because such a solution requires a knowledge of the distribution of all the particles in the matrix to enable specification of the boundary conditions for the diffusion equation. We shall start by discussing an approximate treatment due to Wert and Zener (1950). This treatment is valid only when the supersaturation is low ($\bar{c} - c^{\alpha\beta} << c^{\beta\alpha} - c^{\alpha\beta}$). The calculation also requires the assumption that all nuclei are present at the start of the transformation (*i.e.* the nucleation rate during transformation is 0). It may be reasonable to make such an assumption, since as the precipitating phase forms the mean solute concentration in the matrix will change (to reduce the supersaturation). The nucleation rate, which is very sensitive to changes in the composition may well be reduced by several orders of magnitude by a very small amount of precipitation, and the number of new nuclei will be insignificant.

For a system with low supersaturation the distances between the particles of precipitate are expected to be large, and it may be assumed that the concentration of the matrix tends to a steady mean value, $c^\infty(t)$ in regions remote from the interface. The following boundary conditions apply

$$c^\infty(0) = \bar{c} \text{ and } c^\infty(\infty) = c^{\alpha\beta} \tag{3.52}$$

The equation for the growth velocity of the particles (3.12) now becomes

$$(c^{\beta\alpha} - c^{\alpha\beta})\frac{dr^I}{dt} = \frac{D(c^\infty(t) - c^{\alpha\beta})}{r^I} \tag{3.53}$$

Because all nuclei are present at the start of transformation, and are well separated, the final size of all the particles will be the same and may be written r^f. The fraction of transformed volume is then $\zeta = (r^I/r^f)^3$. We also have the relation $c^\infty(t) - c^{\alpha\beta} = (\bar{c} - c^{\alpha\beta})(1-\zeta)$. Substituting this expression into 3.53 gives

$$\frac{d\zeta}{dt} = \frac{3D}{(r^f)^2}\left(\frac{\bar{c} - c^{\alpha\beta}}{c^{\beta\alpha} - c^{\alpha\beta}}\right)\zeta^{\frac{1}{3}}(1-\zeta) \tag{3.54}$$

The solution to this equation is somewhat complicated, but has been found by Markovitz (1950) to be given by

$$\frac{3}{2}C^{\frac{2}{3}}t = \frac{1}{2}\ln\left(\frac{1+z+z^2}{1-z^2}\right) + \sqrt{3}\arctan\frac{-\sqrt{3}z}{2+z} \text{ where } \zeta = z^3 \tag{3.55}$$

with

$$C^{\frac{2}{3}} = \frac{2(\bar{c} - c^{\alpha\beta})D}{(c^{\beta\alpha} - c^{\alpha\beta})(r^f)^2} \tag{3.56}$$

More complex treatments of the soft impingement problem are also available. Usually such methods involve constructing a “cell” around each nucleus. These cells are then represented by volume equivalent regular bodies. The diffusion equation is then solved by making certain assumptions about the composition profile at the cell boundaries subject to the constraint of mass balance for each cell. For example, Inden *et al.* (1993) have used such an approach to model the precipitation of ferrite from austenite in a binary Fe–C alloy. It is necessary to specify the initial composition profile and phase state. Using this type of technique for the precipitation of spherical particles on a regular cubic lattice Ham (1959) has shown that apart from a brief transition period the results obtained are identical to those produced with the Zener–Wert method.

3.10 Particle Coarsening

The models discussed so far describe how the volume fraction of a phase varies as it approaches equilibrium. When the equilibrium fraction is reached precipitation will stop and there will be distribution of precipitate particles of various sizes, with the larger particles being those which nucleated first. This is not the most energetically stable configuration however, because there is potential to reduce the overall surface area of the particles and hence reduce the total interfacial energy. This is the driving force for particle coarsening, whereby larger particles will grow at the expense of smaller ones whilst the volume fraction of precipitate remains constant. Particle coarsening in power plant alloys is a complex problem due to the different particle morphologies, distributions and multi–component diffusion. The primary aim of the work described in this thesis was to develop models for the evolution of volume fraction of the various phases up until the point equilibrium is reached and therefore coarsening is not addressed. Nevertheless when comparing predicted and measured particle sizes, especially for alloys exposed to severe tempering it is important to be aware that in practice coarsening may have occurred.

3.11 Transformation Models Applied to Power Plant Steels

Many studies have been made of the precipitation sequences observed in power plant steels. The majority of these studies have provided qualitative rather than quantitative data, for example the presence or absence of a phase is often recorded without a measurement being made of the volume fraction. However, in a number of cases quantitative volume fraction data have been obtained and modelled, most often by fitting the observed evolution of volume to the Johnson–Mehl–Avrami equation (3.7) by choosing appropriate values for C and n.

Wilkes (1968) studied the precipitation of Mo_2C in a Fe–Mo–C test alloy at a variety of temperatures using accurate measurements of electrical resistivity. The resistivity increases with the amount of solute in the matrix, the precipitation of Mo_2C leads to a decrease in the matrix solute level leading to a drop in resistivity. Wilkes used TEM observations to demonstrate that the resistivity change was due to the formation of alloy carbide. He found that the reaction could be divided into two stages, the first with $n = 1$ and the second with $n = \frac{1}{2}$. This may be attributed to the dissolution of cementite. This is not consistent with the TEM observations however, and Wilkes attributes the change in exponent to a change in the rate controlling process from one where there is linear growth of needles followed by precipitation on dislocations. This is perhaps an over–interpretation of the results, since as it has been previously stated the Avrami exponent does not uniquely define the nucleation and growth conditions.

Murphy and Whiteman (1970) have also studied the precipitation kinetics of Mo_2C. They have used a magnetic balance technique which relies on the assumption that the precipitation of Mo_2C is completely complimentary to the dissolution of cementite. The decomposition of cementite results in the liberation of iron, and the removal of molybdenum from solid solution as it forms Mo_2C. This results in an increase in the magnetic moment of the specimen. The solubility of molybdenum in cementite is small [Smith, 1959]. Provided the solubility of iron in Mo_2C is also small then the variation in the magnetic moment will be a linear function of the amount of cementite dissolved and hence the amount of Mo_2C precipitated. Lupton (1971) notes that the assumption that precipitation of Mo_2C is complimentary to the dissolution of cementite is not strictly true, since carbon for Mo_2C formation is available not only from the dissolving cementite, but also from the matrix. Because the carbon level in the matrix is expected to be very small this effect should not alter the results considerably. Murphy and Whiteman, like Wilkes, found a discontinuity in the kinetics of Mo_2C precipitation after approximately 65% transformation. They found the first part of the transformation could be described by an Avrami equation with $n \simeq 0.67$ and the second half by an Avrami equation with $n \simeq 0.2$. By studying TEM micrographs taken at the time at which the discontinuity occurs Murphy and Whiteman conclude that the change in kinetics is related to the recovery of the matrix. In contrast to Wilkes, they state that the change in n is due to a change from precipitation on dislocations in the early stages of transformation to growth in the recovered, relatively dislocation free matrix in later stages of transformation. However, as they note, a value of 0.2 for n is very small, and cannot be explained by the usual kinetic models.

Darbyshire and Barford (1968) have used dilatometric changes to track the precipitation of Mo_2C. They find that the kinetics can be fitted to an Avrami equation with $n = 0.65$. They do not observe any discontinuity in the kinetics, but as Murphy and Whiteman note this may be due to matrix volume changes associated with recovery processes which produce an apparent early end point for the carbide transformation. Data for the precipitation of VC in a Fe–V–C alloy are also presented. In this case a value of 0.7 is found for n when the fraction precipitated is less than 0.7, changing abruptly to a value $\simeq 1$ as the fraction precipitated increases. This is interpreted as a change from precipitation on dislocations to a recovery process when the precipitate particles attain some critical size. Wilkes has also studied alloy carbide precipitation in a Fe–V–C alloy. He finds that a single Avrami exponent of 0.5 represents the observed kinetics, and this is attributed to precipitation on dislocations. Darbyshire and Barford note that Wilkes results may be ambiguous because he starts from a virgin martensitic microstructure and so the determination of alloy carbide kinetics is complicated due to the initial precipitation of cementite, whose distribution will be different in samples treated at different temperatures. They use an initial tempering treatment of 2 hours at 350°C to precipitate cementite before measuring the precipitation of alloy carbide in an attempt to disentangle the two processes.

The precipitation kinetics of $M_{23}C_6$ have been investigated in an austenitic stainless steel (18Cr–12Ni–2.5Mo wt%) by Lai and Meshkat (1978). They found at 625°C $M_{23}C_6$ was the only carbide present and they were able to determine the transformation kinetics using a bulk carbide extraction technique. They found the kinetics obeyed the Avrami equation with good agreement when $n = 0.964$. They note that this value of n usually corresponds to the formation of needle shaped precipitates. However no such $M_{23}C_6$ particles were observed. Lai and Meshkat note that putting $n = 1$ gives a simple exponential decay law similar to that encountered in radioactive decay. They suggest that the precipitation of carbide is governed by the probability law of survival, that is the rate of carbide formation is proportional to the number of carbon atoms remaining in solution at any time.

All of the work described above has involved fitting an Avrami type equation to the transformation curves for a specific alloy at specific temperatures. This has been done generally as an aid to interpretation of the experimental results rather than in an attempt to produce a predictive model. More recently attempts have been made to model the kinetics by combining curve fitting techniques with simple physical parameters to produce predictive models. Hald (1994) has used such an approach to model Laves phase precipitation in *Nf–616*, a 9Cr–1.8W–0.5Mo ferritic steel (full composition shown in table XXX). Measurements have been made of the weight percent of tungsten precipitated as a function of time. It is assumed that this is proportional to the volume fraction of Laves phase. This assumption is justified by calculating the equilibrium compositions of the various precipitates which coexist in this steel. It is found that Laves phase contains a greater tungsten level than the other precipitates. Also, since Laves phase forms at very long times, it is expected that precipitation of the other phases is complete so the amount of tungsten removed by them will remain constant whilst Laves phase forms. Data measured at 600°C were fitted to an Avrami equation to find the values for the exponent n and the constant C. By assuming there are a constant number of pre–existing nuclei the constant C may be related to the composition by the following expression (note that this is exactly equivalent to the expression for C given in equation 3.56)

$$C = 2D\left(\frac{4}{3}\pi N\right)^{\frac{2}{3}}\left(\frac{\bar{c} - c^{\alpha\beta}}{c^{\beta\alpha} - c^{\alpha\beta}}\right)^{\frac{2}{3}} \tag{3.57}$$

It was assumed that tungsten diffusion controls the precipitation of Laves phase. The diffusion coefficient appropriate to tungsten was therefore used, and the composition terms were determined by calculating the equilibrium tungsten levels in Laves phase and the ferrite matrix. N, the number of pre-existing nuclei was found by equating this expression to the fitted value for C using the calculated equilibrium composition values. By assuming that N and n are independent of temperature predictions were made for the kinetics of precipitation at 500, 650 and 700°C by recalculating the phase compositions and hence determining C for each temperature. The predicted volume fraction/time curves were then used to produce a TTT–diagram for Laves phase precipitation which compares well with the measured diagram. This model may be applicable to other steels, but the situation is often more complicated because it may be that the other phases are still precipitating as Laves phase forms. Also, the assumption that any one element controls the growth is questionable if the steel contains other elements such as molybdenum which are also soluble in Laves phase.

3.12 Summary

Considerable efforts are being made to model the evolution of the microstructure in the 9-12 wt% Cr steels. The precipitation reactions which occur in these steel involve nucleation and growth. Diffusion controlled growth where there is local equilibrium may be modelled using classical growth theory due to Zener (1946) where the concentration gradients are assumed to be constant. For needle and plate precipitates it is necessary to account for the modification of the equilibrium compositions to allow for the high curvature of the interface. Finding the interfacial compositions which are uniquely defined by a single tie–line in a binary system is harder in ternary or higher systems where there are a number of possible tie–lines. The compositions are then determined by the requirement that the growth rate must be the same regardless of which element is chosen to calculate it.

Nucleation may be modelled using classical nucleation theory, which may be applied to both heterogeneous and homogeneous nucleation. Both nucleation and growth may be combined to calculate the overall transformation kinetics using the Avrami approach which accounts for the physical (hard) impingement of particles. By using the more restrictive assumption that all nuclei are present at the start of transformation Wert and Zener (1950) have developed a model which allows for the overlap of the diffusion fields of neighbouring particles (soft impingement).

Experimental measurements of the precipitation kinetics have been made for some of the observed phases. These results have usually been interpreted using the Avrami theory for transformation kinetics.

CHAPTER FOUR

Experimental Studies

This chapter describes the experimental investigation of a 10CrMoV alloy (COST F), with particular emphasis on determining a carbide stability diagram for this alloy. The aim of this work was to provide suitable experimental data to test and validate the kinetic models, described in chapters five and six. Experiments have also been carried out to assess the uncertain role of nickel on the precipitation kinetics in these steels.

4.1 Introduction

The development of a model for the kinetics of precipitation in power plant steels appropriate experimental data for validation. Many investigations of the carbide precipitation sequences have been carried out on $2\frac{1}{4}$Cr1Mo material as summarised in section 2.3.8. Similar data are lacking for the 9–12 wt% Cr steels. This is because most ageing experiments have been carried out using material which has been severely tempered(*e.g.* many hours at 700 °C). Many of the early stages of tempering are therefore not recorded and the microstructure before ageing can be close to equilibrium.

To study the evolution of microstructure in the early stages of tempering a range of short term heat treatments have been carried out on COST F steel (composition in Table 4.1) in the as quenched condition with the aim of producing a carbide stability diagram for the 10CrMoV steel analogous to that available for $2\frac{1}{4}$Cr1Mo steel [Baker and Nutting, 1959].

Experiments have also been carried out to assess the effect of nickel content on the precipitation kinetics. Nickel is an austenite stabilising element which is added to these steels to counterbalance the ferrite stabilising elements and prevent δ–ferrite formation. However, there is evidence that increasing nickel levels lead to an acceleration in the precipitation kinetics. This is based on the observation that increasing nickel levels can cause the inflexion point[1] in the stress / rupture life plots to occur at shorter times [Marrison and Hogg, 1972]. This inflexion point is thought to be associated with microstructural changes such as the dissolution of M_2X particles, and coarsening of $M_{23}C_6$ and it may be that nickel acts to accelerate these changes. Iseda (1992) also gives evidence which suggests that nickel accelerates Laves phase precipitation (section 2.3.7). Heat treated samples of 12 wt% Cr material with different nickel levels were examined to investigate this effect.

4.2 Materials and Heat Treatments

The 10CrMoV COST F steel was supplied by National Power in the form of a 10 cm square block. Cylindrical specimens, 8 mm in diameter and 12 mm in length were machined from this sealed in silica tubes which were first evacuated and then filled with argon to a pressure of 150 mm Hg to prevent any decarburisation or oxidation during heat treatment. Homogenisation and austenitisation were then carried out for three days at 1200 °C followed by a rapid (water) quench.

[1] The inflexion occurs where a rapid reduction in the creep rupture strength is accompanied by a corresponding increase in rupture ductility and is due to microstructural changes in the material.

C	Si	Mn	P	S	Al	Cr	Mo	Ni	V	Nb	N
0.11	0.03	0.52	0.010	0.005	0.006	10.22	1.42	0.58	0.18	0.05	0.056

Table 4.1: Composition (wt%) of COST F 10CrMoV steel used in experimental investigation

The austenitisation temperature in these alloys is quite critical. This is because there is only a narrow temperature range between the dissolution of carbides and the formation of δ–ferrite. An MTDATA calculation (section 5.1) of the equilibrium phases at 1200 °C is shown in Table 4.2.

Phase	Predicted Amount / Mole Fraction
Austenite	0.9967
Ferrite	0.0029
MX (NbN)	0.0003

Table 4.2: Predicted equilibrium phases in 10CrMoV COST F steel at 1200 °C

At 1200 °C it is predicted that most of the carbides have dissolved, and only a small fraction of δ–ferrite has formed. Note also that some MX phase is also predicted, and this is consistent with experimental studies which show MX is not fully dissolved during austenitisation [Janovec *et al.* 1994]. It was predicted that the δ–ferrite content decreased and MX increased as the temperature was reduced below 1200 °C(Figure 4.1). Therefore 1200 °C was chosen to minimise the amount of precipitate in the as quenched condition.

Following austenitisation and quenching the samples were resealed in silica tubes and heat treated as shown in Table 4.3. The heat treatments at 600 °C were carried out first to establish tempering intervals which identify clearly the precipitation sequence with the minimum number of experiments. In selecting the times it was assumed that the transition lines on the carbide stability diagram for the 10CrMoV steel have similar gradients to those for the $2\frac{1}{4}$Cr1Mo steel.

R / °C	Time /h
600	0.16, 0.5, 1, 4 and 16
650	0.16, 0.5, 2 and 8
800	0.05 and 0.16

Table 4.3: Heat treatments performed on samples of 10CrMoV COST F steel

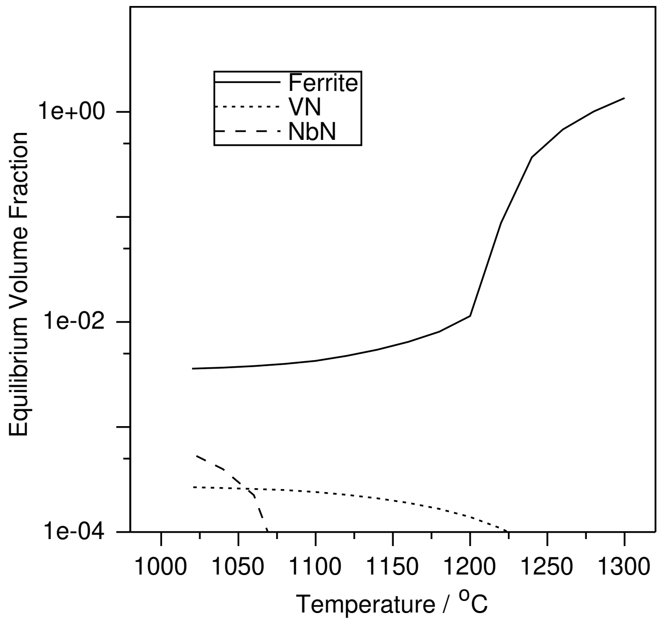

Figure 4.1: Predicted equilibrium fraction of phases in 10CrMoV COST F steel.

Creep specimens for the investigation of the effect of nickel on the transformation kinetics were supplied by GEC Alsthom, Rugby. Two composition variants were studied, one with high a nickel content and the other with a low nickel content. All the material had been exposed to an austenitising treatment of 1 hour at 1050 °C followed by a temper of 3 h at 690 °C. The compositions and thermal histories of all the samples are shown in Table 4.4. In each case the whole creep rupture specimens was supplied to provide material from the gauge length (stressed portion) and specimen head (unstressed portion). Samples for microscopy were prepared only from the unstressed portion so that the effects of a change in nickel level were not confused by stress induced effects. Samples S and R which are in the austenitised and tempered condition were investigated at GEC–Alsthom by Strang and Vodarek (1996a), and their results are summarised here. S1 and R1 show the most interesting differences and the study of these samples is presented in detail here.

4.3 Transmission Electron Microscopy

Both carbon extraction replica specimens and thin foils were used in microstructural investigations. These were prepared from the test material as explained below, and were then examined in a Philips 400T transmission electron microscope (TEM).

4.3.1 Specimen Preparation

To prepare thin foil specimens 3mm discs were punched from thin slices cut from the 8mm

Identification	C	Si	Mn	Cr	Mo	V	N	Ni	Thermal History
S	0.13	0.20	0.70	12.32	0.62	0.17	0.037	0.21	Austenitised+Tempered
S1	0.13	0.20	0.70	12.32	0.62	0.17	0.037	0.21	19 109h at 550 °C
R	0.12	0.37	0.65	12.32	0.60	0.18	0.032	1.28	Austenitised+Tempered
R1	0.12	0.37	0.65	12.32	0.60	0.18	0.032	1.28	14 731h at 550 °C

Table 4.4: The composition and thermal history of the alloys used in the investigation of the effect of nickel on precipitation kinetics. All materials were given the same temper. S1 and R1 were then subject to creep tests.

diameter specimens. The discs were then mechanically ground to 50 μm and then twin jet electropolished to electron transparency at 50 V, with the solution being cooled to 0 °C using liquid nitrogen. The polishing solution contained 10% perchloric acid, 15% glycerol and 75% industrial methylated spirits.

Carbon replica specimens were also prepared from each sample for TEM examination. Replicas have a number of advantages over thin foil samples. By eliminating effects due to the steel matrix the chemical composition of the carbides may be measured more accurately. Working with a magnetic specimen in the electron beam, which can be problematical is also avoided. Furthermore, the area of each sample which may be studies is greater than that for a thin foil, where the region which is electron transparent may be rather small. Single stage extraction replicas were prepared following Smith and Nutting (1959) from surfaces prepared for optical microscopy (etched with Bain–Villela's reagent, 5 ml hydrochloric acid, 1 g picric acid in 100 ml of methanol). A carbon coating of 20-30 nm (brown colour) was deposited in a vacuum of 10^{-5} torr onto the etched specimen. This film was then scored with a sharp blade to divide it into several smaller squares covering the whole area of the sample. Electrolytic etching in a solution of 5% hydrochloric acid in methanol at 1.5 V was used to remove the carbon film, which was then washed in methylated spirits and floated off in distilled water. Each sample yielded approximately six smaller squares of film which were mounted on copper grids and dried before examination in the TEM.

4.3.2 Selected Area Diffraction

The reliable identification of phases is vital when characterising the precipitation sequence. Although composition measurement it may not unambiguously identify the phase. The most reliable technique is selected area diffraction. An aperture is used to isolate a selected particle. The electron diffraction pattern from the particle is then used along with a knowledge of the crystal systems and lattice parameters of the possible phases to match the pattern to a particular phase. Some of the carbide phases have similar lattice parameters and can in some orientations be hard to distinguish without an accurate camera length. The diffraction geometry is shown in Figure 4.2.

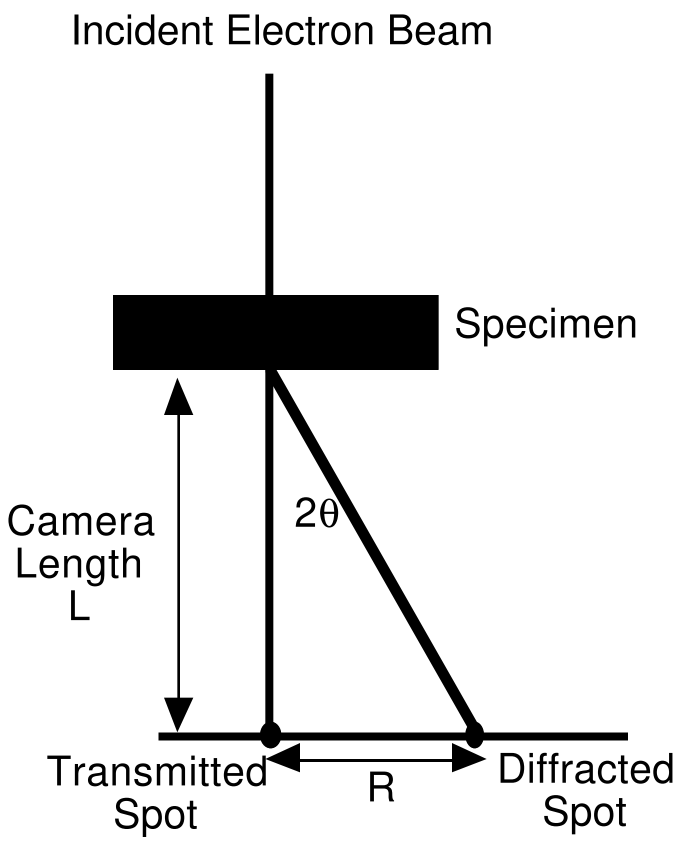

Figure 4.2: A schematic illustration of the relationship between the camera length, distance on the diffraction pattern and Bragg angle θ.

The distance between the transmitted and diffracted spots measured on the diffraction pattern, R_{hkl} and the spacing of the corresponding plane d_{hkl} is given by

$$R_{hkl}d_{hkl} = L\lambda = \text{ camera constant} \tag{4.1}$$

The camera length L multiplied by the electron wavelength λ is, for constant operating conditions, invariant and is referred to as the camera constant. The electron wavelength is given by

$$\lambda = \frac{h}{2m_e eV_{accel}\left(1 + \frac{eV}{2mc^2}\right)} \tag{4.2}$$

where V_{accel} is the accelerating voltage of the electrons, c is the speed of light in vacuum, h is

Parameter	Value
Accelerating voltage	120 kV
Nominal camera length	800 mm
Objective lens current	6.2 – 6.4 A
Electron wavelength	0.0335 Å
Nominal camera constant	2.68×10^{-12}m^2

Table 4.5: Operating conditions used in the 400T TEM during this study

the Planck constant, e is the charge on an electron and m_e is the electron rest mass. In the work presented here the operating conditions shown in Table 4.5 were used

The camera length, and hence the camera constant are subject to small deviations from their nominal values depending on the operating current. A more precise value may be obtained by calibrating the camera constant using the diffraction pattern from a phase whose lattice parameter is well known. The diffraction pattern from a sputtered gold film as described by Thomson (1992) was used to calibrate the 400T microscope, and for a nominal camera length of 800 mm gives a calculated camera constant between 2.71×10^{-12} and 2.66×10^{-12}m as the objective lens current varies between 6.2 and 6.4 A. Another quicker method was used in this work to verify that these values are reasonable, using the ferrite diffraction pattern in a thin foil sample.

4.3.3 Energy Dispersive X–ray Analysis (EDX)

A LINK series 860 energy dispersive X–ray spectrometer attached to the Philips 400T TEM was used in this work. X–ray spectra were recorded at a specimen tilt of 35°. A live time of 100 seconds was used, sufficient to give statistically significant results. The dead time was kept to below 25% and the count rate to below 2500 counts/s. In each case at least ten particles of each phase were examined to ascertain the variation in composition. With these operating parameters the typical accuracy of the system is in the range 5-10% which is adequate for our requirements. The concentrations of C and N cannot be analysed by the EDX system since the beryllium window in front of the EDX detector stops X–rays due to light elements. Further details regarding the principles behind quantitative EDX are given elsewhere [Thomson, 1992].

4.4 Microscopy of the 10CrMoV Steel

Figure 4.3 shows that the microstructure of the 10CrMoV (COST F) steel consists mainly of martensite after austenitisation and quenching, with a small volume fraction of δ–ferrite along

Figure 4.3: An optical micrograph showing the martensitic microstructure after austenitisation and quenching. Some δ–ferrite is also formed.

the prior austenite grain boundaries, consistent with the MTDATA predictions.

4.4.1 Tempering at 600° C

A TEM micrograph of the microstructure after heating for $\frac{1}{2}$ an hour at 600 °C is shown in Figure 4.4 . The most striking features are the aligned plate shaped precipitate particles which appear to be uniformly distributed within the martensite lath. Figure 4.5 shows a selected area diffraction pattern taken from a plate and the surrounding matrix. It can be seen that there is a distinct orientation relationship between the precipitate and the ferrite matrix. The precipitates were found to be cementite. The orientation relationship is consistent with the tempering or Bagaryatski (1950) relationship, which is the most commonly observed between cementite and ferrite. It is usually expressed as

$$\{001\}_\theta \parallel \{211\}_\alpha$$

$$< 100 >_\theta \parallel < 0\bar{1}1 >_\alpha$$

where the subscript θ and α corresponds to cementite and ferrite respectively.

Similar cementite precipitation was observed after 4 h at 600 °C as shown in Figure 4.6. The contrast due to the matrix makes it difficult to determine whether any other precipitate par-

Figure 4.4: A TEM micrograph of a thin foil specimen taken from a sample heated for $\frac{1}{2}$ h at 600 °C. Aligned, plate shaped precipitates can be seen within the martensite laths.

ticles are also present. Carbon extraction replicas were therefore studied to provide further information.

A series of TEM micrographs taken from samples tempered at 600 °C is presented in Figure 4.7, showing the sequence of changes during the early stages of tempering. The dominant precipitate is cementite after 10 min of heat treatment. There is also a very fine distribution smaller needle shaped particles, identified using selected area diffraction patterns (SADP) as M_2X precipitates, the proportion and size of which increased with the half hour treatment. Further tempering led also to the formation of a small number of blocky particles which tended to cluster. These were identified using SADP as $M_{23}C_6$. After 16 h the precipitation of $M_{23}C_6$ is well advanced, especially along lath boundaries. Needles of M_2X were still present in the laths, but cementite had disappeared. In this investigation MX was not identified, although it ought to be present according to thermodynamic calculations. However, MX particles are usually very small and it is difficult to locate and then get diffraction patterns from them. It may well be that some of the finer particles inside the laths are MX rather than M_2X , but direct evidence could not be obtained with the conventional techniques used here.

The precipitation sequence observed may therefore be summarised as follows (bearing in

Figure 4.5: A diffraction pattern from one of the cementite precipitates showing the Bagaryatski (1950) orientation relationship between the ferrite (marked a) and cementite (marked c) phases.

mind that MX may also be present.

$$M_3C + M_2X \rightarrow M_3C + M_2X + M_{23}C_6 \rightarrow M_2X + M_{23}C_6$$

This sequence is similar to that observed by Baker and Nutting (1959) in a $2\frac{1}{4}$Cr1Mo steel, with the exception that they also observed M_7C_3 formation prior to $M_{23}C_6$ precipitation. M_7C_3 was not observed in this investigation; since it can be easily identified by streaks in its diffraction pattern, it may be said confidently that none was present. The observed sequence is consistent with the MTDATA calculated sequence of phase stabilities (see section 5.6). The kinetics of precipitation are considerably faster when compared with those for the $2\frac{1}{4}$Cr1Mo steel. For example at 600 °C Baker and Nutting observed M_2X after approximately 5 h. In the 10CrMoV steel M_2X was present after just ten minutes. Also $M_{23}C_6$, which Baker and Nutting did not observe even after 1000 h at 600 °C was present in the 10CrMoV steel after only one hour.

4.4.2 Tempering at 650 and 800° C

The same precipitation sequence was observed at 650 °C although the rate of transformation was faster. Figure 4.8(a) and (b) show the precipitate distributions after 25 min and 7 h at

Figure 4.6: A TEM micrograph of a thin foil specimen taken from a sample heated for 4 h at 600 °C showing aligned cementite precipitates.

650 °C respectively. Taken at lower magnifications than those at 600 °C they show that $M_{23}C_6$ is present after 25 min at 650 °C. The localisation of $M_{23}C_6$ particles, presumably along lath boundaries, is also clear from these micrographs. Some cementite was identified after 25 min, whereas after 7 h none was found. M_2X was identified at both times.

The two heat treatments at 800 °C were performed to see if any evidence of a C–curve on the time–temperature–transformation (TTT) diagram could be detected. This temperature was chosen on the basis of MTDATA calculations as the highest before the formation of austenite. The time taken for precipitation at 600 °C is longer than at 650 °C. If the time for precipitation at 800 °C is longer than that at 650 °C then this implies that there is a maximum in the precipitation rate between 650 °C and 800 °C and there will be a corresponding 'nose' on the TTT diagram.

Figure 4.9(a) and (b) show the precipitate distributions after 3 and 10 min at 800 °C respectively.After only 3 min a significant amount of $M_{23}C_6$ was formed. M_2X was identified in both samples but cementite was not observed so that 3 min is sufficient time to dissolve the cementite. These results suggest that the precipitation rate continues to increase as the temperature is raised from 650 and 800 °C. Thus, for all practical purposes, the TTT diagram shows an increase in the rate of precipitation with increasing temperature.

Figure 4.7 : Micrographs showing the evolution of microstructure in a 10Cr-MoV steel at 600 °C . (a) 10 min, (b) $\frac{1}{2}$ an hour, (c) 1 hour and (d) 16 h.

Figure 4.8 : Micrographs showing the precipitate distribution in a 10CrMoV steel heated at 650 °C for (a) 25 min and (b) 7 h. In both cases $M_{23}C_6$ is the dominant precipitate.

Figure 4.9 : Micrographs showing the precipitate distribution in a 10CrMoV steel heated at 800 °C for (a) 3 min and (b) 10 h. In both cases $M_{23}C_6$ is present and cementite is not.

The results may be summarised on a carbide stability diagram (Figure 4.10). Points plotted on this diagram correspond to experimental observations. The lines are extrapolated from these observations to identify regions where different precipitates are present.

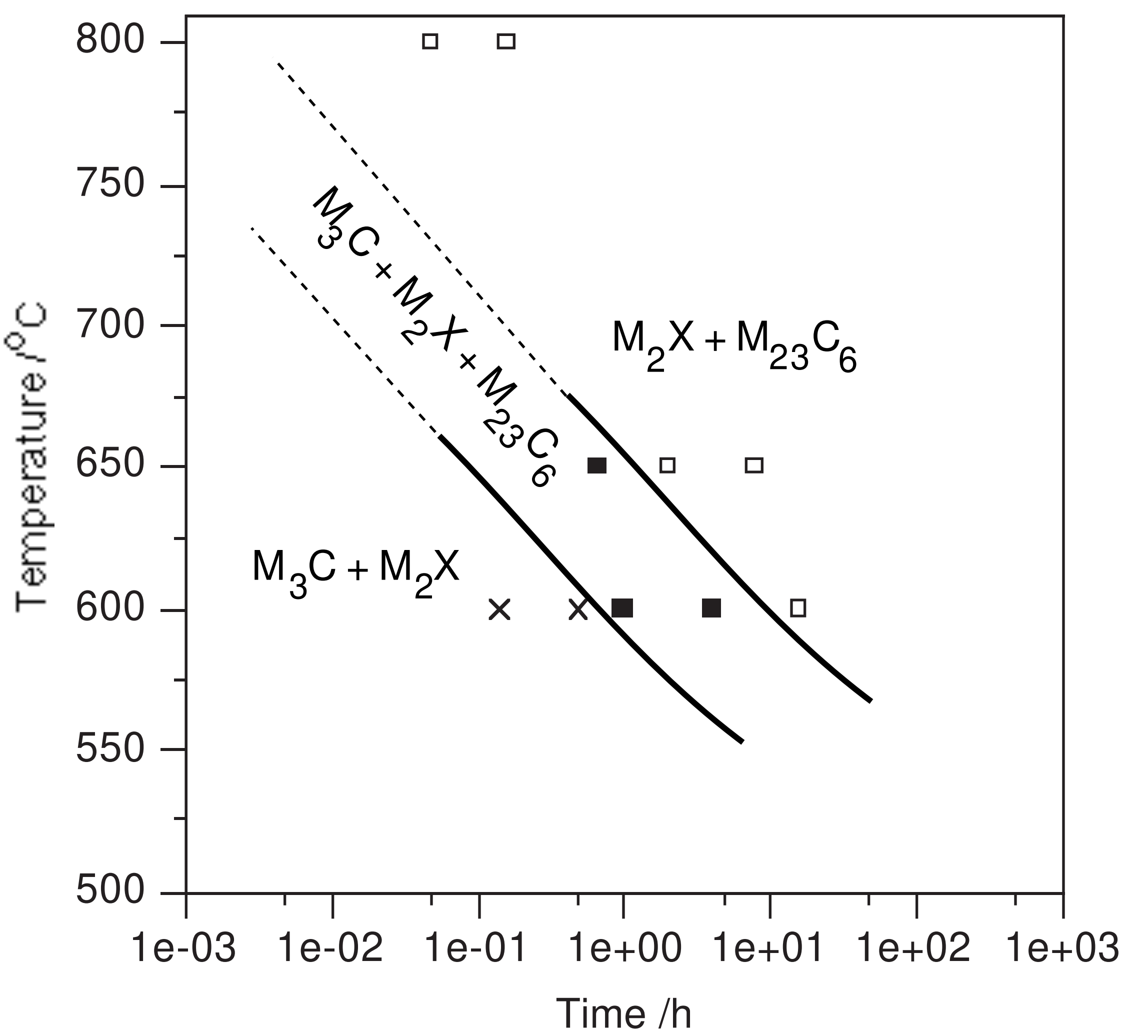

Figure 4.10: A carbide stability diagram summarising the experimental observations on tempered samples of 10CrMoV steel.

4.4.3 EDX Analysis of Precipitates in the 10CrMoV Steel

EDX composition measurements were taken from particles precipitated after 10 min, 1 hour, 4 h and 16 h at 600 °C. It is reasonable to assume a stoichiometric ratio of M and C/N atoms and the results may be normalised allowing for this. The EDX system gives the relative proportions of the elements in weight%. These have been converted to atomic% and normalised to allow for C and N to enable comparisons with MTDATA predictions. Figure 4.11 is a plot for the concentrations of the principal alloying elements in cementite. Cementite was not found at 16 h, so no data can be plotted for this time.

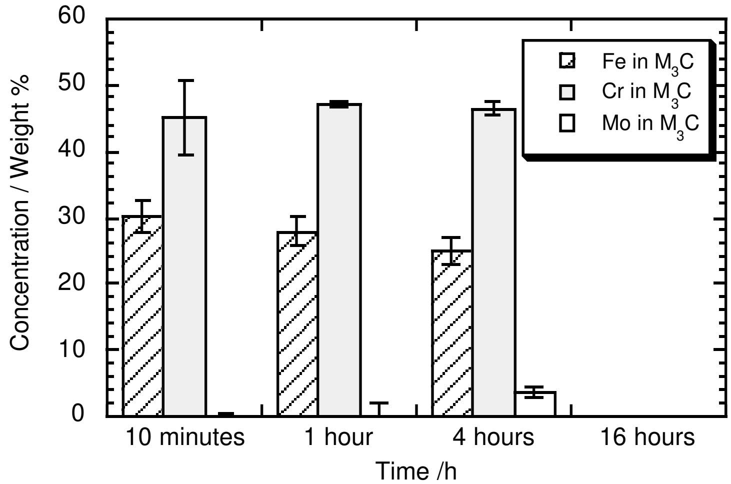

Figure 4.11: The concentration of the principal alloying elements in cementite after heat treatments at 600 °C. Carbon and nitrogen together are assumed to have the stoichiometric atomic fraction, 0.25.

The equilibrium concentrations of iron, chromium and molybdenum in cementite at 600 °C were calculated using MTDATA, allowing ferrite and cementite to coexist. These results and the paraequilibrium concentrations which are those when cementite first forms are shown in Table 4.6. Comparing the measured results with the data in Table 4.6 it is apparent that even after 10 min the cementite has enriched significantly and is closer to its equilibrium than the paraequilibrium composition. Subsequent measurements show a decreasing iron level at longer times, consistent with cementite enrichment.The chromium level in the cementite did not change between 1 and 4 h of tempering, even though the equilibrium composition has not been reached. This is probably due to the formation of other chromium–rich phases, in particular $M_{23}C_6$ which competes with cementite for the available chromium.

Figure 4.12 shows a plot of the measured composition of the principal alloying elements in $M_{23}C_6$. This phase was not observed after 10 min so no data are plotted for this time. As in the case of the cementite, the concentrations have been converted to atomic fractions and normalised to allow for the stoichiometric quantities of carbon and nitrogen. The calculated equilibrium concentrations of iron, chromium and molybdenum in this phase are

$$0.61992\ \mathrm{Cr}\ -\ 0.10268\ \mathrm{Mo}\ -\ 0.07026\ \mathrm{Fe}\ \ \text{(atomicfractions)}$$

	Fe	Cr	Mo
Equilibrium	0.08940	0.64957	0.00076
Paraequilibrium	0.64230	0.08168	0.00062

Table 4.6: Equilibrium concentrations (atomic fraction) of the principal alloying elements in cementite, calculated for a 10CrMoV steel at 600 °C using MTDATA and the paraequilibrium concentration

It can be seen that after 16 h the measured $M_{23}C_6$ composition is in good agreement with the equilibrium composition although the measured iron content is slightly higher than that calculated. At earlier times the deviation from the equilibrium composition is greater. In particular the molybdenum content appears to be low at early times, and increases to reach its equilibrium value after 16 h.

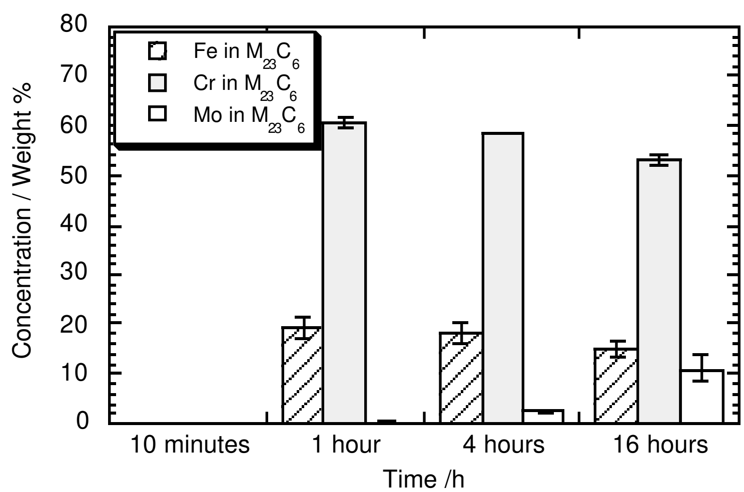

Figure 4.12: The concentration of the principle alloying elements in $M_{23}C_6$ after heat treatments at 600 °C. Carbon and nitrogen together are assumed to have the stoichiometric atomic fraction, $\frac{23}{29}$.

4.4.4 Measurement of M_2X Growth Rate

The growth rate of M_2X is a parameter modelled so experimental data were accumulated for validation purposes. For low chromium steels there exist suitable data in the literature *e.g.* [Hall *et al.* 1972]. However, no equivalent data exist for the high chromium steels. To measure the growth rate of M_2X a number of micrographs were studied, taken from the samples heated at 600 °C. In each case the length of the longest needle present was measured. The longest needles will be those which nucleated earliest. A plot of needle length against time is shown in Figure 4.13.

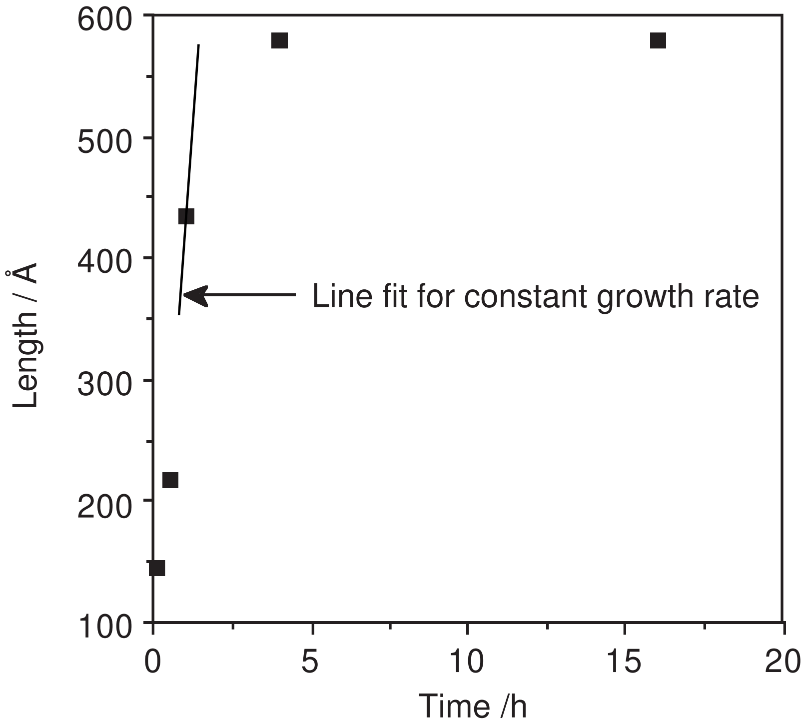

Figure 4.13: The length of the longest M_2X needle in a 10CrMoV steel heated at 600 °C.

The growth rate is given by the gradient of the length *vs* time plot, it is initially constant, as expected from the theory for diffusion controlled growth of needles. At longer times soft impingement becomes significant and the growth rate slows until it eventually becomes zero. Eventually the needle length would be expected to diminish as dissolution begins, but this was not observed in the timescale studied. The growth rate calculated from the initial linear portion of the curve is $0.12\text{Å s}^{-1} \pm 0.04\text{Å s}^{-1}$.

4.5 The Effect of Nickel on the Transformation Kinetics

The results of the investigation on the effect of nickel on transformation kinetics will now be discussed. Work on samples S and R in the austenitised, quenched and tempered condition performed at GEC Alsthom showed that in both cases the phases present were $M_{23}C_6$ and M_2X [Strang and Vodarek, 1996a] .

Micrographs taken using carbon extraction replicas of specimens S1 and R1, both of which have been subjected to creep testing at 500 °C are shown in Figure 4.14. The most striking difference is the presence of large, equiaxed particles in the high nickel sample (R1) which are absent in the low nickel sample.

Selected area diffraction analysis was used to identify the precipitates. The majority of precipitates in the low nickel were best indexed as $M_{23}C_6$. In the high nickel specimen, the smaller precipitates which are similar in size and morphology to those in the low nickel steel were also found to be $M_{23}C_6$. On initial investigation it seemed that the larger precipitates were also $M_{23}C_6$. It is well known however, that in many orientations it is difficult to discriminate between the diffraction patterns due to $M_{23}C_6$ and M_6C. Both phases have a cubic unit cell with similar lattice parameters (a=10.621Å for $M_{23}C_6$ and a=11.082Å for M_6C). They may be differentiated on the basis of their different space group symmetry; $M_{23}C_6$ is Fm3m and M_6C is Fd3m (the diamond structure). Thus, diffraction patterns taken along the [001] axis should appear different. The pattern down this axis for M_6C will have weak spots when $h+k \neq 4n$, where n is an integer and (hkl) is the index of the spot. For $M_{23}C_6$ all the spots are expected to have equal intensity. Figure 4.15 shows one of the large particles and its diffraction pattern, taken down the [001] direction showing the differences in intensity expected for M_6C. It therefore seems likely that the larger particles are M_6C. No such intensity differences were noted for the smaller particles, suggesting these are $M_{23}C_6$ as first proposed.

4.5.1 EDX Analysis of Creep Test Specimens

To explain why large particles of M_6C form in the high but not the low nickel alloy, composition measurements were performed using EDX microanalysis. The compositions of the $M_{23}C_6$ particles were found to be very similar in both steels. The composition of the M_6C particles was found to be significantly different, as demonstrated in Figure 4.16 which shows the mean analysis for both types of particle in the high nickel alloy. Note that these results are normalised ignoring the effects of carbon and nitrogen since it is the proportion of the various metallic species in each phase which is of most interest.

It can be seen from Figure 4.16 that M_6C contains a significant fraction of nickel which is not present in the $M_{23}C_6$. Complimentary to the higher nickel level are lower chromium and iron levels. Attempts to use MTDATA to predict the effect of nickel on the composition of M_6C failed because there are no data for nickel in M_6C and so MTDATA does not allow this element to go into this phase.

These observations provide a compelling argument to explain the effect of nickel in reducing the time before the inflexion in the creep curve. Nickel appears to be highly soluble in M_6C but is far less so in $M_{23}C_6$. An increase in the nickel level therefore stabilises M_6C, encouraging its precipitation. These particles are able to grow more rapidly that $M_{23}C_6$ and

Figure 4.14 : Micrographs for samples S1 and R1 (creep tested at 550 °C.) Large equiaxed particles are present in sample R1 (high nickel) which are absent from sample S1 (low nickel). These particles have been identified as M_6C

Figure 4.15: One of the large equiaxed particles. Inset shows its diffraction pattern taken down [001] revealing lower intensity spots when $h + k \neq 4n$, suggesting this phase is M_6C.

form large, equiaxed precipitates which do not themselves contribute to the creep resistance, but instead degrade it by taking solute out of solid solution in the matrix. It therefore seems that rather than simply accelerating the precipitation of all the phases, as has sometimes been assumed, nickel encourages the formation of M_6C which is able to grow more rapidly than $M_{23}C_6$.

4.6 Summary

Heat treatments of up to 16 h duration have been performed on samples of 10CrMoV steel. TEM studies revealed that at all temperatures studied the precipitation sequence is

$$M_3C + M_2X \rightarrow M_3C + M_2X + M_{23}C_6 \rightarrow M_2X + M_{23}C_6$$

Increasing temperature has been shown to lead to increasingly rapid precipitation kinetics up to at least 800 °C. Particle compositions have been compared with equilibrium values predicted using MTDATA. It has been shown that cementite enrichment is already well advanced after only 10 min at 600 °C. Where $M_{23}C_6$ was observed it was found that it is close to its equilibrium composition.

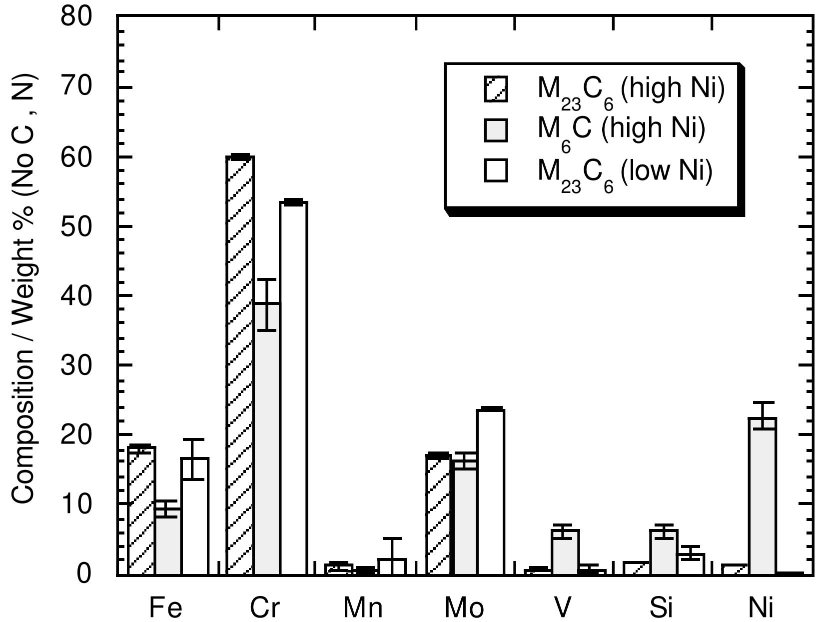

Figure 4.16: Concentration of the metal species in the carbides observed in alloys S1 and R1. Error bars are marked corresponding to one standard deviation. The most striking difference between the two phases is the considerable nickel level in the M_6C.

The effect of the nickel level on the precipitation kinetics in a series of 12 wt% Cr alloys has been studied. It is observed that in the alloys where the nickel level is relatively high (1.28 wt%) M_6C forms as well as the $M_{23}C_6$ observed in all the alloys. The particles of M_6C are larger and more widely spaced than those of $M_{23}C_6$ and their formation may explain the accelerated degradation of the creep resistance when the nickel levels are high.

CHAPTER FIVE

Thermodynamic Calculations

A prerequisite for kinetic modelling is the availability of reliable thermodynamic data. The use of the computer package MTDATA to perform thermodynamic calculations is described. Such calculations can give useful information about the effects of temperature and alloying additions on the composition and stability of the precipitate phases and some interesting examples are presented.

5.1 Introduction

Modelling precipitation in power plant steels requires a knowledge of both the thermodynamic and kinetic parameters for the variety of possible phases. Thermodynamic calculations give the relative stability of the phases and may be used to make estimates of phase fractions and compositions. The final equilibrium state is also determined from the thermodynamics of the system. At any intermediate point, the volume fraction of any phase will depend on the rate at which it forms *i.e.* on the kinetics of transformation.

Recently, the advent of thermochemical data banks has made the calculation of phase equilibria relatively straightforward. In this work the National Physical Laboratory's Metallurgical and Thermodynamic Data Bank (MTDATA) has been used [Hodson, 1989]. This package is capable of calculating phase equilibria for multi–component systems where many phases may be coexisting. It works by combining experimentally determined data from the appropriate unary, binary and perhaps ternary sub–systems using thermodynamic theory to estimate what happens in larger systems. The reliability of the predictions will depend on the available data for all the sub–systems. In general, the more sub–systems for which there are no data, the more unreliable the results. MTDATA warns the user when data are missing so this may be taken into account when interpreting the output. For any given system MTDATA calculates the compositions and volume fractions of the phases present by minimising the Gibbs free energy along with the requirement for conservation of mass. It is possible to suppress the formation of any phase, and recalculate the phase equilibria without that phase present. In this way it is possible to deduce the relative stabilities of the phases, and determine likely precipitation sequences. MTDATA may be used to predict how changes in alloy composition and heat treatment affect the relative stability of the phases and is therefore a useful tool in the design of new alloys. Although it can be used to predict what is possible thermodynamically it cannot predict the time dependence of the microstructure which clearly requires kinetic modelling. Nevertheless, much useful information can be generated on the basis of thermodynamic calculations alone, and some examples are given in the next section.

5.2 Thermodynamic Calculations

Several workers have used thermodynamic data banks to understand power plant steels. Hald (1994) has used Thermocalc, a package similar in operation to MTDATA, to calculate the equilibrium phases in a number of tungsten–alloyed 9-12 wt% chromium steels. Hald has also made predictions for the alloys being investigated in the COST programme (see table 1.3). The phases predicted using Thermocalc correlate well in most cases with the observed phases.

There are, however, a number of significant anomalies primarily due to a lack of appropriate thermodynamic data but also because the equilibrium state may not necessarily represent a commercial microstructure.

Thomson (1992) has used MTDATA to make predictions for a 12Cr1MoV steel. By suppressing the most stable carbide ($M_{23}C_6$) and recalculating the phase equilibria, then suppressing the next most stable carbide (M_7C_3), Thomson predicts a precipitation sequence at 700°C of $M_3C \rightarrow M_7C_3 \rightarrow M_{23}C_6$. This agrees well with experimental observations made at this temperature. The composition of $M_{23}C_6$ after 2 hours at 700°C (stress relief heat treatment) was compared with that predicted by MTDATA and found to be in good agreement. Thomson concluded that unlike in low chromium power plant alloys, the kinetics of transformation in the 12Cr1MoV steel are sufficiently rapid so that equilibrium carbides are present immediately after the stress relief heat treatment.

The work presented here focuses on calculations regarding Laves phase formation. Because this phase forms considerably after the other phases have precipitated, it is reasonable to suppose that when Laves phase forms the other phases have reached their equilibrium volume fractions. Also, because Laves phase is deemed to be detrimental to toughness (section 2.3.7) there is considerable interest in determining the effect individual elements have on its stability.

5.3 The Effect of W and Mo on Laves Phase Precipitation

Both tungesten and molybdenum are highly soluble in Laves phase. It would therefore be expected that they encourage the precipitation of Laves phase. There is certainly evidence that an increased tungsten content leads to formation of Laves phase at higher temperatures and at a faster rate than in tungsten–free steels [Vanstone, 1994].

MTDATA was used to investigate the effects of varying the bulk tungsten and molybdenum content on the equilibrium volume fraction of Laves phase. A typical 10CrMoV steel (COST F, table 4.1) was chosen as the base composition. MTDATA calculations showed that for the base steel composition Laves phase is an equilibrium precipitate below approximately 575°C. Calculations were performed at 600°C to see whether increasing tungsten or molybdenum would stabilise Laves phase and make it an equilibrium precipitate at this temperature. The tungsten level was varied between 0 and 2 wt% whilst the molybdenum level was set to zero. The molybdenum was then varied over the same range, with the tungsten level set to zero. The predicted amount of Laves phase in both cases is shown in Figure 5.1.

It can be seen from Figure 5.1 that adding sufficient tungsten or molybdenum will eventually induce Laves phase formation. Tungsten additions appear to have a greater effect since

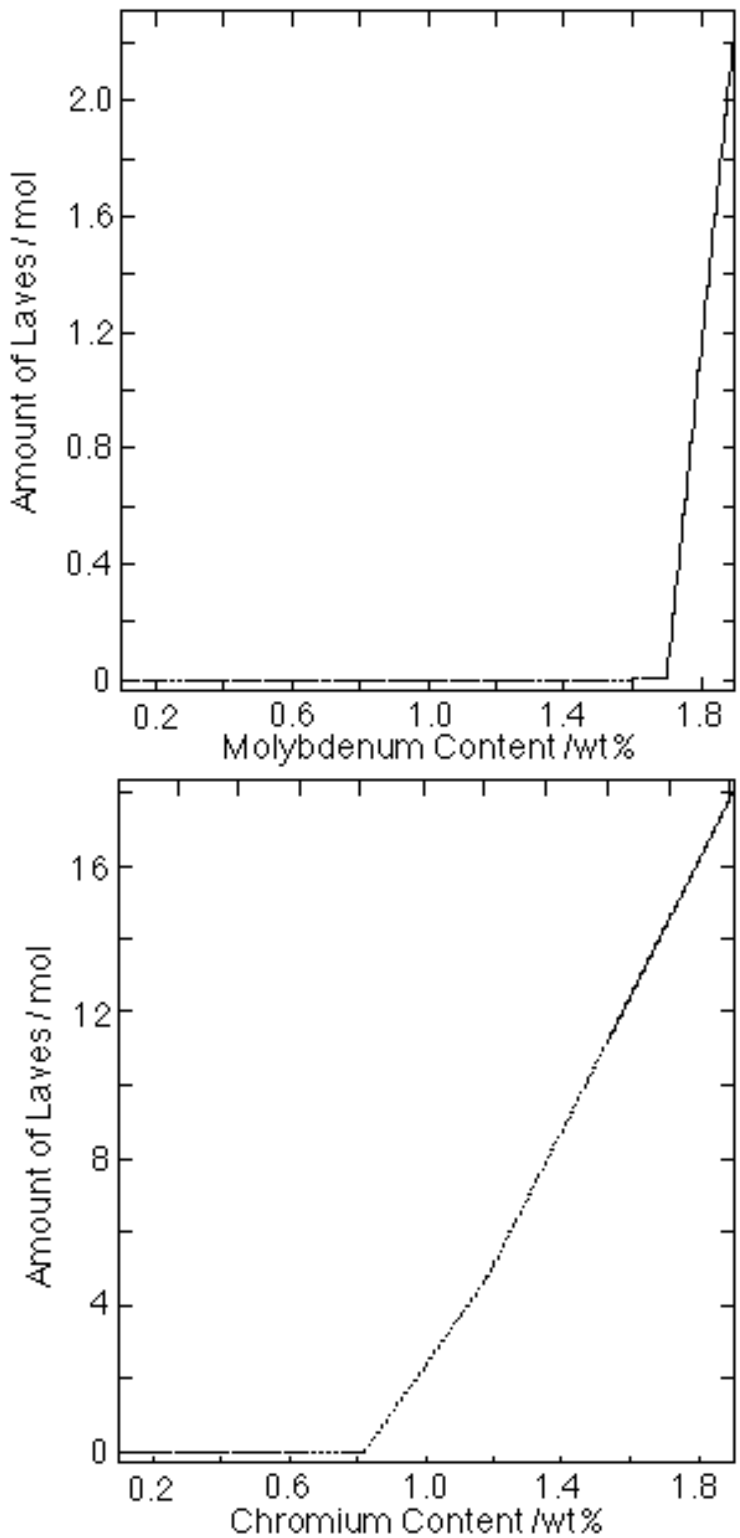

Figure 5.1: The influence of tungsten and molybdenum on the amount of Laves phase in a 10Cr(Mo,W)V alloy, COST F.

Laves phase becomes stable after adding 0.6 wt% compared to the 1.7 wt% of molybdenum required. Addition of further tungsten leads to a predicted amount of Laves phase which is much greater than that for the same added mass of molybdenum. The most likely explanation for this is that the solubility of tungsten in the other phases (carbides, nitrides and ferrite) is less that that of molybdenum. Molybdenum additions are therefore more easily accommodated by partioning more molybdenum into the carbide precipitates than tungsten additions. The tungsten and molybdenum levels in all the equilibrium phases are shown in Table 5.1 for the cases where the alloy contains either 2 wt% tungsten or 2 wt% molybdenum.

Phase	Mo in phase (2 wt% Mo alloy)	W in phase (2 wt% W alloy)
Ferrite	0.00830	0.00205
M_2X	NEP	0.01436
$M_{23}C_6$	0.10299	0.03220
Laves	0.333	0.333

Table 5.1: A table showing the predicted molybdenum and tungsten content (atomic fraction) of the equilibrium phases in 10Cr–2Mo–V steel (COST F with 2 wt% Mo) and a 10Cr–2W–V wt% steel (COST F, with no Mo and 2 wt% W). NEP indicates that the phase in question was not predicted as an equilibrium phase

It is apparent from this table that the molybdenum levels in the ferrite and $M_{23}C_6$ are considerably greater than the equivalent tungsten levels, resulting in a lower volume fraction of Laves phase. To avoid Laves phase formation it therefore seems preferable to tend towards low tungsten levels.

5.4 The Effect of Silicon on Laves Phase Precipitation

Evidence in the literature suggests that increasing silicon levels leads to an increase in the volume fraction of Laves phase which forms [Hosoi *et al.* 1986]. MTDATA was used to investigate whether such an observation could be explained on the basis of an increase in the equilibrium volume fraction of Laves phase with increasing silicon levels. As in the previous section the COST F alloy composition was used as a base. The silicon level was then ranged from 0 to 3 wt%. The iron content was simultaneously balanced to keep the mass of the system constant. Calculations were first performed at 600°C , where Laves phase is not an equilibrium phase for this steel with the usual silicon level. It was found that even at the highest silicon level Laves phase was still not predicted to be an equilibrium phase. The calculation was then repeated for 500°C, at which temperature Laves phase is predicted as an equilibrium precipitate. In this case the way the amount varies with silicon content is shown in Figure 5.2.

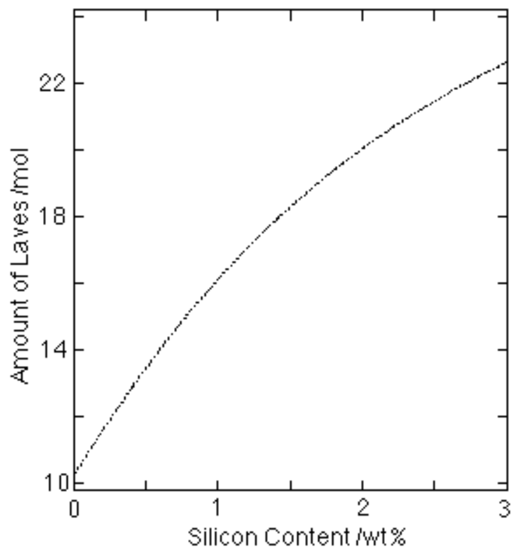

Figure 5.2: The effect of increasing the silicon level on the predicted equilibrium amount of Laves phase in a 10Cr–1.55 wt% Mo alloy (COST F) at 500°C

Figure 5.2 shows that at 500°C it is predicted that adding silicon leads to an increase in Laves phase, which doubles on going from 0 to 2 wt% silicon. The composition and equilibrium volume fractions of Laves phase, ferrite and $M_{23}C_6$ for two cases, high and low silicon are shown in Table 5.2.

It can be seen from these tables that MTDATA does not predict any partitioning of silicon into Laves phase. However, this is most probably due to the fact that there are no data available for this element in this phase. In reality, it may be that some silicon does partition into Laves phase, but to date there is no evidence either way. Nevertheless, the atomic fraction of Laves phase is still increased by silicon. One possible explanation is that silicon additions effect the amount of carbide which forms. It can be seen that in the high silicon alloy, the fraction of $M_{23}C_6$ is reduced. This will increase the molybdenum available for Laves phase formation. Also the addition of silicon to ferrite is predicted to reduce the molybdenum fraction in the matrix by a disproportionate amount, and this will again lead to an increased amount of Laves phase. The MTDATA calculations therefore seem consistent with the hypothesis that silicon increases the amount of Laves phase which forms. It may also be that silicon plays an important role in the kinetics of Laves phase precipitation which cannot be investigated with

(a)

Phase	Fe	Cr	Mo	Si	N_{eq}
Ferrite	0.88901	0.09532	0.00391	0.00020	0.9662
$M_{23}C_6$	0.03561	0.65418	0.10331	0.00000	0.0246
Laves Phase	0.50968	0.15698	0.33333	0.00000	0.0057

(b)

Phase	Fe	Cr	Mo	Si	N_{eq}
Ferrite	0.83596	0.09111	0.00150	0.06014	0.9596
$M_{23}C_6$	0.02438	0.66540	0.10332	0.00000	0.0238
Laves Phase	0.45740	0.20926	0.33333	0.00000	0.0122

Table 5.2: The composition (in atomic fraction) and equilibrium mole fraction (N_{eq}) of the phases in a 10CrMoV steel (COST F) at 700°C, (a) corresponds to the case when the silicon content of the alloy is 0.1 wt% and (b) when the silicon content is 3 wt%.

MTDATA.

5.5 The Effect of Laves Phase Precipitation on the Matrix Composition

It has been suggested that one reason why Laves phase formation is deleterious to mechanical properties is that it dramatically reduces the tungsten and molybdenum in solid solution in the ferrite. MTDATA was used to investigate how much Laves phase depletes the matrix of these elements compared to $M_{23}C_6$ which is the dominant carbide. First, calculations were performed when Laves phase was suppressed to determine the solute depletion due to the carbides. Then Laves phase was allowed to exist and calculations were performed to obtain the solute depletion level when Laves phase is present. For the investigation of molybdenum depletion the COST F alloy (with 10Cr–1.89Mo wt%) composition was used. The resultant molybdenum content in the ferrite is plotted against temperature in Figure 5.3.

It can be seen that at lower temperatures, where the equilibrium volume fraction of Laves phase is greatest, the depletion of molybdenum when Laves phase is present is substantial. The depletion due to $M_{23}C_6$ formation is, at these lower temperatures, considerably smaller than that due to Laves phase. The two lines converge at approximately 650°C, since at and above this temperature Laves phase is no longer an equilibrium precipitate. To investigate tungsten depletion the composition used was that of COST alloy D which contains approximately 2 wt% tungsten. The results are shown in Figure 5.4, and it can be seen that the same trend as in the molybdenum alloy is predicted. Note that in this alloy Laves phase is predicted as an

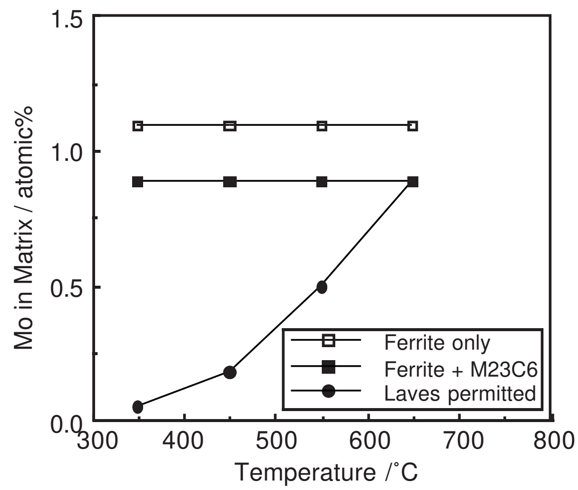

Figure 5.3: The effect of Laves phase formation on the molybdenum level in ferrite in COST alloy F (10Cr–1.8 wt% Mo). Lines are plotted corresponding to the bulk molybdenum concentration (when only ferrite is allowed to exist), for the case where ferrite and $M_{23}C_6$ are permitted phases, and also for the case when Laves phase is also permitted.

equilibrium precipitate up to approximately 700°C. Comparing the depletion at the operating temperature for which these steels are designed (around 600°C) it is apparent that in alloy F the effect of Laves phase on the depletion of molybdenum is comparable with that of $M_{23}C_6$ since at this temperature the equilibrium volume fraction of Laves phase is small. However, at the same temperature in the tungsten containing alloy the predicted depletion due to Laves phase is much larger than that due to $M_{23}C_6$, and this may be attributed to the greater equilibrium volume fraction of Laves phase in this steel. It may be concluded that for alloys where Laves phase is stable to relatively high temperatures precipitation of this phase can significantly deplete the matrix at the operating temperature.

5.6 Relative Phase Stabilities

As mentioned previously, MTDATA can be used to predict the relative stability of the possible phases by successively setting the most stable precipitate phase absent and recalculating the next most stable configuration. The order of phase stabilities gives an indication of the probable precipitation sequence. This is because each step in the sequence is driven by the reduction in the overall Gibbs free energy caused by precipitating the new phase. It is only a probable sequence because for it to hold the kinetics of precipitation must increase as the phase stability decreases otherwise the least stable phases will not form at all. However, this is often the case as a result of the mechanisms of formation of the metastable phases. For example cementite

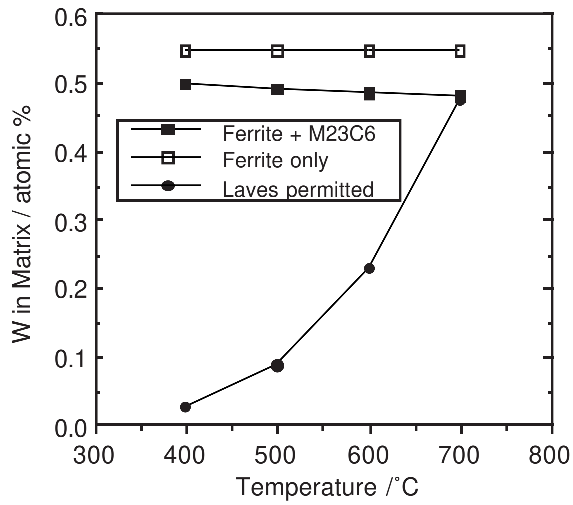

Figure 5.4: The effect of Laves phase formation on the tungsten level in ferrite in COST alloy D. Lines are plotted corresponding to the bulk tungsten concentration (when only ferrite is allowed to exist), for the case where ferrite and $M_{23}C_6$ are permitted phases, and also for the case when Laves phase is also permitted.

will always forms more rapidly than $M_{23}C_6$.

Calculations were performed to deduce the relative stabilities of the carbides at 600°C in a 10CrMoV steel (COST F) and a $2\frac{1}{4}$Cr1Mo alloy. The results are summarised in Table 5.3

	10CrMoV	$2\frac{1}{4}$Cr1Mo
Equilibrium	$M_{23}C_6$	$M_{23}C_6$
2nd most stable	M_2X	M_7C_3
3rd most stable	Cementite	Cementite

Table 5.3: MTDATA calculation of the order of carbide stability in a 10CrMoV steel and a $2\frac{1}{4}$Cr1Mo steel at 600°C

The order of carbide stability predicted by MTDATA is broadly consistent with the observed sequence of precipitates. Note, however that in the $2\frac{1}{4}$Cr1Mo alloy M_7C_3 is predicted to be the next most stable phase after cementite, whereas in practice M_2X is observed prior to M_7C_3 precipitation. The reason for this discrepancy is the mechanism by which cementite forms. The calculations rely purely on the minimisation the Gibbs free energy, *i.e.* it gives the equilibrium composition. Cementite is initially far from this composition however due it paraequilibrium transformation mechanism. Because of this its Gibbs free energy will be greater than that predicted by MTDATA, and there will be the potential for the free energy of the system to be reduced by M_2X formation. Although cementite enriches, reducing its free energy it does so at a slow rate which allows time for M_2X precipitation. Experimental composition measurements [Thomson, 1992] are consistent with the hypothesis that cementite never reaches the equilibrium composition predicted by MTDATA (Table 5.4) because other alloy carbides precipitate which are more stable than the partially enriched cementite. These results suggest that if cementite were to form with its equilibrium composition in these steels then M_2X would not precipitate since it is less stable.

	Fe	Cr	Mn	Mo
Equilibrium	0.38734	0.34399	0.01259	0.00577
Paraequilibrium	0.71569	0.01700	0.00408	0.00380

Table 5.4: Equilibrium concentrations (atomic fraction) of the principle alloying elements in cementite, calculated for a $2\frac{1}{4}$Cr1Mo steel at 600°C using MTDATA and the paraequilibrium concentration

5.7 Effect of Chromium Level on M_2X Composition

M_2X is a phase which is often observed in a wide range of power plant alloys containing chromium and molybdenum. In low chromium steels it is molybdenum–rich with a composition close to the ideal Mo_2C composition [Baker and Nutting, 1959]. In the advanced 9-12 wt% chromium steels containing nitrogen experiments have shown that M_2X is closer in composition to Cr_2N than Mo_2C [Sanderson, 1977]. MTDATA was used to calculate the equilibrium M_2X composition for a range of chromium levels to ascertain the level at which M_2X changes from a molybdenum to a chromium rich phase. The plotted composition of the M_2X in equilibrium with ferrite at 600°C is shown in Figure 5.5 for the COST F alloy with a chromium level between 0 and 12 wt%

It can be seen that for this particular steel the M_2X phase becomes dominated by chromium when the bulk chromium level is as little as 2 wt% . Note that when there is no chromium present, the molybdenum concentration in M_2X is still short of the value expected for stoichiometric Mo_2X. This is because MTDATA predicts significant quantities of iron, vanadium and niobium in the M_2X when no chromium is present.

In practice the composition of M_2X will be modified by the presence of other precipitates, such as cementite, and later on possibly M_7C_3 and $M_{23}C_6$. In general these phases are chromium rich resulting in a lower chromium level in the M_2X than that predicted here.

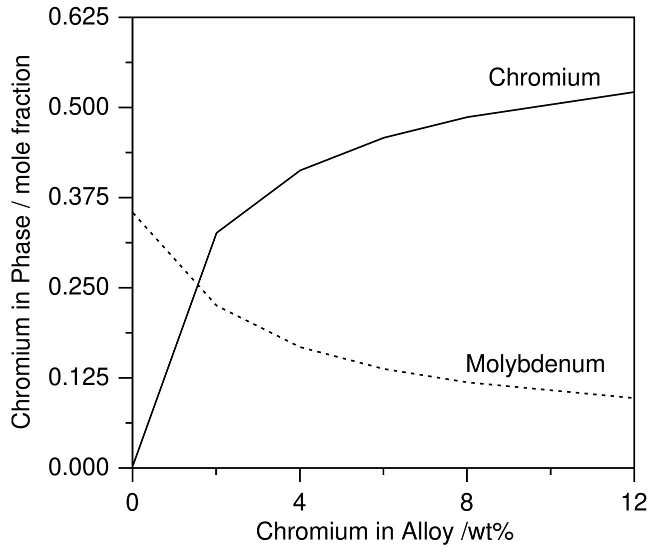

Figure 5.5: The concentration of chromium and molybdenum in M_2X in a xCr–1.24Mo–0.18V steel (COST F with different chromium levels)

5.8 Summary

MTDATA, a computer program which uses critically assessed thermodynamic data to calculate phase equilibria has been used to make predictions for power plant steels.

It has been shown that Laves phase is stabilised by adding tungsten and molybdenum, with the former increasing the equilibrium volume fraction of Laves phase to a greater extent than latter. In turn, the formation of Laves phase can significantly deplete the matrix tungsten and molybdenum levels and would therefore be expected to reduce the solid solution strengthening contribution from these species.

The order of phase stabilities and hence likely precipitation sequences have been predicted for both a 10CrMoV alloy and a $2\frac{1}{4}$Cr1Mo alloy at 600°C. In general the predicted and observed sequences are in good agreement. A notable exception is that it is predicted that cementite is more stable than M_2X in which case M_2X would not be expected to be observed. This contradicts experiment and the explanation lies in the fact that cementite does not ever reach the equilibrium composition predicted by MTDATA.

It has been predicted that the solubility of chromium in M_2X is high and this phase may be dominated by chromium rather than molybdenum when the bulk chromium level is as little as 2 wt% .

CHAPTER SIX

Simple Kinetic Models

This chapter describes the development of models for the kinetics of precipitation in power plant steels. The way growth and nucleation are calculated for the various precipitate phases is described. Classical kinetic theory has been used to make predictions for the overall transformation kinetics. The shortcomings of this theory in describing the precipitation in power plant steels is discussed.

6.1 Introduction

It has been demonstrated that MTDATA is a powerful tool for the computation of equilibrium phase compositions in complex systems. With the exception of cementite experimental measurements have shown that the precipitates in power plant steels form close to their equilibrium compositions. In these cases the MTDATA calculation gives good agreement with the measured composition. Although MTDATA calculations can provide useful information in their own right, perhaps the most exciting use of these predictions is by using them as inputs to a kinetics model so that the time dependence of the microstructure can also be determined.

The philosophy behind the development of a kinetics model was to start with the simplest possible assumptions, compare experimental and predicted results, and introduce additional complications where necessary. The remainder of this chapter describes the early attempts to model the kinetics using some very simple assumptions. In some cases good agreement is found between predictions and experiments. In other cases agreement is poor, and the reasons for this will be discussed.

6.2 Diffusion Coefficients

A knowledge of the appropriate diffusion coefficients is required in all the equations for diffusion controlled transformations. In this work the intrinsic chemical diffusion coefficients due to Fridberg *et al.* (1969) are used. The overall diffusion coefficient is given by

$$D = D_0 \exp\left(\frac{-Q}{RT}\right) \tag{6.1}$$

Fridberg states the values for the self–diffusion of iron in austenite and ferrite are

$$D_0^\gamma = 1.6\,\mathrm{cm^2 s^{-1}} \text{ and } Q^\gamma = 240 \times 10^3\,\mathrm{J\,mol^{-1}} \tag{6.2}$$

$$D_0^\alpha = 0.5\,\mathrm{cm^2 s^{-1}} \text{ and } Q^\alpha = 240 \times 10^3\,\mathrm{J\,mol^{-1}} \tag{6.3}$$

The intrinsic diffusion coefficients of the various alloying elements in ferrite are then determined by comparison with the self–diffusion of iron, the difference being described by a factor which is independent of temperature. These diffusion coefficients refer to the interdiffusion of the alloying elements in a binary system, *i.e.* of chromium in ferrite *etc*, and therefore do not strictly relate to diffusion in a multicomponent system. The values of the interdiffusion coefficients used in this work are shown in Table 6.1.

Element	$D_0/\mathrm{m^2 s^-1}$	$Q/\mathrm{J\,mol^{-1}}$
Cr	1.5×10^{-4}	240×10^3
Mo	1.1×10^{-4}	240×10^3
W	1.3×10^{-4}	240×10^3
V	1.5×10^{-4}	240×10^3
Nb	1.3×10^{-4}	240×10^3

Table 6.1: Chemical interdiffusion coefficients of element in ferrite (Fridberg *et al.* ~1969.

6.3 Modelling the Enrichment of Cementite

It has already been stated that in these steels cementite forms by a paraequilibrium transformation mechanism which involves partitioning of the interstitial but not the substitutional species. As a consequence the growth of cementite is extremely rapid compared to that for the other precipitates. For the purposes of this work it was assumed that the cementite forms instantly on tempering with the paraequilibrium composition. This is reasonable since experiments show that the time taken for cementite precipitation in negligible when compared to the time for the other phases [Baker and Nutting, 1959]. Using this assumption eliminates the need to model the growth of cementite. The subsequent enrichment requires the diffusion of substitutional atoms and therefore takes place over a much longer timescale. The way in which the composition of cementite changes as a function of time has been modelled by Bhadeshia (1989). The time t_c for a cementite plate of thickness d to reach a composition c_t is given by

$$t_c^{\frac{1}{2}} = \frac{d(\bar{c} - c_t)\pi^{\frac{1}{2}}}{4D^{\frac{1}{2}}(c^{\alpha\theta} - \bar{c})} \tag{6.4}$$

This equation shows the time dependence of the concentration obeys a $t^{\frac{1}{2}}$ law which is consistent with published experimental data. It can also be seen that as the plate thickness is reduced the rate of enrichment increases implying that the carbide composition is dependent on its size. For the purposes of a predictive model it was assumed that all the plates have the same thickness. Study of cementite particles in both COST F 10CrMoV steel and $2\frac{1}{4}$Cr1Mo steel (Thomson, 1992) showed that a typical thickness was $\simeq 30$ nm.

The calculation of solute depletion removed from the ferrite as cementite enriches requires a knowledge of the cementite volume fraction and number density of particles. The volume fraction of cementite is limited by the amount of available carbon in the alloy. The carbon content of the ferrite may reasonably be approximated to zero in which case conservation of mass gives the volume fraction of cementite as

$$V_\theta = \frac{\bar{c}}{c^{\theta\alpha}} \text{ with } c^{\theta\alpha} \simeq 0.25 \tag{6.5}$$

The method to find the number density of particles follows that of Takahashi and Bhadeshia [1990]. The average grain size of cementite (in μm) before any Ostwald ripening is given as a function of the tempering temperature by an empirical relationship due to Venugopalan and Kirkaldy [1978]

$$r_0^3 = (2.26 - 6.4 \times 10^{-3}T + 4.6 \times 10^{-6}T^2)V_\theta \times 10^{-3}\,\mu\text{m} \tag{6.6}$$

where T is the tempering temperature in °C and V_θ is the volume fraction of cementite. The number of cementite particles per unit volume may then be written

$$N_0 = \frac{V_\theta}{\frac{4}{3}\pi r_0^3} \tag{6.7}$$

where V_θ is now taken to be the equilibrium volume fraction of cementite.

6.4 Growth of M_2X

M_2X is usually the first precipitate to form after cementite. Because it is important in secondary hardening of $2\frac{1}{4}$Cr1Mo and other power plant steels its precipitation has been studied extensively and this provides experimental data with which to validate any model. M_2X grows as needles, which in the absence of soft impingement are expected to have a constant growth rate (section 3.5.3). Hall *et al.* (1972) have studied the growth kinetics of Mo_2C needles in an Fe–1.95Mo–0.11 wt% C alloy. They measured the needle tip radius and growth rate of the longest needles in samples tempered at 750, 700, 650 and 600°C. This temperature range results in growth rates which span several orders of magnitude. The aim of their work was to demonstrate that the growth of Mo_2C occurs wholly within the ferrite phase. They did this by assuming that the growth rate could be related to the diffusion coefficient of molybdenum in ferrite using the Zener–Hillert equation (section 3.5.3). They then showed that the diffusion coefficient calculated in this way is equal to that of molybdenum in ferrite. By assuming that $m = r$, $c_r^{\alpha\beta} \simeq c^{\alpha\beta}$ and $r = 2r_c$ (from the maximum growth rate hypothesis) the Zener–Hillert equation for the growth rate of needles may be written as

$$v = \frac{3D(\bar{c} - c^{\alpha\beta})}{8r(c^{\beta\alpha} - \bar{c})} \tag{6.8}$$

Hall *et al.* found the value of $c^{\alpha\beta}$ by X–ray measurement of the lattice parameter after prolonged annealing at the appropriate temperature. With the appropriate value for the diffusion coefficient good agreement was found between the measured growth rates and those predicted by this expression.

Attempts have been made to reproduce these results using MTDATA to calculate the concentrations of molybdenum in the ferrite and Mo_2C. Both the Zener–Hillert and the simpler Zener theory were used to calculate the growth rates. The radius of curvature of the needles r was found using the assumption that $r = 2r_c$, and that the critical radius of curvature is given by equation 3.22. To calculate this critical radius requires computation of the capillarity constant (equation 3.23). This is a function of composition, volume increase of Mo_2C per added atom and interfacial energy of Mo_2C. The composition terms were calculated using MTDATA and the volume increase per addition atom was deduced from the unit cell volume, knowing that each cell contains one Mo_2C formula unit. The interfacial energy for Mo_2C is unknown and so the value for cementite was used. This is given by Puls and Kirkaldy (1972) as being equal to 0.6 Jm^{-2}.

Table 6.2 shows a comparison between the measured levels of molybdenum in ferrite in equilibrium with Mo_2C and the levels calculated using MTDATA. Figure 6.1 shows a comparison of the predicted needle tip radius and that measured by Hall *et al.*

Temperature/°C	$c^{\alpha\beta}$ Measured	$c^{\alpha\beta}$ Predicted
650	0.0000±0.0005	0.00137
700	0.0005±0.0008	0.00230
750	0.0040±0.0020	0.00321

Table 6.2: A comparison of the measured molybdenum concentration in ferrite in equilibrium with Mo_2C and the concentration calculated using MTDATA.

It can be seen from Table 6.2 that the measured molybdenum content of the ferrite in equilibrium with Mo_2C is less than that predicted by MTDATA at 650 and 700 °C whilst at 750°C the measured level is greater. Figure 6.1 shows that the radii predicted using the calculated compositions are less than the measured radii, although the error in the experimental data may be greater than that indicated since tip radii are, in practice, difficult to measure and define. Figure 6.2 shows a plot of the measured growth rate against the predicted rate according to the Zener–Hillert and Zener models. The agreement over a wide range of growth rates is reasonably good. Note that in this case the growth rates predicted by the two models differ by an approximately constant factor. This can be demonstrated by dividing the two

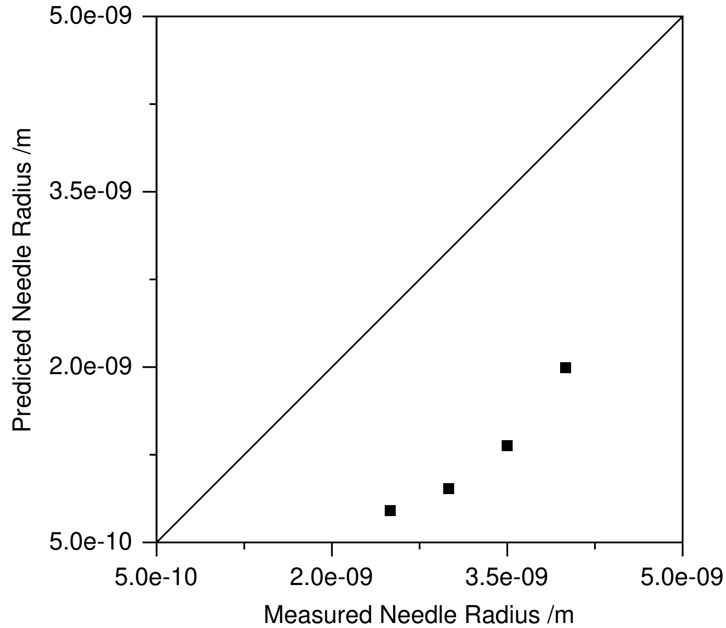

Figure 6.1: A comparison of the measured Mo_2C tip radius and that calculated using phase compositions predicted by MTDATA and the assumption that the needles grow at the maximum rate so that the observed radius of the longest needles is twice the critical radius

expressions and making the substitution $r = 2r_c$. This gives

$$\frac{v_{Zener-Hillert}}{v_{Zener}} = \frac{\frac{3D}{16r_c}\left(\frac{\bar{c}-c^{\alpha\beta}}{c^{\beta\alpha}-\bar{c}}\right)}{\frac{D}{4r_c}\left(\frac{\bar{c}-c^{\alpha\beta}}{c^{\beta\alpha}-c^{\alpha\beta}}\right)} = \frac{3}{4}\left(\frac{c^{\beta\alpha}-c^{\alpha\beta}}{c^{\beta\alpha}-\bar{c}}\right) \text{ note that } \frac{c^{\beta\alpha}-c^{\alpha\beta}}{c^{\beta\alpha}-\bar{c}} \simeq 1 \tag{6.9}$$

This model was then used to make predictions for the M_2X growth rate in COST F alloy (now assuming growth is controlled by chromium rather than molybdenum diffusion) and these were compared with the measured rate (see section 4.4.4). Table 6.3 gives a comparison of the measured and predicted growth rates and tip radii at 600°C.

	Observed	Predicted
COST F, v/Ås^{-1}	0.12	0.00079
r/Å	38	913.2

Table 6.3: A comparison of measured and predicted growth rates and tip radii for two alloys at 600°C.

It can be seen that the predicted growth rate is too low by over two orders of magnitude. This is a consequence of the predicted tip radius being unreasonably high. This contrasts with

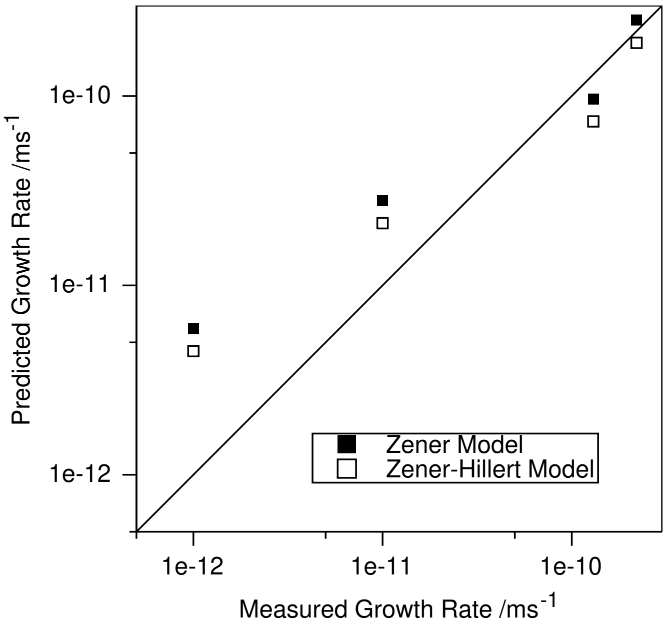

Figure 6.2: A comparison of predicted and measured growth rates in a Fe–1.95Mo–0.11 wt% C alloy (experimental data due to Hall *et al.* 1972)

the predicted tip radii in the chromium–free steel which were too small. This suggests that the discrepancy is not due to a large error in the value of the interfacial energy, which would affect all the predictions in the same way, but is most probably due to the multi–component nature of growth. This may be demonstrated by using other species to calculate the tip radius. Ideally, the predicted radius should be independent of the composition used to calculate it, but it can be seen from Table 6.4 that this is not the case using the equilibrium compositions predicted by MTDATA. It can be seen that the critical radii calculated using the substitutional species are too large, whilst those calculated using the interstitial species are too small

	Cr	Fe	Mo	C	N
r Å	913.2	230.1	1039.4	0.318	0.170

Table 6.4: Predicted tip radii for M_2X precipitation in COST F steel at 600°C. Using the equilibrium concentrations predicted by MTDATA leads to different predicted radii for each species.

To rigorously determine the correct radii requires an evaluation of the compositions by simultaneously solving the growth equations (as described in section 3.6). This is beyond the scope of the model developed here where it is assumed that one species controls growth so that problem is reduced to that for a binary system. To overcome this discrepancy the critical radius was fixed at a constant value. This value was chosen to give the best agreement between the predicted and measured growth rates in the COST F alloy. The predicted and measured growth rates for both the COST F and Fe–1.95-0.11 wt% C alloys using the optimized critical radius are shown in Table 6.5. The predicted and measured growth rates for the Fe–1.95–0.11 wt% C alloy are within an order of magnitude using the fixed value of the critical radius. This assumption is therefore reasonable for the range of compositions used in this work.

Alloy	r_c/Å	v_{obs}/Ås^{-1}	v_{pred} /Ås^{-1}
COST F	3	0.12	0.1200
Fe–1.95Mo–0.11 wt% C	3	0.01	0.0731

Table 6.5: Predicted and measured growth rates at 600°C for COST F and Fe–1.95Mo–0.11 wt% C alloys using a fixed value for the critical radius.

6.5 Overall Kinetics of M_2X

Once the growth rate of M_2X was calculated attempts were made to model the overall precipitation kinetics assuming precipitation is independent of the precipitation kinetics of other phases. The first attempt to do this involved making the simplest possible assumption, that there are a constant number of pre-existing nucleation sites. In this case the evolution volume fraction will be controlled by growth alone.

6.5.1 Assuming a Constant Number of Pre–Existing Nuclei

If there are a constant number of pre–existing nuclei then, following the Avrami approach outlined in section 3.3, the dependence of volume fraction on time may be written

$$\zeta = 1 - \exp - \left(\frac{c^{\beta\alpha} - c^{\alpha\beta}}{\bar{c} - c^{\alpha\beta}} \left(\frac{N_0 \pi v^3 t^3}{4\phi^2} \right) \right) \tag{6.10}$$

where Ω is the supersaturation. N_0 is the number of particles per unit volume. This is unknown, as a starting value the same number density was used as that for cementite (see section 6.3). ϕ is the M_2X needle aspect ratio. Measurements of needle aspect ratios from micrographs published by Honeycombe (1974) and Hall *et al.* (1972) are shown in Table 6.6. The average aspect ratio was found to be approximately 15 .

Calculations were performed for the $2\frac{1}{4}$Cr1Mo steel and COST F. The predicted evolution of the volume fraction of M_2X at 600°C is shown in Figure 6.3.

With this model it is predicted that the kinetics are similar for both steels. This contradicts the experimental evidence which show that M_2X precipitation is much slower in the $2\frac{1}{4}$Cr1Mo

Width measured on micrograph / mm	Length measured on micrograph /mm	ϕ
31.0	2.0	15.5
25.0	1.5	16.7
27.0	2.0	13.5
15.0	1.0	15.0
19.0	1.5	12.6
17.0	1.0	17.0

Table 6.6: Measured M_2X needle aspect ratios

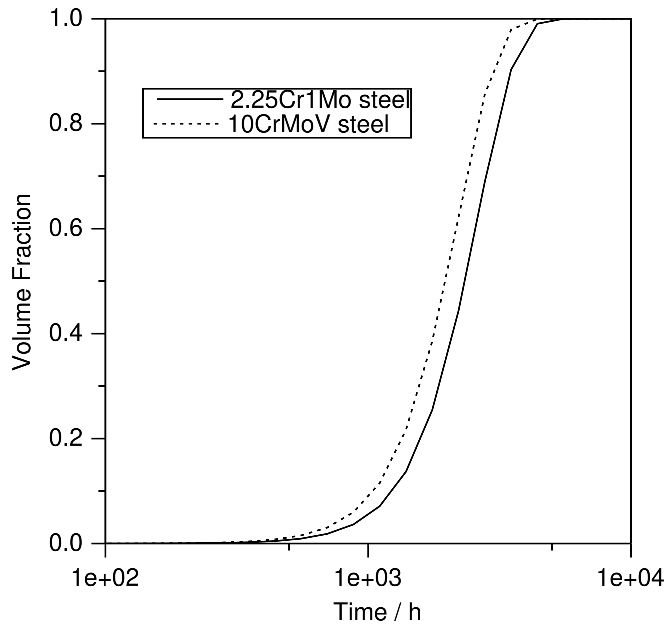

Figure 6.3: The predicted evolution of M_2X volume fraction at 600°C in a $2\frac{1}{4}$Cr1Mo steel and COST F (10CrMoV).

steel than COST F. For example, at this temperature Baker and Nutting (1959) observed M_2X after 5 h in the $2\frac{1}{4}$Cr1Mo alloy, whereas in COST F M_2X was observed after 10 mins (section 4.4). This implies the differences in the kinetics observed in the two steels cannot be attributed solely to differences in the M_2X growth rates. The predicted growth rates are shown in Table 6.7 and it can be seen that the difference in the growth rate is small. From this it is concluded that nucleation as well as growth must be accounted for to correctly predict the large difference observed in the two steels.

6.5.2 Assuming a Constant Nucleation Rate

The simplest way of incorporating nucleation into the model is to assume M_2X precipitates

Alloy	v_{pred} /Ås^{-1}
COST F	0.1200
$2\frac{1}{4}$Cr1Mo	0.1032

Table 6.7: Predicted growth rates at 600°C for COST F and $2\frac{1}{4}$Cr1Mo alloys.

with a constant nucleation rate. The nucleation rate is given from classical nucleation theory (section 3.8) as

$$I = N_0 \frac{kT}{h} \exp\left(\frac{G^* + Q}{kT}\right) \tag{6.11}$$

where the energy barrier to nucleation G^* is given by

$$G^* = \frac{16\pi\sigma^3}{3\Delta G_v^2} \tag{6.12}$$

To evaluate the nucleation rate values must be found for the site density, N_0, the interfacial energy per unit area, σ, and the driving force for nucleation ΔG_v.

The formation of M_2X was assumed to be complementary to the dissolution of M_3C so the reaction to be considered is

$$\alpha + M_3C \rightarrow \alpha' + M_2X$$

Where α and α' refers to the ferrite coexisting with M_3C and M_2X respectively. The free energy change for this transformation was calculated by using MTDATA to calculate the equilibrium free energies for the $\alpha + M_3C$ and the $\alpha' + M_2X$ system and computing the difference. The predicted free energy change for the $2\frac{1}{4}$Cr1Mo steel is shown in Figure 6.4. According to this plot the driving force for M_2X precipitation is zero above 725°C and so M_2X would not be expected. This contradicts observations which show that M_2X is present at 750°C and above. The discrepancy may arise from the incorrect assumption that M_3C has its equilibrium composition when M_2X forms.

The driving force was therefore re–calculated assuming cementite of the paraequilibrium composition. The driving force is significantly increased and, consistent with experiment, M_2X formation is possible across the whole temperature range.

This is the overall free energy change for the reaction, not the free energy change for nucleation (section 3.3). The latter may be estimated from ΔG_0 as illustrated (Figure 6.5) which is for a phase β precipitating from α. The free energy for β nucleation, ΔG_n, is given by the distance PR. It will depend on the curvature of the α free energy curve at the point

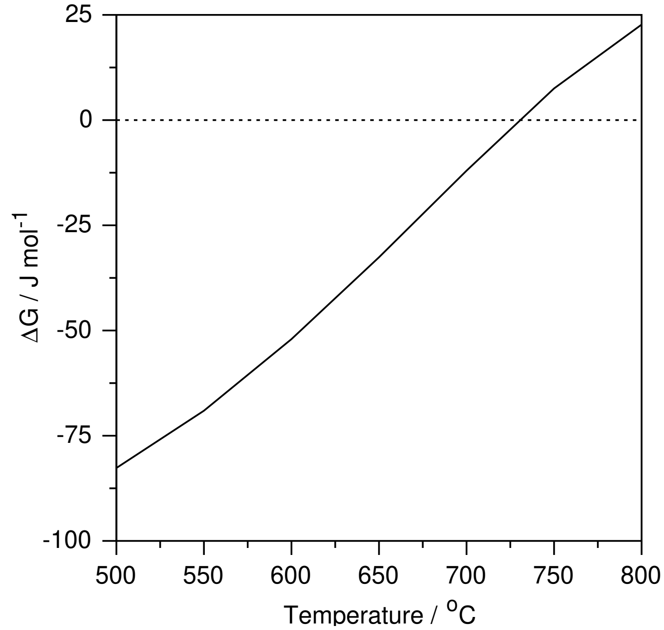

Figure 6.4: The driving force for M_2X precipitation assuming that cementite is at its equilibrium composition when M_2X forms.

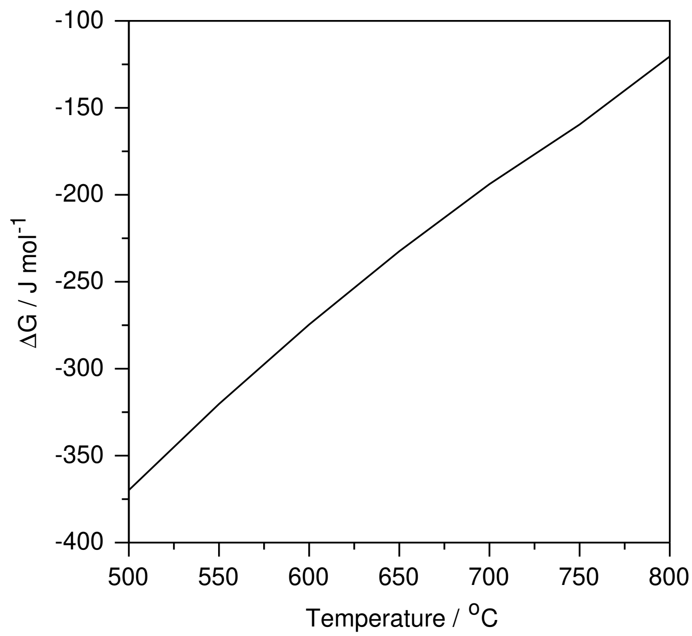

Figure 6.4: The driving force for M_2X precipitation assuming that cementite is at its paraequilibrium composition when M_2X forms.

U. QR may provide a sufficiently accurate approximation to ΔG_n which by similar triangles is given as

$$QR = \frac{RT}{ST} US \tag{6.13}$$

The equilibrium fraction of β, V_β^{eq} is given by the ratio $\frac{ST}{RT}$ so that

$$QR = \frac{\Delta G_0}{V_\beta^{eq}} \simeq \Delta G^n \tag{6.14}$$

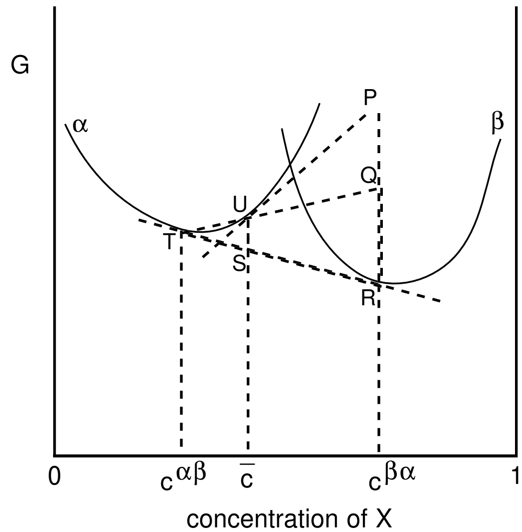

Figure 6.5: Schematic free energy curves for a phase β nucleating in a matrix α showing an approximate method for determining the driving force for nucleation.

If the curvature of the α free energy curve is small at the composition being considered then this approximation will be good. The free energy curves for ferrite and M_2X in an Fe–Cr–C system are shown in Figure 6.6 (projected down the carbon composition axis). The mean composition for a 10 wt% Cr steel is marked. In this case the approximate method gives a driving force which is approximately half that of the usual method. Bearing in mind that the whole treatment is a crude approximation, with factors such as capillarity effects being ignored, this agreement is tolerable. The interfacial energy, which appears in the same term as the free energy change in the nucleation equation has to be obtained by fitting, which has the effect of concealing the error in the free energy term.

The variation of M_2X volume fraction with time (normalised with respect to the equilibrium fraction) is then given by the Avrami method as

$$\zeta = 1 - \exp\left[-\left(\frac{c^{\beta\alpha} - c^{\alpha\beta}}{\bar{c} - c^{\alpha\beta}}\left(\frac{\pi v^3 I t^4}{16\phi^2}\right)\right)\right] \tag{6.15}$$

Predictions were made for the $2\frac{1}{4}$Cr1Mo and COST F alloys for a range of temperatures. These results were then combined to make a TTT diagram by plotting points corresponding

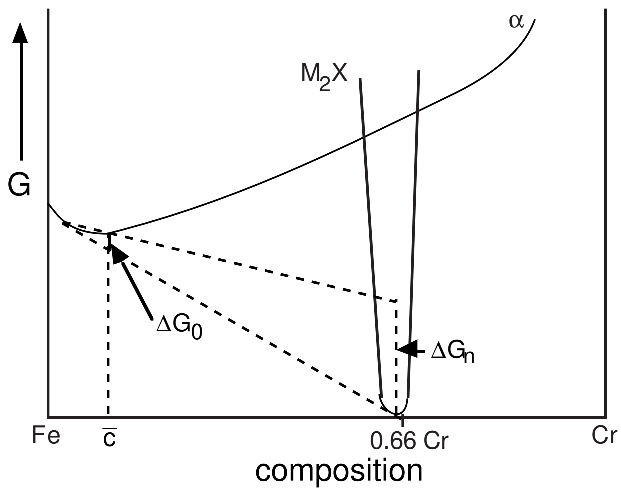

Figure 6.6: Free energy curves for ferrite and M_2X in the Fe–Cr–C system showing the construction used to find the driving force for nucleation.

to a constant volume fraction at each temperature. It is reasonable to suppose that Baker and Nutting first observed M_2X when the absolute volume fraction $\simeq 0.01$. Lines plotted for a predicted volume fraction of 1% were compared with the experimental data. The values of the interfacial energy and site density terms in the nucleation equation were adjusted to give the best fit between the predicted and experimental data. Figure 6.7 shows the best fit values and the TTT diagram produced. The validity of comparing the predicted line for a constant volume fraction with the measured line corresponding to when M_2X was first observed is questionable, since the experimental line is likely to correspond to a range of volume fractions. It can be stated that the form of the predicted and measured curves are similar in that an increase in temperature leads to faster kinetics over the range for which observations have been made. Note that at higher temperatures it is predicted that a "nose" is expected in the TTT curve, with kinetics slowing as temperature is increased above $\simeq$725°C. Further experiments would be required to confirm this.

6.6 Overall Kinetics of $M_{23}C_6$

$M_{23}C_6$ is the predominant carbide in the 9–12wt% Cr steels where it is an equilibrium phase. Its particles have an equiaxed morphology which for the purposes of modelling are assumed to be spherical. Following the procedure used to model M_2X attempts were made to predict its precipitation kinetics starting first with a simple model and then increasing the complexity as required.

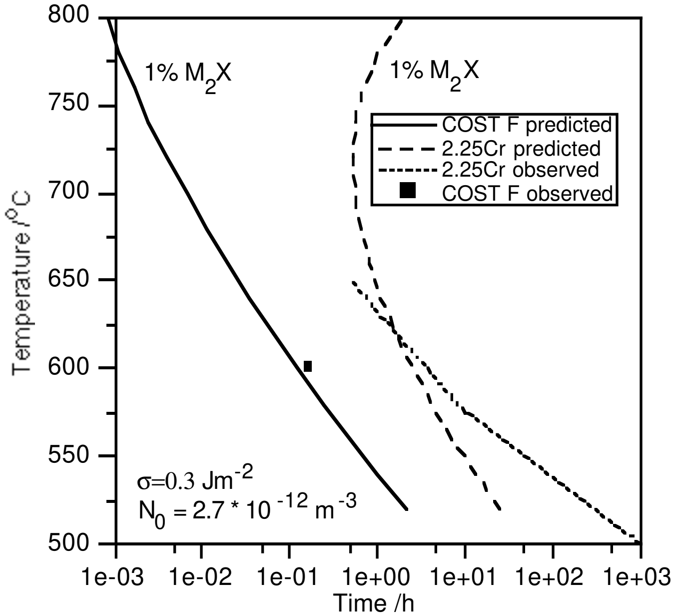

Figure 6.7: Best fit predicted TTT lines for 1% transformation in $2\frac{1}{4}$Cr1Mo and COST F alloys. Also shown is the measured line for the $2\frac{1}{4}$Cr1Mo alloy, corresponding to when M_2X was first observed, and data point for COST F corresponding to an observed volume fraction of 1%. The best fit values of the interfacial energy, σ, and site density, N, are as shown.

6.6.1 Constant Number of Pre–Existing Nuclei

If there are a constant number of pre–existing nuclei then the evolution of volume fraction may be calculated using the Wert and Zener [1950] model (section 3.9.2) which incorporates soft–impingement effects.[1] A constraint is that the model is only valid for low supersaturations. The supersaturation of chromium with respect to $M_{23}C_6$ for three steels is shown in Table 6.8 from which it can be seen that in each case this model is appropriate. The final steel shown in this table is a 18Cr–12Ni–2.5 wt% Mo austenitic steel. This is included because there are quantitative quantitative data on $M_{23}C_6$ precipitation [Lai and Meshkat, 1978].

Alloy	$\bar{c}$	$c^{\alpha\beta}$	$c^{\beta\alpha}$	Ω
COST F	0.1089	0.0961	0.6163	0.0252
$2\frac{1}{4}$Cr1Mo	0.0227	0.0120	0.3302	0.0336
18Cr–12Ni–2.5Mo	0.1765	0.1687	0.6646	0.0158

Table 6.8: Composition and supersaturation of chromium in $M_{23}C_6$ at 600°C.

[1] Because $M_{23}C_6$ precipitation is here being modelled in isolation the soft impingement between $M_{23}C_6$ and any other phase such as M_2X cannot be treated.

$$\frac{3}{2}C^{\frac{2}{3}}t = \frac{1}{2}\ln\left(\frac{1+z+z^2}{1-z^2}\right) + \sqrt{3}\arctan\frac{-\sqrt{3}z}{2+z} \text{ where } \zeta = z^3 \tag{6.16}$$

with

$$C^{\frac{2}{3}} = \frac{2(\bar{c}-c^{\alpha\beta})D}{(c^{\beta\alpha}-c^{\alpha\beta})(r^f)^2} \tag{6.17}$$

Equation 3.55 describes the variation of volume fraction with time. A knowledge of the final size of the $M_{23}C_6$ particles, r_f, is required. This may be expressed in terms of the final (assumed to be equilibrium) volume fraction and the number density of particles as

$$r_f = \sqrt[3]{\frac{3V_\beta^{eq}}{4\pi N_0}} \tag{6.18}$$

where V_β^{eq} is the equilibrium volume fraction of the β phase and N_0 is the number of β particles per unit volume.

The number of particles, N_0, is unknown but was assumed to be the same as cementite. Predictions were first made for the austenitic 18Cr–12Ni–2.5 wt% Mo steel for which volume fraction *vs* time data are available. The agreement is reasonable (Figure 6.8).

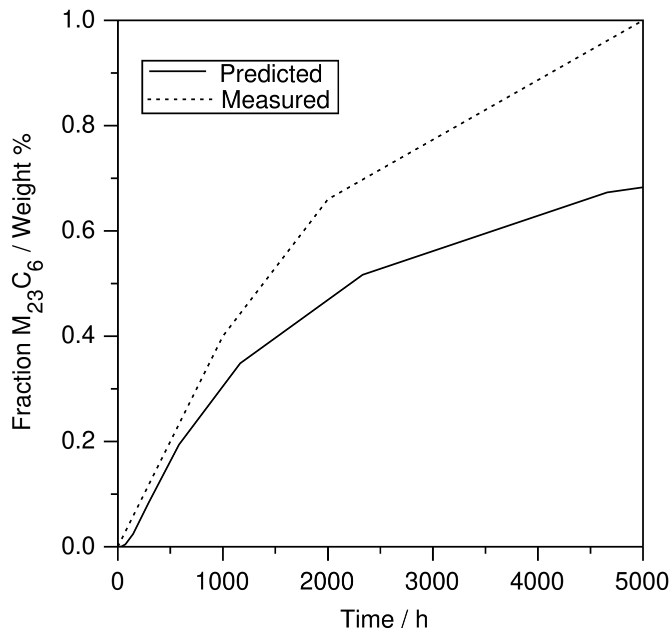

Figure 6.8: Evolution of $M_{23}C_6$ in a 18Cr–12Ni–2.5 wt% Mo alloy showing the measured line due to Lai and Meskat [1978] and the line predicted using the Wert and Zener model for transformation kinetics.

The model was then used to make predictions for COST F and $2\frac{1}{4}$Cr1Mo steels. Figure 6.9 shows the predicted evolution of $M_{23}C_6$ volume fraction at 600°C. The calculated kinetics are almost identical in both steels, even though in reality precipitation of $M_{23}C_6$ is much faster in COST F with particles being observed after as little as 1 hr at 600°C, as opposed to over 1000 hours in the $2\frac{1}{4}$Cr1Mo alloy.

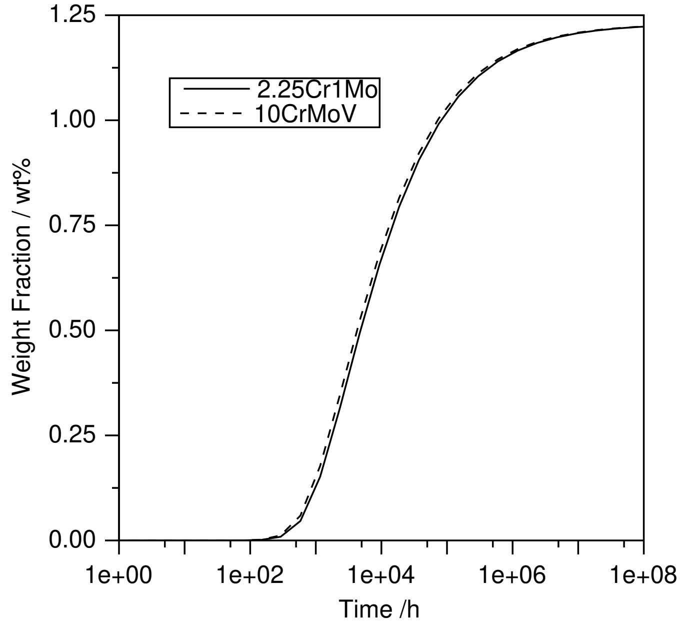

Figure 6.9: Evolution of $M_{23}C_6$ in $2\frac{1}{4}$Cr1Mo and COST F steels predicted using the Wert and Zener model.

While it seems that the Wert and Zener model is able to represent the kinetics of $M_{23}C_6$ precipitation in an austenitic steel it is unable to predict the large differences in kinetics observed in $2\frac{1}{4}$Cr1Mo steel and a 10CrMoV steel. A possible explanation is that in the austenitic alloy, $M_{23}C_6$ is the only carbide. In the ferritic steels other carbides form prior to $M_{23}C_6$ and would be expected to influence its kinetics by changing the matrix composition and the driving force for $M_{23}C_6$ formation; this is not incorporated into this model. The assumption that there are a constant number of pre–existing nuclei also may not be appropriate in the ferritic alloys.

6.6.2 Constant Nucleation Rate

Attempts were made to model $M_{23}C_6$ with a constant nucleation rate. The driving force for nucleation was calculated by suppressing $M_{23}C_6$, in which case MTDATA identifies M_7C ($2\frac{1}{4}$Cr1Mo alloy) and M_2X (COST F alloy; section 5.6) as the stable carbides. Assuming the dissolution of M_7C_3 is complementary to the precipitation of $M_{23}C_6$ the reaction to be considered may therefore be written as

$$\alpha + M_7C_3 + M_2X \rightarrow \alpha' + M_{23}C_6 \tag{6.19}$$

Where α and α' refer to the ferrite in equilibrium with the carbides on the left and right hand side respectively. The results are shown in Figure 6.10. For the COST F steel the driving force is predicted to be positive, which implies $M_{23}C_6$ does not form if M_2X reaches its equilibrium fraction. This contradicts observations which show that $M_{23}C_6$ is the dominant carbide in this steel. Calculations showed that while the free energy of the α+$M_{23}C_6$ system is lower in COST F than the $2\frac{1}{4}$Cr1Mo steel as might be expected, the free energy of the α+M_2X is lower still (Table 6.9). Furthermore, the equilibrium fraction of M_2X in the α+M_2X system is comparable with that of $M_{23}C_6$ and greater than that observed experimentally (see section 4.4). This discrepancy may arise because $M_{23}C_6$ starts to form before M_2X has reached its equilibrium volume fraction. The presence of other phases such as MX has also been ignored, and these would be expected to influence the free energies volume fractions.

Alloy	G_{LHS}/J mol^{-1}	V_{LHS}	G_{RHS}/J mol^{-1}	V_{RHS}
COST F	-36145	0.022	-36192	0.025
$2\frac{1}{4}$Cr1Mo	-35595	0.023	-35653	0.034

Table 6.9: Gibbs energy, G, and equilibrium volume fraction of carbide, V, for the systems on the left–hand side (LHS) and right–hand side (RHS) of the reaction equation for $M_{23}C_6$

It may be concluded that in COST F the assumption that the formation of $M_{23}C_6$ may be described by the reaction shown in equation 6.19 is incorrect. The predicted driving force changes considerably when MX is accounted for in the calculations. If it is assumed that MX is present prior to $M_{23}C_6$ precipitation (which is consistent with observations) then the reaction may be written

$$\alpha + M_{23}C_6 + MX \rightarrow \alpha' + M_{23}C_6 + MX' \tag{6.20}$$

Following the method used previously, the calculated driving force for $M_{23}C_6$ precipitation is now as shown in Figure 6.11. It can be seen that $M_{23}C_6$ is favoured at all temperatures, with the magnitude of the driving force for its formation greater than that in the $2\frac{1}{4}$Cr1Mo alloy as would be expected.

The driving force for nucleation was found using the same approximate method as used for M_2X by dividing the overall driving force for the transformation by the equilibrium volume fraction of $M_{23}C_6$.

The methods used for modelling the growth of spherical particles have been outlined in section 3.5.4. The radius of a particle, r^I, as a function of the time since its nucleation, t, may

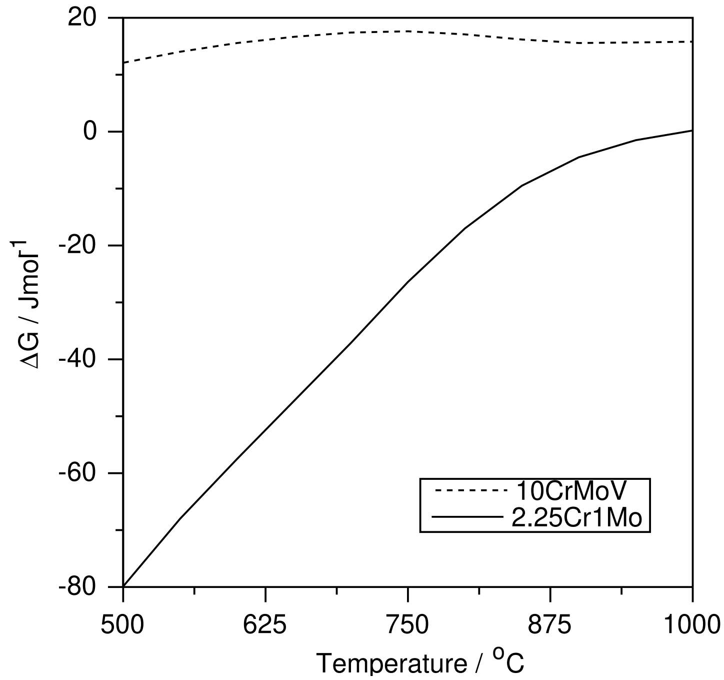

Figure 6.10: The predicted driving force for the formation of $M_{23}C_6$ assuming that the equilibrium volume fraction of M_2X (COST F) or M_7C_3 ($2\frac{1}{4}$Cr1Mo alloy) forms prior to the start of $M_{23}C_6$ formation.

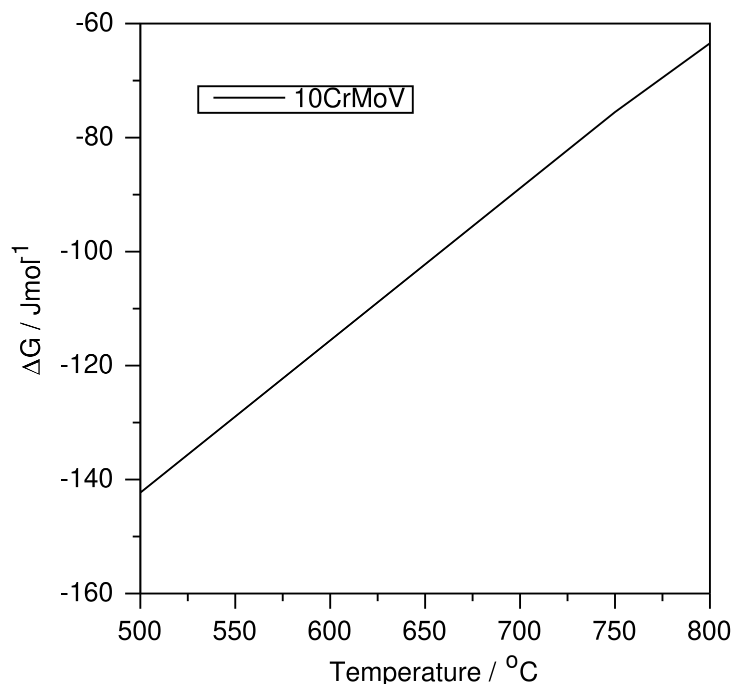

Figure 6.11: The predicted driving force for the formation of $M_{23}C_6$ in COST F allowing for MX

be written as

$$r^I = \chi t^{\frac{1}{2}} \tag{6.21}$$

For low supersaturations (as in this case - table 6.8) the growth constant χ may be written approximately as [Christian, 1975; p. 488]

$$\chi \simeq \sqrt{2D}\frac{(\bar{c} - c^{\alpha\beta})^{\frac{1}{2}}}{(c^{\beta\alpha} - \bar{c})^{\frac{1}{2}}} \tag{6.22}$$

Since $M_{23}C_6$ is largely a chromium carbide it is assumed that chromium diffusion controls the growth rate so the compositions in this equation all refer to chromium. The calculated parabolic growth constant is shown as a function of temperature in Figure 6.12 for COST F and the $2\frac{1}{4}$Cr1Mo alloy. It is predicted that the rates are very similar, confirming the conclusion from the previous section that the large difference in the kinetics observed in the two steels can only be explained by also considering nucleation.

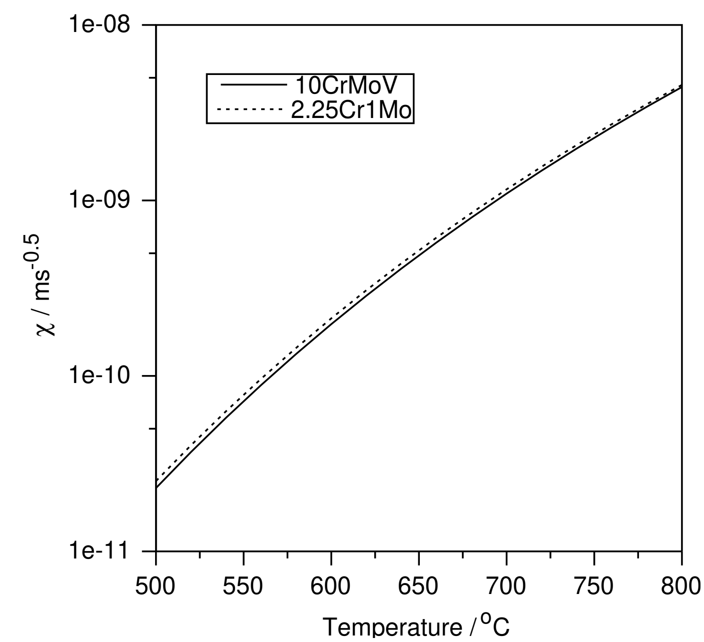

Figure 6.12: Calculated parabolic growth constant, χ, as a function of temperature for COST F and $2\frac{1}{4}$Cr1Mo alloys.

Following the Avrami approach the expression for the normalised volume fraction of $M_{23}C_6$ as a function of the growth constant, nucleation rate and time may be written as

$$\zeta = 1 - \exp\left[-\left(\frac{c^{\beta\alpha} - c^{\alpha\beta}}{\bar{c} - c^{\alpha\beta}}\left(\frac{8\pi\chi^3 I t^{\frac{5}{2}}}{15}\right)\right)\right] \tag{6.23}$$

The predicted TTT–diagram for an absolute volume fraction of 0.01 $M_{23}C_6$ is shown in Figure 6.13. As in the case of the transformation to M_2X the interfacial energy and site density for nucleation have to be found by fitting the predicted and experimental results. A C-curve is predicted for the kinetics in the $2\frac{1}{4}$Cr1Mo alloy which is not observed experimentally. This may be eliminated if the interfacial energy is reduced, but then the time difference between for the $2\frac{1}{4}$Cr1Mo and COST F alloy becomes much smaller than observed experimentally. To get the correct time difference the value of the interfacial energy must be as shown, since this increases the significance of the term containing the driving force for nucleation and therefore leads to a different nucleation rate for both steels. As shown previously a difference in nucleation rates is required to explain the observed kinetics.

Figure 6.13: Best fit predicted TTT lines for a 1% volume fraction of $M_{23}C_6$ in $2\frac{1}{4}$Cr1Mo and COST F alloys. The best fit values of the interfacial energy per unit area, σ, and site density, N_0, are also marked.

6.6.3 Allowing Two Nucleation Rates

In some experiments $M_{23}C_6$ has been observed to nucleate first on prior austenite grain boundaries followed by nucleation within the grains [Baker and Nutting, 1959]. This suggests there are two types of nucleation site, grain boundary and grain interior. The overall nucleation rate will be given by the sum of the nucleation rate for both types of site. The number of grain boundary sites will be less than the number of grain interior sites, however the energy barrier for formation of a stable nucleus is reduced for grain boundary nucleation because of the energy liberated by destroying grain boundary — this is effectively equivalent to a reduction in the interfacial energy for these sites. When there is a small driving force for nucleation few nuclei will overcome the barrier to nucleation within the grains. At grain boundaries the lower energy barrier means there will be a greater number of post–critical nuclei than within the grains despite the lower number of nucleation sites. In this case prior austenite grain boundary nucleation will dominate. Conversely when there is a high driving force for nucleation many nuclei will overcome the barrier to nucleation within the grains. The lower nucleation barrier at the grain boundaries is now more than compensated for by the increased number of nucleation sites within the grains.

The expression for the overall kinetics is identical to that used previously (equation 6.23). The nucleation rate is now the sum of the rates for each site, calculated using the usual nucleation equation (6.11) with the appropriate values of interfacial energy and site density. As previously, these are unknown are were found by fitting the predicted and experimental results. The best fit values are shown in Table 6.10. Note that the site density value for prior austenite grain boundary nucleation is much smaller than makes physical sense.

Site	$\sigma/\mathrm{J\,m^{-2}}$	$N_0/\mathrm{m^{-3}}$
Grain boundary	0.04	5×10^{-4}
Grain interior	0.70	5×10^{6}

Table 6.10: Best fit value for the site density and resultant interfacial energy for nucleation at both prior austenite grain boundary an grain interior sites.

The TTT–diagram produced for the best set of parameters is shown in Figure 6.14. The C–curve behaviour which was incorrectly predicted by the previous model has been eliminated. This is because even when the driving force for nucleation is low (at high temperatures) prior austenite grain boundary nucleation is still possible and so the overall nucleation rate does not fall sharply as in the previous case.

6.7 Summary

The growth of M_2X has been modelled using the simple Zener expression. Predicted and experimental results are in good agreement for a Fe–1.95Mo–0.11 wt% C alloy. However, for COST F the predicted growth rate is much less than that observed experimentally. This is due to incorrect prediction of the critical radius in this steel, probably because of neglect of the complex multi–component nature of the alloy. This discrepancy was resolved by setting the critical radius to some sensible value which is consistent with observed tip radii.

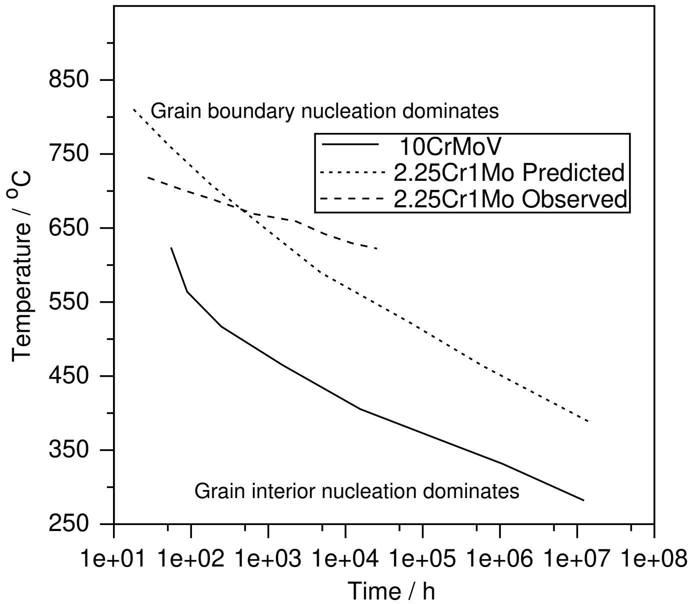

Figure 6.14: Best fit predicted TTT lines for $M_{23}C_6$ precipitation predicted using a model which allows two types of nucleation site. At low temperatures when the driving force for transformation is high grain interior nucleation dominates, at high temperatures prior austenite grain boundary nucleation becomes more important.

Models have been developed for the overall transformation kinetics of M_2X and $M_{23}C_6$. It was assumed that each phase forms independently of the other phases. In both cases models based on growth alone were unable to explain the differences in the observed kinetics, since the growth rates are similar in both steels. Further work was carried out using the assumption that nucleation occurs at a constant rate. To do this the driving force for the transformation must be evaluated. In the case of M_2X it was shown that, consistent with published experimental data, it must be assumed that cementite has not enriched when M_2X precipitation starts. If cementite were to be fully enriched then it is predicted that in the $2\frac{1}{4}$Cr1Mo steel the driving force for M_2X nucleation would be zero at some temperatures where it is observed in practice. In the case of $M_{23}C_6$ nucleation it was shown that MX must be allowed for in the calculation if any driving force is to be predicted in the COST F alloy. For this phase a model based on using a single nucleation rate was unable to reproduce the experimental results. An additional nucleation function was then introduced to represent the possibility of reducing the effective interfacial energy by forming nuclei on prior austenite grain boundaries.

In general, these models, whilst able to reproduce the observed results for two very different power plant steels are not satisfactory. In each case it is necessary to use different special assumptions about the microstructure prior to precipitation. The introduction of an additional nucleation rate function into the model for $M_{23}C_6$ improved the agreement between prediction and experiment but at the expense of introducing two additional fitting parameters. What would be more useful is a model which can predict the whole sequence of precipitation events without any prior assumption about the precipitation sequence. In practice events will occur simultaneously, for example it has been shown that M_2X precipitation must begin while M_3C is still enriching. By ignoring the interaction of simultaneously forming phases the scope for making useful predictions is reduced. The next chapter therefore describes the development of a model for simultaneous kinetics which combines the growth and nucleation theory for each phase which has been developed in this chapter into a single model.

CHAPTER SEVEN

A New Model For Simultaneous Transformation Kinetics

In this chapter a new model which has been developed for simultaneous precipitation transformations is described. The theory is first presented for some simple cases and then is applied to the precipitation in power plant alloys.

7.1 Introduction

It has been shown in the previous chapter that it is not possible to produce a general model for precipitation in power plant alloys on the basis that each phase forms successively, with one precipitation reaction completed before the next one in the sequence commences. In practice precipitation events occur at the same time and the different phases will be compete, not only for untransformed volume, but also for the available solute. It seems this competition has a profound effect on the observed precipitation kinetics. It is therefore necessary to incorporate all the phases into a combined model which allows for these interactions. This is potentially a complex problem, but nevertheless essential to produce a generally applicable model.

First, the simultaneous kinetics model was developed for some simple cases in much the same way the Johnson–Mehl–Avrami theory for the precipitation of a single phase was described in section 3.3. This model was developed further to deal with simultaneous precipitation in power plant alloys.

7.2 Simultaneous Reactions – Simple Cases

The model developed here is adapted from the Johnson–Mehl–Avrami approach and makes use of their extended volume concept to separate the problems of growth and nucleation from that of particle impingement. Consider two phases β and θ which precipitate at the same time from the parent phase, designated α. It is tentatively assumed that the nucleation and growth rates do not change with time and that the particles grow isotropically. Although these assumptions will not be valid for a general diffusion–controlled transformation they provide a simple first test for any model.

Following the method for precipitation of a single phase (section 3.3) the increase in the extended volume of β and θ due to particles nucleated in a time interval $t = \tau$ to $t = \tau + d\tau$ is, therefore, given by

$$dV_\beta^e = \frac{4}{3}\pi v_\beta^3 (t-\tau)^3 I_\beta V \ d\tau \tag{7.1}$$

$$dV_\theta^e = \frac{4}{3}\pi v_\theta^3 (t-\tau)^3 I_\theta V \ d\tau \tag{7.2}$$

For each phase, the increase in extended volume will consist of three separate parts. Thus, for β:

(i) β which has formed in untransformed α.

(ii) β which has formed in regions which are already β.

(iii) β which has formed in regions which are already θ.

Only β formed in untransformed α will contribute to the real volume of β. On average a fraction $\left(1 - \frac{V_\beta + V_\theta}{V}\right)$ of the extended volume will be in previously untransformed material. It follows that the increase in real volume of β is given by

$$dV_\beta = \left(1 - \frac{V_\beta + V_\theta}{V}\right) dV_\beta^e \tag{7.3}$$

and similarly for θ,

$$dV_\theta = \left(1 - \frac{V_\beta + V_\theta}{V}\right) dV_\theta^e \tag{7.4}$$

Generally V_β will be some complicated function of V_θ and it is not possible to integrate these expressions to find the relationship between the real and extended volumes. However, in certain simple cases it is possible to relate V_β to V_θ by multiplication with a suitable constant, K. It is then possible to write

$$V_\theta = KV_\beta \tag{7.5}$$

The equations relating the increment in the real volume to that of the extended volume may now be written as

$$dV_\beta = \left(1 - \frac{V_\beta + KV_\beta}{V}\right) dV_\beta^e \tag{7.6}$$

$$dV_\theta = \left(1 - \frac{V_\theta + KV_\theta}{KV}\right) dV_\theta^e \tag{7.7}$$

Equations 7.6 and 7.7 may then be integrated to find an analytical solution relating the extended and real volumes analogous to that for single phase precipitation.

$$\frac{V_\beta^e}{V} = \frac{-1}{1+K} \ln\left[1 - \frac{V_\beta}{V}(1+K)\right] \tag{7.8}$$

$$\frac{V_\theta^e}{V} = \frac{-K}{1+K} \ln\left[1 - \frac{V_\theta}{V}\left(\frac{1+K}{K}\right)\right] \tag{7.9}$$

The total extended volume is found for each phase by integrating equations 7.1 and 7.2 with respect to τ. After rearranging, the final expressions for the volume fractions of β and θ phases are

$$\zeta_\beta = \left(\frac{1}{1+K}\right)\left(1 - \exp\left[-\frac{1}{3}(1+K)\pi v_\beta^3 I_\beta t^4\right]\right) \tag{7.10}$$

$$\zeta_\theta = \left(\frac{K}{1+K}\right)\left(1 - \exp\left[-\frac{1}{3}\left(\frac{1+K}{K}\right)\pi v_\theta^3 I_\theta t^4\right]\right) \tag{7.11}$$

These equations resemble the Avrami equation for single phase precipitation with extra factors to account for the presence of a second precipitate phase. When the volume fraction of both precipitating phases is very small equations 7.10 and 7.11 approximate to the expressions for each phase precipitating alone. This is because in the early stages of transformation nearly all of the extended volume lies in previously untransformed material and contributes to the real volume. As transformation proceeds, the volume fraction of each phase predicted for the phases precipitating simultaneously becomes less than that predicted if the phases were precipitating alone. This is expected, since additional phases reduce the fraction of the extended volume which lies in previously untransformed material.

Since the nucleation and growth rates were assumed to be constant, it is possible to calculate explicitly the value of K. The volume of each phase at any time depends on its nucleation rate and the cube of its growth rate. The ratio V_θ/V_β is then constant and given by

$$K = \frac{V_\theta}{V_\beta} = \frac{I_\theta v_\theta^3}{I_\beta v_\beta^3} \tag{7.12}$$

Some example calculations for the case of a constant growth rate are presented in Figure 7.1. When the nucleation and growth rates of β and θ are set to be exactly identical, their curves for volume fraction versus time are exactly superimposed and each phase eventually achieves a fraction of 0.5 (Figure 7.1 a). When the nucleation rate of θ is set to equal twice that of β, then for identical growth rates, the terminal fraction of θ is, as expected, twice that of β (Figure 7.1 b). The case where the growth rate of θ is set to be twice that of β (with identical nucleation rates) is illustrated in Figure 7.1 c. The final volume fraction of the θ phase is eight times that of the β phase because volume fraction is a function of the growth rate cubed.

7.3 Complex Simultaneous Reactions

In practice, the multiple reactions found in power plant steels have important complications not included in the simple model described above. The phases interfere with each other not only by reducing the volume available for transformation, but also by removing solute from the matrix surrounding them and thereby changing its composition. The change in matrix composition leads to different growth and nucleation rates of the phases. Therefore there are no simple analytical relationships between the volume fraction of all the phases and a different approach is needed.

7.4 Soft–Impingement

All widely spaced particles will at first grow without interfering until eventually their diffusion fields overlap significantly which marks the onset of soft–impingement. Once soft–impingement has started particles will be competing for an ever decreasing amount of solute and their growth rates will decrease more rapidly than would be the case in a semi–infinite matrix. Also, because the supersaturation in solute–depleted regions is less, the driving force for nucleation in these

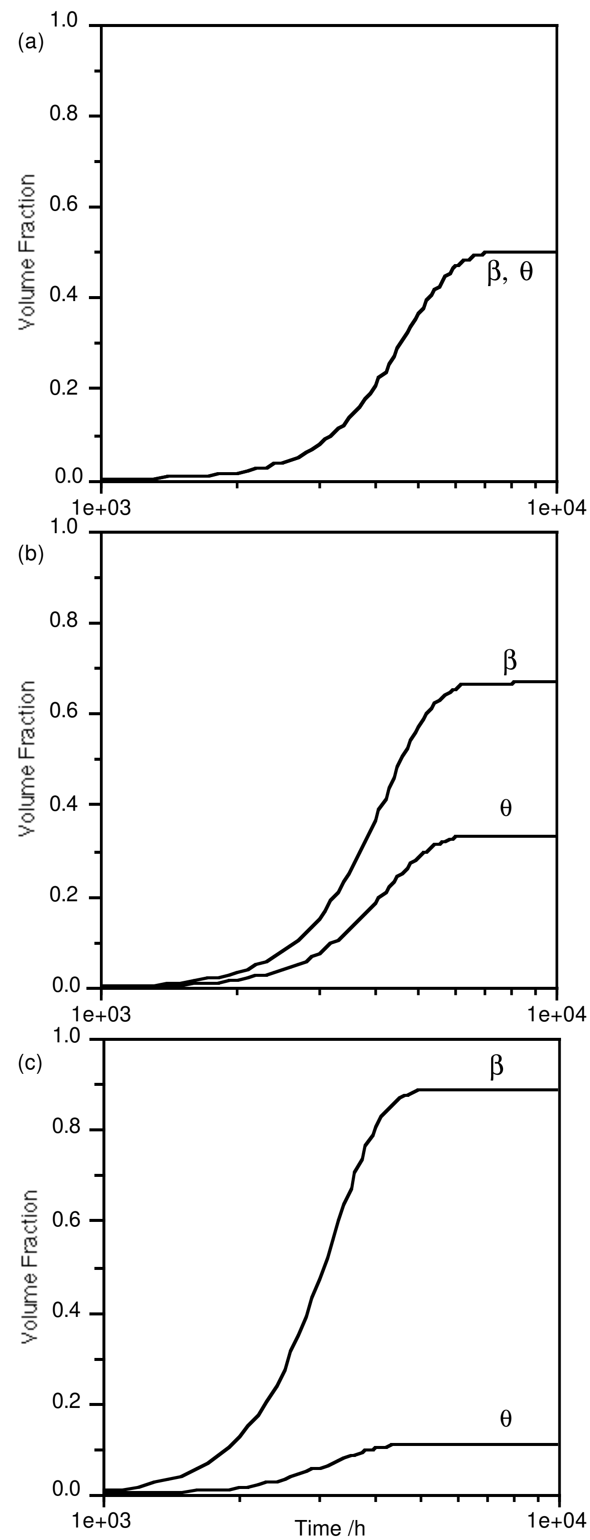

Figure 7.1 : Simultaneous precipitation of θ and the β (a) When the two phase have identical nucleation and growth rates. (b) Identical growth rates but with the β having twice the nucleation rate of θ. (c) Identical nucleation rates but with β particles growing at twice the rate of the θ particles.

areas is reduced and the nucleation rate will fall. Eventually, the excess solute will be exhausted and both nucleation and growth stop.

7.4.1 An Approximate Treatment of Soft–Impingement

It is not possible to account rigorously for soft–impingement in a method based on the extended volume concept, and for a problem as complex as power plant steels. However, the observed effects undoubtedly cannot be simulated without soft–impingement. A common approximation in these circumstances is to assume that solute is distributed uniformly in the matrix for the purposes of soft–impingement

Each precipitating phase will consume or reject solute into the matrix, whose subsequent transformation behaviour will therefore be altered. Consider the precipitation of β and γ from α which initially has a uniform composition. Figure 7.2 shows how the distribution of solute might change during precipitation: (a) at an intermediate stage when both β and γ are precipitating and, (b) at a later time when the formation of β is just complete.

For the situation illustrated, the maximum fraction of each phase is designated f_M and the fraction at any instant, f. The maximum fraction is given by a lever rule,

$$f_M^\beta = \frac{\overline{c} - c^{\alpha\beta}}{c^{\beta\alpha} - c^{\alpha\beta}} \tag{7.13}$$

It is then possible to define a parameter Φ for each phase, such that $\Phi = f/f_M$, which changes from $0 \rightarrow 1$ during the course of the transformation. When there is more then one precipitating phase, Φ can be generalised to account for concentration changes caused by each new phase. Identifying each of the n precipitating phases by a subscript $i = 1 \ldots n$, gives

$$\Phi_i = \frac{\sum_{i=1}^{n}(f_i)(c^{i\alpha} - c^{\alpha i})}{(\bar{c} - c^{\alpha i})} \tag{7.14}$$

Physically Φ represents the amount of the available solute removed from the matrix into all the precipitates as a fraction of the amount of solute removed when phase i stops precipitating.

We now proceed to make the approximation that the chemical driving force ΔG for the formation of each phase is related linearly to Φ_i:

$$\Delta G_i\{\Phi_i\} = (1 - \Phi_i)\Delta G_i\{\Phi_i = 0\} \tag{7.15}$$

where the braces are used to identify that ΔG is a function of Φ_i.

The definition of Φ is a little different for cementite, which in the present context precipitates rapidly by paraequilibrium transformation. Φ is therefore defined to reflect its subsequent change in composition by the diffusion of solute into the cementite so that a value of $\Phi = 0$

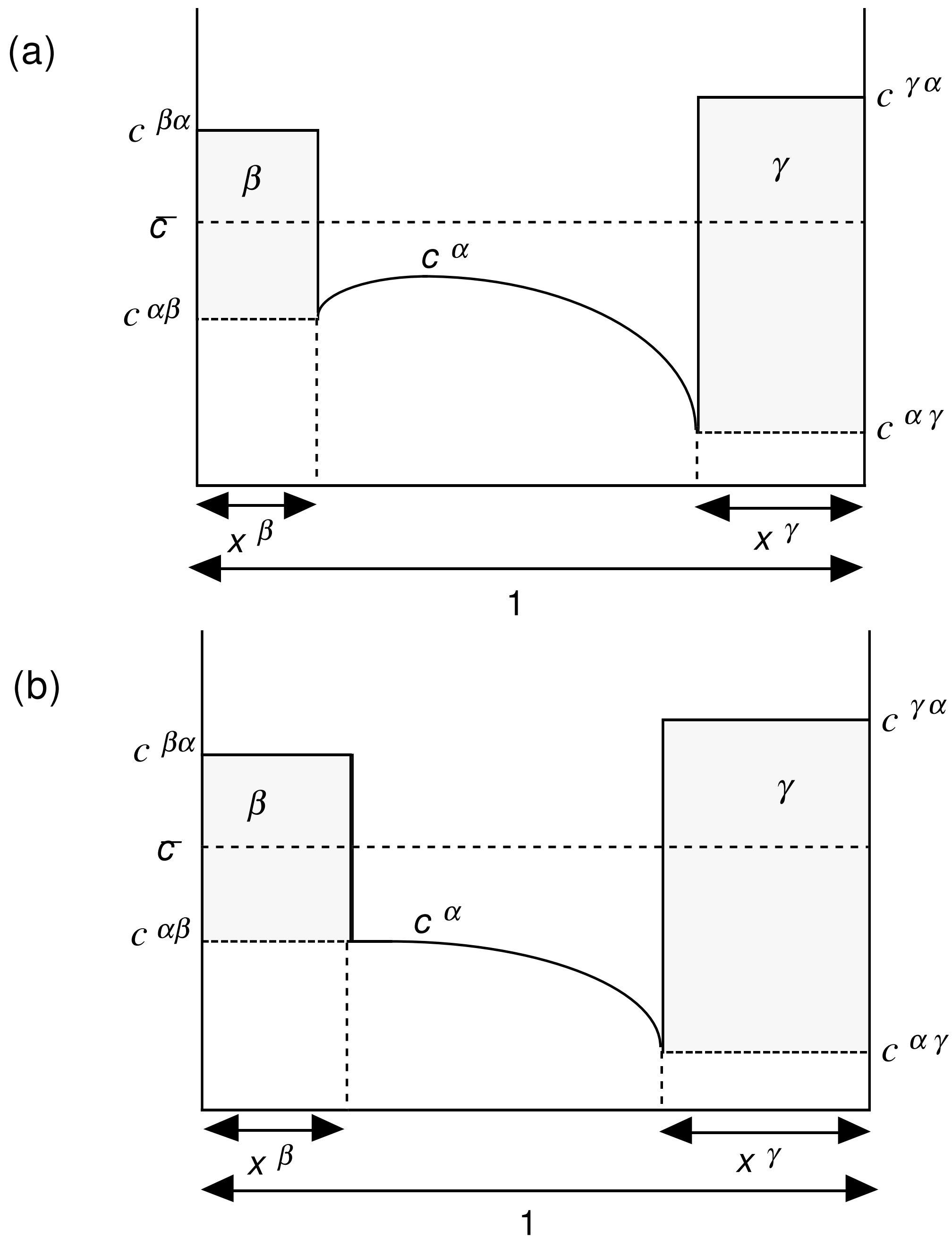

Figure 7.2 : Distribution of solute when (a) both β and γ precipitating, and at a stage (b) where the precipitation of β has been completed.

corresponds to the paraequilibrium solute concentration in cementite, and $\Phi = 1$ corresponds to the equilibrium concentration for cementite in the absence of other precipitates.

$$\Phi_{M_3C} = \frac{c - \overline{c}'}{c^{M_3C\alpha} - \overline{c}'} \tag{7.16}$$

where $\overline{c}'$ is the mean solute level in the matrix at any instant, a function of all the other phases as well:

$$\overline{c}' = \frac{\overline{c} - \sum_{i=1}^{n} f_i c^{i\alpha}}{1 - \sum_{i=1}^{n} f_i} \tag{7.17}$$

The analysis in terms of Φ gives a crude approximation to soft impingement phenomena. The concentration gradients in the ferrite for the precipitation reactions that occur in power plant steels are very shallow, so the approximation may be justified. Also, in reality soft impingement will not occur until the diffusion fields of neighbouring particles overlap and so there will be a period at the start of transformation where the growth rates are not influenced by the presence of other particles. This differs from the analysis here in which Φ, and hence the growth and nucleation rate, changes as soon as precipitation begins.

Note that in Figure 7.2 β is a metastable phase which will tend to dissolve as soon as the solute concentration in the ferrite falls below that which is consistent with metastable equilibrium (in this case when $\overline{c}' < c^{\alpha\beta}$).

7.4.2 Multicomponent Solute Depletion

In practice there may be many solute species diffusing during precipitation, and for each of these, it is possible to calculate a value of Φ.

Ideally Φ should be independent of the species as is always the case in a binary system where the compositions are interdependent. However, for ternary or higher systems equation 7.14 will only apply when there are only two phases are in equilibrium as shown in Figure 7.3.

When three phases coexist a tie–triangle fixes the compositions and equation 7.14 is no longer correct (as shown in Figure 7.4). It may nevertheless be a good approximation for the present work.

For the case of carbide precipitation in power plant alloys both the mean composition and the final ferrite composition lie close to the iron corner of the phase diagram, while the carbide compositions will lie closer to the chromium and carbon corners. Calculations were performed to compare how close the equilibrium fractions calculated using equation 7.14 are to the true equilibrium fraction calculated using MTDATA. The results are shown in Table 7.1 for $M_{23}C_6$ and M_2X in COST F steel at 600°C. It can be seen that the agreement between the fractions calculated is good. The use of Φ as defined above may therefore be justified, and the value of Φ is expected to be approximately independent of which species is chosen to calculate it.

7.5 Computing Overall Transformation Kinetics

The theory for calculating the growth and nucleation rates of the various precipitate phases as a function of compositions and driving forces has already been presented in chapter 6.

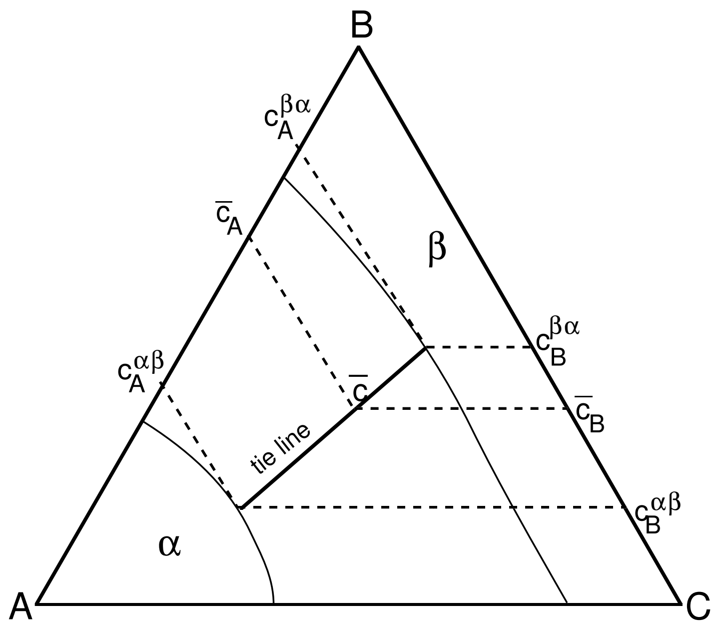

Figure 7.3: A ternary diagram showing the case where only two phases are in equilibrium. In this case Φ is species independent.

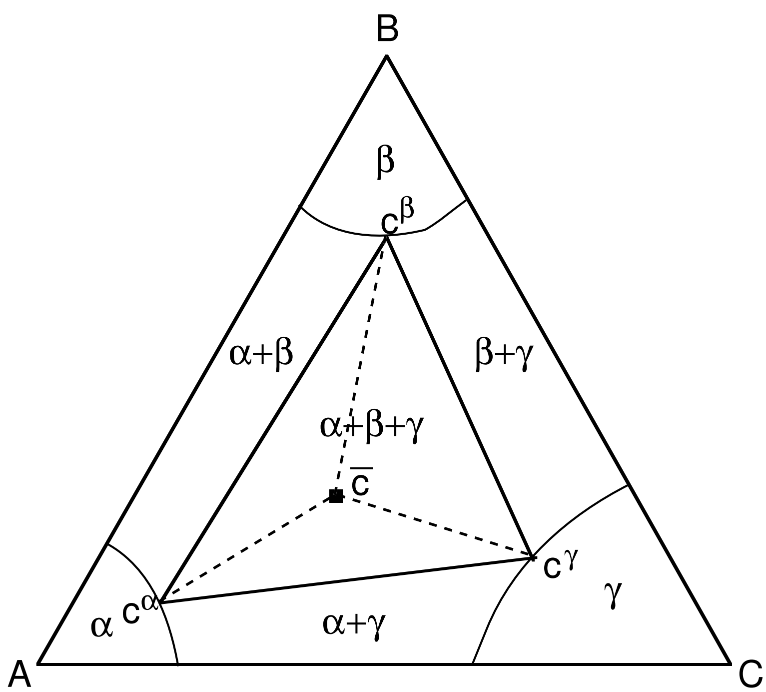

Figure 7.4: In general in ternary and higher systems there will not be a straight line connecting $c^{\alpha\beta}$, $c^{\beta\alpha}$ and $\bar{c}$ and equation 7.14 is no longer valid.

Having incorporated these phenomena into a computer program it becomes possible to solve for simultaneous transformation kinetics using an iterative procedure. This enables the matrix

Phase	equation 7.14 (Fe)	equation 7.14 (Cr)	equation 7.14 (C)	MTDATA
M_2X	0.02454	0.02517	0.02456	0.02455
$M_{23}C_6$	0.02195	0.02196	0.02246	0.02197

Table 7.1: Equilibrium mole fractions calculated using equation 7.14 using different components and the correct fraction calculated using MTDATA.

composition, growth and nucleation rates to be updated at each step, something which is not possible analytically. The following explanation is, for the sake of simplicity, based on three precipitation reactions though the method can be made much more general. The three precipitates are designated θ, β and γ, to represent M_3C, M_2X and $M_{23}C_6$ respectively.

An iterative procedure is used, as described earlier:

(1) The time t and volume fractions of β and γ set initially to zero. The concentration of substitutional solute in the cementite, θ, is set to mean solute composition, consistent with its paraequilibrium growth mechanism.

(2) The growth and nucleation rates for β and γ calculated using the current value for the solute concentration in the matrix.

(3) The time t incremented by a small step Δt. The additional volume of each phase precipitated in interval $t \rightarrow t + \Delta t$ is calculated whilst at the same time allowing cementite to change its chemical composition (*i.e.* tend towards equilibrium).

(4) The volumes of β and γ are updated, as is the composition of the cementite.

(5) The amount of solute removed from ferrite due to the precipitation of β and γ, and due to the change in cementite composition is calculated, and the mean ferrite composition modified accordingly. All the driving force terms and nucleation and growth rate terms are modified to be consistent with the change in ferrite chemical composition.

(6) Steps 2$\rightarrow$5 are repeated until $t = t_f$, where t_f is the time of heat treatment at the temperature concerned.

(7) The volume fractions of β and γ at time t_f are thus output along with the composition of the θ.

7.5.1 Volume increment β and γ

A detailed description of the method used for spherical precipitates (*e.g.* $M_{23}C_6$) is now given, and its adaptation for other shapes.

During diffusion–controlled growth of spherical particles each dimension of the growing particle increases in proportion to the square root of the time (section 3.5.4). Considering small increments in time, each of magnitude Δt, it follows that the corresponding change in the extended volume of spherical particles beginning with the first increment of time is given by:

$$\Delta V_1^e = (I_1 V \Delta t_1)(C\chi_1^3 \Delta t_1^{\frac{3}{2}}) \tag{7.18}$$

where $C = 4\pi/3$ and the numerical subscripts identify the sequence of time increments. The two terms on the right represent the number of particles nucleated and the contribution of each particle to the extended volume respectively.

The change in extended volume for the second interval Δt_2 is then

$$\Delta V_2^e = (I_2 V \Delta t_2)(C\chi_2^3 \Delta t_2^{\frac{3}{2}}) + \frac{3}{2} I_1 V C \chi_2^3 (\Delta t_1 + \Delta t_2)^{\frac{1}{2}} \tag{7.19}$$

where the second term on the right is the contribution due to the increase in the size of particles which were nucleated in the first time interval. Since the time intervals are of equal size, this equation can be written:

$$\Delta V_2^e = CV\Delta t^{\frac{5}{2}} \chi_2^3 \left[I_2 + \frac{3}{2} I_1 \sqrt{2} \right] \tag{7.20}$$

or in general, for the mth time increment, the corresponding change in extended volume is given by:

$$\Delta V_m^e = CV\Delta t^{\frac{5}{2}} \chi_m^3 \left[I_m + \frac{3}{2}\sqrt{2} I_{m-1} \ldots + \frac{3}{2}\sqrt{m} I_1 \right] \tag{7.21}$$

For each interval, the increase in extended volume for a specific phase γ is converted to a corresponding change in real volume of γ as before, allowing now for the coexistence of n phases:

$$\Delta V_\gamma = \left(1 - \frac{\sum_{i=1}^{n} V_i}{V} \right) \Delta V_\gamma^e \tag{7.22}$$

where V_i is the real volume of the ith phase. The total volume of γ is thus updated:

$$V_\gamma^{new} = V_\gamma^{old} + \Delta V_\gamma \tag{7.23}$$

This procedure is repeated for all the intervals from $t = 0 \rightarrow t_f$, at which time the final volume is output along with the time. The same approach is used for all phases with a spherical morphology (Laves phase and $M_{23}C_6$ in this case). For needle shaped particles the basic method is the same but the expression for the extended volume is different. The volume of a single needle shaped particle of β at a time $(t - \tau)$ after its nucleation is given by

$$V_\beta = \frac{\pi v^3}{\phi^2}(t - \tau)^3$$

This may also be written as $V_\beta = C_\beta(G(t-\tau))^3$ where $C_\beta = \frac{\pi}{\phi^2}$. It follows that

$$\Delta V_m^e = C_\beta V \Delta t_m^4 (v_m)^3 \left[I_m + 3(2)^2 I_{m-1} \ldots 3(m+1)^2 I_1\right] \tag{7.24}$$

This approach can be used for any number of phases at the risk of increasing the computational time and memory requirements. The accuracy of the iterative procedure will depend on the step size which is used. After experimenting it was found that in most cases using 1000 time steps gave optimum performance. Increasing the number of steps further increases computational time without a significant improvement in accuracy.

7.5.2 Dissolution of Phases

Metastable phases must eventually dissolve as equilibrium is approached. Figure 7.5 illustrates the circumstances where metastable β begins to dissolve when the concentration in the matrix away from the β particle drops below $c^{\alpha\beta}$, with a tendency for solute to be released from the dissolving β to the more stable γ.

During diffusion–controlled dissolution of a particle of radius r, a consideration of mass balance at the β/α interface requires that:

$$\frac{dr}{dt}(c^{\beta\alpha} - c^{\alpha\beta}) = -D_\alpha \frac{dc}{dr} \tag{7.25}$$

The term on the left hand side is the rate at which solute is released into the matrix as the particle dissolves, which must be carried away by diffusion as represented by the right hand side of the equation. If the concentration gradient is assumed to be constant (the Zener linearized gradient approximation) then

$$\frac{dc}{dr} = -\frac{(c^{\alpha\gamma} - c^{\alpha\beta})}{\overline{d}} \tag{7.26}$$

where $\overline{d}$ is the mean diffusion distance between the β and γ particles, given by

$$\overline{d} = (N_\beta + N_\gamma)^{-\frac{1}{3}} \tag{7.27}$$

where N is a number density of particles, assumed constant throughout dissolution; smaller particles should in reality vanish before larger ones but for simplicity, it is assumed that the whole process can be represented by a mean particle size of radius $\overline{r}$. With this approximation, it follows that

$$\frac{dV_\beta}{dt} = 4\pi\overline{r}^2 \frac{D_\alpha}{\overline{d}} \frac{(c^{\alpha\beta} - c^{\alpha\gamma})}{(c^{\beta\alpha} - c^{\alpha\beta})} \tag{7.28}$$

In the case of a needle shaped particle dissolving (*e.g.* M_2X) the reduction in volume is given by

$$\frac{dV_\beta}{dt} = -\frac{3\pi\overline{l}^3(c^{\alpha\beta} - c^{\alpha\gamma})}{\phi\overline{d}(c^{\beta\alpha} - c^{\alpha\beta})} \tag{7.29}$$

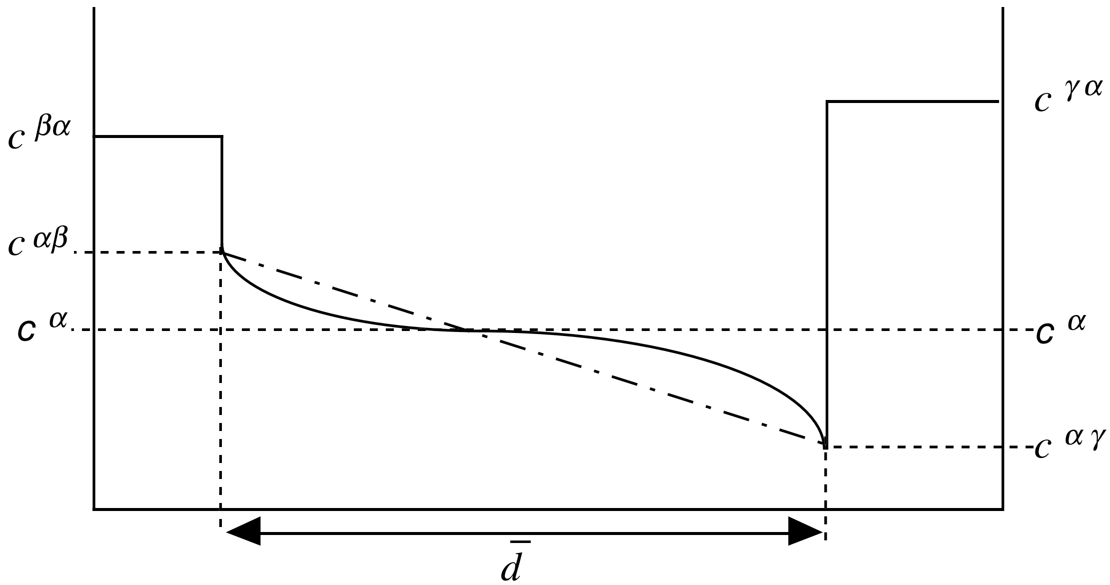

Figure 7.5 : Schematic of the composition profile when β is dissolving and γ is precipitating. The dashed line shows the mean concentration gradient from β to γ

where $c^{\beta\alpha}$ and $c^{\alpha\beta}$ now refer to the concentrations of solute in the needle shaped phase. $\bar{l}$ is the needle length which decreases as the particles dissolve.

There is a slight difference when considering the dissolution of M_3C since its composition varies with time. Enrichment will stop, and dissolution will start when the extent of reaction Φ for M_3C equals 1. Dissolution may then be dealt with in the same way as for other phases, with the solute concentration in the M_3C fixed from the point enrichment stopped.

7.6 Calculation of Growth and Nucleation Rates

The theory describing how the growth and nucleation rates are related to the chemical composition and driving force for precipitation has already been presented in chapter 6. The same theory has been used in the simultaneous kinetics model, the difference being that the driving force and compositions have been modified as transformation proceeds to account for solute depletion. Also, in the simple models a certain precipitation sequence was assumed in which each phase forms successively, *i.e.* the precipitation of one phase is completed before the next begins. With the simultaneous kinetics model no a priori assumption is made about the precipitation sequence; it is assumed that all phases can form from the start of the transformation, and the sequence arises naturally as rapidly precipitating metastable phases give way to slow forming stable phases. As a result of this the way in which the phase compositions and initial driving forces are calculated is somewhat different to the simple case.

7.6.1 Initial Driving Force For Nucleation

The chemical driving force for the nucleation of a phase is given in the simultaneous kinetics model by equation 7.16. This equation contains a term giving the initial driving force and a modification factor which accounts for the decrease in the driving force as transformation proceeds. Because cementite forms extremely rapidly compared to the other precipitates the starting microstructure may be considered as consisting of ferrite and cementite with the paraequilibrium composition. The appropriate reaction to be considered when calculating the free energy change on forming carbides is (for the example of $M_{23}C_6$):

$$\alpha + M_3C_{para} \rightarrow \alpha' + M_{23}C_6 \tag{7.30}$$

Note that it is implicitly assumed that the cementite dissolves to provide the carbon for the carbide precipitate. In the case of Laves phase a similar reaction is considered.

$$\alpha + M_3C_{para} \rightarrow \alpha' + Laves \tag{7.31}$$

Because Laves phase contains no carbon the ferrite on the right hand side of the equation would be predicted to contain a high carbon level. In practice this is not the case since the carbon will be removed from the matrix by carbide precipitation. To allow for this, the ferrite on the right hand side of the equation α_2 has its carbon level set to zero.

MTDATA was used to calculate the free energies for both sides of the equations 7.32 and 7.33. These were then subtracted to find the free energy change for the reactions. To calculate the free energy of $\alpha + M_3C_{para}$ the paraequilibrium composition of cementite was first determined. Since the ratio of the concentrations of the substitutional elements is the same as in the bulk alloy this is simply a matter of scaling all the bulk concentrations by 0.75 to account for the carbon in the cementite. MTDATA was then used to calculate the free energy for cementite of this composition, and also of ferrite which was assumed to contain zero carbon. The free energy of the $\alpha + M_3C_{para}$ system is given by

$$G_{LHS} = V_\theta G_\theta + V_\alpha G_\alpha \tag{7.32}$$

Where the volume fraction of cementite, V_θ is given by equation 6.2, and the volume fraction of ferrite is $(1 - V_\theta)$.

To calculate the free energies for the right hand side of equations 7.32 and 7.33 the precipitate (*e.g.* $M_{23}C_6$) and ferrite were allowed to coexist. The composition and volume fraction for both phases corresponding to the minimum free energy was calculated. This minimum free energy was taken to be the free energy of the right hand side G_{RHS}, and the free energy difference was then calculated

$$\Delta G_0 = G_{RHS} - G_{LHS} \tag{7.33}$$

ΔG_0 was then related to the driving force for nucleation by dividing by the equilibrium volume fraction of the precipitating phase as discussed in section 6.4.2.

7.6.2 Calculating the Nucleation Rate

Once the free energy for nucleation was determined the nucleation rate was calculated for each phase using exactly the same method as described previously (section 1.4.2). Once again, the nucleation site density and nucleus interfacial energy are unknown and are found by fitting predicted and experimental results. This is discussed in more detail in the next chapter.

7.6.3 Determining the Phase Compositions

The equations which govern the growth of the various precipitates have already been presented in chapter 6. To calculate the phase compositions, on which the growth rates depend, requires some *a priori* assumption to be made about the microstructure. In chapter 6 it was assumed that the precipitation of one phase was complete before the next one one forms. In this case the new phase will be precipitating in a matrix which has a composition which is in equilibrium with the precipitates which are already existing. Alternatively if all phases are allowed to precipitate simultaneously then at the start of transformation each phase will be forming in ferrite with the average composition. As transformation proceeds the ferrite composition will change, approaching its equilibrium value. This is explained pictorially in Figure 7.6 for the precipitation of $M_{23}C_6$.

MTDATA was used to predict how the composition of the M_2X depends on the composition of the ferrite in which it forms. The ferrite composition was ranged from its initial value (the mean composition) to its final value when equilibrium is reached. Figure 7.7 shows how the composition of M_2X (which is chromium rich in this case) varies over this range. It can be seen that the composition change is in fact rather small (the Cr level decreases by $\simeq$3%). For the purposes of calculating the growth rate this difference is negligible. In simultaneous model the composition of the precipitating phases is taken as being that in equilibrium with ferrite only. This means that no assumption has to be made about the order in which the phases precipitate.

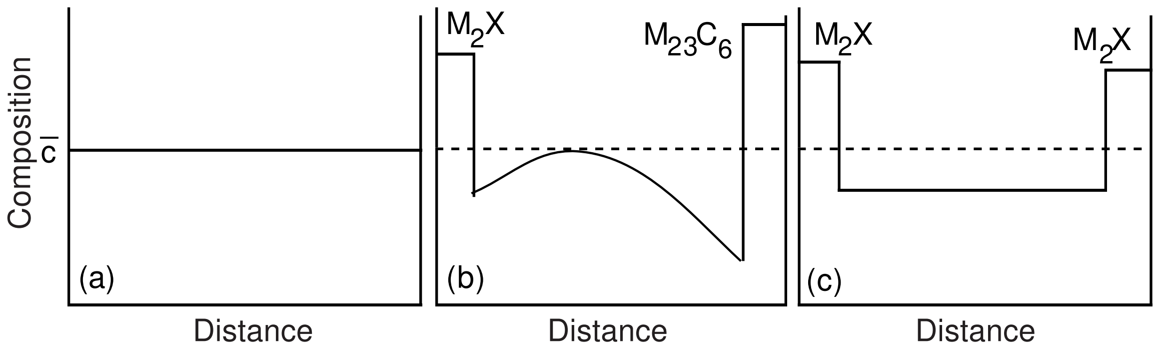

Figure 7.6: Schematic composition profiles (a) before any precipitation (b) at an intermediate stage if both M_2X and $M_{23}C_6$ form simultaneously (c) when M_2X precipitation is complete without $M_{23}C_6$ formation (making the assumption that the phases form successively)

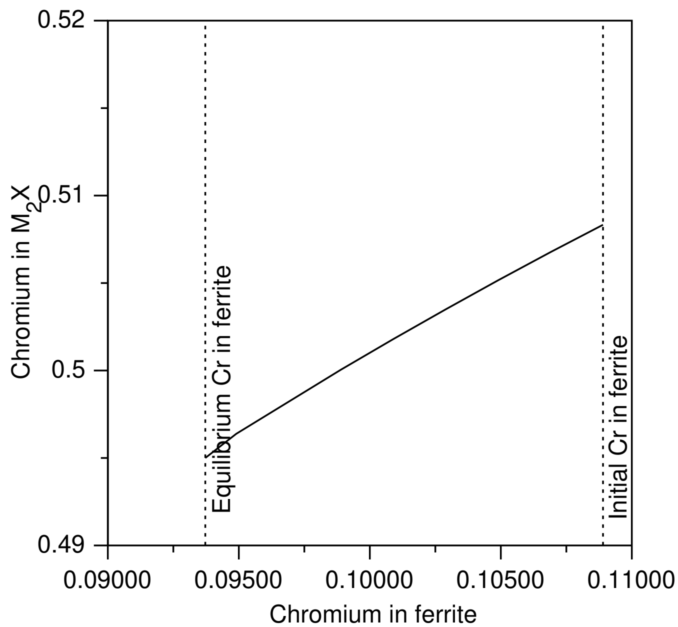

Figure 7.7: A plot showing how the predicted chromium content of M_2X changes as the chromium level in ferrite varies from its initial to final, equilibrium value in a 10CrMoV steel at 600°C.

7.6.4 Complications When Modelling Dissolution

Although this approach is adequate when calculating the growth rate of precipitating phases, difficulties arise for dissolution. According to the criteria shown in section 7.4.1 dissolution begins when the concentration of the controlling species in ferrite falls below the equilibrium concentration at the interface. Consider M_2X in alloy F which is predicted by

MTDATA to be an equilibrium phase at 750°C. Table 7.2 shows the predicted chromium concentration in the ferrite when M_2X is the only precipitate allowed and the final equilibrium chromium level.

	Chromium in ferrite
α+M_2X	0.09957
Equilibrium	0.09809

Table 7.2: MTDATA calculated chromium concentration in ferrite for the case when ferrite + M_2X are the only permitted phases and for the equilibrium case (all phases permitted)

It can be seen that there is a slight difference in the two chromium levels with that in equilibrium with just M_2X being higher than the final equilibrium level. In the early stages of tempering M_2X which precipitates more rapidly than $M_{23}C_6$ will form with the composition as if it were in equilibrium with ferrite alone. Its volume fraction is likely to exceed the equilibrium fraction since at this point the amount of $M_{23}C_6$ is small and there is considerable excess solute. Eventually, as the $M_{23}C_6$ volume fraction increases the solute level in the ferrite will fall. In terms of the model M_2X will be predicted to dissolve completely as the chromium level in the ferrite falls below the concentration in equilibrium with M_2X alone. In reality it is probable that as the M_2X dissolves its composition will change so that eventually it reaches a state where it is in equilibrium with all the other phases, at which point dissolution stops. The way the model would predict the evolution of volume fraction compared with what would be expected in reality is shown in Figure 7.8.

To account for the multi–component diffusion away from the dissolving M_2X, and thereby work out the composition change with time is a complex problem which is beyond the scope of the model in which only accounts for the dominant species (chromium in the case of M_2X). The problem is solved in an approximate way by ensuring that the volume fraction of dissolving phases does not fall below the equilibrium volume fraction (which will be zero for non–equilibrium phases). This lead to a sharp rather than a smooth end to dissolution (as shown in Figure 7.8) but outside the transition region the agreement between reality and prediction should be good.

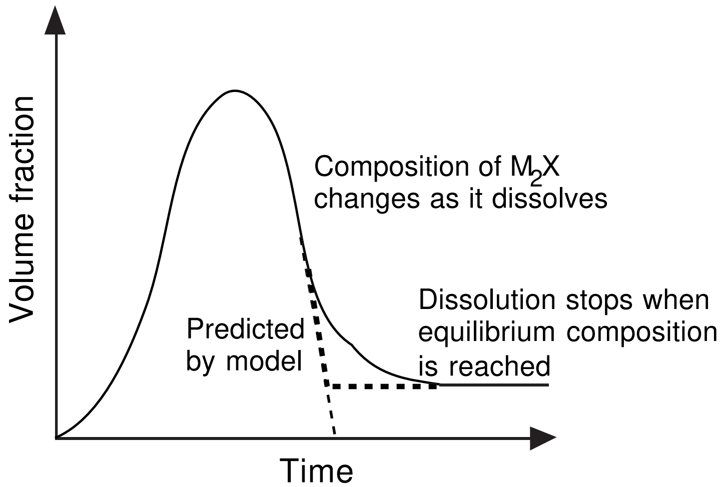

Figure 7.8: A schematic plot showing how the volume fraction of M_2X would be expected to vary when it is an equilibrium phase. Initially, because the volume fraction of $M_{23}C_6$ is small the volume fraction of M_2X can exceed its equilibrium value. As M_2X dissolves its composition changes until it is in equilibrium with the other phases. The model does not account for this and will therefore predict complete dissolution unless the volume fraction is not allowed to go below the equilibrium value.

CHAPTER EIGHT

Application of Simultaneous Kinetics Model

This chapter describes the predictions that have been made using the simultaneous kinetics model on both real and hypothetical alloys. Where available, experimental data have been compared with predicted results. Hypothetical alloy compositions were also used to investigate the effects of specific alloying elements on the predicted kinetics. The effects of tempering treatment and the reason why "C–curve" kinetics are not observed were also studied.

8.1 Introduction

A computer program (see appendix 2) was written to describe the simultaneous transformation kinetics in power plant steels based on the method described in the previous chapter. The method is totally general, enabling predictions to be made for a wide range of alloys once the appropriate compositions and driving forces have been calculated using MTDATA. The program then gives the volume fraction of all the phases incorporated as a function of time for the temperature in question. It is also possible to record other information. For example, the extent of reaction parameter, Φ and the mean particle size. Also the iterative nature of the method makes it possible to track the size[1] of particles nucleated in each interval, and thereby give a size distribution.

Before making any predictions it was necessary to find the unknown parameters in the nucleation equation, namely the site density, N_0, and interfacial energy, σ. For the model to be of practical use one set of parameters should be applicable to all the steels to be studied. Once these parameters had been determined they were tested by making predictions for other steels and then comparing with experiment. Finally, the model was used to make predictions for some hypothetical alloy compositions.

8.2 Calibration of the Model

For each phase incorporated into the model there are two unknown parameters which must be found by fitting predicted and experimental results. These are the site density and interfacial energy for nucleation. Due to the large number of phases and limited data a range of alloys must be used to find all the parameters. These must then be tested by making predictions for other steels to ensure that the parameters are generally applicable. Experimental data of particular use are in the form of volume fraction *vs* time curves for each phase as these enable the model to be verified over the whole range of transformation. More commonly, the data are simply indicate the presence of absence of a phase after heat treatment. Such data are also valuable and may be used to check whether the onset of precipitation is predicted at the correct time.

8.2.1 M_2X and $M_{23}C_6$

The micrographs taken from the tempered samples of 10CrMoV material, described in chapter 4, provide a good source of data for both M_2X and $M_{23}C_6$ precipitation. The volume

[1] Strictly speaking this will be an *extended* size, but since as the volume fraction of precipitates is small for power plant steels the difference between extended and real sizes is negligible

fractions of M_2X and $M_{23}C_6$ were measured in samples heat treated at 600 °C. These measurements helped to optimize σ and N_0 by minimizing the square of the difference between the measured and predicted volume fractions. Predictions were then made for the temperature range 500 to 800 °C for comparison with the measured carbide stability diagram.

The fractions of M_2X and $M_{23}C_6$ were measured by tracing micrographs taken from carbide extraction replicas examined in the TEM at relatively low magnifications ($\simeq \times 7000$ for $M_{23}C_6$ and $\simeq \times 50\,000$ for M_2X) to ensure the area being studied was representative of the sample as a whole. Only the particles of interest as identified by selected area diffraction (*i.e.* $M_{23}C_6$ or M_2X) were included on the tracing. The area fractions were then measured using a "Seescan" image analysis system. Any stereological effects were assumed to be negligible and so that the area and volume fractions were the same, this may be justified because the particles are in a number of orientations, and by using extraction replicas the thickness errors introduced in thin foil analysis are not present. The measured values are shown in Table 8.1.

Phase	Heat Treatment	Volume Fraction
M_2X	10 mins at 600 °C	0.001±0.005
$M_{23}C_6$	1 h at 600 °C	0.02±0.005

Table 8.1: Measured fractions of M_2X and $M_{23}C_6$ in 10CrMoV COST F steel.

Once the optimum values were determined for the 10CrMoV steel, predictions were made for the $2\frac{1}{4}$Cr1Mo alloy and were compared with the Baker and Nutting diagram assuming the carbide was noticed in their TEM when its fraction exceeded 0.01. This is sufficient to asses whether the predicted lines follow the correct trends.

The set of fitting parameters which simultaneously gave the best fit to the Baker and Nutting data and that for the 10CrMoV steel are shown in Table 8.2.

Phase	σ / Jm^{-2}	N_0 / m^{-3}
M_2X	0.248	2.7×10^{16}
MX	0.260	5.4×10^{13}
$M_{23}C_6$	0.269	2.7×10^{15}
Laves	0.331	2.7×10^{8}

Table 8.2: Values for interfacial energy, σ, and site density, N_0, for nuclei of each phase which give the best fit between prediction and experiment

It is possible that a different set could equally well describe the experimental data. However, it is noteworthy that the interfacial energy correlates with the known place in the precipitation sequence (*i.e.* M_2X forms before $M_{23}C_6$). The predicted TTT–diagrams are shown in Figure 8.1 with lines plotted corresponding to the observed volume fractions. The agreement is reasonable, and in particular it should be noted that the large difference in the kinetics between the two steels has been reproduced using one set of fitting parameters.

8.2.2 Laves Phase

The quantity of data giving Laves phase volume fractions as a function of time and temperature in the COST F steel is insufficient to find the optimum values of the fitting parameters. However, there are published data for the 9CrMoWV steel *NF-616* (composition shown in Table 8.3) [Mimura *et al.* 1993; Hald, 1994].

C	Cr	Mo	W	V	Nb	N	Fe
0.106	8.96	0.47	1.83	0.20	0.069	0.051	bal

Table 8.3: Concentration of the major alloying elements in 9CrMoWV steel *NF616* in wt%

Hald (1994) already has a model for Laves phase precipitation in this steel as described in section 3.11. This model has not been successfully applied to any other steels and is only valid when the other phases have reached their equilibrium volume fractions before Laves phase starts to form, as is the case in *NF-616*. The predictions from the simultaneous kinetics model were compared with those of Hald. The simultaneous kinetics model also accounts for the prior formation of M_2X and $M_{23}C_6$ keeping the fitting parameters constant. The interfacial energy and site density for Laves phase were then found by minimising the square of the difference between the two sets of predicted results. The optimum values are shown in Table 8.3. Figure 8.2 shows a comparison between the TTT–curve estimated using the simultaneous kinetics model and the results of Hald's model for the same volume fraction. The lines for M_2X and $M_{23}C_6$ predicted by the simultaneous kinetics model are also shown. For all phases the kinetics are predicted to be faster than in the COST F alloy. The deviation of the line for Laves phase predicted by the simultaneous kinetics model with that of Hald at higher temperatures is probably due to differences in way thermodynamic calculations have been performed.

8.2.3 MX

MTDATA does not treat MX as a single phase, but instead is able to give driving force and

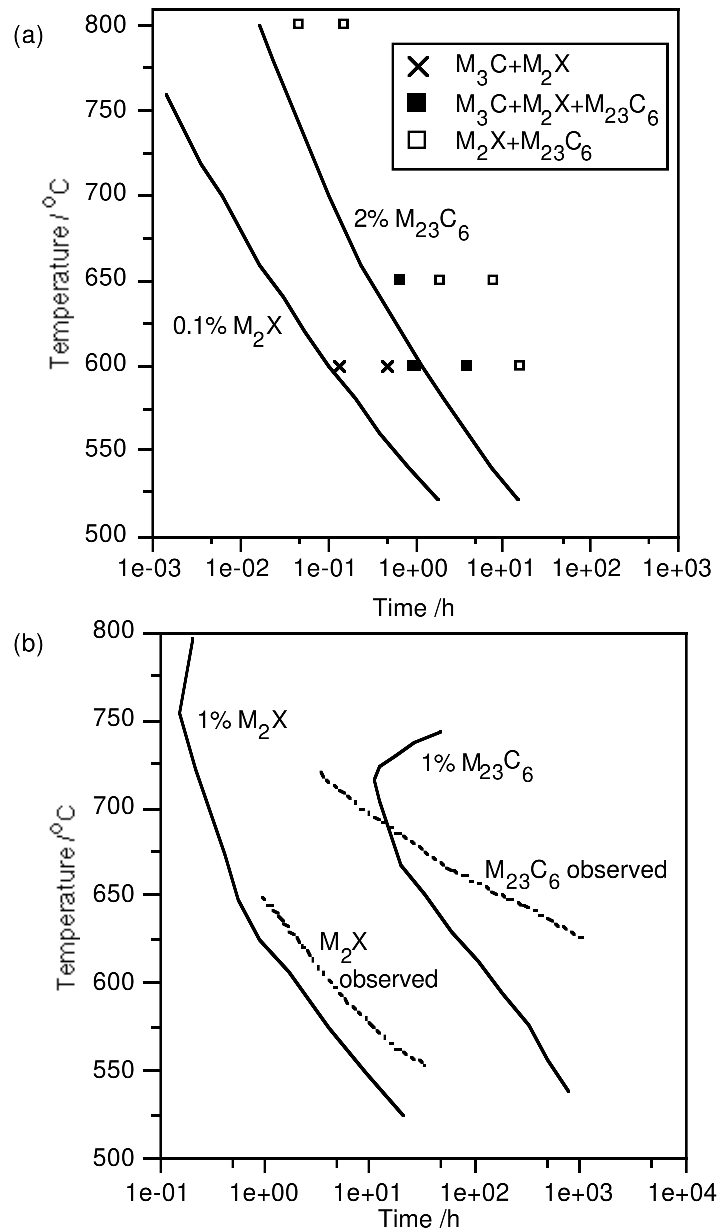

Figure 8.1: (a) Predicted TTT–diagram for M_2X and $M_{23}C_6$ precipitation in a 10CrMoV steel. Experimental points are from the TEM investigation are also marked on the diagram (b) Predicted TTT–diagram for a $2\frac{1}{4}$Cr1Mo alloy, together with Baker and Nutting's measured lines.

compositions for the stoichiometric compounds VN, NbN and NbC. These three are therefore treated as separate phases in the model, with the total MX content being taken as the sum of their volume fractions. Unfortunately, although a number of studies have been made of MX precipitation in 9–12 wt% Cr steels, there is a lack of suitable quantitative data with which to calibrate the model. In this case it is necessary to make a realistic estimate of the values

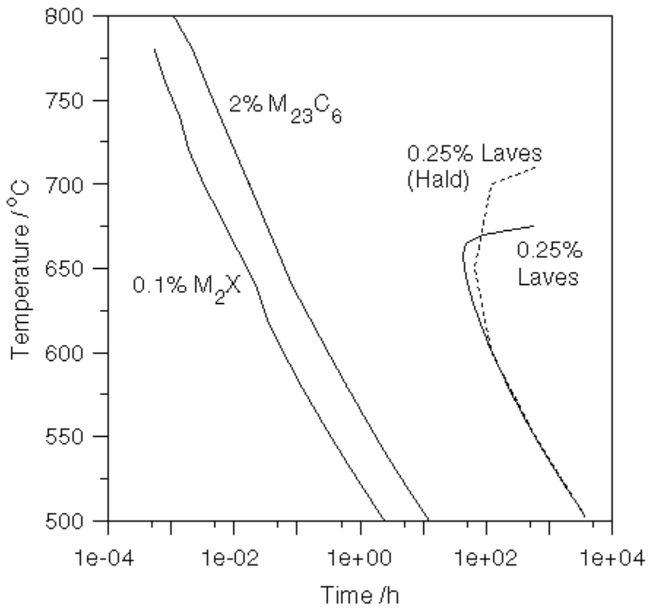

Figure 8.2: Predicted TTT–diagram for a 9CrMoWV steel *NF-616*. Also plotted is the TTT–line for Laves phase precipitation predicted by Hald's (1994) model which is limited to the estimation of Laves phase volume fraction only.

for σ and N_0. Evidence from thermodynamics suggests that MX precipitates after M_2X and before $M_{23}C_6$ during isothermal heating. It was assumed that the σ and N_0 values for all three stoichiometric MX type compounds are the same. The interfacial energy was therefore set intermediate to the values for M_2X and $M_{23}C_6$ and the site density was adjusted so that MX precipitation started at approximately the right time. The optimum values are shown in Table 8.3.

8.3 Comparison of Different Power Plant Steels

The model was first applied to make predictions for three power plant steels which span a wide composition range and exhibit very different precipitation kinetics. The steels investigated were 10CrMoV COST F (see Table 4.1), $2\frac{1}{4}$Cr1Mo and 3Cr1.5Mo (compositions shown in Table 8.4).

The predicted TTT–diagrams for the $2\frac{1}{4}$Cr1Mo and COST F alloys have already been presented. The predicted diagram for the 3Cr1.5Mo alloy is shown in Figure 8.3; the precipitation is faster in the $2\frac{1}{4}$Cr1Mo alloy and slightly slower than in the 10CrMoV steel. These results are consistent with data reported by Klueh and Nasreldin (1987) who showed that $M_{23}C_6$ formation is virtually completed within 8 hours at 688 °C in the 3Cr1.5Mo steel,

	C	Mn	Cr	Mo	Ni	V	Fe
$2\frac{1}{4}$Cr1Mo	0.15	0.50	2.12	0.9	0.17	–	bal
3Cr1.5Mo	0.1	1.0	3.0	1.5	0.1	0.1	bal

Table 8.4: Concentration (in wt%) of the major alloying elements in two of the steels used in the comparison of power plant alloys

whereas Baker and Nutting did not observe any $M_{23}C_6$ in the $2\frac{1}{4}$Cr1Mo alloy until after 20 hours at the same temperature

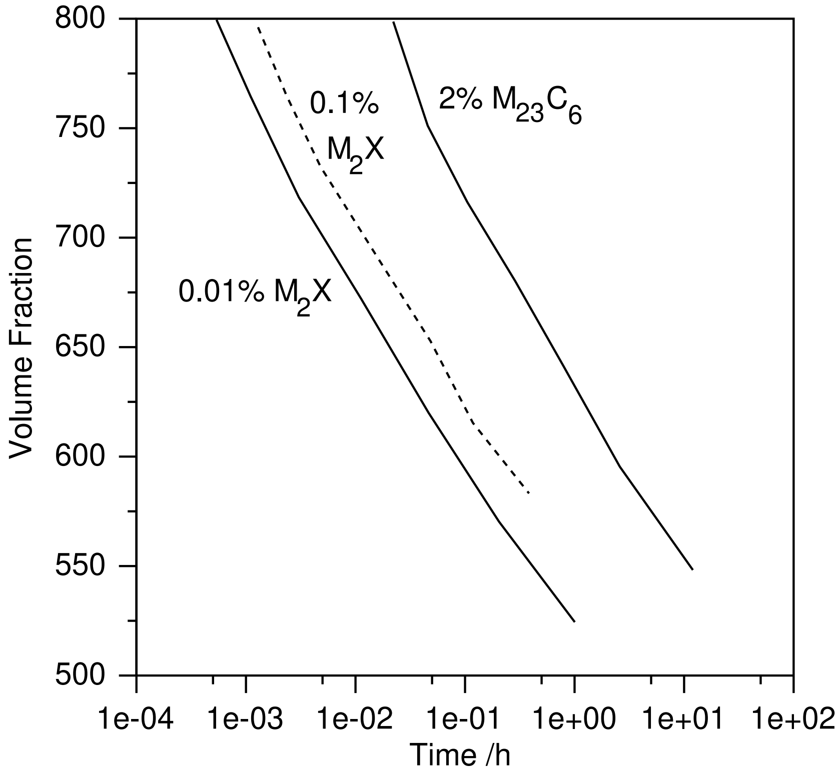

Figure 8.3: Predicted TTT–diagram for a 3Cr1.5Mo alloy.

Figure 8.4 demonstrates the differences between the steels more clearly. It can be seen that in the $2\frac{1}{4}$Cr1Mo steel the M_2C precipitates well before the $M_{23}C_6$. A larger volume fraction of M_2C then forms, which further suppresses $M_{23}C_6$ precipitation. In the 3Cr1.5Mo alloy M_2C and $M_{23}C_6$ start to precipitate at similar times. Both phases compete for solute, but the $M_{23}C_6$ dominates and M_2C starts to dissolve before it has reached a volume fraction which is sufficient to delay $M_{23}C_6$ precipitation. In the COST F alloy although M_2X starts to form first, it does not reach a large volume fraction before dissolution begins so that its effect in suppressing $M_{23}C_6$ is small.

Other information may be obtained by studying plots showing the variation of the extent of reaction with time. Figure 8.5 shows such plots for the three steels investigated here at 600 °C. The most significant differences occur between the $2\frac{1}{4}$Cr1Mo alloy and the other two steels. In the $2\frac{1}{4}$Cr1Mo alloy the start of M_2X dissolution (which occurs when $1 - \Phi$ for this phase reaches 0) is accompanied by a sharp change in the gradient of the $M_{23}C_6$ line. This is because at this point there is a large volume fraction of M_2X present, which, as it dissolves, supplies solute to the precipitating $M_{23}C_6$ and enables it to form without further depleting the matrix solute level. $M_{23}C_6$ consequently forms at after an exaggerated time at temperature. In the other two steels the fraction of M_2X is smaller when precipitation stops and its dissolution is of less significance to the precipitation of $M_{23}C_6$ thus the change in gradient of the $M_{23}C_6$ line is much less pronounced.

8.4 Effect of Composition and Tempering within the 9–12 wt% Cr Steels

Once it had been verified that the model was able to successfully reproduce experimental results for a range of power plant steels, attention was focussed on variations within the 9–12 wt% Cr alloys.

8.4.1 Shape of the TTT Curves

On feature of both the predicted and measured kinetics for the 10CrMoV steel is that over the temperature range studied an increase in the temperature always leads to a shorter time for precipitation unlike the generally expected 'C' shape as described in section 3.2. It is possible that all of the observations and predictions correspond to temperatures in the lower part of the C–curve, below the nose. To understand this predictions were made for higher temperatures, artificially assuming that the matrix remains ferritic. The predicted lines are shown in Figure 8.6 and the expected C–curve behaviour was obtained. However, the noses of these curves lie well above the Ae_3 temperature. Clearly, in practice the matrix at these temperatures will have transformed to austenite and the carbides will not precipitate at all.

8.4.2 Effect of Chromium on Precipitation Kinetics

To assess the influence of chromium content on M_2X and $M_{23}C_6$ precipitation, calculations were performed for a hypothetical alloy, which is a 12wt% chromium variant of the COST F 10CrMoV steel (Figure 8.7). An increase in chromium level causes a slight increase in the rate of precipitation of both M_2X and $M_{23}C_6$ but the order of events remains unchanged. The final (equilibrium) volume fraction of $M_{23}C_6$ is not significantly changed by the addition of extra chromium, as confirmed by MTDATA calculations.

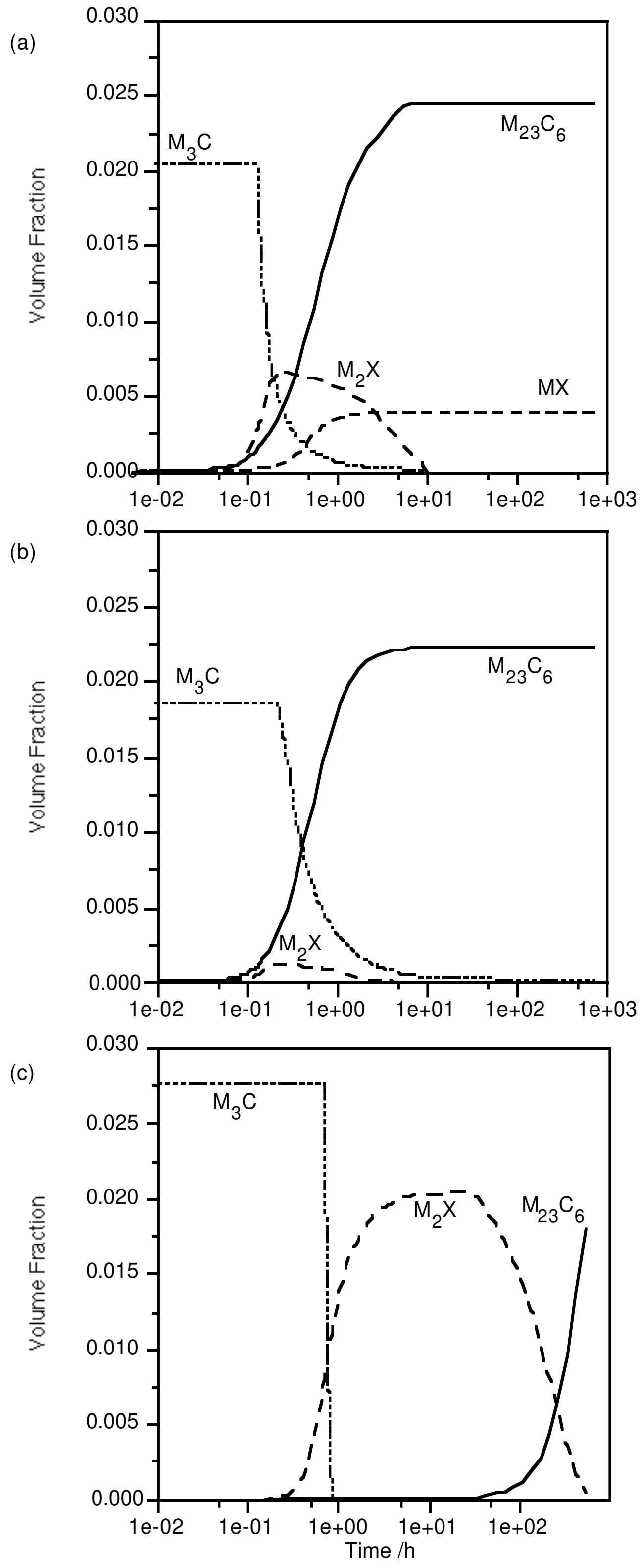

Figure 8.4: Evolution of volume fraction with time at 600 °C for (a) a 10Cr-MoV alloy, (b) a 3Cr1.5Mo alloy and (c) a $2\frac{1}{4}$Cr1Mo alloy.

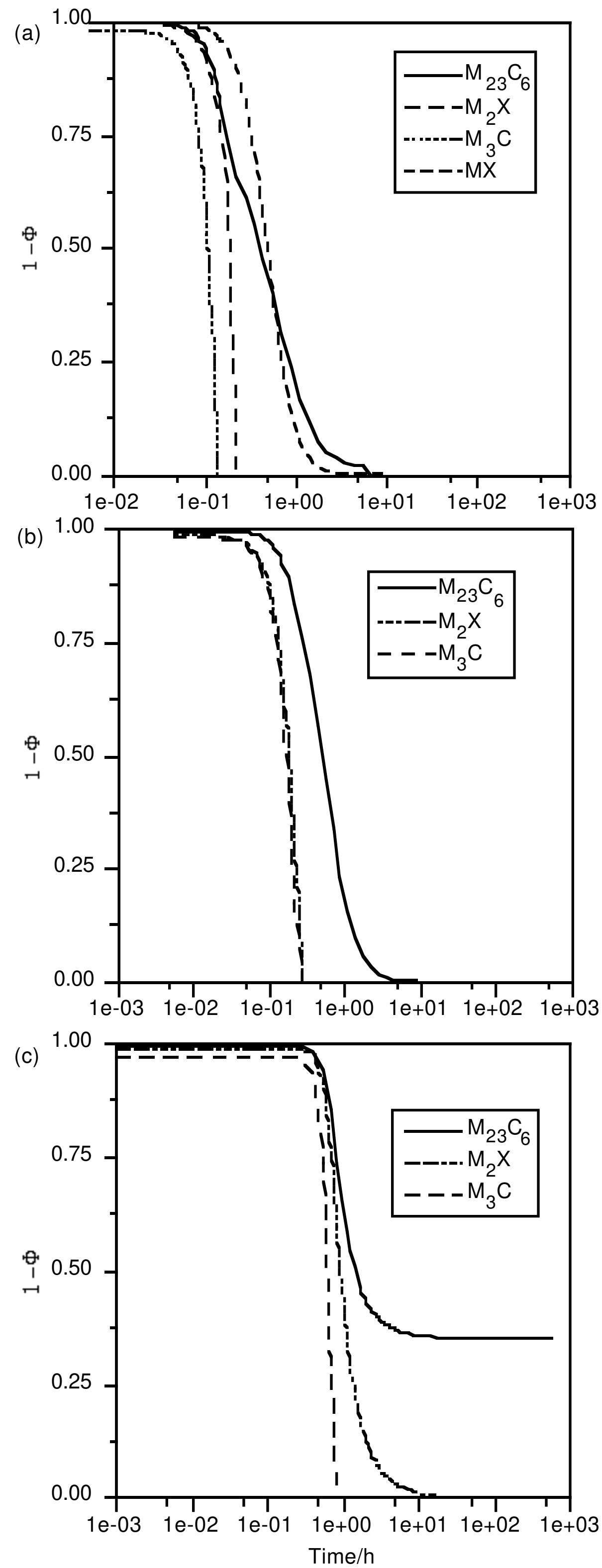

Figure 8.5: Variation of the extent of reaction with time at 600 °C for (a) a 10CrMoV alloy, (b) a 3Cr1.5Mo alloy and (c) a $2\frac{1}{4}$Cr1Mo alloy.

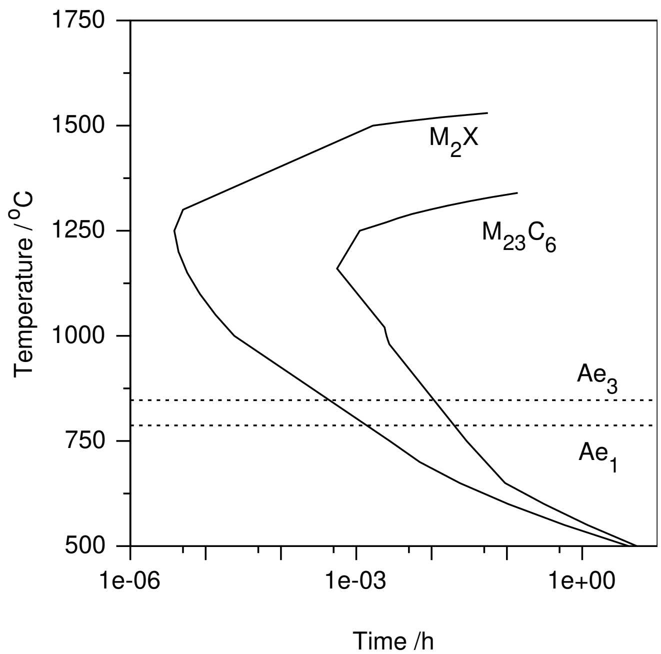

Figure 8.6: Predicted TTT diagram for a 10CrMoV steel for a greater temperature range showing hypothetical C–curve behaviour if ferrite remains stable at all temperatures. Also shown are the Ae_1 and Ae_3 lines calculated using MTDATA. In practice C–curve behaviour is not observed since the upper part of both curves lie at temperatures well above the ferrite/austenite phase boundary and carbides will not precipitate.

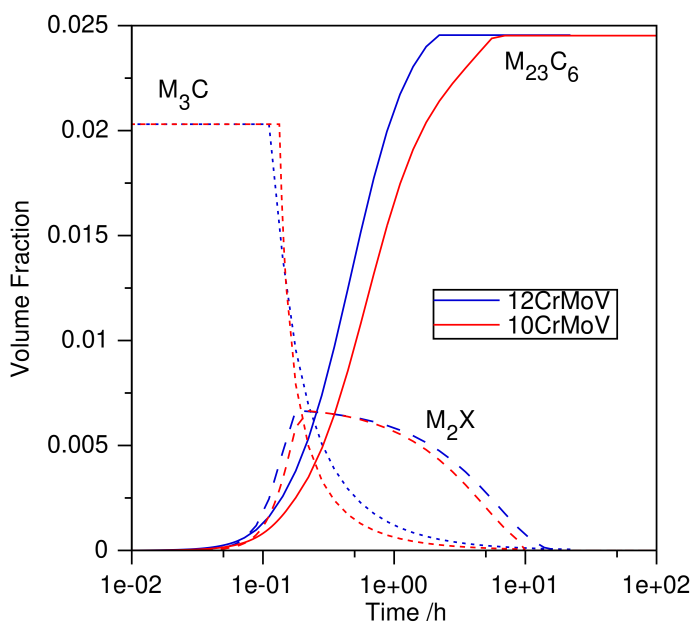

Figure 8.7 : Predicted evolution of volume fraction for phases precipitating at 600 °C in a 10CrMoV and a 12CrMoV steel

8.4.3 Effect of Nitrogen on Precipitation Kinetics

The nitrogen content of the 9–12 wt% Cr steels is often adjusted by alloy designers to optimize performance. Its calculated effect on the kinetics of precipitation in COST F steel is shown in Figure 8.8. Additional nitrogen stabilizes M_2X which becomes an equilibrium phase at 600 °C. Therefore, unlike in the standard COST F alloy (see Fig. 8.4a) M_2X does not completely redissolve as $M_{23}C_6$ precipitates. Also, the volume fraction of M_2X which forms before dissolution begins is greater with additional nitrogen. However, it is not predicted to be sufficient to retard $M_{23}C_6$ precipitation which occurs at approximately the same time in both steels. The addition of nitrogen does not appear to change the volume fraction of MX . This is because MTDATA predicts that the maximum fraction of this phase is limited in this alloy by the availability of suitable 'M' atoms (*i.e.* V and Nb). In practice, if other alloying elements also partition slightly into MX then the nitrogen content may limit the MX volume fraction, in which case additional nitrogen would result in an increase in the amount of MX precipitate.

8.4.4 Effect of Tempering Treatment on Precipitation Kinetics

In practice the 9-12wt% chromium steels are subjected to severe tempering treatments before entering service. To study how a high temperature temper affects the subsequent formation of Laves phase two predictions were made. One for *NF-616* steel held at 600 °C and the other for the same steel held at 700 °C for ten minutes, followed by a hold at 600 °C. Figure 8.9 shows a comparison between the evolution of volume fraction in both cases. At 700 °C the carbides rapidly reach their equilibrium volume fractions. At this temperature the driving force for Laves phase formation is very small and the volume fraction which forms is insignificant. On lowering the temperature to 600 °C the driving force for Laves phase formation increases and it starts to precipitate, albeit very slowly compared to the carbo–nitrides. The time at which a measurable volume fraction of Laves phase forms is similar for the two kinds of heat treatment. This is because, even at a reduced temperature the carbo–nitrides form their equilibrium volumes in a small fraction of the time it takes Laves phase to precipitate. With reference to Laves phase precipitation, the two cases are therefore essentially the same. Increasing the time of the high temperature temper to several hours would not be expected to change this result, since this would only lead to coarsening of the carbo–nitride phases.

8.5 'Blind' Predictions for a 12wt% Cr steel

The ultimate test for the model is to use it to make predictions for a steel without access to any experimental data. A composition and heat treatment for a 12wt% Cr steel were supplied

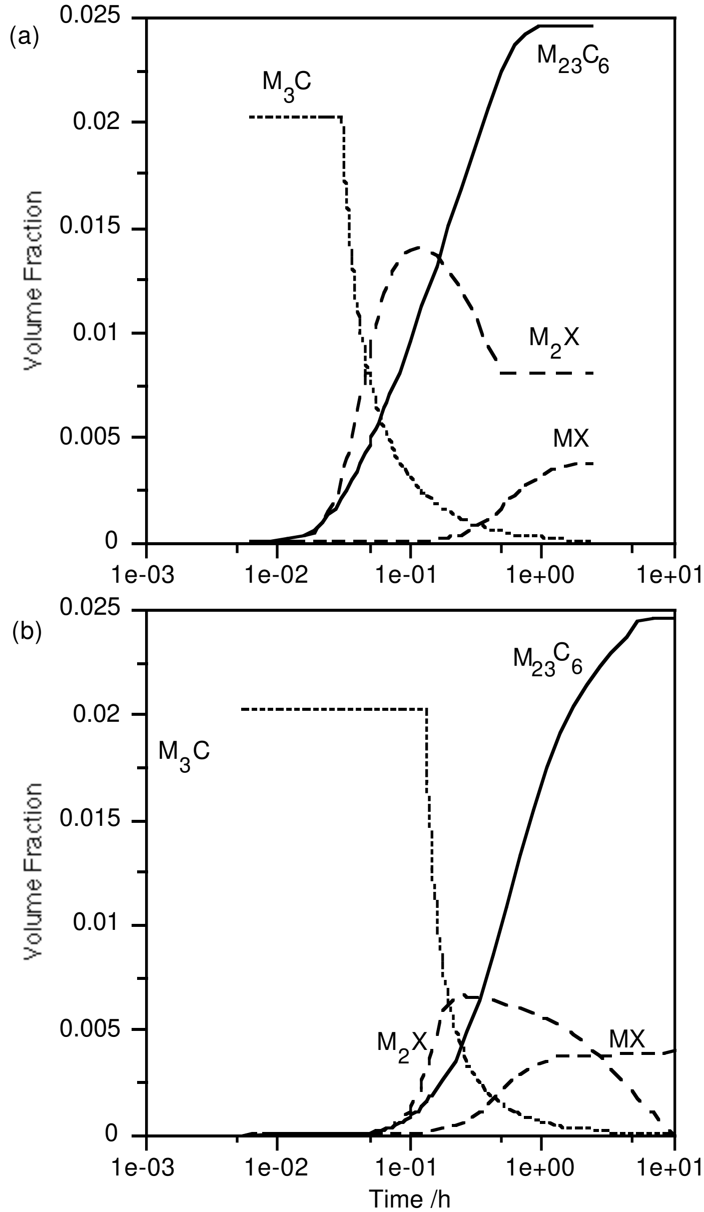

Figure 8.8: Predicted precipitation kinetics at 600 °C for COST F (10CrMoV) alloy (a) with an enhanced nitrogen content (0.1 wt% N) (b) without additional nitrogen (0.05 wt% N).

by GEC Alsthom (steel ME, full composition shown in Table 8.5).

Volume fraction and size predictions were then made for this alloy without reference to any experimental data. These results were then compared with the observations made during experiments carried out at GEC Alsthom, Rugby.

Following austenitisation at 1150 °C for 1 h this alloy is tempered at 650 °C for 6 h. The predicted evolution of volume fraction for this treatment is shown in Figure 8.10. The time of

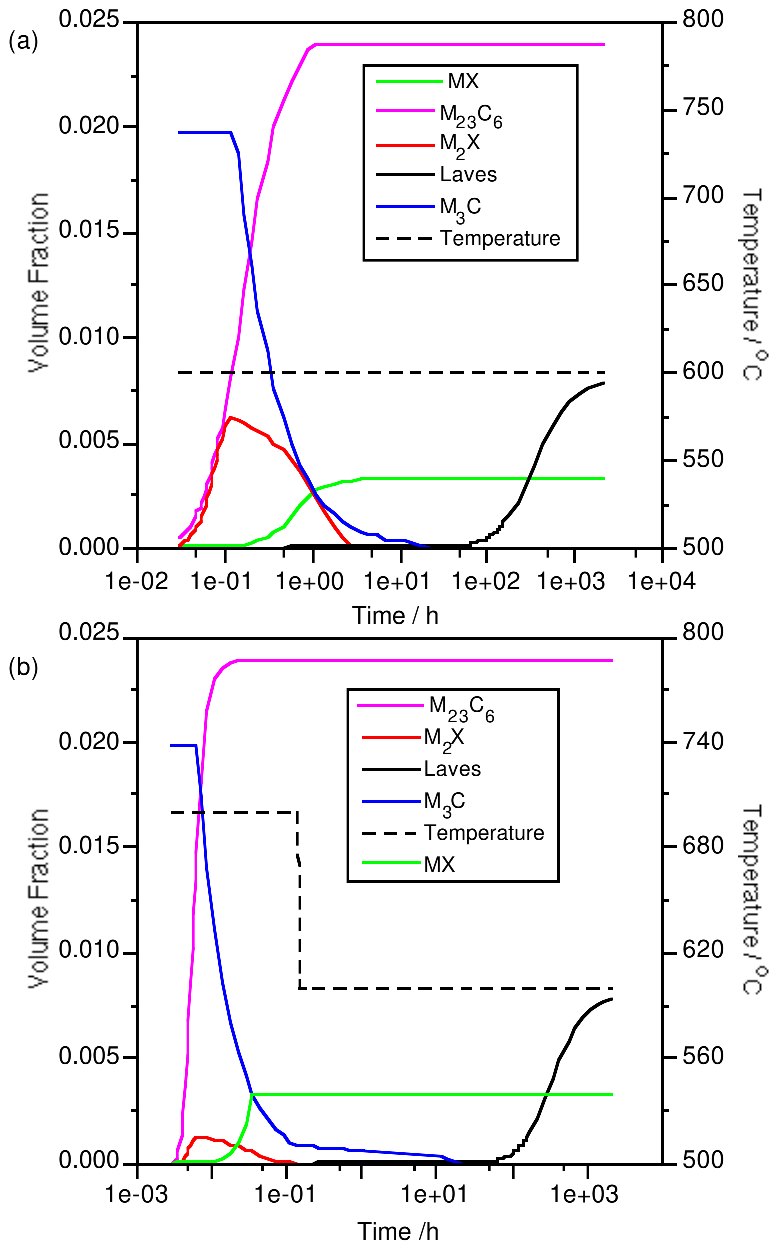

Figure 8.9 : Predicted evolution of volume fraction in a 9CrMoVW steel. Two cases are shown (a) isothermal hold at 600 °C and (b) where a 700 °C temper has been simulated prior to holding at 600 °C.

C	Si	Mn	P	S	Cr	Mo	Ni	Al	B	N	V	W	Nb	Fe
0.16	0.28	0.74	0.22	0.15	11.2	0.61	0.52	0.05	0.008	0.065	0.28	0.10	0.29	bal

Table 8.5: Composition of steel ME in wt%.

the 1150 °C austenitisation has been reduced so that the whole treatment can be plotted on one graph. This will not make a difference since equilibrium is very rapidly reached at this temperature and subsequent changes will only involve coarsening which is not incorporated into the model.

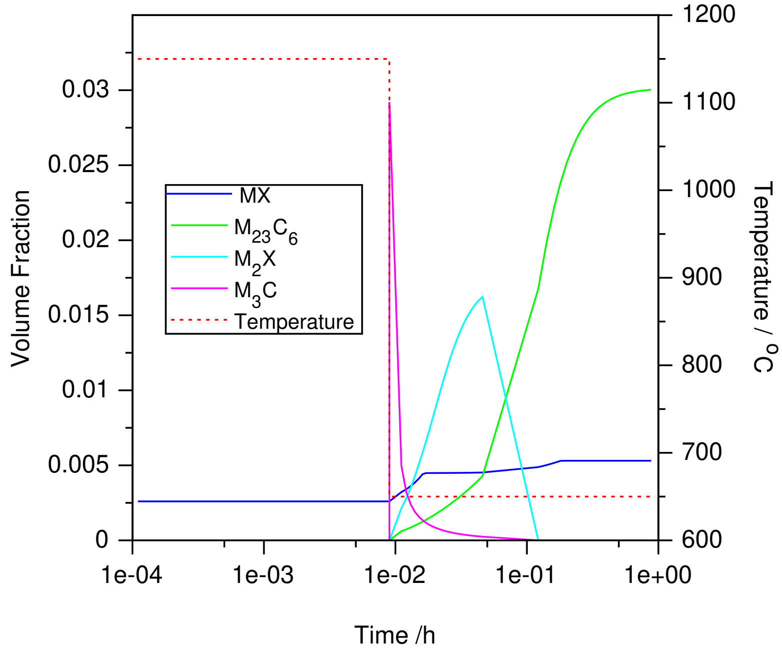

Figure 8.10: Predicted evolution of volume fraction in a 12wt% Cr steel, ME for a two stage heat treatment.

MX is thought to be an important phases in making a positive contribution to the creep strength and so more detailed predictions were made for this phase. Figure 8.11 shows the evolution of volume fraction for the three stoichiometric phases which are of the MX type, NbN, VN and NbC. It can be seen that even at 1150 °C it is predicted that some MX is present with composition NbN. At lower the lower temperature of 650 °C VN and NbC also precipitate, with VN rapidly becoming dominant.

An MTDATA calculation showing how the equilibrium fractions of the various MX type phases vary with temperature is shown in Figure 8.12. It can be seen that the equilibrium fractions of VN and NbC pass through a maximum at approximately 900 °C and that this is coincident with a minimum in the equilibrium volume fraction of NbN. The total equilibrium fraction of MX is also predicted to be at a maximum at a temperature of 900 °C.

These predictions were then compared with the experimental results for this steel due to Strang and Vodarek (1996b). A comparison of the observed and predicted phases is shown in Table 8.6.

It can be seen that whilst the predictions and observations agree for material in the

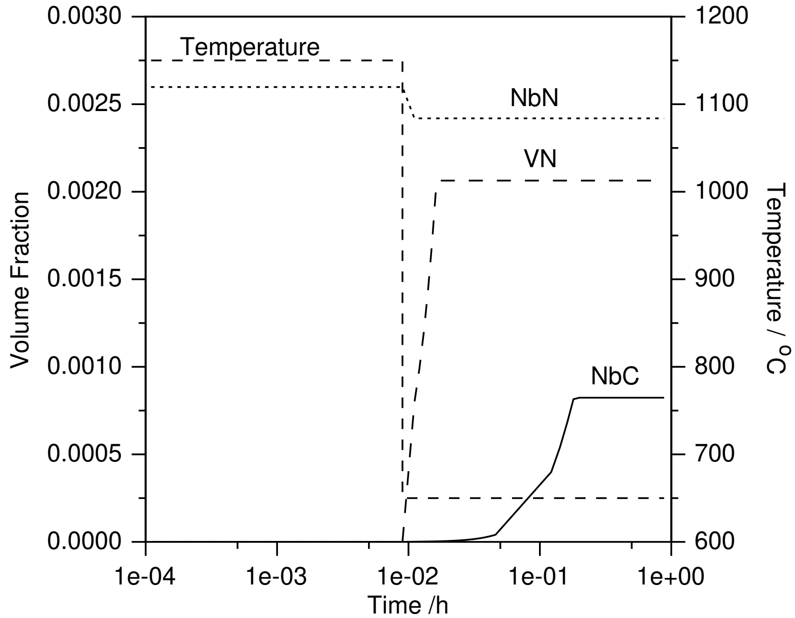

Figure 8.11: Predicted volume fraction of MX type precipitates for a two stage heat treatment.

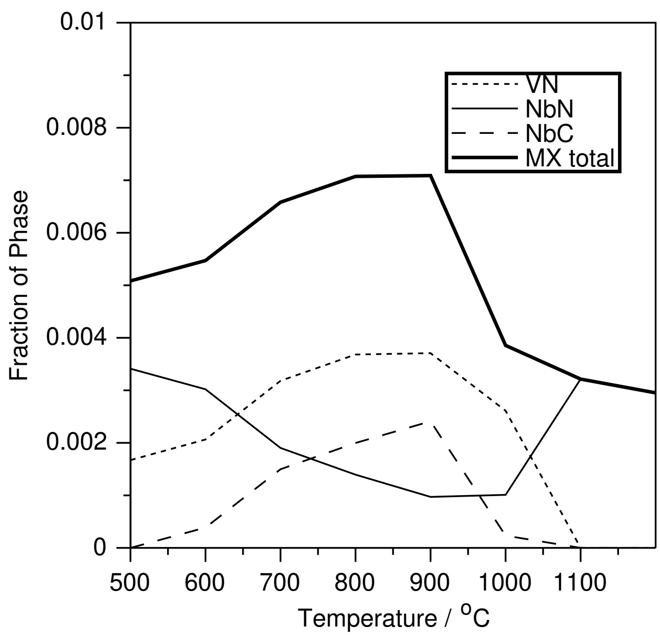

Figure 8.12: MTDATA calculation showing the variation in the equilibrium fraction with temperature of the MX type phases in steel ME.

austenitised condition, there are notable differences in the phases predicted and those observed after tempering. The model predicts that by the time tempering is complete, M_2X will have redissolved, and secondary MX (VN and NbC) will have precipitated. Measurements show that

Condition	Phases Observed	Phases Predicted
1150°C, 1 h	NbX	NbN
1150°C,1 h + 650°C, 6 h	NbX, $M_{23}C_6$, M_2X	NbN, VN, NbC, $M_{23}C_6$

Table 8.6: A comparison of the predicted and measured phases in steel ME (experimental data due to Strang and Vodarek, 1996b).

after tempering M_2X is still present there is no secondary MX . The predicted dissolution of M_2X and precipitation of secondary MX is observed, but only at later times during subsequent creep testing. The discrepancy between predictions and measurement may be attributed to over–estimating the kinetics of secondary MX precipitation. This is perhaps not surprising, because for this phase the fitting parameters could only be approximately determined due to a lack of suitable data.

The predicted size distribution of NbN particles following austenitisation at 1150°C is shown in Figure 8.13. It can be seen that there are fewer smaller particles than larger ones. This is expected since the smaller particles are those which nucleated later on in the transformation by which time the nucleation rate will have fallen. The maximum predicted particle radius is $\simeq 0.02\mu$m. Because this calculation neglects the effects of coarsening, which is expected to be well advanced after this heat treatment, it is perhaps not surprising that the predicted maximum size is considerably smaller than a typical measured particle radius of 0.22μm. In cases where coarsening is significant the size distributions predicted by the model are still useful and could be used as inputs into a model for coarsening.

8.6 Summary

The new model for simultaneous transformation kinetics, described in chapter 7 has been applied to a range of power plant alloys, with compositions from $2\frac{1}{4}$Cr1Mo to 10CrMoV. The site density and surface energy for nucleation, which are unknown parameters were found for each phase by fitting predicted and experimental results, same set of parameters was used for all steels. The model has correctly predicted the large difference in the kinetics observed in the $2\frac{1}{4}$Cr1Mo steel compared with the 10CrMoV alloy. Hald's results for Laves phase precipitation in 9CrMoWV alloy *NF-616* have also been reproduced, taking into account the prior formation of M_2X, $M_{23}C_6$ and MX.

The reason for the slower kinetics observed in the $2\frac{1}{4}$Cr1Mo alloy, particularly of $M_{23}C_6$ has been attributed to the relatively large volume fraction of M_2X which forms in this steel. This reduces the driving force for $M_{23}C_6$ and suppresses its formation to longer times. Without

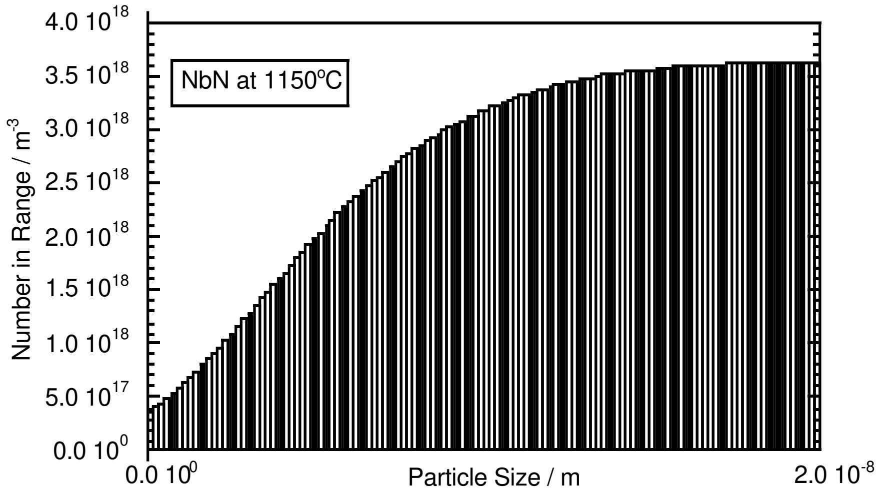

Figure 8.13: Predicted size distribution of NbN particles in steel ME after 1 h at 1150°C.

accounting for simultaneous kinetics it is not possible to reproduce this effect and this explains why the simple models, described in chapter 6, failed.

The model has also been used to make predictions for some hypothetical compositions. It has been shown that an increase in chromium level is predicted to lead to a slight acceleration in the precipitation kinetics in the 10CrMoV steel. Nitrogen additions are predicted to stabilise M_2X in this steel so that it becomes an equilibrium phase at 600°C and does not completely redissolve. It has been demonstrated that in the 10CrMoV steel for all practical purposes the kinetics of precipitation will become more rapid as the temperature is increased, this corresponds to the lower portion of the kinetics C–curve.

Predictions have been made for a 12 wt% Cr steel, ME, and these have been compared with experimental observations. After austenitisation predictions and experiments agree, on tempering the predicted kinetics are faster than those observed experimentally although the precipitation sequences are the same. This is probably due to the need for further refinement of the fitting parameters for MX nucleation – this requires more experimental data.

CHAPTER NINE

Conclusions and Suggestions for Further Work

Experiments have shown that whilst the precipitation sequence is similar in a 10 wt% Cr steel compared with a conventional $2\frac{1}{4}$Cr1Mo alloy, the precipitation kinetics are much faster.

To model this difference in kinetics it is necessary to account for the simultaneous formation of competing phases. A new model has been developed which allows the simultaneous precipitation and dissolution of 6 phases, accounting for the competition of solute. This model has been shown to be generally applicable to a wide range of power plant steels using a single set of fitting parameters.

It is therefore now possible to predict the complete evolution of volume fraction for all the precipitates up from the initial conditions up until equilibrium is reached. By recalculating the appropriate thermodynamic parameters it is also possible to study how changes in composition and heat treatment will affect this evolution.

The model was used to make a number of predictions for a 10CrMoV steel where it was shown that adding nitrogen stabilises M_2X, chromium additions accelerate the kinetics and the upper portion of the kinetics C–curve will not be observed in practice since it occurs at temperatures where the matrix is austenitic and carbides do not precipitate.

Using MTDATA it was predicted that both Mo and W encourage the formation of Laves phase, with W being the more potent. Complimentary to this it was demonstrated that Laves phase formation is expected to deplete the matrix of W and Mo and is therefore expected to lead to a reduction in solid solution strengthening.

MTDATA calculations have also shown that in a $2\frac{1}{4}$Cr1Mo alloy cementite with the equilibrium composition is more stable than M_2X for some temperatures. The fact that M_2X forms after cementite at these temperatures implies that cementite is initially far from equilibrium and its enrichment is not completed when M_2X precipitation begins.

This work has highlighted a number of areas where further study would be of practical and theoretical interest. To provide further verification of the model requires generating more quantitative data, particularly for MX precipitation. It would also be useful to be able to predict the sizes of particles after long term tempering. This requires a model for coarsening to be added to that for precipitation. Ulimately the effects of stress and particle position need to be accounted for.

It may also be desirable from a theoretical point of view to allow for the multi–component nature of growth and nucleation in a more rigorous way. However, it should be noted that this will increase considerably the complexity of the model and also the computation time and may not lead to a significant improvement in the predictions.

APPENDIX ONE

Neural Network Modelling of Dislocation Density

1. Introduction

It is recognised that the dislocation density of power plant steels is an important parameter in determining the creep properties. The forest strengthening due to persistent dislocations is believed to lead to better steels. The work presented here is an attempt to give a quantitative interpretation of the experimental data for the 9-12wt% steels shown in table 1.3.

A modern, computer intensive method for the recognition of patterns in experimental data, employs an artificial neural network. In normal regression methods the analysis begins with the prior choice of a relationship (usually linear) between the output and input variables. A major advantage of the neural network is that it can in principle find the best fit relationship automatically, irrespective of the complexity with which the variables might be associated. Only the input and output data have to be presented to the computer, which in effect tries out all kinds of relationships in its search for an optimum fit. As in regression analysis, the results then consist of a series of coefficients (called weights) and a specification of the kind of function which in combination with the weights relates the inputs to the outputs. Obviously, the search for the optimum representation can be very computer intensive, but once the process is completed (ie the network trained) the estimation of the outputs becomes very rapid.

Blind models can be susceptible to over representation, in which case even interpolation becomes dangerous. MacKay (1992a, 1992b, 1994a, 1994b) has developed a neural network method which is based on a Bayesian framework. In essence, this allows the probability of a model being a true representation, out of a choice of models, to be assessed quantitatively. A neural network like this is capable of realizing a great variety of non-linear relationships of considerable complexity. Data are presented to the network in the form of input and output parameters, and the optimum non-linear relationship found by minimizing a penalized likelihood. The network in effect tries out many kinds of relationships in its search for an optimum fit.

2. Variables

All the measured variables which it was thought could possibly influence the dislocation density are used as input variables for the network. These variables are shown in Table 1.and described below.

The dislocation cell size would be expected to vary with dislocation density. The cell size is characterised by the maximum and minimum cell dimensions, l_{max} and l_{min}.

The temperatures and times of the various tempering treatments would clearly be expected to influence the dislocation density. Not all of the samples receive the third temper. In this case the time for the third temper has been set to zero, and the temperature to that of the second temper.

Creep time, temperature and stress would all be expected to be significant in determining dislocation density. A creep stress of zero was input for samples from the head of the creep specimen as well as as-received samples. The position of the sample in the creep specimen is also an input variable. Samples from as received material, those from the head of creep test specimens and those from the gauge length were all assigned a different value for position.

The concentrations of the carbide and nitride forming elements in the steel are also input. These concentrations will affect the volume fraction and chemical composition of the precipitates which will influence the dislocation density.

3. Data Used in the Analysis

The data used in this analysis are those which have been generated by COST programme for the alloys shown in table XXX. It is desirable to use as many data as are available to produce and test the model. A network which has been trained with a large dataset will be more likely to model real trends in the noisy data. There are a total of 36 data–sets for these alloys.

4. Analysis

The analysis was conducted using variables normalised between +0.5 and -0.5; this normalisation is not essential to the neural net approach but allows a convenient comparison of the influence of individual input variables on an output. The normalisation procedure is expressed quantitatively as follows:

$$x_N = \frac{x - x_{min}}{x_{max} - x_{min}} - 0.5 \tag{1}$$

where x_N is the normalised value of x; x_{min} and x_{max} are respectively the minimum and maximum values of x in the entire dataset.

The normalisation is straightforward for all the quantitative variables. The position variable was represented by assigning a value of -0.5 to samples from as–received material, 0 to samples from the head of creep specimens and 0.5 to gauge length samples.

The network consisted of 21 input nodes, a number of hidden nodes and an output node representing the dislocation density. The network was trained using a randomly chosen 19 of

Identifier	Description of Variable	Minimum	Maximum
l_{min}	Minimum distance across dislocation cell (mean value)	207 nm	1115 nm
l_{max}	Maximum distance across dislocation cell (mean value)	498 nm	2774 nm
T_1	Temperature of 1st temper	550°C	570°C
t_1	Time of 1st temper	8 h	20 h
T_2	Temperature of 2nd temper	700°C	730°C
t_2	Time of 2nd temper	12 h	24 h
T_3	Temperature of 3rd temper (if any)	0°C	720°C
t_3	Time of 3rd temper (if any)	0 h	17 h
B	Boron content of steel (wt.%)	0	0.01
N	Nitrogen content of steel (wt.%)	0.015	0.065
Creep T	Creep temperature	600°C	650°C
Creep t	Creep time	0 h	33410 h
Creep stress	Creep stress experienced	0 MPa	161 MPa
Position	As received, head or gauge length material	0	2
Cr	Chromium content of steel (wt.%)	9.34	11.10
V	Vanadium content of steel (wt.%)	0.20	0.27
W	Tungsten content of steel (wt.%)	0.012	1.810
Ni	Nickel content of steel (wt.%)	0.12	0.86
C	Carbon content of steel (wt.%)	0.11	0.17
Mo	Molybdenum content of steel (wt.%)	0.320	0.155
Nb	Niobium content of steel (wt.%)	0.030	0.066

Table 1. Input Parameters

the examples from the total of 36, the remaining 17 examples being as test data. The training data are used to develop the model. The test data are new experiments (previously unseen by the model, with which to test its reliability)

Training of the network involves minimisation of the regularised sum of squares errors between the output from the network and the measured dislocation density. Details of how the network is trained are discussed elsewhere (MacKay, 1992a). The dislocation density data are known to be noisy. If any form of analysis is used which does not recognise an intrinsic level of noise, then the resulting model may represent the training data quite precisely but fail to make any reasonable predictions. This is illustrated in Figure 1.

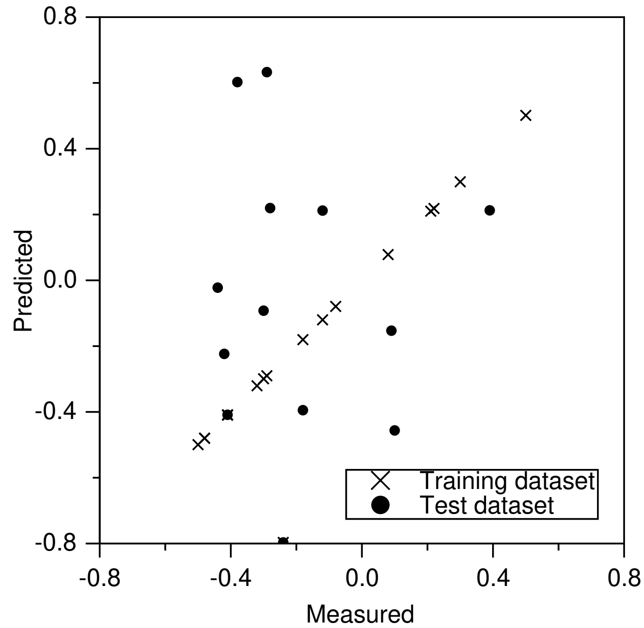

Figure 1: Normalised predicted dislocation density plotted against normalised measured dislocation density when the noise level is unset.

To eliminate this problem it is necessary to assign to the network an estimate of the noise level in the output data. The network will not then attempt to overfit the training data and a more reliable model results.

An approximate noise level was estimated by assuming the error in measurement of dislocation density is equal to the maximum difference between measurements from different laboratories. This gave a fractional error of approximately 0.6. This was taken as the error for 95% confidence. Assuming a normal distribution the error for 65% confidence is 0.3. The noise level was set to equal to 0.3. Figure 2 shows the graph of normalised predicted dislocation density *vs.* normalised measured dislocation density when the noise level was set to 0.3. The level of fit for the training and test data is now similar and the scatter in the data lies within the error associated with the measurements. This suggests that while the degree of fit for the training data is worse than previously the model used to produce Figure 2 likely to be more useful.

To verify the choice of 0.3 as the noise level was sensible the network was retrained with different noise levels ranging from 0.2 to 0.4. When the noise level was < 0.2 it was found that the level of fit for the training data was considerably better than that for the test data, suggesting that the noise was being modelled as in figure 1. When the noise level was $>$ 0.3 the correlation between the predicted dislocation density and the measured dislocation density became extremely poor. This suggests the network had not trained sufficiently to find

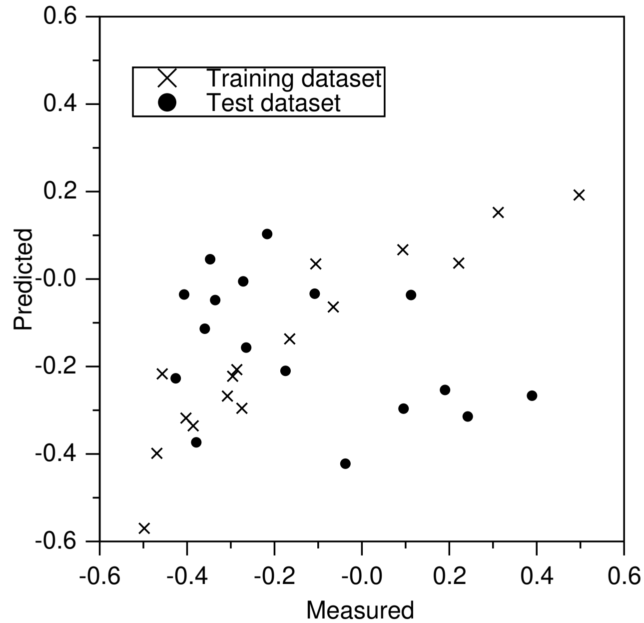

Figure 2: Normalised predicted dislocation density plotted against normalised measured dislocation density when the noise level is set to 0.3.

relationships between the inputs and output before the required noise level was reached and training stopped. Figure 3 shows a plot of the test and data energy vs. noise level. The data energy is related to the training data and the test energy to the test data. The energy is a measure of how good the fit is - a high energy implies a poor fit. It can be seen that as the noise level is increased the test and data energy converge.

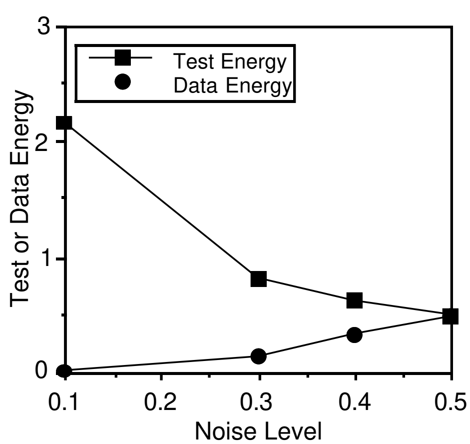

Figure 3: Variation of test and data energy with noise level. The energy gives a measure of the fit between prediction and experiment. As noise level is increased the fit becomes similar for both training and test data-sets.

5. Significance of Variables

One of the potentially useful results which the neural network approach gives is the significance of a variable. This is a measure of how important each of the input variables are, as perceived by the network in influencing the dislocation density. This significance will often be related to the real importance of a variable provided the following effects are allowed for:

The significance of a variable, as perceived by the network will depend on the range of that input variable in the training dataset. The extreme case occurs if a variable is constant throughout the training dataset. It will seem to the network that this variable has no influence on the output and its significance will be small, although in reality its importance in determining dislocation density may be large. The risk of misinterpreting the significance of a variable is reduced if the network is used to make predictions using data in which this variable is changed and all other variables are held constant. If the change of the variable is outside the range of the variation in the training dataset then the network will assign a large error to the predictions. The range of the variable over which the network is able to give predictions with a small error indicates how reliable the significance of that variable is likely to be. If the range over which predictions have a small error is large then the significance of the variable is more likely to be a true reflection of the importance of that variable.

It is often the case that there are two or more variables in the input dataset which are strongly dependent on each other, e.g. creep stress and position. The neural network may attribute all the significance to only one of the variables.

The estimated noise level in the training data which is input to the network would also be expected to affect the significance of the variables. This is because when this noise level is changed it changes the point at which the network will stop training and the significance of the variables will be those at this point. To investigate this effect the significance of the variables were recorded for three models which had been trained noise levels of 0.2, 0.3 and 0.4. It was found that there was some variation of significance with noise level. However, the variables which had a high significance at one noise level also had a high significance at the other noise levels although the order of the significance changed. This suggests that the choice of noise level is not critical when using the significance to differentiate between variables which have a large influence on dislocation density and those which have a small influence.

The significance of the variables produced using the best model (that corresponding to a noise level of 0.3) are shown in Figure 4.

Certain variables stand out on this graph as being more significant than others. In particular nitrogen concentration, boron concentration, minimum dislocation cell dimension, tem-

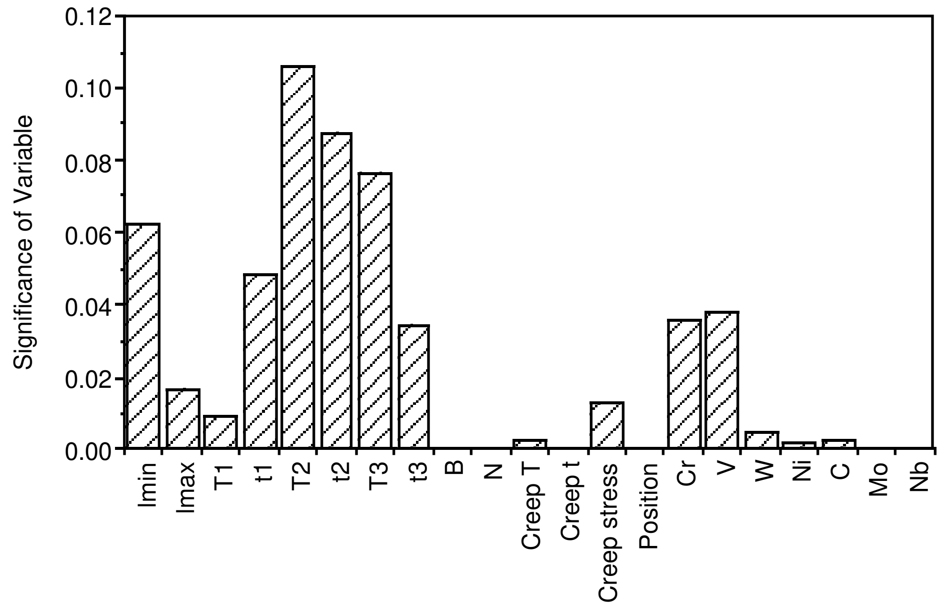

Figure 4: Significance of variables. A large significance implies that the variable concerned explains a large amount of the variation in th dislocation density. It does not imply that the dislocation density is necessarily sensitive to that variable.

perature of third temper and time of the third temper. It is perhaps surprising that the creep stress and position have low significance. It is possible that the effect of creep stress is closely related to a change in the minimum cell dimension and so the importance of the creep stress is represented by the high significance of lmin.

It must be emphasized that the ability to recognise patterns in the noisy experimental data depends on the number of available data. For example, Figure 5 shows the different results from an earlier model produced without using data from one of the alloys. The large difference between the results implies that the robustness of the model is poor. To produce highly reliable dislocation density predictions requires

- Improved accuracy in the experimental data
- More experimental data

6. Summary

An attempt has been made to empirically model dislocation density using the neural network

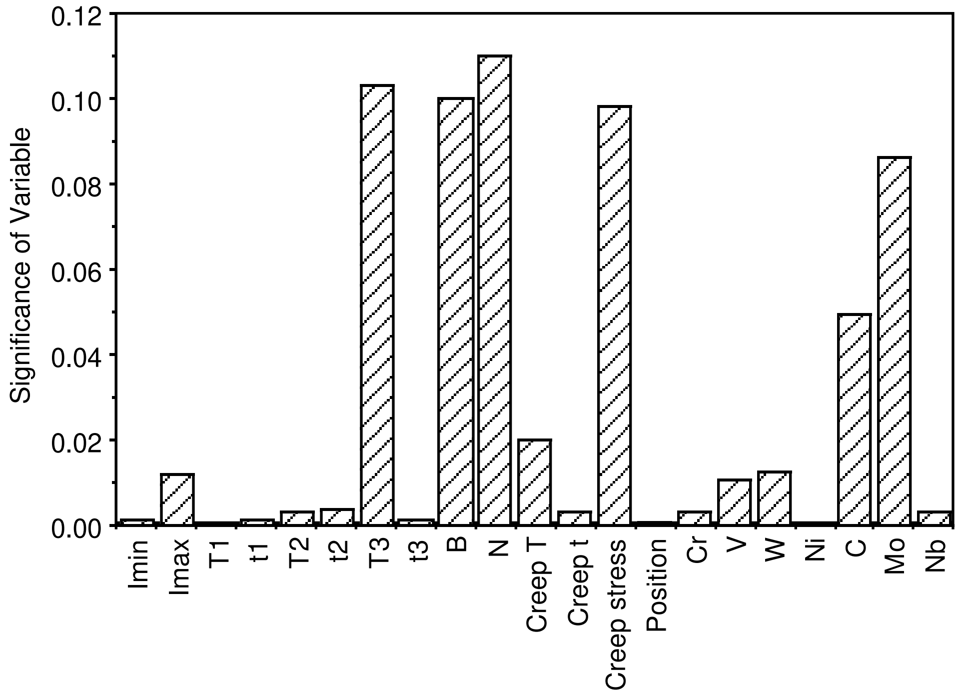

Figure 5: Significance of variables without additional data from one of the alloys.

approach. To produce a meaningful model it has been necessary to account for the high level of inaccuracy associated with the measurement of dislocation density.

The significance of each variable in influencing dislocation density, as perceived by the model has been recorded. Certain variables appear to have greater significances in all the analyses. These variables are B, N and T_3.

The ability to recognise patterns in the data is limited by the small number of imprecise available data and the inaccuracy in the measured dislocation density. Whilst it has been shown that the neural network approach is a promising technique for interpreting the results more data is required if any robust and useful conclusions are to be made.

APPENDIX TWO

Computer Program

This appendix presents the simultaneous kinetics program listing and associated documentation following the MAP format [Bhadeshia, 1995].

MAP FORTRAN LIBRARY

Program MAP_SIM_POWER

0. Provenance of Source Code

J.D. Robson, Phase Transformations Group, Department of Materials Science and Metallurgy, University of Cambridge, Cambridge, U.K.

1. Purpose

To calculate the overall transformation kinetics of phases precipitating under diffusion controlled growth, with particular reference to the precipitation in power plant steels.

2. Specification

This is a self-contained program.

3. Description

The program reads thermodynamic data (e.g. from MTDATA or Thermocalc) from a pre–established database. It then calculates the evolution of volume fraction with time for up to six precipitates forming simultaneously.

4. References

1. J. D. Robson, PhD Thesis, University of Cambridge, 1996

2. J. D. Robson and H. K. D. H. Bhadeshia, 'Simultaneous Kinetics in Power Plant Steels: Part 1 Kinetic Theory', *Mat. Sci. Tech*, Submitted July 1996.

5. Parameters

Input parameters

TC - double precision
    Temperature in °C

TEND- double precision array
    End time for calculation (hours)

DG(6) - double precision array
    Driving force for formation of phase 1–6

XB(6) - double precision array
    Mean composition of species 1–6 (mole fraction)

XC(6,6) - double precision array
    Equilibrium composition of species 1–6 in phase 1–6 (mole fraction)

XA(6,6) - double precision array

Composition of species 1–6 matrix in equilibrium with phase 1–6 (mole fraction)

VMAX(6) - double precision array

Maximum volume fraction of phase 1–6

SFEN(6) - double precision array

Interfacial energy for nuclei of phase 1–6 ($J\,m^{-2}$)

NAD(6) - double precision array

Nucleation site density factor for phases 1–6

CTYPE(6) - double precision array

Morphology for phases 1–6
1 = Needle shaped
2 = Spherical

DS(6) - double precision array

Species assumed to be controlling growth for phase 1–6
1 = Chromium
2 = Molybdenum / Tungsten
3 = Vanadium / Niobium

Output parameters

V(6) - double precision array
Volume fraction of phases 1–6

THRS - double precision
Time in hours

GMOD(6) - double precision array
Extent of reaction parameter for phases 1–6

6. Error Indicators

User is warned if he attempts to input a temperature outside the range for which data is available

7. Accuracy

8. Further Comments

9. Example

9.1 Program data

TC = 600, TEND = 1, STEEL = 1 (Corresponds to 10CrMoV alloy)

9.2 Program results

```
TIME /H VOLUME FRACTIONS (V1 - V6)
0.51000D-01 0.20304D-01 0.74094D-05 0.34489D-04 0.81121D-11 0.28546D-09 0.00000D+00
0.10000D+00 0.20304D-01 0.38936D-04 0.49153D-03 0.42908D-10 0.15387D-08 0.00000D+00
```

```
0.15000D+00 0.20304D-01 0.10028D-03 0.21722D-02 0.11058D-09 0.42385D-08 0.00000D+00
CEMENTITE ENRICHMENT COMPLETE
0.20000D+00 0.17717D-01 0.18089D-03 0.51889D-02 0.19862D-09 0.86902D-08 0.00000D+00
0.25000D+00 0.98748D-02 0.26616D-03 0.85971D-02 0.29045D-09 0.15200D-07 0.00000D+00
0.30000D+00 0.68505D-02 0.34476D-03 0.11515D-01 0.37711D-09 0.24004D-07 0.00000D+00
0.35100D+00 0.52220D-02 0.41464D-03 0.13775D-01 0.45863D-09 0.35559D-07 0.00000D+00
0.40100D+00 0.42359D-02 0.47406D-03 0.15408D-01 0.53299D-09 0.49611D-07 0.00000D+00
0.45100D+00 0.35634D-02 0.52625D-03 0.16624D-01 0.60330D-09 0.66544D-07 0.00000D+00
0.50100D+00 0.30755D-02 0.57274D-03 0.17545D-01 0.67077D-09 0.86531D-07 0.00000D+00
0.55100D+00 0.27052D-02 0.61473D-03 0.18257D-01 0.73628D-09 0.10974D-06 0.00000D+00
0.60100D+00 0.24145D-02 0.65308D-03 0.18818D-01 0.80051D-09 0.13632D-06 0.00000D+00
0.65100D+00 0.21803D-02 0.68847D-03 0.19268D-01 0.86394D-09 0.16643D-06 0.00000D+00
0.70100D+00 0.19876D-02 0.72138D-03 0.19636D-01 0.92693D-09 0.20020D-06 0.00000D+00
0.75100D+00 0.18262D-02 0.75219D-03 0.19940D-01 0.98974D-09 0.23778D-06 0.00000D+00
0.80100D+00 0.16890D-02 0.78121D-03 0.20195D-01 0.10526D-08 0.27931D-06 0.00000D+00
0.85100D+00 0.15710D-02 0.80866D-03 0.20411D-01 0.11156D-08 0.32490D-06 0.00000D+00
0.90100D+00 0.14685D-02 0.83473D-03 0.20596D-01 0.11790D-08 0.37469D-06 0.00000D+00
0.95100D+00 0.13785D-02 0.85956D-03 0.20756D-01 0.12428D-08 0.42879D-06 0.00000D+00
** CALCULATION COMPLETE
```

10. Auxiliary Routines

The subroutines called by this program are

Subroutine in program
CONST
GROWTH
LINEARGROWTH
PARABOLGROWTH
SIZE
NURATE
DIFCO
USER
LINECALC

11. Keywords

simultaneous transformation, power plant steel

Program Listing

```
C SIMULTANEOUS PRECIPITATION KINETICS IN POWER PLANT STEELS
C CALCULATES THE EVOLUTION OF VOLUME FRACTION AS A FUNCTION
C OF TIME.
C ALLOWS FOR SIMULTANEOUS PRECIPITATION AND DISSOLUTION OF
C UP TO 6 PHASES. TAKES ACCOUNT OF SOLUTE DEPLETION FOR TWO
C SPECIES. INCORPORATES A CALCULATION FOR MEAN PARTICLE SIZE
C AND PARTICLE DISTRIBUTION.
C
C
C
      IMPLICIT DOUBLE PRECISION(A-H,K-Z),INTEGER(I,J)
      DOUBLE PRECISION SFEN(6)
      DOUBLE PRECISION NAD(6),XB(6,6),XA(6,6)
      DOUBLE PRECISION XC(6,6),VMAX(6),VDIV(6),V(6)
      DOUBLE PRECISION GMOD(6,6),DV(6),OGMOD(6,6)
      DOUBLE PRECISION DG(6),GRT(6),DVEXT
      DOUBLE PRECISION DVADD(6),VEQ(6)
      DOUBLE PRECISION OMINST(6,6),GROLD(6)
      DOUBLE PRECISION RM(6),DGCHEM(6)
      DOUBLE PRECISION XBINST(6,6),C(6)
      DOUBLE PRECISION DVOLD(6),OMEGA(6,6),NP(6)
      DOUBLE PRECISION DVINC,NR(6),SR(6)
      DOUBLE PRECISION XCI(6),DXCI(6)
      DOUBLE PRECISION SZ(6,10000),GREC(6,10000)
      DOUBLE PRECISION NM(6,10000),TN(6,10000),NRT(6,10000)
      DOUBLE PRECISION M1(7),M2(7),C1(7),C2(7),TMAX(7),TEND
      INTEGER REG,STENO,NSTEELS,DS(6),CTYPE(6)
      INTEGER FLG(6),CNT
      IN1 = 1
      OU2 = 2
      OU3 = 3
      IN2 = 4
      OU4 = 7
      OPEN(UNIT = OU1,FILE='/users/joe/simultrans/volume.d')
      OPEN(UNIT = OU2,FILE='/users/joe/simultrans/nvary.d')
      OPEN(UNIT = OU3,FILE='/users/joe/simultrans/sdist.d')
      OPEN(UNIT = OU4,FILE='/users/joe/simultrans/gvary.d')
      OPEN(UNIT = IN1,FILE='/users/joe/simultrans/constants.d')
      OPEN(UNIT = IN2,FILE='/users/joe/simultrans/thermo.d')
      PI = 3.141592654
      CALL USER(STENO,NSTEELS,TK,IN2,TEND)
      DO 10 I = 1,NSTEELS
       READ(IN2,*) TH,IP
       READ(IN2,*) XB1,XB2,XB3
       DO 15 II = 1,IP
        READ(IN2,*) CT,DSP,VDI,VM,SF,ND,VOBS
        DO 17 IJ = 1,7
         READ(IN2,*) MONE,CONE,TTOP,MTWO,CTWO
         IF (I .EQ. STENO) THEN
```

```
         XB(1,IJ)=XB1
         XB(2,IJ)=XB2
         XB(3,IJ)=XB3
         CTYPE(II)=CT
         DS(II)=DSP
         VMAX(II)=VM
         M1(IJ)=MONE
         M2(IJ)=MTWO
         C1(IJ)=CONE
         C2(IJ)=CTWO
         TMAX(IJ)=TTOP
         IPHASE = IP
         THI = TH
         SFEN(II)=SF
         NAD(II)=ND
         ENDIF
17      CONTINUE
        IF (I .EQ. STENO) THEN
         CALL LINECALC(DG(II),M1(1),M2(1),C1(1),C2(1),TMAX(1),TK)
         CALL LINECALC(XC(1,II),M1(2),M2(2),C1(2),C2(2),TMAX(2),TK)
         CALL LINECALC(XA(1,II),M1(3),M2(3),C1(3),C2(3),TMAX(3),TK)
         CALL LINECALC(XC(2,II),M1(4),M2(4),C1(4),C2(4),TMAX(4),TK)
         CALL LINECALC(XA(2,II),M1(5),M2(5),C1(5),C2(5),TMAX(5),TK)
         CALL LINECALC(VDIV(II),M1(6),M2(6),C1(6),C2(6),TMAX(6),TK)
         CALL LINECALC(VEQ(II),M1(7),M2(7),C1(7),C2(7),TMAX(7),TK)
C
C MX CONTAINS NO CR. VARIABLW WHICH DEFINES CR CONTENT IS USED TO
C DEFINE V OR NB CONTENT OF MX.
C
         IF (DS(II) .EQ. 3) THEN
          XC(3,II) = XC(1,II)
          XA(3,II) = XA(1,II)
          XC(1,II) = 0.0D0
C
C SET XA FOR MX TO APPROPRIATE (EQUILIBRIUM) VALUE
C
          XA(1,II) = XA(1,4)
         ENDIF
        ENDIF
15     CONTINUE
10    CONTINUE
7     FORMAT(2I5,9D13.5)
      CALL DIFCO(D,TK)
C
C READS ASPECT RATIO FOR M2X NEEDLES
C READS IN NEW SFEN AND NAD FOR EACH PHASE FROM SEPERATE
C DATAFILE TO SIMPLIFY ADJUSTING THESE CONSTANTS
C
      READ(IN1,*)BETA,RC,NP(1)
      DO 20 I=1,IPHASE
       READ(IN1,*)SFEN(I),NAD(I)
```

```
20    CONTINUE
C
C ROUTINE FOR OVERALL TRANSFORMATION KINETICS
C
      WRITE(*,*)'  TIME /H     VOLUME FRACTIONS (V1 - V6)'
      WRITE(*,*)
      V(1) = VMAX(1)
      SR(1) = 0.0D0
      SR(2) = 0.0D0
      XCI(1) = XB(1,1)
      XCI(2) = XB(2,1)
C
C IPPF FLAG - SET TO 1 WHEN MAXIMUM VOLUME FRACTION IS REACHED
C
      DO 30 I=2,IPHASE
       GROLD(I) = 1.0D0
       OGMOD(1,I)=2.0D0
       OGMOD(2,I)=2.0D0
       FLG(I) = 0
30    CONTINUE
C
C DT IS STEP SIZE FOR NUMERICAL SUMMATION
C
      DT = (TEND/1000.0D0)
      CNT = 0
      TINST = 0.0D0
40    J = J + 1.0D0
       T = (TEND/100.0D0) * J
       REG = 1
50    TINST = TINST + DT
        N = TINST / DT
        CNT = CNT + 1
        IF (CNT .EQ. 1000) THEN
         WRITE(*,*)'** CALCULATION COMPLETE'
         WRITE(*,*)'** SAVING SIZE DATA TO FILE'
C
C DATA IS SAVED IN REVERSE TIME ORDER (SO SMALLEST SIZE IS FIRST)
C
         DO 45 JI=1,CNT
          JJ = (CNT+1) - JI
          WRITE(OU3,47) SZ(2,JJ),NM(2,JJ),SZ(3,JJ),NM(3,JJ),SZ(4,JJ),
     &    NM(4,JJ),SZ(5,JJ),NM(5,JJ)
          WRITE(OU2,47) TN(2,JJ),NRT(2,JJ),TN(3,JJ),NRT(3,JJ),TN(4,JJ),
     &    NRT(4,JJ),TN(5,JJ),NRT(5,JJ)
          WRITE(OU4,47)  TN(2,JJ),GREC(2,JJ),TN(3,JJ),GREC(3,JJ),
     &    TN(4,JJ),GREC(4,JJ),TN(5,JJ),GREC(5,JJ)
45       CONTINUE
         STOP
         ENDIF
47       FORMAT(8D12.5)
C
```

```
C SR(1) GIVES THE TOTAL SOLUTE REMOVED BY ENRICHMENT AND PRECIPITATION
C
        SR(1) = (V(1)*(XCI(1)-XA(1,1)))
        SR(2) = (V(1)*(XCI(2)-XA(2,1)))
        SR(3) = (V(1)*(XCI(3)-XA(3,1)))
        DO 55 I = 2,IPHASE
         SR(1) = SR(1) + ((V(I)*(XC(1,I)-XA(1,I))))
         SR(2) = SR(2) + ((V(I)*(XC(2,I)-XA(2,I))))
         SR(3) = SR(3) + ((V(I)*(XC(3,I)-XA(3,I))))
55       CONTINUE
         DO 60 I = 1,IPHASE
          IF (FLG(I) .EQ. 0) THEN
           IF (XA(1,I) .NE. XB(1,I)) THEN
            GMOD(1,I) = 1.0D0 - (SR(1)/(XB(1,I)-XA(1,I)))
           ENDIF
           IF (XA(2,I) .NE. XB(2,I)) THEN
            GMOD(2,I) = 1.0D0 - (SR(2)/(XB(2,I)-XA(2,I)))
           ENDIF
           IF (XA(3,I) .NE. XB(3,I)) THEN
            GMOD(3,I) = 1.0D0 - (SR(3)/(XB(3,I)-XA(3,I)))
           ENDIF
C
C SETS GMOD FOR PHASE EQUAL TO THE GMOD VALUE FOR GROWTH CONTROLLING SPECIES
C
           GMOD(1,I)=GMOD(DS(I),I)
           GMOD(2,I)=GMOD(DS(I),I)
           GMOD(3,I)=GMOD(DS(I),I)
          ELSE
           GMOD(1,I)=0.0D0
           GMOD(2,I)=0.0D0
           GMOD(3,I)=0.0D0
          ENDIF
          IF (GMOD(1,I) .LE. 0.0D0) THEN
           GMOD(1,I) = 0.0D0
           GMOD(2,I) = 0.0D0
           IF (FLG(I) .NE. 2) THEN
            FLG(I) = 1
           ENDIF
          ENDIF
          OGMOD(1,I)=GMOD(1,I)
          OGMOD(2,I)=GMOD(2,I)
          DGCHEM(I) = GMOD(1,I) * DG(I)
          XBINST(1,I) = (GMOD(1,I) * (XB(1,I)-XA(1,I))) + XA(1,I)
          XBINST(2,I) = (GMOD(2,I) * (XB(2,I)-XA(2,I))) + XA(2,I)
          XBINST(3,I) = (GMOD(3,I) * (XB(3,I)-XA(3,I))) + XA(3,I)
          OMINST(1,I) = GMOD(1,I) * OMEGA(1,I)
          DVADD(I) = 0.0D0
60        CONTINUE
C
C ENRICHMENT OR VOLUME DECREASE OF CEMENTITE
C
```

```
          RM(1) = (3.0D0 * V(1))/((4.0D0 * NP(1) * PI))
     &     **(1.0D0/3.0D0)
          DV(1) = 0.0D0
          IF (FLG(1) .EQ. 0) THEN
           DXCI(1) = ((4.0D0 * (D**(0.5)) * (XBINST(1,1)-XA(1,1))
     &     * (DT**(0.5)))/(THI * (PI**(0.5))))
           DXCI(2) = ((4.0D0 * (D**(0.5)) * (XBINST(2,1)-XA(2,1))
     &     * (DT**(0.5)))/(THI * (PI**(0.5))))
           XCI(1) = XCI(1) + DXCI(1)
           XCI(2) = XCI(2) + DXCI(2)
          ELSE
C
C CEMENTITE DISSOLVES TO PROVIDE SOLUTE TO REMAINING PRECIPITATES
C DIFFUSION FROM CEMENTITE TO PRECIPITATES CONTROLS THE DISSOLUTION OF
C CEMENTITE
C
           DO 70 I = 2,IPHASE
C
C THERE WILL ONLY BE A FLUX FROM CEMENTITE TO ANOTHER PHASE IF XA FOR
C THE CORRECT SPECIES IN THE PRECIPITATING PHASE IS LESS THAN
C XA FOR THE CORRECT SPECIES IN THE DISSOLVING PHASE
C
           IF (XA(1,1) .GT. XA(1,I)) THEN
            DVFLUX = -(4.0D0 * PI * (RM(1)**2.0D0)) *
     &      (4.0D0 * ((NP(1)+NP(I))**(1.0D0/3.0D0))) * D *
     &      (((XA(1,1) - XA(1,I)) * DT)/(XCI(1)
     &       - XA(1,1)))
            DV(1) = DV(1) + (NP(1) * DVFLUX)
           ENDIF
70        CONTINUE
         ENDIF
         DXCI(1) =0.0D0
         DXCI(2) =0.0D0
         V(1) = V(1) + DV(1)
         IF (V(1).LT. 0.0D0) V(1) = 0.0D0
C
C PRECIPITATION OR VOLUME DECREASE OF OTHER PHASES
C
         DO 80 I = 2,IPHASE
          IF (FLG(I) .EQ. 0) THEN
           IF (DGCHEM(I) .LT. 0.0D0) THEN
            CALL NURATE(NR(I),DGCHEM(I),SFEN(I),NAD(I),VDIV(I),TK)
           ELSE
            NR(I) = 0.0D0
           ENDIF
           NP(I) = NP(I) + (NR(I) * DT)
C
C ONLY HAVE GROWTH IF COMPOSITION IS DIFFERENT FROM BULK COMPOSITION
C
           IF (XC(DS(I),I) .NE. XA(DS(I),I)) THEN
            CALL GROWTH
```

```
     &       (GRT(I),CTYPE(I),XBINST(DS(I),I),XA(DS(I),I),XC(DS(I),I),
     &       D,RC)
            ELSE
             GRT(I) = 0.0D0
            ENDIF
           ENDIF
           CALL SIZE(RM(I),CTYPE(I),GRT(I),V(I),NP(I),BETA)
           CALL CONST(C(I),CTYPE(I),GRT(I),BETA)
C
C FOR SIZE DISTRIBUTION OF PARTICLES NUCLEATING/ GROWING
C
           DVEXT = 0.0D0
C
C FINDING THE INCREASE IN THE EXTENDED VOLUME, DVEXT(I)
C
           IF (FLG(I) .EQ. 0) THEN
            TN(I,CNT)=TINST/3600.0D0
            NM(I,CNT)=(NR(I) * DT)
            NRT(I,CNT)=NR(I)
            GREC(I,CNT)=GRT(I)
            DO 87 IIJJ = 0,CNT
             IF (CTYPE(I) .EQ. 2) THEN
              NUTERM = (IIJJ**0.5D0)*NRT(I,CNT-IIJJ)
              DVINC = (C(I)*(DT**(5.0D0/2.0D0))
     &        * NUTERM)
              IF (IIJJ .LT. CNT) THEN
               SZ(I,IIJJ)= SZ(I,IIJJ) +
     &         (0.5D0 * GRT(I) * (((CNT-IIJJ)*DT)**-0.5)
     &          * DT)
              ENDIF
              DVEXT = DVEXT + DVINC
             ENDIF
             IF (CTYPE(I) .EQ. 1) THEN
              NUTERM = (IIJJ**2.0D0) * NRT(I,CNT-IIJJ)
              DVINC = (C(I) * (DT**4.0D0)
     &        * NUTERM)
              SZ(I,IIJJ)=SZ(I,IIJJ) + (GRT(I) * DT)
              DVEXT = DVEXT + DVINC
             ENDIF
87          CONTINUE
            DV(I) = (1.0D0 - (V(1)+V(2)+V(3)+V(4)
     &      +V(5)+V(6))) * (DVEXT)
           ELSE
C
C OTHER NON-EQUILIBRIUM PHASES DISSOLVE TO PROVIDE SOLUTE TO THE
C REMAINING PRECIPITATES. DIFFUSION FROM THE DISSOLVING PHASES TO
C THE PRECIPITATING PHASES CONTROLS THE DISSOLUTION RATE
C
           DO 90 II = I+1,IPHASE
C
C THERE WILL ONLY BE A FLUX FROM ONE PHASE TO ANOTHER IF XA FOR
```

```
C THE CORRECT SPECIES IN THE PRECIPITATING PHASE IS LESS THAN
C XA FOR THE CORRECT SPECIES IN THE DISSOLVING PHASE
C
C THERE WILL ALSO ONLY BE A FLUX IF THE PHASE IS PRESENT IN THE
C FIRST PLACE - IE COMPOSITION DIFFERS FROM THAT OF BULK
C
           IF(XC(DS(I),I) .NE. XA(DS(I),I)) THEN
            IF (XA(DS(I),I) .GT. XA(DS(I),II)) THEN
             IF (CTYPE(I) .EQ. 1) THEN
              DVFLUX = -4.0D0 *
     &        ((NP(II) + NP(I))**(1.0D0/3.0D0)) *
     &        (PI/BETA**2.0D0) * 3.0D0 * (RM(I)**2.0D0)
     &        * ((D * DT * (XA(DS(I),I) - XA(DS(I),II)))
     &        /(XC(DS(I),I) - XA(DS(I),I)))
             ENDIF
             IF (CTYPE(I) .EQ. 2) THEN
              DVFLUX = - (4.0D0 * PI * (RM(I)**2.0D0)) *
     &        (4.0D0 * ((NP(II) +NP(I))**(1.0D0/3.0D0))
     &         * D * (XA(DS(I),I) - XA(DS(I),II)) * DT)/
     &        (XC(DS(I),I) - XA(DS(I),I))
             ENDIF
             DV(I) = DV(I) + (NP(I) * DVFLUX)
C
C DO NOT LET VF FALL BELOW EQUIM VALUE
C
             IF (V(I) .LE. VEQ(I)) THEN
              DV(I) =0.0D0
              DVADD(II) =0.0D0
             ENDIF
            ENDIF
           ENDIF
90        CONTINUE
         ENDIF
         V(I) = V(I) + DV(I) + DVADD(I)
         IF (V(I) .LT. 0.0D0) V(I) = 0.0D0
         IF (V(I) .GT. VMAX(I)) THEN
          V(I) = VMAX(I)
          GRT(I) = 0.0D0
          NR(I) = 0.0D0
          IF (FLG(I) .NE. 2) THEN
           FLG(I) = 1
         ENDIF
        ENDIF
C
C STOPS M23C6 EXCEEDING ITS EQUILIBRIUM COMPOSITION
C THIS IS REQUIRED BECAUSE THE M23C6 CR LEVEL IS ASSUMED TO BE
C THE EQUILIBRIUM LEVEL. IF THIS IS NOT TRUE THEN THE EQUILIBRIUM
C LEVEL OF M23C6 IS SET ZERO
C
        IF (V(I) .GT. VEQ(I)) THEN
C
```

```
C DS(I)=1 AND CTYPE(I)=2 CORRESPONDS UNIQUELY TO M23C6
C
         IF ((DS(I) .EQ. 1) .AND. (CTYPE(I) .EQ. 2)) THEN
          V(I) = VEQ(I)
          GRT(I) = 0.0D0
          NR(I) = 0.0D0
          IF (FLG(I) .NE. 2) THEN
           FLG(I) = 1
          ENDIF
         ENDIF
        ENDIF
        IF (GRT(I) .GT. 0.0D0) GROLD(I) = GRT(I)
         DVOLD(I) = DV(I)
         DV(I) = 0.0D0
         IF (FLG(I) .EQ. 1) THEN
          WRITE(*,*)'PRECIPITATION OF PHASE COMPLETE FOR PHASE ',I
          FLG(I) = 2
         ENDIF
80      CONTINUE
        REG = 0
        IF (FLG(1) .EQ. 1) THEN
         WRITE(*,*)'CEMENTITE ENRICHMENT COMPLETE'
         FLG(1) = 2
        ENDIF
        IF (TINST .GE. T) THEN
         WRITE(*,200) TINST/3600.0D0,V(1),V(2),V(3),V(4),
     &   V(5),V(6)
         WRITE(OU1,200) TINST/3600.0D0,V(1),V(2),V(3),V(4)
     &   ,V(5),V(6)
        GOTO 40
       ELSE
       IF ((GMOD(1,1) .EQ. 0.0D0) .AND.
     &  (GMOD(1,2) .EQ. 0.0D0)
     &  .AND. (GMOD(1,3) .EQ. 0.0D0)
     &  .AND. (GMOD(1,4) .EQ. 0.0D0)
     &  .AND. (GMOD(1,5) .EQ. 0.0D0)) THEN
        WRITE(*,*)'**ALL TRANSFORMATIONS COMPLETE**'
        WRITE(*,200) TINST/3600.0D0,V(1),V(2),V(3),V(4),
     &  V(5),V(6)
        STOP
       ELSE
        GOTO 50
       ENDIF
      ENDIF
200   FORMAT(7D12.5)
      STOP
      END
C
C************************************************************
C
C CALCULATES CONSTANT IN KINETICS EQUATION FOR CORRECT
```

```
C PARTICLE TYPE
C
      SUBROUTINE CONST(C,CTYPE,GRT,BETA)
      IMPLICIT DOUBLE PRECISION(A-H,K-Z),INTEGER(I,J)
      INTEGER CTYPE
      PI = 3.141592654
      IF (CTYPE .EQ. 1) THEN
          C = (3.0D0 * (GRT**3.0D0) * PI)/(4.0D0 * (BETA **2.0D0))
      ENDIF
      IF (CTYPE .EQ. 2) THEN
          C = (3.0D0/2.0D0) * PI * (GRT **3.0D0)
      ENDIF
      RETURN
      END
C
C************************************************************
C
C CALLS SUBROUTINE FOR GROWTH DEPENDING ON PARTICLE TYPE
C
      SUBROUTINE GROWTH(GRT,CTYPE,XB,XA,XC,D,RC)
      INTEGER CTYPE
      IMPLICIT DOUBLE PRECISION(A-H,K-Z),INTEGER(I,J)
      IF (CTYPE .EQ. 1) THEN
         CALL LINEARGROWTH (GRT,XA,XC,XB,D,RC)
      ENDIF
      IF (CTYPE .EQ. 2) THEN
         CALL PARABOLGROWTH(GRT,XB,XA,XC,D)
      ENDIF
      RETURN
      END
C
C************************************************************
C
C CALCULATES THE GROWTH RATE FOR LINEAR GROWTH (I.E. NEEDLES)
C
      SUBROUTINE LINEARGROWTH(GR,XA,XC,XB,D,RC)
      IMPLICIT DOUBLE PRECISION(A-H,K-Z),INTEGER(I,J)
      OMEGA = (XB - XA)/(XC - XA)
      GR = (D * OMEGA)/(4 * RC)
      RETURN
      END
C
C************************************************************
C
C CALCULATES THE GROWTH CONSTANT (ALPHA3) FOR PARABOLLIC GROWTH
C
      SUBROUTINE PARABOLGROWTH(GC,XB,XA,XC,D)
      IMPLICIT DOUBLE PRECISION(A-H,K-Z),INTEGER(I,J)
      OMEGA = (XB - XA)/(XC - XA)
C
C GROWTH PARAMETER (P. 488 CHRISTIAN)
```

```
C
      ALPHA = (2.0D0**(0.5D0)) * ((XB - XA) ** (0.5D0))
     & / ((XC - XB) ** (0.5D0))
      GC = ALPHA * (D**(0.5D0))
      RETURN
      END
C
C*******************************************************
C
C CALCULATES AVERAGE PARTICLE SIZES
C
      SUBROUTINE SIZE(RM,CTYPE,GRT,V,NP,BETA)
      IMPLICIT DOUBLE PRECISION(A-H,K-Z),INTEGER(I,J)
      INTEGER CTYPE
      PI = 3.141592654
      IF ((V .EQ. 0.0D0) .OR. (NP .EQ. 0.0D0)) THEN
         RM = 0.0D0
      ELSE
        IF (CTYPE .EQ. 1) THEN
          RM = (((BETA**2.0D0) * V)/(PI * NP)) ** (1.0D0/3.0D0)
        ENDIF
        IF (CTYPE .EQ. 2) THEN
          RM =((3.0D0 * V)/(4.0D0 * NP * PI)) ** (1.0D0/3.0D0)
        ENDIF
      ENDIF
      RETURN
      END
C
C*******************************************************
C
C CALCULATES NUCLEATION RATE
C
      SUBROUTINE NURATE(NR1,DGCHEM,SFEN1,NAD1,VMAX,TK)
      IMPLICIT DOUBLE PRECISION(A-H,K-Z),INTEGER(I,J)
       K = 1.380662D-23
       NA = 6.022045D23
       H = 6.626176D-34
       SHAPE=1.0D0
       DGVOL = (DGCHEM/VMAX) * 1.437D5
       ACTIVE = (240.0D3/2.0D0)/NA
       PI = 3.141592654
       CALL TSITES(NUSITES,TK)
       N1 = NAD1 * NUSITES
       DGCRIT1 = (16.0D0*PI*((SFEN1*SHAPE)**3.0D0))/
     &  (3.0D0*(DGVOL**2.0D0))
       EPENT1 = -(DGCRIT1 + ACTIVE)/(K * TK)
       CONST1 = (N1 * K * TK)/H
       NR1 = CONST1 * DEXP(EPENT1)
       RETURN
       END
C
```

```
C*******************************************************
C
C CALCULATES THE TOTAL NUMBER OF SITES FOR NUCLEATION FOR
C M3C. THIS IS SCALED TO GIVE THE NUMBER OF SITES FOR OTHER
C PRECIPITATES
C
      SUBROUTINE TSITES(NUSITES,TK)
      IMPLICIT DOUBLE PRECISION(A-H,K-Z),INTEGER(I,J)
      PI = 3.141592654
         RIN = (2.26D0 - (6.4D-3 * TK) + (4.6D-6 * (TK**2)))
     &         * 1D-21
        NUSITES = 1.0D0/((4.0D0/3.0D0) * PI * RIN)
      RETURN
      END
C
C*******************************************************
C
C  CALCULATES DIFFUSION COEFFICIENT OF CR IN FE
C
      SUBROUTINE DIFCO(D,TK)
      IMPLICIT DOUBLE PRECISION(A-H,K-Z),INTEGER(I,J)
          D0 = 1.5D-04
          Q = 240D03
          R = 8.314408694
          D = D0 * DEXP(-Q/(R*TK))
      RETURN
      END
C
C*******************************************************
C
C  USER INPUT
C
      SUBROUTINE USER(STENO,NSTEELS,TK,IN2,TEND)
      IMPLICIT DOUBLE PRECISION(A-H,K-Z),INTEGER(I,J)
      INTEGER STENO,NSTEELS
      CHARACTER*20 STEEL
      WRITE(*,*)'** SIMULTANEOUS TRANSFORMATIONS PROGRAM **'
      WRITE(*,*)
      WRITE(*,*)'DATA ARE AVAILABLE FOR THE FOLLOWING STEEL(S)'
      WRITE(*,*)
      READ(IN2,*) NSTEELS
      DO 5 IIS = 1,NSTEELS
         READ(IN2,51) STEEL
         WRITE(*,*) IIS,'-',STEEL
5     CONTINUE
51    FORMAT (A20)
      WRITE(*,*)
      WRITE(*,*)'SELECT STEEL TO USE FOR CALCULATIONS'
52      READ(*,*) STENO
      IF ((STENO .LT. 1) .OR. (STENO .GT. NSTEELS)) THEN
         WRITE(*,*)'**OUT OF RANGE, ENTER NEW STEEL NUMBER'
```

```
         GOTO 52
      ENDIF
53    WRITE(*,*)'WHAT TEMPERATURE FOR CALCULATIONS (500-800 degC) ?'
      READ(*,*) TC
      IF ((TC .LT. 500.0) .OR. (TC .GT. 800.0)) THEN
         WRITE(*,*)'**TEMPERATURE OUT OF RANGE, SELECT AN OPTION'
         WRITE(*,*)
         WRITE(*,*)'1-PROCEED, RESULTS LIKELY TO BE UNRELIABLE'
         WRITE(*,*)'2-ENTER A DIFFERENT TEMPERATURE'
         READ(*,*) IOPT
         IF (IOPT .NE. 1) GOTO 53
      ENDIF
      WRITE(*,*)'WHAT END TIME FOR CALCULATION (HRS) ?'
      READ(*,*) TENDH
      TEND = TENDH*3600.0D0
      TK = TC + 273.0D0
      RETURN
      END
C
C************************************************************
C
C  CALCULATES COMPOSITIONS/FREE ENERGIES FROM LINE FIT
C
      SUBROUTINE LINECALC(Y,M1,M2,C1,C2,TMAX,TK)
      IMPLICIT DOUBLE PRECISION(A-H,K-Z),INTEGER(I,J)
      IF (TK .GE. TMAX) THEN
         Y = (M2 * TK) + C2
      ELSE
         Y = (M1 * TK) + C1
      ENDIF
      RETURN
      END
```

REFERENCES

Andrews, K. W., Dyson, D. J. and Keown, S. R.: 'Intepretation of Electron Diffraction Patterns', Hilger and Watts, London (1967)

Avrami, M.: *J. Chem. Phys.* **7** (1939) p. 1103

Avrami, M.: *J. Chem. Phys.* **8** (1940) p. 212

Avrami, M.: *J. Chem. Phys.* **9** (1941) p. 177

Bagaryatski, Y. A.: *Dokl. Akad. Nauk. SSSR* **73** (1950) p. 1161

Baker, R. G. and Nutting J.: *J. Iron Steel Inst.* **192** (1959) p. 257–268

Balluffi, R. W., Cohen, M. and Averbach, B. L.: *Trans Am. Soc. Met.* **43** (1951) p. 497–526

Beech, J. and Warrington, D. H.: *J. Iron Steel Inst.* **204** (1966) p. 460–468

Berger, C., Beech, S. M., Mayer K. H., Staubli M. and Thornton D. V.: International Joint Power Generation Conference, Kansas, U.S.A. (1993)

Berger, C.: COST 501, WP 11 Minutes of Seventh Meeting, Vienna (1995)

Bhadehia, H. K. D. H.: MAP – Materials Algorithms Project (1995)

Bhadeshia, H. K. D. H. and Christian, J. W.: *Met. Trans A* **21A** (1990) p. 767–797

Bhadeshia, H. K. D. H.: 'Bainite in Steels', Institute of Materials, London (1992)

Bjärbo, A.: 'Microstructural Changes in a 12% Chromium Steel During Creep', Report, Royal Institute of Technology, Stockholm, Sweden (1994) p. 11

Blum, R., Hald, J., Benidick, W., Rosselet A. and Vaillant J.: 'Newly Developed High Temperature Ferritic–Martensitic Steels from USA, Japan and Europe', International VGB Conference – Fossil-fired Power Plant with Advanced Design Parameters, Kolding, Denmark (June, 1993)

Briggs J. Z. and Parker T. D.: 'The Super 12% Cr Steels', Climax Molybdenum Company (1965)

Callister, W. D.: 'Materials Science and Engineering – An Introduction', John Wiley and Sons, Inc. New York (1991) p. 228

Cerjak, H.: COST 501, WP 11 Minutes of Eighth Meeting, Cambridge (1995)

Christian, J. W.: 'Theory of Transformations in Metals and Alloys', Part 1, 2nd Edition, Pergamon Press, Oxford (1975)

Darbyshire, J. M. and Barford, J.: Central Electricity Research Laboratory Report (1966)

Darbyshire, J. W. and Barford, J.: 'lq The Mechanism of Phase Transformations in Crystalline Solids', Institute of Metals (1969) p. 65

Davison, J. K. and Yeldham, D. E.: 'Materials in Power Plant', Boiler Tube Failures and their Causes **3–3** (1975)

Fridberg, J., Torndahl, L–E and Hillert, M.: *Jernkontorets Ann.* **153** (1969) p. 263–276

Frost, H. J. and Ashby, M. F.: 'The Plasticity and Creep of Metals and Ceramics', Pergammon Press, Oxford (1982)

Fujita, T.: *Advanced Materials and Processes* **4** (1992) p. 42–47

Fujita, T.: *Trans JIM* **9** (1968) Suppliment

Gooch, D. J.: *Metals Science* **16** (1982) p. 79–89

Gooch, D. J.: 'Turbine Materials for Advanced Steam Cycles', National Power Report (March 1993) p. 1

Greenwell, B. S. and Beech, S. M.: 'The Rupture Ductility of High Alloy Ferritic Steels' power industry conference, Leige, Belgium (1994)

Hald, J.: COST 501, WP 11 Report (1994)

Hall, M. G., Kinsman, K. R. and Aaronson, H. I.: *Met. Trans A* **3A** (1972) p. 1320

Ham, F. S.: *J. Appl. Phys.* **30** (1959) p. 915

Harvey P. D.: 'Engineering Properties of Steel', Am. Soc. Met. (1982)

Hillert, M.: *Jernkontorets Ann.* **141** (1957) p. 757

Hodson, S. M.: MTDATA–Metallurgical and Thermochemical Databank, National Physical Laboratory, Teddington, U. K. (1989)

Honeycombe, R. W. K.: 'Tempering of Molybdenum Steels', Chapter 5 (1974)

Horvay, G. and Cahn, J. W.: *Acta Metall.* **9** (1961) p. 695

Hosoi, Y., Wade, N. and Urita T.: *Trans Iron Steel Inst. Japan* **26** (1986) B-30

Hultgren, A.: *Trans Am. Soc. Met.* **39** (1947) p. 415

Inden, G., Franke, P. and Knoop, U.: 'Computer Simulation of Phase Transformations and Microstructural Evolution', Computer Inovation of New Materials II, Elsevier Science Publications (1993) p. 701–706

Irvine K. J. and Pickering F. B.: 'High–Strength 12% Chromium Steels' (1964)

Iseda, A., Sawaragi Y., Kato, S. and Masuyama, F.: 5th International Conference on Creep of Materials, Lake Buena Vista, Florida, U.S.A. (1992)

Janovec, J., Vyrostkova, A. and Svoboda, M.: *Met. Trans A* **25A** (1994) p. 267–275

Johnson, W. A. and Mehl, R. F.: *Trans Am. Inst. Min. (Metall.) Engrs.* **135** (1939) p. 416

Klueth, R. L. and Nasreldin, A. M.: Met. Trans A **18A** (1987) p. 1279

Kuo, K.: *J. Iron Steel Inst.* **173** (1953) p. 363–375

Kurzydlowski, K. J. and Zielinski, W.: *Metal Science* **18** (1984) p. 223–224

Lai, J. K. L. and Meshkat, M.: *Metal Science* (September, 1978) p. 415–420

Lupton, J. B.: *Met. Sci. J* **5** (1971) p. 160

MacKay, D. J. C.: *Network* (1994a) in press

MacKay, D. J. C.: *Neural Computation* **4** (1992a) p. 415–447

MacKay, D. J. C.: *Neural Computation* **4** (1992b) p. 448–472

MacKay, D. J. C.: 'Maximum Entropy and Baysian Methods', ed. G. Heidbreder, Santa Barbara (1994b) in press

Marrison, T. and Hogg: *J. Met. Soc.* **151** (1972)

Mimura, H., Ohgami, M. Naoi, H. and Fujita, T.: TMS Fall Meeting, Pittsburgh (1993)

Murphy, S. and Whiteman, J. A.: *Met. Sci. J* **4** (1970) p. 58–62

Nickel, H., Ennis P. J., Wachter O.: 'The Effect of Heat Treatment on the Microstructure and Creep Properties of 9Cr–0.5Mo–1.8W Steel' , Am. Soc. Met.E/JSME Pressure Vessels and Piping Conference, Honolulu, Hawaii (1995)

Norton, F. H.: 'Creep of Steel at High Temperatures', Mc-Graw–Hill, New York (1929) p. 67

Park, I. M. and Fujita, T.: *Trans Iron Steel Inst. Japan* **20** (1982) p. 830–837

Pickering F. B.: 'Historical Development and Microstructure of High Chromium Ferritic Steels, Microstructural Development and Stability in High Chromium Ferritic Power Plant Steels', Cambridge, U.K. (1995)

Pickering, F. B. and Vassiliou, A. D.: *Metals Technology* (October, 1980) p. 409–413

Pitsch, W. and Schrader, A.: *Arch. Eisenhuettenw* **29** (1958) p. 715

Porter, D. A. and Easterling, K. E.: 'Phase Transformations in Metals and Alloys', 2nd Edition, Chapman and Hall, London (1993)

Purdy, G. R.: *Met. Sci. J.* **5** (1971) p. 81

Raynor D., Whiteman, J. A. and Honeycombe, R. W. K.: *J. Iron Steel Inst.* (April, 1966) p. 349–354

Reed–Hill, R. and Abbachian, R.: 'Physical Metallurgy Principles', PWS Kent, Boston (1992) p. 844

Sakuma, T., Yong Wey, M. and Nishizawa, T.: *Trans Japan. Inst. Met.* **22** (1981) p. 733–742

Sanderson, S. J.: 'Mechanical Properties and Metallurgy of 9% Cr–1% Mo Steel', Ferritic Steels for High Temperature Applications, Am. Soc. Met. (1983) p. 85–99

Senior, B. A.: *Mat. Sci. Eng.* **119A** (1989)

Shaw, S. W. K. and Quarrell, A. G.: *J. Iron Steel Inst.* **185** (1957) p. 10–22

Smith, R. and Nutting, J.: *British Journal of Applied Physics* **7** (1957) p. 214–217

Smith, R.: Ph.D. Thesis, University of Sheffield (1959)

Spiradek, K., Bauer, R. and Zeiler, G.: Materials for Advanced Power Engineering, Leige, Belgium (1994) p. 251–262

Strang A. and Vodarek V.: Private communication (1996a)

Strang A. and Vodarek V.: 'Z–Phase Formation in a Martensitic 12CrMoVNb Steel' *Mat. Sci Tech.* (Submitted March 1996b)

Straub, S., Meier, M, Ostermann, J. and Blum, W.: *VGB Kraftwerkstechnik* **73** (1993) p. 646–653

Takahashi, M. and Bhadeshia, H. K. D. H.: *Mat. Sci. Tech.* **6** (1990) p. 562–603

Takeda, Y. and Masuyama, F.: 1st International Conference on Heat Resisting Materials, Wisconsin, U.S.A. (1991)

Thomson, R. C.: Ph.D. Thesis, University of Cambridge, U.K. (1992)

Trevedi, R.: *Acta metall.* **18** (1970) p. 287

Tsuchiyama, T. and Fujita, T.: *J. Soc. Mater. Sci. Japan* **30** (1981) p. 421–423

Vanstone, R. W.: 'Microstructure and Creep Mechanisms in Advanced 9–12% Cr Creep Resisting Steels', Materials for Advanced Power Engineering, Liege, Belgium (1994)

Venogopulan, D. and Kirkaldy, J. S.: 'Hardenability Concepts with Applications to Steels', AIME Conference, New York (1978) p. 249

Wachter, O. and Ennis, P. J.: Ph.D. Thesis, Teshnische Hohschule, Aachen, Germany (1995) p. 6–16

Weisman, J. and Eckhart, R.: 'Modern Power Plant Engineering', Prenice Hall (1985)

Wert, C. and Zener, C.: *J. Appl. Phys.* **21** (1950) p. 5

Wilkes, P.: *Met. Sci. J.* **2** (1968) p. 8–11

Williams K. R., and Wilshire, B.: *Mat. Sci. Eng.* **28** (1977) p. 289–296

Woodhead, J. H. and Quarrell, A. G.: *J. Iron Steel Inst.* **203** (1965) p. 605–620

Yakel, H. L.: *International Metals Reviews* **30(1)** (1985) p. 17–40

Zener, C.: *Trans Am. Inst. Min. (Metall.) Engrs.* **167** (1946) p. 550